Vibroacoustics of timber-frame structures excited by structure-borne sound sources

Thesis submitted in accordance with the requirements of the University of Liverpool for the degree of Doctor in Philosophy

by

Fabian Schöpfer

February 2019

To Helena and Anian

"In theory, there is no difference between theory and practice. But, in practice, there is."

- Walter J. Savitch

Vibroacoustics of timber-frame structures excited by structure-borne sound sources

Fabian Schöpfer

This thesis investigates the measurement and prediction of machinery noise in timber-frame buildings. To quantify the structure-borne sound power input from multi-point sources, simplified approaches were assessed that reduce the required data for out-of-plane force excitation. This identified approaches that give estimates within ±5 dB from 20 Hz to 2000 Hz. To investigative the importance of out-of-plane moment excitation, inverse methods were used to determine the power input; these were affected by noise but processing was used to overcome this shortcoming. A series of experimental investigations were carried out on a timber-frame structure undergoing mechanical point excitation. The driving-point mobility showed orthotropic plate characteristics at low frequencies, ribbed-plate characteristics in a narrow frequency band and infinite plate characteristics in mid- and high-frequency ranges. The moment mobility above or in-between studs was similar to infinite beam or plate theory with interpolation between these theories where necessary. The experimental work indicated the potential to use Statistical Energy Analysis (SEA) to predict sound transmission. The first experimental finding was that above the mass-spring-mass resonance frequency, the vibrational response of the wall leaves was uncorrelated. The second was a significant decrease in vibration across the wall from the excitation point, with structural intensity showing a decrease in net power flow across successive timber studs. The third was that tongue and groove connections between chipboard sheets significantly reduce the vibration transmission above 500 Hz. This led to different SEA models being used to model a timber-frame wall undergoing mechanical point excitation. A 41-subsystem model was found to be necessary to reproduce the measured vibration levels on both leaves within ≈10 dB. As there is a significant decrease in vibration with distance in the mid- and high-frequency range, the region close to the excitation point is particularly important and the SEA model has better accuracy in this region. An alternative engineering approach to the prediction of machinery noise in timber-frame buildings was introduced and validated that used measured transmission functions between the injected power and the spatial-average sound pressure level in a receiving room. A field survey and case studies indicate this is a feasible and practical approach.

Acknowledgements

I would like to express my sincere gratitude to my supervisor Professor Carl Hopkins for his guidance and motivation throughout the thesis. The passion and effort he put into the supervision motivated me during all the years. His confidence in my work was key a factor especially in periods when I was disappointed by drawbacks. I would also like to thank my secondary supervisor Professor Barry Gibbs. He inspired me with his immense experience and knowledge in the field of structure-borne sound source characterization and his ideas for practical approaches of complex aspects. The kindness of both my supervisors made the thesis work and meetings very enjoyable.

My sincere thanks go to Professor Dr Ulrich Schanda and Dr Andreas Mayr of the Technical University of Applied Sciences Rosenheim. Their idea for the research topic, the application for funding and confidence in me made this thesis possible in the first place. I am very grateful for the unfailing support of Professor Dr Ulrich Schanda during all the years in the Laboratory for Sound Measurement (LaSM) since my Diploma thesis. I highly appreciate how he provided me with the best circumstances I could imagine to do a PhD thesis. Having Dr Andreas Mayr as a kind of mentor was a key factor for me as he guided and encouraged me throughout the thesis work. I gained a lot from the personal advices he gave me based on his own experience.

I thank my colleagues in the LaSM for the stimulating discussions and the support in measurements and construction work in the laboratory. A major role in the LaSM played Simon Mecking who is my constant fellow labmate since our early years in the field of acoustics. Being in the same situation we gained a lot from our teamwork. Thanks also to Katja Heinrich and Dennis Grünewald by contributing to this work with their Bachelor thesis.

I thank the Technical University of Applied Sciences Rosenheim for hosting my PhD work. In particular I thank the administrative team of the research and development department for the support in administrative tasks that come along in research projects.

Thanks to Dr Pyoung Jik Lee, Dr Simone Graetzer and Dr Gary Seiffert, and the fellow students at the Acoustics Research Unit (ARU) for

the nice hospitality during visits in Liverpool. I enjoyed every work stay and particularity the Christmas dinners.

This thesis was part of a research project in collaboration between the University of Applied Sciences Stuttgart, the Technical University of Applied Sciences Rosenheim and the University of Liverpool. I greatfully acknowledge the funding by the German Federal Ministry of Education and Research in the program FHprofUnt (grant reference: 03FH089PB2). Many thanks to the building acoustics research group at the University of Applied Sciences Stuttgart, Professor Dr Heinz-Martin Fischer, Steffi Reinhold, Dr Jochen Scheck and Professor Dr Bernd Zeitler, for the collaboration work. I also thank the industrial partners that joined this project.

My sincere gratitude goes to my parents Renate and Hannes for their unfailing support that made it possible for me to pursue the way through studies and the PhD work. I also thank my sisters Teresa and Lucia for their interest in my work and the hours spent for proofreading.

Finally I would like to express my sincere thanks to my wife Anna. Her support, sacrifice and appreciation for my work where the most important factors for the completion of this work.

In the end I can say that although a PhD thesis is a personal issue, I never felt left alone due to the support of all these people, following the anthem of the Liverpool Football Club: *You'll never walk alone.*

Declaration

I declare that this thesis is an original report of my research, has been written by me and has not been submitted for any previous degree. Parts of the experimental work were done in collaboration with two Bachelor degree students at the Technical University of Applied Sciences Rosenheim that have been supervised by me. The experimental results shown in section 5.5.2 were determined in collaboration with Grünewald [2016]. The work of Betz [2015] supported the results presented in sections 6.2.3 and 6.4.3. For both students, the experimental work was designed by me and I gave the students guidance in how to carry out the measurements. To process the data, the students started with MATLAB codes provided by me which they adapted for their Bachelor thesis. For this PhD thesis I have reprocessed and visualized the data in a different way. The interpretation of the data developed in discussions with the two students, their examiners Dr Andreas Mayr and Professor Dr Ulrich Schanda and with my supervisor Professor Carl Hopkins. The collaborative contributions from these Bachelor students are acknowledged and have been indicated clearly in the document.

Fabian Schöpfer
February 2019

Contents

List of Figures

List of Tables

List of Symbols

Latin

a	Acceleration	$\mathrm{m/s^2}$
c_0	Phase velocity of sound in air	m/s
c_L	Quasi-longitudinal phase velocity	m/s
$c_\mathrm{B,b}$	Bending phase velocity for beams	m/s
$c_\mathrm{B,p}$	Bending phase velocity for plates	m/s
$c_\mathrm{g,B,p}$	Bending group velocity for plates	m/s
$c_\mathrm{L,b}$	Quasi-longitudinal phase velocity for beams	m/s
$c_\mathrm{L,p}$	Quasi-longitudinal phase velocity for plates	m/s
d	Sensor spacing	m
d_R	Spacing of ribs (wall studs or floor joists)	m
f	Frequency	Hz
$f_\mathrm{B,thin}$	Thin beam/plate limit for bending waves	Hz
f_c	Coincidence/critical frequency	Hz
f_msm	Mass-spring-mass resonance frequency	Hz
f_p	Mode frequency for 1D-systems (p)	Hz
$f_{p,q}$	Mode frequency for 2D-systems (p, q)	Hz
$f_{p,q,r}$	Mode frequency for 3D-systems (p, q, r)	Hz
i	Imaginary unit, $\sqrt{-1}$	–
h	Plate thickness or beam height	m
k_0	Wavenumber of air	rad/m
k_B	Bending wavenumber	rad/m
m	Mass	kg
m''	Mass per unit area, surface density	$\mathrm{kg/m^2}$
m'	Mass per unit length	kg/m
m_acc	Mass of accelerometer	kg

n	Sample size	–
$n(f)$	Modal density	modes/Hz
$n_\mathrm{b}(f)$	Modal density for bending waves on (thin) beams	modes/Hz
$n_\mathrm{p}(f)$	Modal density for bending waves on (thin) plates	modes/Hz
p	Sound pressure	Pa
r_rd	Reverberation distance	m
u	Sound particle velocity	m/s
v	Velocity	m/s
v_Sf	Source free velocity	m/s
w	Displacement	m
A	Absorption area	m^2
B	Bandwidth	Hz
B	Bending stiffness	$\mathrm{N\,m}$
B_b	Bending stiffness for a beam	$\mathrm{N\,m}^2$
B_p	Bending stiffness per unit width for a plate	$\mathrm{N\,m}$
D_TF	Transmission function	dB
E	Young's modulus	$\mathrm{N/m}^2$
E	Energy	J
E_kin	Kinetic energy	J
E_pot	Potential energy	J
E_vib	(Total) vibrational energy	J
F	Force	N
F_b	Blocked force	N
F_pI	Pressure-intensity index	dB
I	Moment of inertia of the cross-sectional area	m^4
I	Sound intensity	$\mathrm{W/m}^2$
I_s	Structural intensity	W/m
$I_{\mathrm{s},x,\mathrm{F}}$	Structural intensity in x-direction (force)	W/m
$I_{\mathrm{s},x,\mathrm{M}}$	Structural intensity in x-direction (moment)	W/m
$I_{\mathrm{s},x,\mathrm{BM}}$	Structural intensity in x-direction (bending moment)	W/m
$I_{\mathrm{s},x,\mathrm{TM}}$	Structural intensity in x-direction (twisting moment)	W/m
L	Length (dimension of (building) element)	m
L_a	Acceleration level	dB (re $1 \times 10^{-6}\,\mathrm{m/s}^2$)

L_p	Sound pressure level	dB (re 2×10^{-5} Pa)
L_v	Velocity level	dB (re 1×10^{-9} m/s)
L_E	Energy level	dB (re 1×10^{-12} J)
L_F	Force level	dB (re 1×10^{-6} N)
L_I	Sound intensity level	dB (re 1×10^{-12} W/m^2)
$L_{I,\mathrm{s}}$	Structural intensity level	dB (re 1×10^{-12} W/m)
L_W	(Structure-borne) sound power level	dB (re 1×10^{-12} W)
L_Y	Mobility in decibels; $L_Y = 20 \lg\left(\frac{Y}{Y_0}\right)$	dB (re 1 m/(N s))
L_η	Loss factor in decibels	dB (re 1×10^{-12})
L_σ	Radiation index	dB (re 1)
M	Moment	N m
M	Modal overlap factor	–
M	Moment per unit width	N
N	Total number of samples, subsystems	–
N	Mode count	–
N_s	Statistical mode count	–
P	Reactive power (imaginary part of complex power)	W
Q	Complex power	W
Q	Shear force per unit width	N
R	Sound reduction index	dB
S	Area	m^2
T	Reverberation time	s
T_s	Structural reverberation time	s
V	Volume	m^3
W	Active power (real part of complex power)	W
Y	Mobility	m/(N s)
Y_dp	Complex driving-point mobility	m/(N s)
Y_M	Complex moment mobility	1/(N m s)
Y_R	Receiver mobility	m/(N s)
Y_S	Source mobility	m/(N s)
Z	Impedance	N s/m
Z_R	Receiver impedance	N s/m
Z_S	Source Impedance	N s/m

Bold

$\mathbf{Y}$	Mobility matrix	$\mathrm{m/(N\,s)}$
$\mathbf{Y}_\mathrm{R}$	Receiver mobility matrix	$\mathrm{m/(N\,s)}$
$\mathbf{Y}_\mathrm{S}$	Source mobility matrix	$\mathrm{m/(N\,s)}$
$\mathbf{v}_\mathrm{Sf}$	Source free velocity vector	m/s

Greek

α	Angular velocity	rad/s
δ_pI0	Pressure-residual intensity index	dB
η	Loss factor	–
η_int	Internal loss factor	–
η_tot	Total loss factor	–
θ	Propagating angle	rad or deg
λ_B	Bending wavelength	m
ν	Poisson's ratio	–
ρ	Density	$\mathrm{kg/m^3}$
ρ_0	Density of air	$\mathrm{kg/m^3}$
σ	Radiation efficiency	–
σ	Standard deviation	–
τ_r	Resonant transmission coefficient	–
τ_nr	Non-resonant transmission coefficient	–
ϕ	Phase	rad or deg
ϕ_p	Characteristic beam function for mode p	–
ϕ_q	Characteristic beam function for mode q	–
ψ_{pq}	Plate mode shape for (pq)-th mode	–
ω	Angular frequency, $\omega = 2\,\pi\,f$	rad/s

Mathematical symbols and operators

x	Dummy variable used in this list
$\underline{x}$	Complex value
$\underline{x}^*$	Complex conjugate
$\hat{x}$	Peak value

$\tilde{x}$	Root Mean Square (RMS) value
$\|x\|$	Absolute value
$\mathrm{Re}\{x\}$	Real part
$\mathrm{Im}\{x\}$	Imaginary part
$\langle x \rangle_t$	Temporal average
$\langle x \rangle_s$	Spatial average
$\langle x \rangle_{t,s}$	Temporal and spatial average
$\langle x \rangle_T$	Temporal average for one period $T = 2\,\pi$

Acronyms

CLF	Coupling Loss Factor
ETICS	External Thermal Insulation Composite System
FEM	Finite Element Method
FFT	Fast Fourier Transform
FRF	Frequency Response Function
FRAC	Frequency Response Assurance Criterion
ILF	Internal Loss Factor
LaSM	Laboratory for Sound Measurement
LDV	Laser Doppler Vibrometer
MLS	Maximum Length Sequence
OSB	Oriented Strand Board
RMS	Root Mean Square
SBS	Structure-Borne Sound
SI	Structural Intensity
SEA	Statistical Energy Analysis
S/N	Signal-to-noise
SPL	Sound Pressure Level
TLF	Total Loss Factor
1D	One-dimensional
2D	Two-dimensional
3D	Three-dimensional

1 Introduction

1.1 Specification of the research topic

Machinery noise can cause annoyance and is therefore an important issue for engineers, architects and consultants. A vibrating machine radiates airborne sound from its enclosure (see Figure 1.1). If it is positioned in a room, the resulting airborne sound field will excite the walls, the ceiling and the floor. This vibrational energy propagates through the building and is finally radiated in remote rooms. Through the connecting points the source will also directly inject vibrational energy into the structure (Figure 1.1) which propagates and radiates in the same way. Hence the resulting Sound Pressure Level (SPL) in any remote room comprises an *airborne* and a *structure-borne* component. Both types of noise emission can be treated separately. However since airborne sound sources and their characterization are understood quite well, only the Structure-Borne Sound (SBS) component is addressed in this work.

Structure-borne sound sources in buildings mainly comprise service equipment like heating devices, pumps or ventilation systems and sanitary installations. However any vibrating machine that is installed in a building can act as a structure-borne sound source. To prove that le-

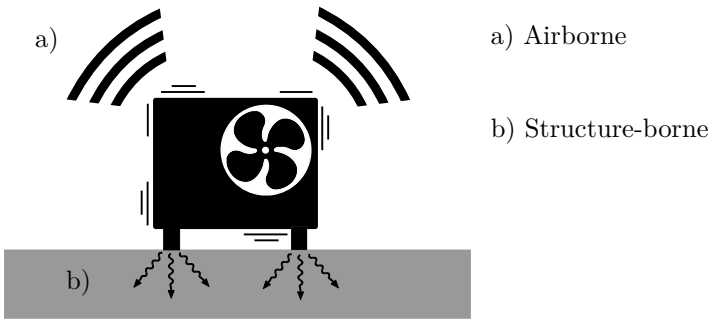

Figure 1.1: Noise emission from machinery

gal requirements are satisfied at the design stage of a new building, the sound pressure level due to machinery or service equipment needs to be predicted. The total transmission from the source to the receiver involves separate stages. These stages, described by Petersson and Gibbs [2000] are shown in Figure 1.2. In the first stage, the emission of structure-borne sound from the source in the specific building situation has to be estimated. Once the transmitted vibrational energy is known, the propagation across the building structure including the sound radiation into a remote room needs to be predicted in order to quantify the sound pressure level in a room. This involves both direct and flanking transmission. Direct transmission only regards the separating wall or floor between two adjacent rooms or an exterior wall. Flanking transmission includes the propagation of vibrational energy across junctions between building elements.

Hence for the prediction of machinery noise in buildings, models are required for the different transmission paths. However practical tools to estimate machinery noise only exist for monolithic heavyweight buildings, for example [EN 12354-5:2009]. For lightweight constructions, including timber-frame structures, no validated methods exist to-date. Therefore this work focuses on the vibro-acoustics of timber-frame structures excited by structure-borne sound sources.

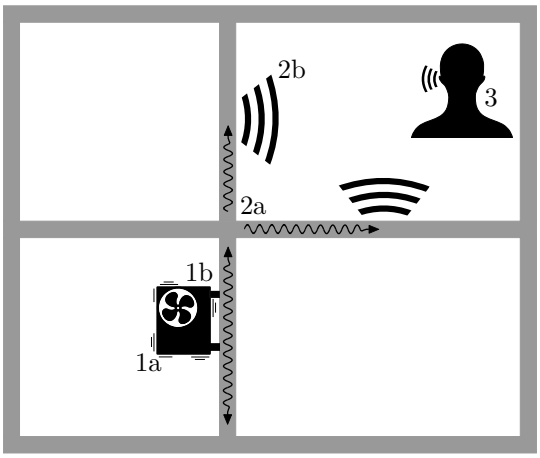

1) Structure-borne sound emission
   1a) Generation
   1b) Transmission
2) Building transmission
   2a) Propagation
   2b) Radiation
3) Human response

Figure 1.2: Stages involved in the generation and transmission of structure-borne sound

1.2 Background

Due to climate change and the increasing shortage in natural resources, sustainable and energetically optimized building concepts are becoming ever more popular.

To fulfil requirements on the energy consumption and expectations of the occupants on comfort, modern buildings are highly engineered. They incorporate additional machinery such as heat pumps, ventilation systems or engine-driven appliances like automated roller-shutters. All these sources inject structure-borne sound and therefore potentially cause annoyance. Other conventional appliances like sanitary installations, heating devices or white goods also act as structure-borne sound sources.

Timber-frame buildings are currently gaining popularity because of their high thermal insulation. Recent developments in timber engineering, standardization and legislation now allow the construction of multi-storey timber buildings in an increasing number of countries. This involves challenges in the design of such projects. Concerning sound insulation in dwellings legal requirements based on national standardization,

for example [DIN 4109-1:2016-07] in Germany, have to be met. Hence it is necessary to predict the sound pressure levels due to structure-borne sound sources at the design stage.

However, to-date no planning tools are available for machinery noise in timber-frame buildings and the design is mainly based on previous project experience. Consultants and architects are therefore very inflexible in the choice and combination of equipment and construction type. High uncertainties increase the building costs due to conservative design which reduces the competitiveness of timber-frame buildings.

1.3 Problem and approach

Two main issues are addressed in this work. The first concerns the challenges due to the complex nature of SBS transmission in timber constructions. The second is the need for simplified methods in buildings acoustics. Both are described briefly in the following two sections.

1.3.1 Challenges related with lightweight structures

Compared to classical monolithic buildings made from concrete or bricks, lightweight, framed structures are very complex. A concrete wall or floor can often be considered as a homogeneous plate. Timber-frame structures, however, comprise detailed connections involving different materials. The construction comprises a framework with a sheeting typically made from thin sheets. The cavities are often filled with sound absorptive material. The cross-sectional area of the timber studs or beams as well as their spacing varies depending on the required structural strength of the building element. Floor joists are deeper and potentially need a narrower spacing than walls studs. In addition the material properties of wood are based on the direction of the fibres and annular rings that can vary depending on the sawing pattern. To reduce impact sound, floor coverings such as floating screeds are common and can be regarded as state-of-the-art. Additional mass, like gravel in the floor cavities for example, or

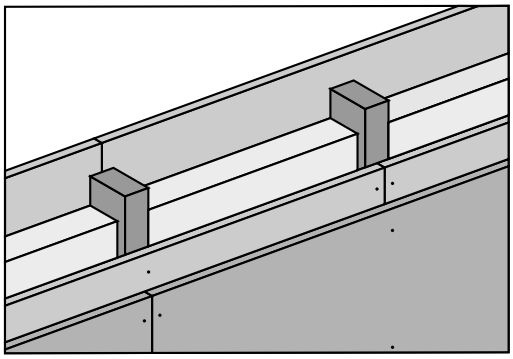

Figure 1.3: Sketch of typical timber-frame double wall.

various kinds of suspended ceilings are also used to improve sound insulation. A collection of common constructions and their associated sound insulation is given in [DIN 4109-33:2016-07].

Figure 1.3 shows an example of a timber-frame wall construction with a single framework. The sheeting can have one or multiple layers that are typically screwed or nailed to the framework. Common sheet materials are plasterboard or wood composites like chipboard or Oriented Strand Board (OSB). Gypsum boards are butt jointed and grouted, whereas wood composites are normally tongue and grooved. The choice of material, its thickness and the number of layers can vary depending on requirements on load bearing, fire protection or sound insulation. Hence there is a high degree of detail inherent in the construction of timber-frame walls and floors. This leads to many different junction details between building elements.

Although there are industrial standards on the dimensions of building material or common stud and screw spacings for example, the variety of possible structural variations is large. Due to the complexity of timber buildings the mechanical behaviour is also influenced by craftsmanship and this causes additional uncertainties.

Compared to homogeneous heavyweight building elements, the complexity of timber-frame structures provides more sound transmission paths within a single element and at junctions between walls and floors. In com-

bination with high internal damping of the wood, wood-composite and gypsum based materials, this leads to high material damping which is a major characteristic of such structures [e. g. Schoenwald 2008]. Concerning mechanical excitation, the vibrational energy is significantly attenuated with increasing distance within a timber-frame wall [e. g. Nightingale and Bosmans 1999]. However, common engineering prediction models in building acoustics are typically based on the laboratory measurement of direct sound insulation of the walls and floors [e. g. ISO 12354-1:2017]. In addition to direct sound transmission, flanking transmission is modelled by introducing coupling terms across the junctions between the elements. This approach typically requires building elements to have a uniform vibro-acoustic behaviour and energy distribution across its spatial dimensions. This is provided by weakly damped monolithic building elements of concrete and masonry [e. g. Schoenwald 2008]. However due to the high damping of timber-frame structures, these approaches may not always be applicable.

In terms of direct sound transmission, lightweight double leaf constructions show characteristics that differ to those of heavyweight homogeneous structures. Although there is structural coupling between the leaves through the framework, sound transmission across timber-frame constructions is characterized by a mass-spring-mass behaviour where the air in the cavity acts as a spring. At and below this frequency the performance of double wall constructions is weak compared to monolithic structures with a similar total thickness. Above the mass-spring-mass resonance frequency the sound insulation of double wall constructions increases rapidly until the frequency where the bending wavelength of the structure and the wavelength of airborne sound waves match. At this coincidence frequency, sound radiation is very efficient. For timber frame-constructions the coincidence frequency is significantly higher than with monolithic structures because of the thin sheet material. Below the coincidence frequency, both resonant and non-resonant components are involved in the sound transmission. For timber-frame structures the coi-

ncidence frequency is well within the buildings acoustics frequency range; hence both components are involved.

In building acoustics single number ratings are determined in the frequency range from 100 Hz to 3.15 kHz, but this range is sometimes extended down to 50 Hz and up to 5 kHz. For heavyweight impact sound insulation, maximum sound pressure levels $L_{i,\mathrm{F,max}}$ are measured from 63 Hz. Typically the mass-spring-mass resonance frequency of common timber-frame constructions is below 100 Hz. Hence the poor sound insulation of lightweight buildings is not covered by these values although spectral adaptation terms were introduced to expand the range down to 50 Hz. As the audible frequency range typically starts at 20 Hz occupants can be annoyed by low frequency sound transmission in lightweight constructions [Rabold 2010; Ljunggren et al. 2014]. Additionally machinery tends to inject most vibrational energy at low frequencies. As lightweight structures are not as inert as heavyweight constructions they are prone to structural excitation by machinery. To estimate the vibration transmission the mechanical characteristics of the source and the receiver are required at the contact points. However the prediction of parameters for inhomogeneous timber-frame constructions is very complex as the vibration field varies significantly across the surface.

To cope with these challenges related to the the complexity of lightweight structures two main approaches are applied in this thesis: (a) Statistical methods that use averaging procedures, such as SEA. SEA provides the possibility to investigate the transmission paths individually which can be used to identify dominant or weak paths, and (b) an empirical approach, based on measured data to globally describe the transmission from the power input of a source to the spatial average sound pressure level in a distant room including all paths. Deterministic approaches like Finite Element Methods (FEMs) are not considered in this thesis because of the problems related with the determination of the actual material properties, complex unknown boundary conditions and relatively high computation times.

1.3.2 Challenges in the field of building acoustics

Structure-borne sound emission, the first stage of the total transmission, is not only an issue in buildings but also in trains, ships, vehicles and aircraft. In all these fields the energy transfer from an active vibrating source to a passive receiving structure is of interest. This requires knowledge about the structural dynamic properties of the source and the receiver.

Hence the determination of structure-borne sound emission is more complex compared to the situation with airborne sound, where the surrounding fluid (air) is the only present receiver for which the characteristics are well known. For the characterization of airborne sound sources there are well-established measurement standards [ISO 3740:1980][1].

Receiving structures can differ largely due to a wide range of material properties in combination with various possible geometries (e. g. beams or plates), arbitrary finite dimensions and construction types (e. g. rib-stiffened plates or sandwich constructions). Variations also exist in the design of the source mount that can be point, line or plane shaped, for example. The position of the source can have significant influence on the strength of energy transmission due to spatial variations in the receiving structure properties (especially for rib-stiffened constructions). Additionally at each contact point, excitation for six degrees of freedom (three forces and three moments about the orthogonal axis of these forces) can occur. For multi-point sources the interaction of the individual contact points needs to be taken into account, too. Because of all these aspects, the prediction of structure-borne sound emission can be a complex time-consuming task. As mentioned in section 1.3.1 there are challenges in modelling the sound transmission across timber-frame structures.

However, practical and effective engineering procedures are required in the field of building acoustics where the resources in time, manpower and equipment for the planing process can be low compared to other sectors of industry where serial production is more common. However, both the

[1] Note the latest revision of this standard: [ISO 3740:2000]

machinery manufacturers and the building industry seek simple practical methods, ideally based on single number quantities.

The approach in this work is to gain insight into structure-borne sound excitation and propagation in timber-frame constructions and derive simplification steps from this based on experimental investigations. As there are no common rating schemes available for structure-borne sound power, one-third octave band data is used rather than single number values.

1.4 Aims

The main aims of this work can be summed up as follows:

Existing models for Internal Loss Factors (ILFs) and Coupling Loss Factors (CLFs) that are required to model a timber-frame construction are assessed using experimental work on a laboratory test structure. This includes the determination of the material properties for the buildings elements, such as the sheeting chipboard plates and spruce studs and joists. Specifically the transmission across tongue and groove plate junctions is considered by determining a CLF experimentally. An additional aim of the experimental work is to gain insight into the vibrational behaviour of a timber-frame construction undergoing mechanical point excitation Therefore measured data is used to visualize and quantify the spatial variation in the vibration field and the energy propagation. Further experimental work aims to confirm and expand the knowledge about the spatial variation of the driving-point mobility on timber-frame structures. In addition the spatial variation of the moment mobility is considered.

Concerning the prediction of the SBS power input the aim is to assess simplified approaches for the application in building acoustics consultancy. This requires an assessment of the importance of moment excitation in relation to force excitation using investigations in experimental methods to determine rational excitation components by measurement.

Based on the experimental work this study investigates two approaches for prediction with different specific aims: a) SEA is used to model a timber-frame wall undergoing mechanical point excitation with the main

aim to assess the applicability of SEA for this purpose and to gain insight into the transmission process, b) an empirical approach based on measured transmission functions is used with the aim to develop the framework for a simple and practical method to estimate the sound pressure level caused by machinery in timber-frame buildings.

1.5 Significance of this work

The European standards for the prediction of sound transmission in buildings were originally not applicable to lightweight, inhomogeneous constructions [e. g. EN 12354-1:2000]. The developments in the building sector towards increasing mechanization and a higher market share of timber-frame constructions for multi-storey dwellings require a revision of the currently available standards. This involves methods for prediction but also experimental procedures for the determination of input data for these models.

Recently, revised versions of part 1 and 2 of the EN 12354 series on airborne and impact sound transmission have been published as ISO standards [ISO 12354-1:2017; ISO 12354-2:2017]. These parts now include procedures to predict sound transmission in lightweight constructions. The ISO 10848 series describes experimental procedures to determine input data for the prediction of flanking transmission and has been revised recently. The work in this thesis has been incorporated into the latest version of the ISO 10848 series [ISO 10848-1:2017]. Although these revised standards are now available, the described methods are not yet representative for all kinds of timber-frame constructions. The practicability of the methods needs to be approved through their application by consultants where standardized prediction tools for machinery noise in timber-frame buildings are not yet available.

This thesis contributes to these developments in the field of building acoustics. As manufacturers of machinery and people involved in the acoustical planning process of buildings seek practical methods, the focus in this research is on simplifications. By providing planning tools for

timber-frame buildings, that are equivalent to those for monolithic constructions, the competitiveness of this construction type can potentially be increased.

1.6 Outline

The structure of this thesis comprises the following four main parts:

- A review of theory and literature in 2 and Chapters 3.
- The methodology, i. e. the test structures and the experimental techniques, in chapter 4.
- The main investigations and results in chapters 5, 6, 7 and 8.
- A summary in Chapter 9.

The content of the individual chapters is briefly described here and indicates links between the chapters.

Chapter 2 provides a review of the relevant literature and discusses the available concepts to predict structure-borne sound emission of machinery and the transmission in buildings, particularly lightweight buildings. The review identifies gaps that form the motivation for this thesis.

Chapter 3 describes the theory for bending wave vibration on beams and plates, an introduction to SBS source characterization on a power basis and an overview of SEA providing the relevant equations and the main assumptions. This chapter focuses on the specific application of the theories described in chapters 4 to 8.

Chapter 4 describes the test structures, experimental procedures and instrumentation used for measurements. Experimental investigations are used in this thesis to investigate SBS sources, the vibrational behaviour of timber structures (chapter 5), the coupling between source and receiver (chapter 6) or the global transmission (chapter 8).

Chapter 5 presents and analyses the results and findings of experimental investigations on a specific timber-frame structure in the laboratory.

The aim of this chapter is to gain insight into the vibrational behaviour of a typical timber-frame construction undergoing mechanical point excitation. The investigations also include the determination of the material properties for the individual building elements (beams and plates) comprising the structure. The experimental work on the timber-frame structure involves investigations concerning the vibration field and the decay of vibration, the spatial variation of the driving-point mobility and the moment mobilities as well as the radiation of structure-borne sound and the resulting sound fields in the cavities and the adjacent rooms. The measured data and the findings of this experimental work are used in chapters 6, 7 and 8 as input data or for the validation and interpretation of results.

Chapter 6 describes investigations concerning the experimental characterization of SBS sources as well as the calculation of the power input into timber-frame structures. Based on the motivation to develop practical engineering methods, this chapter assesses simplifications in the determination of the power input from machinery using findings from chapter 5. The investigations concern artificial sources and a real SBS source. In addition to force excitation, indirect methods are applied to determine the moment power for a single contact point. The applicability of the methods is assessed and the relative importance of rotational excitation components is discussed. As machinery typically has multiple contact points, the power input for multi-point force excitation is of particular interest in order to reduce the experimental effort to obtain a reasonable estimate for the power input. The SBS power is used as input data for prediction models in chapters 7 and 8.

Chapter 7 describes the application of SEA to model a timber-frame wall undergoing mechanical point excitation. The modelling is based on the results and findings from the experimental investigations described in chapter 5. SEA is used to analyse the sound transmission from point excitation by identifying dominant transmission paths. An assessment is made as to whether SEA can be used to reproduce the vibrational behaviour of the timber-frame structure observed in the experiments.

The investigations are focused on modelling rather than prediction of machinery noise. Nevertheless the SEA model is used in a case study to predict the resulting sound pressure level in an adjacent room using the power input for an artificial source from chapter 6.

Chapter 8 introduces an empirical approach based on measured transmission functions. This specifically aims to develop are framework for a simple and practical approach to predict machinery noise in buildings. The relevant quantities and the proposed measurement protocols are introduced based on experimental procedures described in chapter 4. Experiments in the laboratory and the field are used to assess the practical application of the proposed measurement protocol, to identify potential limitations and to test variations of the protocol to adapt it for a broad application. To form the basis for the empirical prediction model, a survey of existing transmission functions in timber-frame buildings is presented and assessed in terms of the potential to identify an average transmission function for similar situations. From chapter 6, moment power is used to determine the transmission function for moment excitation in the laboratory. In case studies with SBS sources introduced and characterized in chapter 6, the proposed approach to predict machinery noise is applied and validated with measured data following the procedures described in chapter 4.

Chapter 9 gives a summary of the thesis focusing on the main findings to draw conclusions and to give recommendations for further work.

2 Literature review

2.1 Introduction

This chapter reviews the literature on structure-borne sound emission from machinery and sound transmission in buildings that is related to this thesis.

2.2 Structure-borne sound emission

The need for procedures to describe machinery as structure-borne sound sources was pointed out by Kihlman [1978]. This led to an ISO working group that was concerned with the development of standardized methods [Ten Wolde and Gadefelt 1987]. In the 1980s and 90s a range of approaches for structure-borne sound source characterization were suggested [Petersson and Plunt 1982a; Mondot and Petersson 1987; Vercammen and Heringa 1989; Moorhouse and Gibbs 1993; Ohlrich and Larsen 1994; Verheij et al. 1995]). To allow flexibility in the prediction of machinery noise, an independent source characterization is preferred. This can be achieved with mobility methods (respectively impedance methods) that allow the description of coupling between individual mechanical systems

and the implementation of resilient foundations. A comprehensive survey on the application and the origins of mobility methods in structural dynamics is given by Gardonio and Brennan [2002]. Using these methods the vibrational energy transmitted from a source to a receiver can be obtained from three independent quantities [Moorhouse and Gibbs 1993]: (a) Source activity, (b) source mobility and (c) receiver mobility.

2.2.1 Determination of the source quantities

Structure-borne sound source characterization involves the determination of the active and passive properties of the source at the accessible contact points. This black-box approach involves the assumption of a linear source whose properties do not alter when it is mounted on a receiving structure. A validation of the black-box approach is shown by Mondot and Petersson [1987] in a case study with an idealized source and also shown in [Moorhouse 2001]. An alternative approach was presented by Moorhouse and Gibbs [1995] to determine the power emission in-situ. This approach was extended by Elliott [2009] and Moorhouse et al. [2009] to determine independent source quantities using in-situ characterization. However the black-box approach is widely accepted particularly in the field of building acoustics and was therefore included in [EN 15657:2017]. For this reason it is applied in this thesis.

For the measurement of the blocked force, a large inert receiving structure is necessary. At the interface between source and receiver, force transducers are required which potentially modify the mounting conditions. Hence the free velocity is generally preferred to describe the active property of a structure-borne sound source [Gibbs and Petersson 1996]. Procedures for the experimental determination of the free velocity are standardized in [ISO 9611:1996].

2.2.2 Description of source emission on a power basis

The use of a power-based descriptor is a trade-off between physical accuracy and required simplicity [Gibbs 2003]. As noted by Petersson and

Gibbs [2000] and Höller [2013], manufacturers seek simple data to describe their machines in terms of structure-borne sound emission. This can be provided by the power delivered by the source involving all the complexities. Excitation components (forces *and* moments) can be compared and rank-ordered, since problems that occur with different units are eliminated. In building acoustics a detailed description of the mechanical system is not required nor possible due to limited resources. Hence prediction models for sound transmission involve averaging over space, time and frequency. SEA or SEA-based prediction models like [EN 12354-5:2009] require power as the main quantity.

A power-based descriptor allows the comparison of different sources in a similar way to airborne sound sources [ISO 3740:2000]. Hence research and standardization work has focused on power-based methods in recent years. Moorhouse [2001] formulated a more general form of the approach based on characteristic power as a source descriptor from Mondot and Petersson [1987]. As this method requires a huge amount of data, Gibbs et al. [2007] suggested approaches to simplify the calculation and to reduce data. Based on theory by Cremer and Heckl [1967] and earlier approaches, [e. g. Vercammen and Heringa 1989; Lu et al. 1990], a simplified procedure, the reception plate method was revisited by Gibbs et al. [2007] and Späh and Gibbs [2009]. This practical procedure is particularly suited to building acoustics and is standardized in [EN 15657:2017][1]. It allows the estimation of the injected structural power to building elements, the so-called *installed power*. The simplest situation for the application of this standard is the case of small and light sources on heavy receivers such as concrete or masonry building structures. A more complicated case concerns installations in lightweight constructions such as timber-frame buildings which is addressed in the following section.

[1] Note that this standard supersedes [EN 15657-1:2009].

2.2.3 Structure-borne sound sources in timber-frame constructions

Due to the increasing popularity of timber buildings more consideration has been given to machinery noise in lightweight building constructions in recent years. Lievens [2008] applied the black-box approach in a case study of a washing machine on a lightweight floor using either full mobility matrices or reduced data sets. Work by Mayr [2009; 2016] focused on simplifications for the complex vibration transmission of multi-point structure-borne sound sources in lightweight buildings [see also Ohlrich 2011]. Mathiowetz and Bonhoff [2013] investigated multi-component power transmission [see also Petersson 1993a; Petersson 1993b] into lightweight structures. However the presented case studies concerned lightweight metal structures rather than timber-frame constructions. Work by Bailhache and Villot [2015] investigated the prediction of power input from a waste water installation into lightweight framed receivers using the procedure described in [EN 15657:2017]. Using a measured TLF for the receiving structure, the spatial average velocity was estimated and compared with measurements which gave reasonable agreement.

The challenges in the prediction of the structure-borne sound power input in framed structures are now considered: Receiver mobility can be predicted or determined experimentally and prediction is usually preferred due to a more general application. For homogeneous plates, there are both finite and infinite plate models, e. g. [Warburton 1954; Heckl 1961; Cremer and Heckl 1967; Gardonio and Brennan 2004; Soedel 2004]. However lightweight constructions are generally ribbed plate systems, i. e. single or multi layers of plates of the same or differing material mounted (screwed or nailed) on top of a frame made of timber or metal studs. Although industrial standards (for example on stud spacings or on dimensions of building material) reduce the amount of possible constructions types, there is still a very large variety. However White and Liasjo [1982] noted that for timber floors there was not always a significant variation between different positions. Nightingale and Bosmans [2007] and

Mayr [2009] described the variation of mobilities for framed constructions based on the distance of regarded points to a stud in relation to the bending wavelength of the sheeting material. Therefore the prediction of the receiver mobility is more complicated compared to a homogeneous plate. Further work by Mayr and Gibbs [2011] suggested an approximate method for the prediction of point and transfer mobilities based on infinite plate and beam behaviour in combination with reactive forces at structural discontinuities.

For multi point sources a major step of simplification is the reduction to one equivalent excitation point [Petersson and Plunt 1982a; Petersson and Plunt 1982b]. For lightweight structures, Mayr [2009; 2012] proposed a single equivalent approximation for lightweight receivers and additional simplifications as well as their application [Mayr and Gibbs 2016]. This showed that an approximation to a representative point is feasible, however the work only focused on out-of-plane force excitation.

Perpendicular forces are generally considered to be dominant [Gibbs et al. 2007] especially in the central area of plate-like structures [Yap and Gibbs 1998]. However moments can be important in relation to perpendicular forces for framed constructions where translatory motion is potentially constrained by discontinuities [e. g. Petersson 1993a; Yap and Gibbs 1998].

2.3 Sound transmission in a building

Once the structure-borne sound power input from machinery is known, the transmission across the building structure needs to be modelled in order to predict sound pressure levels in remote rooms. Similar to the field of source characterization, the development of transmission models for timber-frame constructions is not as well established and validated as for heavyweight constructions due to the complex nature of inhomogeneous framed structures.

2.3.1 Approaches to model the vibrational response of framed building structures

Due to the stiffening ribs, the vibrational response of framed walls or floors can be considerably different to homogeneous plate-like structures. Classical ribbed plate models use wave theory to describe thin plates that are rigidly line-connected to stiffening ribs at periodic distances [e. g. Mead 1996]. A survey on ribbed-plate models is given by Brunskog and Hammer [2000] and mainly applies to moulded structures or welded connections typically used in aerospace or naval applications. A study concerning vibration transmission in a framed building was presented by Steel et al. [1994]. For a ribbed concrete floor slab it was shown that there is a significant decrease in vibration perpendicular to the ribs. Using CLFs for inline plate joints according to [Cremer and Heckl 1967] the decrease was modelled using SEA. However the prediction underestimated the attenuation. Timber-frame walls or floors are typically fabricated using spaced point connections between the sheeting plates and the stiffening timber joists. An experimental study by Nightingale and Bosmans [1999] indicated that the vibrational response of timber-frame structures shows typical characteristics of periodic beam-plate-structures. The results indicated that both line-connected and point-connected characteristics occur in different frequency ranges. However no model was presented that describes the vibrational response. Craik and Smith [2000b] also found line-connected and point-connected characteristics in measurements on timber-frame and metal stud constructions. To model the velocity level difference across a plate-beam junction, wave theory was applied for the line-connected behaviour. The point-connected behaviour was modelled using SEA with a structural CLF for the fixing points. The results showed reasonable agreement with measurements, however only isolated test structures with two plates and one beam were considered. Further work by Bosmans and Nightingale [2001] as well as Nightingale and Bosmans [2007] suggested approaches using either SEA or an analytical wave based approach to model the vibration transmission across

bolted junctions between plates and beams. The results indicated that both approaches can be used when all wave types are included in SEA. However, the investigations were carried out using small mock-ups made from perspex beams and plates. Schoenwald [2008] described the line and point-connected characteristics of timber and metal stud walls in the wavenumber domain. To model the attenuation of vibration levels, Schoenwald used the model of Bosmans and Nightingale [2001] for the line-connected behaviour. For the point-connected behaviour the stiffening ribs were neglected and only the sheeting plate was modelled as a damped finite rectangular plate with simply supported boundary conditions. It was shown that for the majority of the building acoustics frequency range framed lightweight building structures can be described with point-connected behaviour.

2.3.2 Review of approaches for transmission models

Due to the challenges mentioned in section 1.3.1, there are no practical and generally applicable predictions models for structure-borne sound transmission in timber-frame buildings. However there is a lot of research activity in this field which will be presented in the following. To organize the literature, the following three groups will be used to subdivide existing transmission models. Detailed models are the results of basic fundamental research on sound transmission and mainly form the foundation for the second group, the standardized prediction methods. The third group are empirical approaches.

2.3.2.1 Detailed models

The fundamental research work in this topic can be considered in terms of direct and flanking transmission. For the latter only the resonant components are relevant as only these are transmitted across junctions [Nightingale 1995]. The direct path however involves both resonant and non-resonant transmission. Hongisto [2006] gives an extensive survey on

existing approaches for direct transmission across double walls distinguishing between cavity walls with and without structural coupling.

For double walls of infinite size with no connections between the leaves, Beranek and Work [1949] and London [1950] introduced early models. These models are mentioned here because they describe non-resonant transmission across cavity walls. Based on these methods, Sharp [1978] suggested guidelines for the design of framed walls by splitting up the characteristics into frequency ranges where either mass law, mass-spring-mass behaviour or coincidence occurs. Vigran [2009; 2010] presented a transfer matrix approach that included structural coupling. Further improvements to analytical models were presented by Davy [2010; 2012] with a model that uses a four pole system to model the transmission by considering either massless point- or line connections. However both consider the transmission loss of the wall for airborne excitation and are therefore not suitable for the mechanical point excitation of SBS sources considered in this thesis.

More detailed approaches for double walls of finite size can be found in work based on SEA. Early work by Price and Crocker [1970] described a five-subsystem-model (room-plate-cavity-plate-room) that considers resonant and non-resonant transmission, but omits structural coupling. Based on that Craik and Smith presented an enhanced model that incorporates both acoustical [2000a] and structural transmission paths [2000b]. However these models were validated using a uniform excitation (airborne or mechanical excitation at various positions across the surface). This thesis however considers local mechanical excitation by an SBS source. Nevertheless, further improvements were presented later concerning the coupling between the cavity and the plate [Craik 2003] as this was inaccurate previous models. Galbrun [2010] presented investigations to assess the limitations in modelling the structural coupling using point connections. Suggestions to expand these SEA approaches to flanking transmission were presented for example by Craik and Galbrun [2005], Schoenwald [2008] or Kouyoumji [2012].

In recent years deterministic approaches to model sound transmission in lightweight timber structures were presented [e. g. Flodén 2014; Kohrmann 2017]. A comprehensive survey of existing models is given by Brunskog and Hammer [2000].

Although these detailed methods give insight into the different paths of sound transmission in timber-frame buildings, they are usually too detailed for an engineering application in consultancy for example. For this reason standardized simpler methods have been developed as described in the next section.

2.3.2.2 Standardized prediction methods

A comprehensive survey on standardization work, particularly related with airborne and structure-borne noise prediction for lightweight constructions is given by Villot et al. [2016]. Based on first order path analysis from SEA, the European standard series EN 12354 was developed including suggestions of Gerretsen [1979] and Gerretsen [1994] for the prediction of airborne and impact sound transmission in buildings [EN 12354-1:2000; EN 12354-2:2000].

Gerretsen [2000] presented initial ideas for an additional part that covers machinery noise which was later added as part 5 to this series [EN 12354-5:2009]. This part was directly developed from part 1 and therefore used the propagation model for airborne sound.

The models in the EN 12354 series were not developed for framed, lightweight buildings with high damping, non-diffuse vibration fields and complicated junction details. Hence their application was restricted to monolithic structures except two specific example constructions that were included for lightweight junctions. Due to the increasing popularity of timber buildings a lot of research work was carried out in recent years to include lightweight constructions in EN 12354. Most of the work was collected in the COST Action FP0702 [2012]. Additional papers were presented for example by Guigou-Carter et al. [2006], Guigou-Carter and Villot [2015] as well as Gerretsen [2015] leading to the latest revision of

part 1 and 2 and the publication as an ISO standard [ISO 12354-1:2017; ISO 12354-2:2017][2].

Although this was a major improvement, Villot et al. [2016] noted that this was just a starting point and more studies were required to increase the data base for timber-frame buildings. This is necessary as junction transmission for lightweight constructions needs to be characterized globally by measured data [Villot and Guigou-Carter 2006] which could be provided in a catalogue. Methods for laboratory and field measurements to determine flanking transmission are described in the latest version of the ISO 10848 series[3].

The estimation of machinery noise as described in [EN 12354-5:2009] is only applicable for heavyweight constructions to-date and needs to be revised, too. This was also stated by Villot [2017] who suggested approaches for the prediction of sound levels generated by structure-borne sound sources.

Although the intention of the standardized methods is to provide simplified, practical prediction tools, they are viewed by some as being too complicated for effective application in building acoustic consultancy. For this reason, this thesis investigates an empirical method based on a catalogue of measured average transmission functions to simplify the estimation of machinery noise in timber-frame buildings.

2.3.2.3 Empirical approaches

An alternative approach to 'prediction' is to use measured transfer functions between the emission of the source and the sound pressure level in a distant receiving room. Steenhoek and Ten Wolde [1970] defined mechanical-acoustical transfer functions concerning reciprocal measurements. Transfer functions for discrete excitation and response points were determined and proposed to describe the transmission of machinery noise in buildings. However typically spatial average data is considered

[2] Note that these standards also supersede [ISO 15712-1:2005; ISO 15712-2:2005]
[3] [ISO 10848-1:2017; ISO 10848-2:2017; ISO 10848-3:2017; ISO 10848-4:2017]

in buildings acoustics. Ten Wolde et al. [1975] carried out further experiments to identify individual excitation components for each of the six degrees-of-freedom. As mainly out-of-plane forces are considered in building acoustics this is not necessary. Cremer and Heckl [1967] described the reciprocal relationship between radiation and response by interchanging observation points. Based on that, Buhlert and Feldmann [1979] defined structure-borne sound sensitivity as the ratio of the radiated sound power to the mean-square force applied by a machine multiplied by a normalization term. The normalization term allowed the determination of the structure-borne sound sensitivity by measuring the mean-square pressure at a point in a room and mean-square velocity at the excitation point. This can be used to find advantageous positions for machinery that result in low sound pressure levels [Cremer and Heckl 1967]. However only single-point excitation is regarded and typically machines have multiple connection points so this might only apply to relatively compact machines.

Vercammen and Heringa [1989] revisited structure-borne sound sensitivity but considered the ratio of sound power radiated into the receiving room to the mean-square force (i.e. without the normalisation term used by Buhlert and Feldmann [1979]). By assuming that the mobility of the machine is much higher than the mobility of the receiving structure they introduced the reception plate method to give the structure-borne sound power from which the mean-square force was calculated (a similar approach was used by Gerretsen [1993]).

Scholl [2005] presented a test facility to investigate transmission functions in timber buildings that considered the ratio between the exciting force and the spatial average sound pressure. Moorhouse et al. [2011] presented an approach based on measured FRFs between the force from an impulse hammer and the the resulting sound pressure in distant rooms for the prediction of noise from building-mounted wind turbines. The approach uses the sound pressure level in a reference installation as basis, which is determined from in-situ blocked forces [Elliott 2009; Moorhouse et al. 2009] and the measured FRF in this situation. By applying correcti-

ons for the construction, the room size and its location in the building (e. g. diagonal adjacent to the reference room) the sound pressure level was estimated for other situations. The application is however limited due to a small survey of transmission data in the field.

Arnold and Kornadt [2014] defined a transfer function of pressure over the input force as an alternative to the predictive approach of [EN 12354-5:2009] for lightweight buildings following the work of Scholl [2005]. In field measurements these transfer functions were determined for eleven separating walls of horizontally-adjacent rooms. The data was arithmetically averaged to get a spatial-average value. The variation of the data was between 20 dB to 40 dB and could be reduced to between 10 dB to 30 dB by introducing normalization to the driving-point impedance of the excited structure and the reverberation time of the receiving room. An additional normalization concerned the airborne sound insulation of the separating wall. However this only applies to adjacent rooms and not for the general situation of transmission of machinery noise in buildings to any receiving room. Nevertheless the approach was applied by Vogel et al. [2016] in a particular situation with promising results.

3 Theory

3.1 Introduction

This chapter describes the theory that is applied in later chapters of the thesis. Section 3.2 describes bending wave vibration on beams and plates as well as sound radiation of bending waves. To describe the excitation of bending waves, the mechanical mobility is introduced. Section 3.3 gives a brief introduction to SBS source characterization on a power basis. Different methods are described that are applied in chapter 6. Section 3.4 gives an overview of SEA with the fundamental equations and the main underlying assumptions.

3.2 Bending wave vibration

This section gives expressions to describe bending wave vibrations on thin beams and plates that are applied in this thesis. A thorough derivation of the bending wave equation can be found in [Cremer and Heckl 1967], for example. The expressions use the notation and direction conventions given in Figure 3.1 for beams and Figure 3.2 for plates.

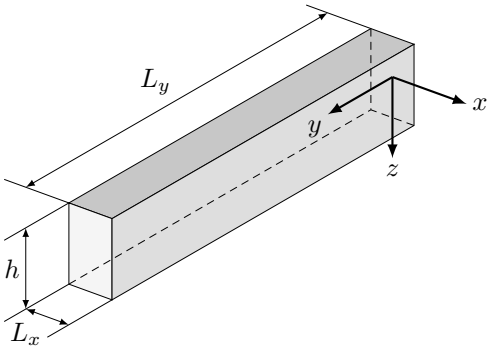

Figure 3.1: Direction conventions and dimensions for beams.

3.2.1 Beams

The bending stiffness for a solid beam, B_b, is

$$B_\mathrm{b} = E\, I_\mathrm{b} \tag{3.1}$$

where the Young's modulus, E, can be determined from the quasi longitudinal phase velocity, $c_\mathrm{L,b}$ and the density, ρ using

$$E = c_\mathrm{L,b}^2\, \rho \tag{3.2}$$

The moment of inertia, I_b, about the x-axis for a beam with rectangular cross section is given by

$$I_\mathrm{b} = \frac{L_x\, h^3}{12} \tag{3.3}$$

For thin beams the bending wavenumber, k_B, is

$$k_\mathrm{B} = \sqrt[4]{\frac{\omega^2\, m'}{B_\mathrm{b}}} = \frac{2\,\pi}{\lambda_\mathrm{B}} \tag{3.4}$$

where m' is the mass per unit length. The phase velocity, $c_\mathrm{B,b}$, is

$$c_\mathrm{B,b} = \sqrt[4]{\frac{\omega^2 B_\mathrm{b}}{m'}} = \sqrt[4]{\frac{\omega^2\, c_\mathrm{L,b}^2\, I_\mathrm{b}}{S_{xz}}} \tag{3.5}$$

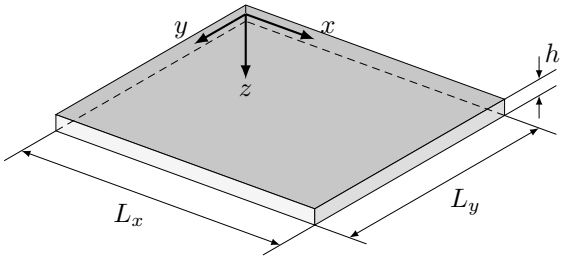

Figure 3.2: Direction conventions and dimensions for plates.

where S_{xz} is the cross-sectional area. The phase velocity is frequency dependent and therefore bending waves are described as dispersive.

Note that these equations are valid for bending about the x-axis. By interchanging the variables related with the x-dimension by those for the z-dimension, the equations are also valid for bending about the z-axis. For framed constructions only one of these is relevant for out-of-plane deflections. In this thesis, the z-axis corresponds to the bending wave deflections, hence the notation for bending about the x-axis is most relevant as in-plane deflections are not considered.

3.2.2 Plates

The bending stiffness for a thin isotropic plate is defined as

$$B_{\mathrm{p}} = \frac{E\, I_{\mathrm{p}}}{1-\nu^2} \tag{3.6}$$

where ν is the Poisson's ratio. Similar to the beam, the Young' modulus can be determined from the quasi-longitudinal phase velocity, $c_{\mathrm{L,p}}$ and the density, ρ using

$$E = c_{\mathrm{L,p}}^2\, \rho\, (1-\nu^2) \tag{3.7}$$

For the plate, the moment of inertia, I_{p}, is

$$I_{\mathrm{p}} = \frac{h^3}{12} \tag{3.8}$$

The bending wavenumber for thin plates is defined as

$$k_{\mathrm{B}} = \sqrt[4]{\frac{\omega^2 m''}{B_{\mathrm{b}}}} = \frac{2\pi}{\lambda_{\mathrm{B}}} \tag{3.9}$$

where m'' is the mass per unit area. Hence the bending phase velocity, $c_{\mathrm{B,p}}$ is given by

$$c_{\mathrm{B,p}} = \sqrt[4]{\frac{\omega^2 B_{\mathrm{p}}}{m''}} = \sqrt[4]{\frac{\omega^2 {c_{\mathrm{L,p}}}^2 h^2}{12}} \tag{3.10}$$

3.2.3 Thin beams and plates

The definitions in sections 3.2.1 and 3.2.2 are only valid for thin beams and plates. Thin beam/plate theory assumes pure bending waves and does not account for shear deformation and rotatory inertia. It can be applied as long as the bending wavelength, λ_{B}, is large compared to the thickness dimension, i. e. h for the beam or plate. Hence there is an upper frequency limit for thin beam and thin plate theory. However the transition is not abrupt as the errors slowly accumulate due to neglecting shear deformation and rotatory inertia. Cremer and Heckl [1967] proposed a cross-over frequency from thin to thick bending wave theory when $\lambda_{\mathrm{B}} = 6\,h$.

Using the equations in sections 3.2.1 and 3.2.2 the upper frequency limit for thin beam and plate theory, $f_{\mathrm{B,thin}}$, can be estimated as follows

$$f_{\mathrm{B,thin}} = \frac{2\pi}{6^2\sqrt{12}}\,\frac{c_{\mathrm{L}}}{h} \approx 0.05\,\frac{c_{\mathrm{L}}}{h} \tag{3.11}$$

where c_{L} is the quasi-longitudinal phase velocity for beams or plates.

3.2.4 Equivalent orthotropic plates

This thesis considers timber-frame constructions formed from a combination of beams and plates. To describe the dynamic behaviour of a

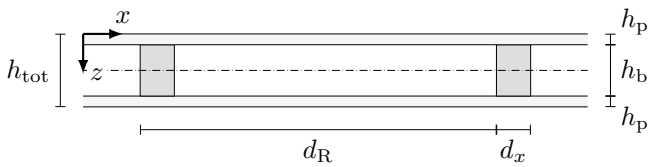

(a) Timber-frame wall

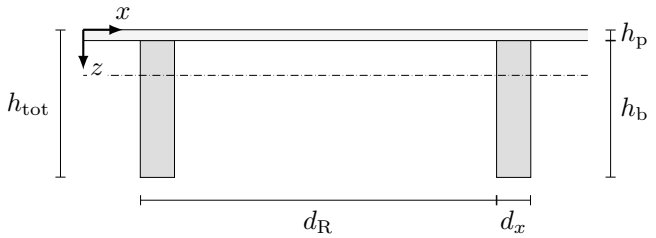

(b) Timber-joist floor

Figure 3.3: Cross section of the timber-frame wall and the timber-joist floor that shows the notation applied for the equivalent orthotropic plate model.

timber-frame wall with a symmetrical cross-section and a timber-joist floor, the bending stiffness is determined using the notations given in Figure 3.3.

The bending stiffness in y-direction, B_y, parallel to the ribs can be determined according to Troitsky [1976]. For the timber-frame wall it is

$$B_{y,\mathrm{wall}} = 2\left(\frac{E_{\mathrm{p}}\, h_{\mathrm{p}}^3}{12\,(1-\nu^2)} + \frac{E_{\mathrm{p}}\, h_{\mathrm{p}}\, z_{x,\mathrm{p}}^2}{1-\nu^2}\right) + \frac{E_{\mathrm{b}}\, I_{\mathrm{b}}}{d_{\mathrm{R}}} \tag{3.12}$$

and for the asymmetric timber-joist floor it is

$$B_{y,\mathrm{floor}} = \frac{E_{\mathrm{p}}\, h_{\mathrm{p}}^3}{12\,(1-\nu^2)} + \frac{E_{\mathrm{p}}\, h_{\mathrm{p}}\, z_{x,\mathrm{p}}^2}{1-\nu^2} + \frac{E_{\mathrm{b}}\, I_{\mathrm{b}}}{d_{\mathrm{R}}} \tag{3.13}$$

In these equations, $z_{x,\mathrm{p}}$ is the distance between the neutral axis of the plate and the neutral axis of the whole construction (dash-dotted lines in Figure 3.3).

For the timber-frame wall the neutral axis is in the mid-plane of the whole construction. For the timber-joist floor the z-coordinate of the neutral axis in the global coordinate system in Figure 3.3b can be determined by

$$z_{\mathrm{n}} = \frac{z_{\mathrm{p}}\, S_{\mathrm{p}} + z_{\mathrm{b}}\, S_{\mathrm{b}}}{S_{\mathrm{p}} + S_{\mathrm{b}}} \tag{3.14}$$

where z_{p} and z_{b} are the distances of the plate and the beam mid-planes relative to the x-axis of the global coordinate system.

The bending stiffness in x-direction perpendicular to the ribs, B_x, can be determined following an approach by Huffington [1967] which has been applied to timber constructions by Churchill and Hopkins [2016]. Following this, $B_{x,\mathrm{wall}}$, for the timber-frame wall is

$$B_{x,\mathrm{wall}} = \frac{d_{\mathrm{R}}\, 2h_{\mathrm{p}}}{12} \left[\frac{E_{\mathrm{p}} \left(E_{\mathrm{p}}\, 2h_{\mathrm{p}}^3 + E_{\mathrm{b}}\, (h_{\mathrm{tot}}^3 - 2h_{\mathrm{p}}^3) \right)}{(d_{\mathrm{R}} - d_x)\, E_{\mathrm{b}}\, (h_{\mathrm{tot}}^3 - 2h_{\mathrm{p}}^3) + d_{\mathrm{R}}\, E_{\mathrm{p}}\, 2h_{\mathrm{p}}^3} \right] \tag{3.15}$$

For the timber-joist floor it is

$$B_{x,\mathrm{floor}} = \frac{d_{\mathrm{R}}\, h_{\mathrm{p}}}{12} \left[\frac{E_{\mathrm{p}} \left(E_{\mathrm{p}}\, h_{\mathrm{p}}^3 + E_{\mathrm{b}}\, (h_{\mathrm{tot}}^3 - h_{\mathrm{p}}^3) \right)}{(d_{\mathrm{R}} - d_x)\, E_{\mathrm{b}}\, (h_{\mathrm{tot}}^3 - h_{\mathrm{p}}^3) + d_{\mathrm{R}}\, E_{\mathrm{p}}\, h_{\mathrm{p}}^3} \right] \tag{3.16}$$

where E_{p} and E_{b} are Young's moduli for the sheeting plate and the stiffening rib respectively.

Regarding the construction as one equivalent orthotropic plate, an effective bending stiffness, $B_{\mathrm{p,eff}}$, can be approximated by [Cremer and Heckl 1967])

$$B_{\mathrm{p,eff}} = \sqrt{B_x\, B_y} \tag{3.17}$$

To calculate the mass per unit area of this equivalent orthotropic plate, an equivalent density, ρ_{eq}, and height, h_{eq}, is determined according to Kimura and Inoue [1989]. For the timber-frame wall the equivalent density is

$$\rho_{\mathrm{eq,wall}} = \frac{2\,\rho_{\mathrm{p}}\,S_{\mathrm{p}}}{2\,S_{\mathrm{p}} + S_{\mathrm{b}}} + \frac{\rho_{\mathrm{b}}\,S_{\mathrm{b}}}{2\,S_{\mathrm{p}} + S_{\mathrm{b}}} \tag{3.18}$$

and for the timber joist floor it is

$$\rho_{\mathrm{eq,floor}} = \frac{\rho_{\mathrm{p}}\,S_{\mathrm{p}}}{S_{\mathrm{p}} + S_{\mathrm{b}}} + \frac{\rho_{\mathrm{b}}\,S_{\mathrm{b}}}{S_{\mathrm{p}} + S_{\mathrm{b}}} \tag{3.19}$$

In these equations, S_{p} and S_{b} are the cross-sectional areas of the plate and the beam respectively where the stud spacing, d_{R}, is used as effective plate width.

The equivalent height is given by

$$h_{\mathrm{eq}} = \sqrt[3]{12\,I_x} \tag{3.20}$$

where I_x is the second moment of area for the whole construction that can be determined using the parallel-axis theorem (also known as Steiner's theorem) [e. g. Gross et al. 2011]. For the timber-frame wall it is

$$I_{x,\mathrm{wall}} = 2\left(\frac{d_{\mathrm{R}}\,h_{\mathrm{p}}^3}{12} + d_{\mathrm{R}}\,h_{\mathrm{p}}\,z_{x,\mathrm{p}}^2\right) + \frac{d_x\,h_{\mathrm{b}}^3}{12} \tag{3.21}$$

and for the timber-joist floor it is

$$I_{x,\mathrm{floor}} = \frac{d_{\mathrm{R}}\,h_{\mathrm{p}}^3}{12} + d_{\mathrm{R}}\,h_{\mathrm{p}}\,z_{x,\mathrm{p}}^2 + \frac{d_x\,h_{\mathrm{b}}^3}{12} + d_x\,h_{\mathrm{b}}\,z_{x,\mathrm{b}}^2 \tag{3.22}$$

where $z_{x,\mathrm{p}}$ and $z_{x,\mathrm{b}}$ represent the distance between the neutral axis and the mid-plane of the plate and the beam respectively.

This equivalent orthotropic plate model implies no shear deformation between the sheeting plates and wall studs or floor joists. Typically plates are screwed or nailed to the ribs (with or without glue), hence the bending stiffness is likely to be overestimated and can be regarded as an upper limit.

3.2.5 Bending modes on finite beams and plates

When the boundary conditions of a finite beam or plate are known, the bending mode frequencies can be calculated analytically.

The mode frequencies for bending modes ($p = 1, 2, 3, \dots$) of a simply supported beam that has the length, L_y, are given by [e. g. see Gardonio and Brennan 2004, section 9.6.5]

$$f_p = \frac{\pi}{2} \sqrt{\frac{B_\mathrm{b}}{m'}} \left(\frac{2\,p}{L_y} \right)^2 \tag{3.23}$$

The mode frequencies for bending modes ($p = 1, 2, 3, \dots$) of a beam with clamped or free boundary conditions and the length, L_y are

$$f_p = \frac{\pi}{8} \sqrt{\frac{B_\mathrm{b}}{m'}} \left(\frac{2\,p-1}{L_y} \right)^2 \tag{3.24}$$

Note that for free boundary conditions there are rigid body modes (even and rocking) in addition to the bending modes.

The mode frequencies for a finite thin rectangular plate with the dimensions, $L_x \times L_y$ are given by [Gardonio and Brennan 2004, section 9.8.4]

$$f_{p,q} = \frac{\pi}{2} \sqrt{\frac{E\,h}{12\,\rho\,(1-\nu^2)}}\, \frac{\varphi_{pq}}{L_x^2} \tag{3.25}$$

where φ_{pq} is

$$\begin{aligned} \varphi_{pq}^2 = G_x^4(p) + G_y^4(q) \left(\frac{L_x}{L_y} \right)^4 \\ + 2 \left(\frac{L_x}{L_y} \right)^2 [\nu H_x(p) H_y(q) + (1-\nu) J_x(p) J_y(q)] \end{aligned} \tag{3.26}$$

The constants G, H and J are given in Table 3.1 for free boundary conditions. Further boundary conditions can be found in [Gardonio and Brennan 2004, Table 9.9]. The subscripts x and y with the constants in

Table 3.1: Constants G, H and J to determine mode frequencies of a plate with free-free boundary conditions.

p	G	H	J
Even	0	0	0
Rocking	0	0	$\frac{12}{\pi^2}$
1	1.506	1.284	5.017
2,3,4,...	p+$\frac{1}{2}$	$\left(p+\frac{1}{2}\right)^2\left[1-\frac{4}{(2p+1)\pi}\right]$	$\left(p+\frac{1}{2}\right)^2\left[1+\frac{12}{(2p+1)\pi}\right]$

equation (3.25) indicate the boundary to which the values from Table 3.1 apply. Idealized boundary conditions can be approximated in laboratory mock-ups by resiliently supporting plates to approximate free boundary conditions. However in real buildings the actual boundary conditions are rarely ideal (or known). In this thesis analytically determined mode frequencies are used to estimate the mode count, N in a frequency band for comparison with statistical approaches.

As the determination of the actual mode frequency is difficult, a statistical descriptor, the modal density, $n(f)$ can be used. This gives the number of modes per Hertz. For thin beams it is defined as

$$n_{\mathrm{b}}(f) = \frac{L_y}{c_{\mathrm{B,b}}} \tag{3.27}$$

where L_y is the length of the beam and $c_{\mathrm{B,b}}$ is given by equation (3.5). For a thin plate the modal density, $n_{\mathrm{p}}(f)$ of bending waves is given by

$$n_{\mathrm{p}}(f) = \frac{S\sqrt{3}}{h\, c_{\mathrm{L,p}}^2} \tag{3.28}$$

where S is the surface area of the plate.

3.2.6 Direct vibration field on finite plates due to local point excitation

For a local point excitation on a plate, the bending waves that radiate out from this point are attenuated by geometrical spreading and internal damping. Close to the excitation point there is a direct vibration field given by [e. g. Lyon and DeJong 1995]

$$\langle v_{\mathrm{d}}^2 \rangle_t = \frac{W_{\mathrm{in}}}{2\,\pi\,r\,c_{\mathrm{g,B,p}}\,m''} \exp\left(-\frac{\omega\,\eta_{\mathrm{int}}\,r}{c_{\mathrm{g,B,p}}}\right) \tag{3.29}$$

where r is the distance from the local point excitation, and $c_{\mathrm{g,B,p}}$ is the group velocity for bending waves on plates. For thin plates, $c_{\mathrm{g,B,p}} = 2\,c_{\mathrm{B,p}}$.

3.2.7 Structural intensity

The time-average surface velocity can be used to describe the vibrational energy and velocities on a measurement grid to identify or visualize the mode shapes of a structure. However, this does not give insight into the power flow across the structure.

In a finite, vibrating structure there is a continuous alternating interchange of energy between spatial areas of kinetic and potential energy. This oscillatory transport of energy is called reactive power flow of which the time average is zero. However, in any real vibrating mechanical system there are losses due to internal friction, radiation, or boundaries. Therefore there is an active component of the power flow "beneath the seething sea of local reactive energy flux" [Fahy 1995a, p. 54] which transports vibrational energy from sources to sinks. This active component describes the net-energy transport, hence the time average is non-zero. However as the magnitude and direction of the active intensity vector changes with time, time-averaged values are necessary.

This active component can be visualized by measuring the structural intensity, I_{s}, on the surface of a structure as energy flux density (power per unit width). As bending waves are the most important wave type for

building acoustics, structural intensities of in-plane wave types are not addressed in this thesis.

In the following the structural intensity is derived for the x-direction denoted as $I_{\mathrm{s},x}$. From Noiseux [1970] the structural intensity is the sum of a force component $I_{\mathrm{s},x,\mathrm{F}}$ and a moment component $I_{\mathrm{s},x,\mathrm{M}}$, where the moment component in turn comprises a bending, $I_{\mathrm{s},x,\mathrm{BM}}$, and a twisting component $I_{\mathrm{s},x,\mathrm{TM}}$.

$$\begin{aligned} I_{\mathrm{s},x} &= I_{\mathrm{s},x,\mathrm{F}} + I_{\mathrm{s},x,\mathrm{M}} \\ &= I_{\mathrm{s},x,\mathrm{F}} + I_{\mathrm{s},x,\mathrm{BM}} + I_{\mathrm{s},x,\mathrm{TM}} \end{aligned} \tag{3.30}$$

The force component can be expressed by the time average of the product of shear force Q_x and the lateral velocity v_z following the notation from Figure 3.4[1]. Similarly the moment components for bending, M_{xy} and twisting, M_{xx} are described by the time-average of the product with their corresponding angular velocities α_y and α_x, respectively.

$$I_{\mathrm{s},x} = \langle Q_x \, v_z \rangle_t + \langle M_{xy} \, \alpha_y \rangle_t + \langle M_{xx} \, \alpha_x \rangle_t \tag{3.31}$$

Following Kirchhoff's plate theory, the shear force, the bending moment and the twisting moment can be rewritten using derivatives and partial derivatives of the displacement with respect to x and y. Hence the structural intensity components can be expressed in terms of the displacement by additionally using partial derivatives to describe the angular velocities.

$$I_{\mathrm{s},x,\mathrm{F}} = -B_{\mathrm{p}} \left\langle \frac{\partial}{\partial x} \left(\frac{\partial^2 w}{\partial x^2} + \frac{\partial^2 w}{\partial y^2} \right) \frac{\partial w}{\partial t} \right\rangle_t \tag{3.32}$$

[1] Note about the notation in Figure 3.4: Bending moments on the x-axis are often denoted as M_x in literature, although the moment is rotating about the y-axis. In this work bending moments on the x-axis are denoted as M_{xy}, where the first subscript indicates the axis to which the moment acts perpendicularly and the second subscript indicates the direction in which the moment acts on. The same applies for the notation of twisting/torsional moments.

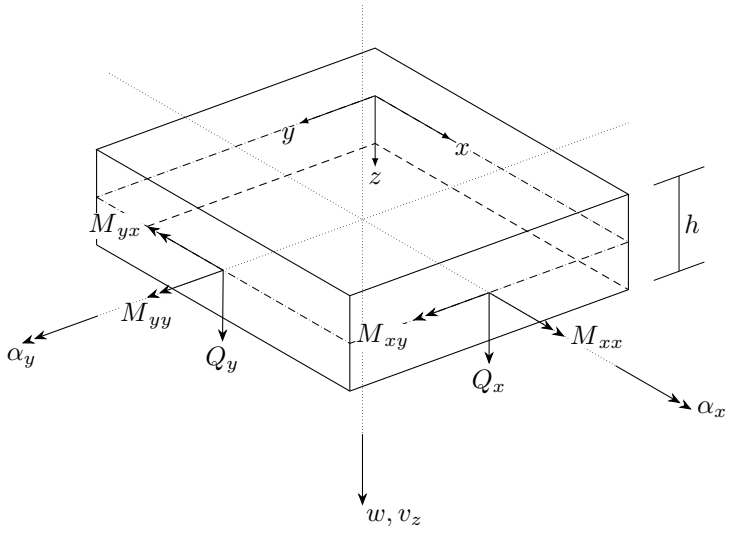

Figure 3.4: Internal forces and moments (shear forces Q, bending and twisting moments M) at 'positive' cross sections (outward pointing x- and y-axis). Additionally the displacement w (lateral velocity v_z) and the angular velocities α are indicated.

$$I_{\mathrm{s},x,\mathrm{BM}} = -B_\mathrm{p} \left\langle \left(\frac{\partial^2 w}{\partial x^2} + \nu \frac{\partial^2 w}{\partial y^2} \right) \frac{\partial^2 w}{\partial t \, \partial x} \right\rangle_t \tag{3.33}$$

$$I_{\mathrm{s},x,\mathrm{TM}} = -B_\mathrm{p} \left(1 - \nu\right) \left\langle \frac{\partial^2 w}{\partial x \, \partial y} \frac{\partial^2 w}{\partial t \, \partial x} \right\rangle_t \tag{3.34}$$

where the bending stiffness B_p for plates is given in equation (3.6).

3.2.8 Sound radiation from bending waves

3.2.8.1 Radiation efficiency

Sound radiation from bending waves on plates can be described by the radiation efficiency, σ. This quantity relates the radiated sound power to the power radiated by a baffled piston with uniform velocity distribution

and dimensions that are large compared to the wavelength of air [Cremer and Heckl 1967].

$$\sigma = \frac{W_{\mathrm{rad}}}{S\,\rho_0\,c_0\,\langle v^2\rangle_{t,s}} \tag{3.35}$$

Hence the radiation efficiency is unity when the plate radiates the same power as a baffled piston with the same area and velocity.

3.2.8.2 Critical frequency

As bending waves are dispersive, there is one particular frequency at which the bending wavelength matches the wavelength in air. This is called (lowest) coincidence frequency or critical frequency, f_{c}. Above the critical frequency the radiation efficiency tends towards a value of one. For thin plates the critical frequency can be calculated as follows

$$f_{\mathrm{c}} = \frac{{c_0}^2\,\sqrt{3}}{\pi\,h\,c_{\mathrm{L,p}}} \tag{3.36}$$

where c_0 is the phase velocity of sound in air.

3.2.8.3 Frequency-average radiation efficiency of rectangular plates

Estimates of the frequency-average radiation efficiency came from work by Maidanik [1962] and Crocker and Price [1969]. Leppington et al. [1982] developed more accurate methods to calculate a frequency-average radiation efficiency for rectangular plates. Similar to Maidanik, the model of Leppington et al. describes the radiation efficiency in terms of μ, which is the ratio of the bending wavenumber to the wavenumber in air. This can be written in terms of the coincidence frequency as follows.

$$\mu = \frac{k_{\mathrm{B}}}{k_0} = \sqrt{\frac{f_{\mathrm{c}}}{f}} \tag{3.37}$$

The radiation efficiency is defined for three regimes. Below the critical frequency, where $\mu > 1$, Leppington et al. [1982] give the radiation efficiency as

$$\sigma = \frac{(L_1 + L_2)}{\pi\,\mu\,k_0\,L_1\,L_2\,\sqrt{\mu^2 - 1}} \left[\ln\left(\frac{\mu+1}{\mu-1}\right) + \frac{2\,\mu}{\mu^2-1}\right] \quad \text{for} \quad \mu > 1 \tag{3.38}$$

At the critical frequency, where $\mu = 1$ it is

$$\sigma = \sqrt{k_0\,L_1}\,H\left(\frac{L_1}{L_2}\right) \quad \text{for} \quad \mu = 1 \tag{3.39}$$

with

$$H(x) = \frac{4}{15\,\pi^{\frac{3}{2}}}\,x^{\frac{1}{2}} \int_0^1 (5-t)\,\left[(t^2+x^2)^{-\frac{3}{4}} + (1+x^2\,t^2)^{-\frac{3}{4}}\right]\,\mathrm{d}t \tag{3.40}$$

And above the critical frequency, where $\mu < 1$, it is defined as

$$\sigma = \frac{1}{\sqrt{(1-\mu^2)}} \quad \text{for} \quad \mu < 1 \tag{3.41}$$

In equations (3.38) and equation (3.39) L_1 is the smaller dimension of the plate dimensions L_x and L_y:

$$L_1 = \min(L_x, L_y) \quad \text{and} \quad L_2 = \max(L_x, L_y) \tag{3.42}$$

Above the coincidence frequency, the radiation efficiency is independent of the dimensions. With μ approaching unity, equations (3.38) and (3.41) tend towards infinity. Hence the radiation efficiency at $\mu = 1$ gives an upper limit. As this is only valid at this particular frequency, it overestimates the radiation efficiency compared to values averaged in one-third octave bands for example.

To provide a continuous function, Leppington provided extensive transition formulas in a later paper [1986]. The radiation efficiency close to the coincidence frequency is given as

$$\sigma = I(L_1, L_2) + I(L_2, L_1) \quad \text{for} \quad \mu \approx 1 \tag{3.43}$$

with

$$I(L_1, L_2) = \int_0^{\sec\theta_0} G(t) \left[-\theta_0 + t \operatorname{cosec}\theta_0 (\cos\theta_0 - \cos 2\theta_0) - \frac{1}{4} t^2 \sin 2\theta_0 \right] \mathrm{d}t + \int_1^{\sec\theta_0} G(t) \left[\operatorname{arcsec} t - (t^2 - 1)^{\frac{1}{2}} + \frac{1}{2} (1 - t)^2 \cot\theta_0 \right] \mathrm{d}t \tag{3.44}$$

where

$$\theta_0 = \arctan\left(\frac{L_2}{L_1}\right) \tag{3.45}$$

$$G(t) = \frac{(2\,k_0\,L_1)^{\frac{1}{2}}}{\pi^{\frac{3}{2}}}\, t^{-\frac{1}{2}} \sin\left(\chi_0\, t - \frac{1}{4}\,\pi\right) \tag{3.46}$$

$$\chi_0 = k_0\, L_1\, (\mu - 1) = k_\mathrm{B}\, L_1 - k_0\, L_1 \tag{3.47}$$

For $I(L_2, L_1)$, L_1 and L_2 need to be interchanged in equation (3.44).

Based on these equations the radiation efficiency was determined in this thesis in a similar manner to the methodology applied by Schoenwald [2008]: As a first step the radiation efficiency was calculated according to equations (3.38) to (3.41) in narrow bands. It was then additionally calculated using Leppington's transition formulas. From this, a continuous narrow-band radiation efficiency was assembled using the intersection of the graphs. Finally the narrow band values were averaged for one-third octave bands to give a frequency average radiation efficiency.

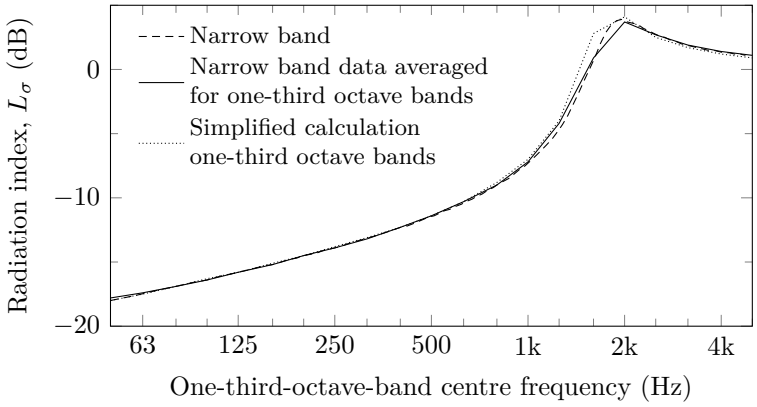

Figure 3.5: Radiation efficiency of 19 mm chipboard (0.565 m × 2.53 m) according to Leppington.

Note that Leppington et al. also suggested a simplified calculation method as the variation of the function $H(x)$, given in (3.40), is small for plates with similar x- and y-dimensions. However as narrow plates with small aspect ratios are considered in this thesis, the simplified method is not suitable, and therefore the detailed calculation was applied. All three calculation methods are shown in Figure 3.5 for a 19 mm chipboard sheet.

3.2.8.4 Sound intensity

To determine the radiation efficiency experimentally, the sound intensity as well as the surface velocity of the structure have to be measured. The sound intensity, I, i. e. the energy flux density (power per area) is the time-averaged product of the sound pressure and the particle velocity

$$I = \langle p\, u \rangle_t \tag{3.48}$$

For a surface area, S, the radiated power is given as

$$W_{\mathrm{rad}} = \int_S I \,\mathrm{d}S \tag{3.49}$$

3.2.8.5 Nearfield radiation from point excitation

In this thesis mechanical excitation by point connected machinery is considered. Hence the radiation of the nearfield from the excitation point also needs to be considered. From Cremer and Heckl [1967] the radiated power from the nearfield of a local point force excitation, W_{nf}, can be calculated using the mean-square force, $\tilde{F}^2$.

$$W_{\mathrm{nf}} = \frac{\rho_0\, c_0\, k_0^2\, \tilde{F}^2}{2\,\pi\,\omega^2\, m''^2} \quad \text{for} \quad f << f_{\mathrm{c}} \tag{3.50}$$

For an excitation that acts over an area, Cremer and Heckl [1967] further describe the nearfield radiation in terms of a piston with a radius $r + \lambda_{\mathrm{B}}/4$. This can be expressed using the mean-square force and the driving point mobility, Y_{dp} [e. g. see Hopkins 2007]

$$W_{\mathrm{nf}} = \frac{1}{2}\,\rho_0\, c_0\, k_0^2\,\pi \left(r + \frac{\lambda_{\mathrm{B}}}{4}\right)^4 \tilde{F}^2\, Y_{\mathrm{dp}}^2 \quad \text{for} \quad f << f_{\mathrm{c}} \tag{3.51}$$

3.2.9 Mobility

The complex mobility, $\underline{Y}$, is given by the ratio between the velocity and the exciting force. The mobility is the inverse of the impedance, however in this thesis, mobility is used throughout. The excitation and the response can be either translational or rotatory and in-plane or out-of-plane. Bending wave vibrations are related with deflection perpendicular to the surface. Therefore the mobilities for the out-of-plane components (F_z, v_z, M_x, α_x, M_y and α_y) are defined in the following sections and the notation and direction conventions are given in Figure 3.6.

3.2.9.1 Driving-point mobility

The complex driving-point mobility, Y_{dp}, describes the ratio of the complex out-of-plane velocity, $\underline{v}_{z,i}$, at position i to the complex point force perpendicular to the surface at the same position, $\underline{F}_{z,i}$. Using sub- and superscripts, the complex driving-point mobility can be denoted uniquely

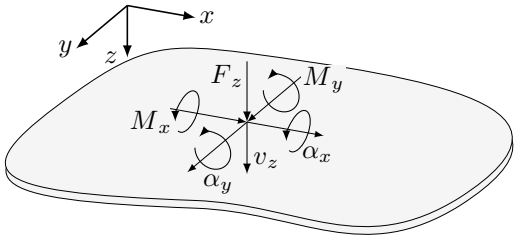

Figure 3.6: Notation and direction conventions for forces and moments.

using m and n for the degree of freedom of the response and excitation respectively, with i indicating the excitation and j the response position. Hence the driving-point mobility is of type $\underline{Y}_{ii}^{mm}$ and can be written as $\underline{Y}_{ii}^{v_z F_z}$. However in the following, this is only used if unique notation is necessary and normally the complex driving-point mobility is simply denoted as Y_{dp}.

$$Y_{\mathrm{dp}} = \underline{Y}_{ii}^{v_z F_z} = \frac{\underline{v}_{z,i}}{\underline{F}_{z,i}} \tag{3.52}$$

3.2.9.2 Moment mobility

The complex moment mobility is described similarly to the driving-point mobility. Hence, for rotation about the x-axis, $Y_{\mathrm{M}x}$ is the ratio of the complex angular velocity $\underline{\alpha}_{x,i}$ at a position i, to the complex moment exciting the structure at the same position, about the same axis, $\underline{M}_{x,i}$. Sub- and superscripts can be used to obtain unique notation, which gives $\underline{Y}_{ii}^{\alpha_x M_x}$ for the complex point moment mobility about the x-axis at position i. As for the driving-point mobility, this notation is only used if necessary and normally the simpler notations, $Y_{\mathrm{M}x}$ and $Y_{\mathrm{M}y}$ are used for the complex moment mobility about the x-axis

$$Y_{\mathrm{M}x} = \underline{Y}_{ii}^{\alpha_x M_x} = \frac{\underline{\alpha}_{x,i}}{\underline{M}_{x,i}} \tag{3.53}$$

and about the y-axis:

$$Y_{\mathrm{M}y} = \underline{Y}_{ii}^{\alpha_y M_y} = \frac{\underline{\alpha}_{y,i}}{\underline{M}_{y,i}} \tag{3.54}$$

3.2.9.3 Mobility of infinite beams and plates

As the boundary conditions of beams and plates forming building structures can not always be described exactly, analytical models for the mobility of finite beams or plates [e. g. see Gardonio and Brennan 2004] are not suitable. Hence infinite beam and plate mobilities according to [Cremer and Heckl 1967] can be used.

The driving-point mobility of an infinite plate excited in the central section is frequency-independent and given by

$$Y_{\mathrm{dp,inf,p}} = \frac{1}{8\sqrt{B_{\mathrm{p}}\,\rho\,h}} \tag{3.55}$$

Note that this is only valid for thin plates, i. e. $h < \lambda_{\mathrm{B}}/6$.

For a semi-infinite plate excited at the edge, the driving-point mobility is given as

$$Y_{\mathrm{dp,sinf,p}} = \frac{1}{3.5\sqrt{B_{\mathrm{p}}\,\rho\,h}} \tag{3.56}$$

The driving-point mobility for an infinite beam excited in the central part is complex and given by

$$Y_{\mathrm{dp,inf,b}} = \frac{1}{2\,\rho\,S\,c_{\mathrm{B,b}}\,(1+\mathrm{i})} \tag{3.57}$$

where S is the cross sectional area of the beam.

The complex moment mobility for an infinite plate and excitation in the central region is [Gardonio and Brennan 2004]

$$Y_{\mathrm{M,inf,p}} = \frac{\omega}{16\,B_{\mathrm{p}}}\left(1 - \mathrm{i}\,\frac{4}{\pi}\,\ln\frac{k_{\mathrm{B,p}}\,R}{2}\right) \tag{3.58}$$

where R is the radius of the circular excitation area.

The moment mobility for a beam excited in the central section is defined as [Gardonio and Brennan 2004]

$$Y_{\mathrm{M,inf,b}} = \frac{\omega}{4\,B_{\mathrm{b}}\,k_{\mathrm{B,b}}}\,(1+\mathrm{i}) \tag{3.59}$$

3.2.9.4 Transfer and cross-transfer mobilities

A transfer mobility describes the complex transfer function between the excitation acting at a position i and the response at a position j for excitation in the same direction (e. g. F_z and v_z, see Figure 3.7). Cross-transfer mobility describes the transfer function between, for example, a force excitation and an angular velocity response.

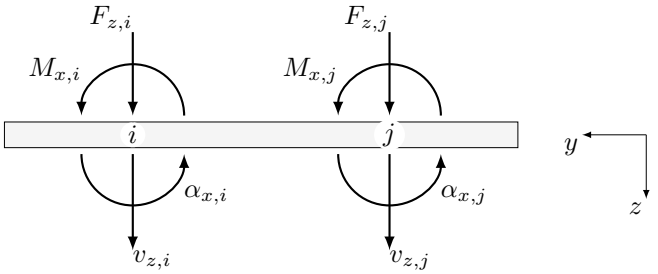

Figure 3.7: Notation for forces and moments, as well as out-of-plane and angular velocities at two positions i and j.

To describe all out-of-plane point, transfer and cross-transfer mobilities for these two points, i and j, the following 6×6 mobility matrix is necessary.

$$\mathbf{Y} = \begin{pmatrix} \underline{Y}_{ii}^{v_z F_z} & \underline{Y}_{ii}^{v_z M_x} & \underline{Y}_{ii}^{v_z M_y} & \underline{Y}_{ij}^{v_z F_z} & \underline{Y}_{ij}^{v_z M_x} & \underline{Y}_{ij}^{v_z M_y} \\ \underline{Y}_{ii}^{\alpha_x F_z} & \underline{Y}_{ii}^{\alpha_x M_x} & \underline{Y}_{ii}^{\alpha_x M_y} & \underline{Y}_{ij}^{\alpha_x F_z} & \underline{Y}_{ij}^{\alpha_x M_x} & \underline{Y}_{ij}^{\alpha_x M_y} \\ \underline{Y}_{ii}^{\alpha_y F_z} & \underline{Y}_{ii}^{\alpha_y M_x} & \underline{Y}_{ii}^{\alpha_y M_y} & \underline{Y}_{ij}^{\alpha_y F_z} & \underline{Y}_{ij}^{\alpha_y M_x} & \underline{Y}_{ij}^{\alpha_y M_y} \\ \underline{Y}_{ji}^{v_z F_z} & \underline{Y}_{ji}^{v_z M_x} & \underline{Y}_{ji}^{v_z M_y} & \underline{Y}_{jj}^{v_z F_z} & \underline{Y}_{jj}^{v_z M_x} & \underline{Y}_{jj}^{v_z M_y} \\ \underline{Y}_{ji}^{\alpha_x F_z} & \underline{Y}_{ji}^{\alpha_x M_x} & \underline{Y}_{ji}^{\alpha_x M_y} & \underline{Y}_{jj}^{\alpha_x F_z} & \underline{Y}_{jj}^{\alpha_x M_x} & \underline{Y}_{jj}^{\alpha_x M_y} \\ \underline{Y}_{ji}^{\alpha_y F_z} & \underline{Y}_{ji}^{\alpha_y M_x} & \underline{Y}_{ji}^{\alpha_y M_y} & \underline{Y}_{jj}^{\alpha_y F_z} & \underline{Y}_{jj}^{\alpha_y M_x} & \underline{Y}_{jj}^{\alpha_y M_y} \end{pmatrix} \tag{3.60}$$

3.2.9.5 Point and transfer mobilities of finite free plates

For known boundary conditions, the point and transfer mobilities of finite plates can be determined as described by Gardonio and Brennan [2004] using characteristic beam functions, ϕ_p and ϕ_q. For a free beam these are given as

$$\phi_q(x) = \begin{cases} 1 & \text{even} \\ \sqrt{3}\left(1 - \frac{2x}{L_x}\right) & \text{rocking} \\ \sqrt{2}\left\{\cos\gamma_i\left(\frac{x}{L_x}\frac{1}{2}\right) + k_q \cosh\gamma_i\left(\frac{x}{L_x}\frac{1}{2}\right)\right\} & q = 1,3,5,\ldots \\ \sqrt{2}\left\{\sin\gamma_j\left(\frac{x}{L_x}\frac{1}{2}\right) + k_q \sinh\gamma_j\left(\frac{x}{L_x}\frac{1}{2}\right)\right\} & q = 2,4,6,\ldots \end{cases} \tag{3.61}$$

where k_q is

$$k_q = \begin{cases} -\frac{\sin\frac{1}{2}\gamma_i}{\sinh\frac{1}{2}\gamma_i} & \text{for} \quad q = 1,3,5,\ldots \\ \frac{\sin\frac{1}{2}\gamma_j}{\sinh\frac{1}{2}\gamma_j} & \text{for} \quad q = 2,4,6,\ldots \end{cases} \tag{3.62}$$

and the γ-functions are

$$\begin{aligned} \tan\frac{1}{2}\gamma_i + \tanh\frac{1}{2}\gamma_i = 0 \quad \text{for} \quad q = 1,3,5,\ldots \\ \tan\frac{1}{2}\gamma_j - \tanh\frac{1}{2}\gamma_j = 0 \quad \text{for} \quad q = 2,4,6,\ldots \end{aligned} \tag{3.63}$$

The zeros of the gamma functions are given in Table 3.2 according to Gardonio and Brennan [2004]; however the notation of Höller [2013] is used.

For each bending mode (pq) the mode shape, ψ_{pq}, is calculated using the products and derivatives of the beam functions ϕ_p and ϕ_q as follows

$$\begin{aligned} \psi_{pq}(x,y) &= \phi_p(x)\,\phi_q(y) \\ \psi^x_{pq}(x,y) &= \phi_p(x)\,\frac{\partial\phi_q(y)}{\partial y} \\ \psi^y_{pq}(x,y) &= \frac{\partial\phi_p(x)}{\partial x}\,\phi_q(y) \end{aligned} \tag{3.64}$$

Table 3.2: Zeros of the gamma functions γ_i and γ_j with $i = (q + 1/2)$ for q = 1,3,5,... and $j = q/2$ for q = 2,4,6,....

i, j	$\tan\frac{1}{2}\gamma_i + \tanh\frac{1}{2}\gamma_i = 0$	$\tan\frac{1}{2}\gamma_j - \tanh\frac{1}{2}\gamma_j = 0$
1	4.73004	7.8532
2	10.9956	14.13716
3	17.27876	20.4204
4	23.5620	26.7036
5	29.8452	32.9868
6,7,8,...	$\frac{(4i-1)\,\pi}{2}$	$\frac{(4j+1)\,\pi}{2}$

Using modal summation the point and transfer mobilities can be determined as follows

$$
\begin{aligned}
Y^{v_z F_z}(\omega, x_1, y_1, x_2, y_2) &= \mathrm{i}\,\omega \sum_{p=1}^{\infty}\sum_{q=1}^{\infty} \frac{\psi_{pq}(x_2, y_2)\,\psi_{pq}(x_1, y_1)}{\rho\, h\, L_x\, L_y \left[\omega_{pq}^2\ (1 + \mathrm{i}\eta) - \omega^2\right]} \\
Y^{\alpha_x M_x}(\omega, x_1, y_1, x_2, y_2) &= \mathrm{i}\,\omega \sum_{p=1}^{\infty}\sum_{q=1}^{\infty} \frac{\psi^x_{pq}(x_2, y_2)\,\psi^x_{pq}(x_1, y_1)}{\rho\, h\, L_x\, L_y \left[\omega_{pq}^2\ (1 + \mathrm{i}\eta) - \omega^2\right]} \\
Y^{\alpha_y M_y}(\omega, x_1, y_1, x_2, y_2) &= \mathrm{i}\,\omega \sum_{p=1}^{\infty}\sum_{q=1}^{\infty} \frac{\psi^y_{pq}(x_2, y_2)\,\psi^y_{pq}(x_1, y_1)}{\rho\, h\, L_x\, L_y \left[\omega_{pq}^2\ (1 + \mathrm{i}\eta) - \omega^2\right]}
\end{aligned}
\tag{3.65}
$$

where the mode frequencies, ω_{pq}, are determined as described in section 3.2.5. For the formulation of cross and cross transfer mobilities and other boundary conditions the reader is referred to [Gardonio and Brennan 2004].

An example for a 19 mm chipboard with dimensions 0.93 m × 2.05 m is shown in Figures 3.8 and 3.9. The magnitude and phase of the finite plate driving-point mobility is shown in Figure 3.8 for comparison with the infinite plate mobility according to equation (3.55). Figure 3.9 shows magnitude and phase of the moment mobility about the x-axis for the

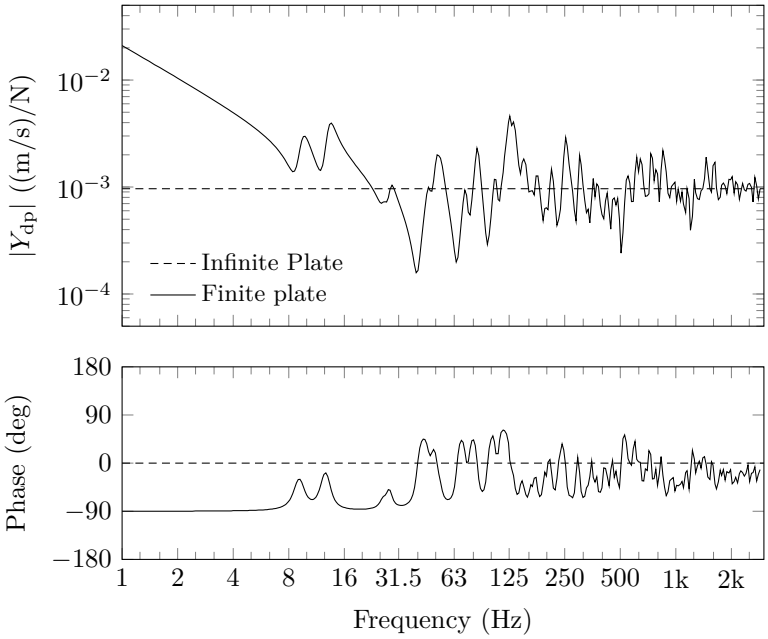

Figure 3.8: Magnitude and phase of driving-point mobility for a 19 mm chipboard plate with dimensions 0.93 m × 2.05 m. The excitation position is located at (0.31 m, 0.28 m).

same plate and the infinite plate according to equation (3.58). Both figures show that towards high frequencies the behaviour of finite plates tends towards that of infinite plates.

3.3 Structure-borne sound source characterization on a power basis

Source characterization covers the determination of the active and passive characteristics of the source. The machine is regarded in its entirety and therefore internal source mechanisms are not considered in detail and the active and passive parameters are determined at the accessible contact points (terminals). This black-box approach [Mondot and Petersson 1987; Moorhouse 2001; Höller 2013] is shown in Figure 3.10.

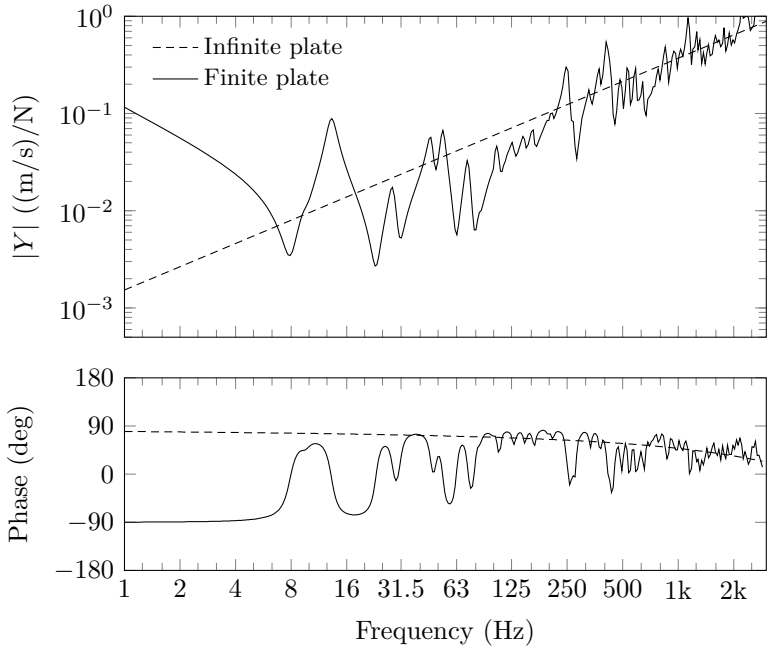

Figure 3.9: Magnitude and phase of moment mobility for the same plate and excitation position as in Figure 3.8. The infinite plate moment mobility is shown for an indenter radius R of 35 mm.

Note that in this thesis force and moment excitation components are considered separately and only out-of-plane excitation components are concerned.

3.3.1 Source parameters

3.3.1.1 Source activity

Considering only the translational motions, the active properties of the source are described either by the (source) free velocity, v_{Sf}, or by the blocked force, F_{b}, at the terminals. Both are complex and a function of frequency. They can be derived from each other using the source mobility, Y_{S}, or the source impedance, Z_{S}, respectively.

$$\underline{v}_{\mathrm{Sf}}(f) = \underline{Y}_{\mathrm{S}}(f)\,\underline{F}_{\mathrm{b}}(f) \tag{3.66}$$

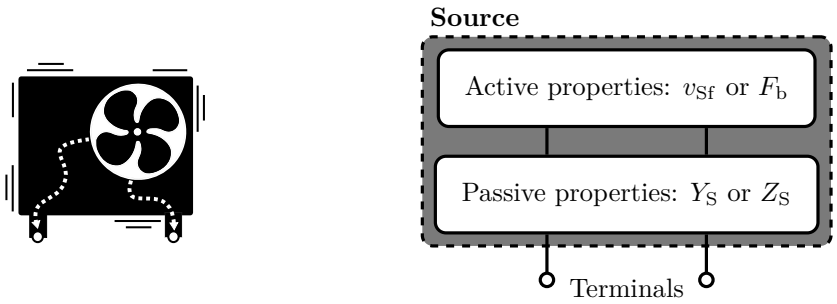

Figure 3.10: Structure-borne sound source characterization. Sketch based on Höller [2013]

$$\underline{F}_{\mathrm{b}}(f) = \underline{Z}_{\mathrm{S}}(f)\,\underline{v}_{\mathrm{Sf}}(f) \tag{3.67}$$

In the free condition the source is freely suspended. In the blocked condition the source is mounted on a large inert receiving structure. For both it is assumed that the excitation caused by internal mechanisms is transmitted linearly to the contact points.

3.3.1.2 Source mobility

Similar to the active parameters, the source is either regarded in a free or a blocked situation for the determination of its passive parameter, that is its mobility (introduced in section 3.2.9). With the source resiliently suspended, the source mobility, Y_{S}, can be measured at the accessible contact points. A measurement of the source impedance, Z_{S}, requires the contact points to be blocked with an inert receiver. Hence it is more practical to determine the mobility experimentally. However the impedance can easily be derived from the inverse of the mobility.

3.3.2 Installed structure-borne sound power

For passive receiving structures the receiver mobility, Y_{R}, (or the receiver impedance, Z_{R}, respectively) at the positions where the source is

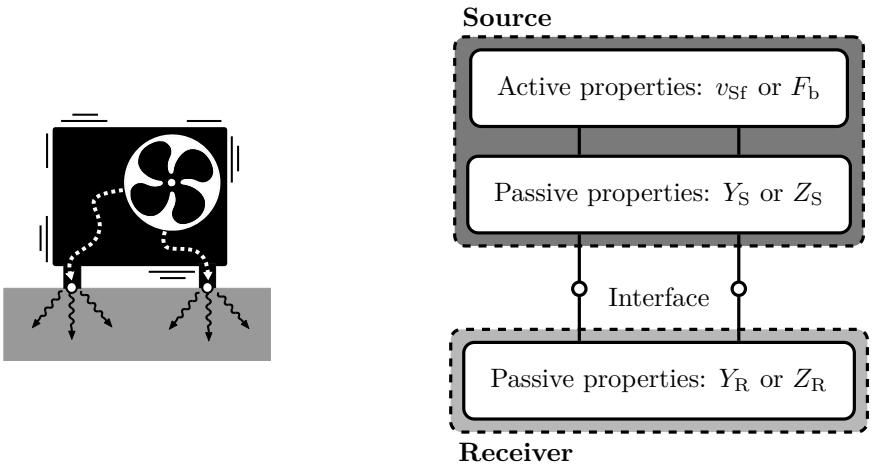

Figure 3.11: Source receiver coupling. Sketch based on Höller [2013]

connected is required. Based on the parameters of the source and the receiver the transmission of vibrational energy (stage 1b in Figure 1.2) can be obtained as indicated in Figure 3.11. This is particularly influenced by the ratio of source and receiver mobilities [Mondot and Petersson 1987].

In building acoustics, power is the primary quantity often used in prediction models, hence a power-based descriptor to describe structure-borne sound emission is advantageous. When a source is attached to a receiver it will deliver a certain power in this particular situation, the so-called installed power. The complex power $\underline{Q}$ comprises a real part W, the active power, and an imaginary part P, the reactive power.

$$\underline{Q} = W + \mathrm{i}P \tag{3.68}$$

The real part describes the power that propagates through the structure causing a net power flow away from the point of excitation. In contrast, the imaginary part only affects the nearfield as it is not efficiently transmitted and only alternates between source and receiver [e. g. Petersson

and Plunt 1980]. Hence for the prediction of machinery noise from an installed machine, the active power is of particular interest.

3.3.3 Methods to determine the installed structure-borne sound power

3.3.3.1 Direct method

For a single point the installed structure-borne sound power can be determined from the exciting force and the resulting velocity at that point [Cremer and Heckl 1967].

$$\underline{Q} = \frac{1}{2}\,\underline{\hat{F}}\,\underline{\hat{v}}^{*} \tag{3.69}$$

The active power is then given by

$$W = \mathrm{Re}\left\{\underline{Q}\right\} = \frac{1}{2}\,\mathrm{Re}\left\{\underline{\hat{F}}\,\underline{\hat{v}}^{*}\right\} \tag{3.70}$$

3.3.3.2 Mobility method

For a source with one contact point, the injected active power to a receiving structure can be predicted using either the free velocity or the blocked force in combination with the coupling conditions described by the source and receiver mobility.

Using the free velocity, the input power is [Mondot and Petersson 1987]

$$\underline{Q} = \frac{1}{2}\,|\underline{\hat{v}}_{\mathrm{Sf}}|^{2}\,\frac{\underline{Y}_{\mathrm{R}}}{|\underline{Y}_{\mathrm{S}} + \underline{Y}_{\mathrm{R}}|^{2}} \tag{3.71}$$

As, $W = \mathrm{Re}\left\{\underline{Q}\right\}$, the active power is

$$W = \frac{1}{2}\,|\underline{\hat{v}}_{\mathrm{Sf}}|^{2}\,\frac{\mathrm{Re}\left\{\underline{Y}_{\mathrm{R}}\right\}}{|\underline{Y}_{\mathrm{S}} + \underline{Y}_{\mathrm{R}}|^{2}} \tag{3.72}$$

For heavyweight constructions, the receiver mobility is typically much lower compared to the source mobility. Hence equation (3.72) can be

written in the following simplified form.

$$W \approx \frac{1}{2} \frac{|\hat{\underline{v}}_{\mathrm{Sf}}|^2}{|\underline{Y}_{\mathrm{S}}|^2} \operatorname{Re}\{\underline{Y}_{\mathrm{R}}\} = \frac{1}{2} |\hat{\underline{F}}_{\mathrm{b}}|^2 \operatorname{Re}\{\underline{Y}_{\mathrm{R}}\} \tag{3.73}$$

For a source with a mobility that is much lower than the receiver mobility the following simplification can be applied.

$$W \approx \frac{1}{2} \frac{|\hat{\underline{v}}_{\mathrm{Sf}}|^2}{|\underline{Y}_{\mathrm{R}}|^2} \operatorname{Re}\{\underline{Y}_{\mathrm{R}}\} = \frac{1}{2} \frac{|\hat{\underline{v}}_{\mathrm{Sf}}|^2}{\operatorname{Re}\{\underline{Y}^*_{\mathrm{R}}\}} \tag{3.74}$$

However, these approximations can not always be applied in lightweight buildings because the mobility of such constructions can be similar for some service equipment [e. g. Lievens 2008].

Equation (3.71) is for the ideal case of a source with one contact point. For multi-contact sources the interaction between the contact points needs to be taken into account. In addition three out-of-plane and three in-plane excitation components can occur at each contact point. This results in the following equation[2] using a free velocity vector $\mathbf{v}_{\mathrm{Sf}}$ (peak velocities, $\hat{\underline{v}}_{\mathrm{Sf},i}$) and the mobility matrices $\mathbf{Y}_{\mathrm{S}}$ and $\mathbf{Y}_{\mathrm{R}}$ [e. g. see Moorhouse 2001]

$$\underline{Q} = \frac{1}{2} {\mathbf{v}_{\mathrm{Sf}}}^{\mathrm{T}} \left(\mathbf{Y}_{\mathrm{S}} + \mathbf{Y}_{\mathrm{R}}\right)^{-1\,\mathrm{T}} {\mathbf{Y}_{\mathrm{R}}}^{\mathrm{T}} \left(\mathbf{Y}_{\mathrm{S}} + \mathbf{Y}_{\mathrm{R}}\right)^{-1\,*} {\mathbf{v}_{\mathrm{Sf}}}^{*} \tag{3.75}$$

Using all six excitation components, $6N \times 6N$ mobility matrices are required for N contact points.

3.3.3.3 Reception plate method

The reception plate method was proposed by Cremer and Heckl [1967], Kihlman [1978], Ten Wolde and Gadefelt [1987], and Vercammen and Heringa [1989] where the power is determined indirectly. Therefore the unknown source is attached to a receiving structure (i. e. the reception plate) and operated under the desired conditions. Implying conservation

[2] Note the comment by Höller [2013] on the sometimes incorrect formulation of equation (3.75) in literature.

of energy, the unknown power input of the machine, W_{in}, can be determined based on the power balance according to equation (3.76) [Cremer and Heckl 1967]. Therefore the dissipated power, W_{d} is determined from the plate energy and the losses per radian cycle (described by the loss factor η).

$$W_{\mathrm{in}} = W_{\mathrm{d}} = E\,\omega\,\eta \tag{3.76}$$

The power determined with the reception plate method includes the components of all six degrees of freedom. However the results are only valid for this specific combination of source and receiver. Nevertheless [EN 15657:2017] describes procedures to obtain independent source data from the reception plate method on the basis that most building machinery excites bending wave motion.

3.4 Statistical Energy Analysis

The SEA framework was introduced in the 1960s and is used as an engineering tool in different industrial sectors to predict and analyse transmission of sound and vibration [Lyon and DeJong 1995]. It is a statistical approach to model complex systems, where the main variable is energy. The basic theory was derived from two weakly coupled oscillators [Lyon and Maidanik 1962].

To model sound transmission in real structures, such as buildings, the approach is extended to coupled sets of oscillators. These sets are called subsystems and represent modes within frequency bands that occur on structural elements (walls or floors) or in volume spaces (rooms or cavities). Consider two weakly coupled subsystems, 1 and 2. Within each subsystem it is assumed, that the total energy is equally shared by all modes. The modal energy, E_{m}, which is the same for each mode, can therefore be defined as

$$E_{\mathrm{m}} = \frac{E}{N} = \frac{E}{n(f)\,B} \tag{3.77}$$

where E is the total energy of the subsystem and N is the number of modes in the regarded frequency band that can also be written in terms of the modal density, $n(f)$, for the bandwidth, B.

The energy flow from subsystem 1 to 2, W_{12}, can be expressed as the power that is lost from subsystem 1 due to coupling to subsystem 2. By introducing the CLF, η_{12}, this can be written as

$$W_{12} = \omega\,\eta_{12}\,E_1 \tag{3.78}$$

where the CLF describes the loss of energy per radian cycle. As there is also power lost from subsystem 2 to 1 due to coupling, the net energy flow, $W_{12,\mathrm{net}}$, from subsystem 1 to 2 is

$$W_{\mathrm{net},12} = W_{12} - W_{21} = \omega\,\eta_{12}\,E_1 - \omega\,\eta_{21}\,E_2 \tag{3.79}$$

implying a higher energy in subsystem 1 for a positive net power transfer. Lyon and DeJong [1995] showed that the power transfer between two coupled subsystems is proportional to the difference in their modal energies, $E_{\mathrm{m},1}$ and $E_{\mathrm{m},2}$.

By introducing the consistency relationship

$$\frac{\eta_{12}}{n_2(f)} = \frac{\eta_{21}}{n_1(f)} \tag{3.80}$$

and using equation (3.77) the net energy flow can be written in terms of the difference in the modal energies.

$$W_{\mathrm{net},12} = \omega\,\eta_{12}\,N_1\,(E_{\mathrm{m},1} - E_{\mathrm{m},2}) \tag{3.81}$$

3.4.1 SEA assumptions

SEA assumes that the energy of a subsystem is stored in local resonant modes. Note that this excludes direct field, bending wave nearfield and non-resonant transmission [Craik 1996]. Within each subsystem, equipartition of the modal energy is assumed. Further the modal energy should

be distributed uniformly over the frequency band of interest. This implies that the subsystem must have sufficient modes in a frequency band and that the excitation equally excites all these modes. Therefore external excitation should be broadband. Hence equipartition of modal energy is closely linked to the excitation. Ideally statistically independent excitation forces are required such as rain-on-the-roof excitation. This multi-point excitation with unity magnitude and random phase provides the desired uncorrelated modal response [Lyon and DeJong 1995; Hopkins 2007; Schoenwald 2008].

To describe the modal properties of a subsystem the modal density, $n(f)$, and the mode count, N, are used. To quantify uniform distribution of modal energy, the modal overlap factor, M, can be used which is defined as [Lyon and DeJong 1995; Hopkins 2007]

$$M = \frac{\Delta f_{3\,\mathrm{dB}}}{\Delta f} = f\,\eta\,n(f) \tag{3.82}$$

where $\Delta f_{3\,\mathrm{dB}}$ is the half-power bandwidth and Δf is the average frequency spacing between the individual modes of a subsystem.

The coupling between the subsystems is assumed to be weak [Lyon and DeJong 1995]. Although this is an SEA criterion there has been much debate about its definition. To some extent weak coupling for predictive SEA occurs when the modal behaviour of an uncoupled subsystem does not alter much when it is coupled to the other subsystem [James and Fahy 1994]. Hence the energy flow can be related to the energy of the local modes in the individual subsystem.

3.4.2 General matrix solution

In this thesis, SEA is used to determine the subsystem energies from a known input power and predicted loss factors. This concept is called predictive SEA and is now introduced for the two-subsystem model in Figure 3.12. For this system, the power balance equations are

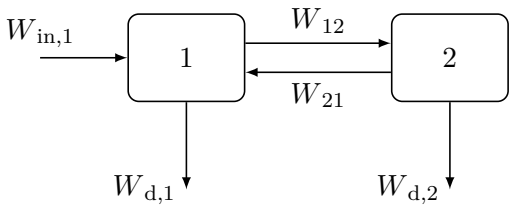

Figure 3.12: SEA-model for two subsystems.

$$\begin{aligned} W_{\mathrm{in},1} + W_{21} &= W_{\mathrm{d},1} + W_{12} \\ W_{12} &= W_{\mathrm{d},2} + W_{21} \end{aligned} \tag{3.83}$$

These can also be written in terms of energies and loss factors

$$\begin{aligned} W_{\mathrm{in},1} + \omega\,\eta_{21}\,E_2 &= \omega\,\eta_{\mathrm{d},1}\,E_1 + \omega\,\eta_{12}\,E_1 \\ \omega\,\eta_{12}\,E_1 &= \omega\,\eta_{\mathrm{d},2}\,E_2 + \omega\,\eta_{21}\,E_2 \end{aligned} \tag{3.84}$$

where $\eta_{\mathrm{d},1}$ and $\eta_{\mathrm{d},2}$ are the ILFs of subsystems 1 and 2, respectively that describe dissipative losses. In general for a subsystem i, the TLF, $\eta_{\mathrm{tot},i}$, or simply η_i, is given by the sum of the ILF and the CLFs.

$$\eta_{\mathrm{tot},i} = \eta_i = \eta_{\mathrm{d},i} + \sum_{j=1,\,j\neq i}^{N} \eta_{ij} \tag{3.85}$$

For more complicated systems with more than two subsystems, the power balance equations can be written in the following matrix form [Lyon and DeJong 1995; Craik 1996].

$$\begin{pmatrix} \eta_1 & -\eta_{21} & -\eta_{31} & \cdots & -\eta_{N1} \\ -\eta_{12} & \eta_2 & -\eta_{32} & & \\ -\eta_{13} & -\eta_{23} & \eta_3 & & \\ \vdots & & & \ddots & \\ -\eta_{1N} & & & & \eta_N \end{pmatrix} \begin{pmatrix} E_1 \\ E_2 \\ E_3 \\ \vdots \\ E_N \end{pmatrix} = \begin{pmatrix} W_{\mathrm{in},1}/\omega \\ W_{\mathrm{in},2}/\omega \\ W_{\mathrm{in},3}/\omega \\ \vdots \\ W_{\mathrm{in},N}/\omega \end{pmatrix} \tag{3.86}$$

The subsystem energies can be determined by inverting the loss factor matrix.

Besides predictive SEA, experimental SEA is also applied in this thesis. This concept uses a known input power and a measurement of the system response (subsystem energies) to determine unknown loss factors [Lyon 1975] (see sections 5.2.1.3, 5.2.2 and 5.2.3).

3.4.3 Path analysis

Path analysis considers the power flow along each transmission path independently. Hence it can be used to analyse individual transmission paths from a subsystem 1 to a subsystem N in the model, for example in terms of their relative importance. Therefore the energy ratio between the two subsystems is expressed by the TLFs and the CLFs. For the path along the subsystems, $1 \rightarrow 2 \rightarrow 3 \cdots \rightarrow N$, the energy ratio is [e. g. see Craik 1996].

$$\frac{E_1}{E_N} = \frac{\eta_2 \, \eta_3 \ldots \eta_N}{\eta_{12} \, \eta_{23} \cdots \eta_{(N-1)N}} \tag{3.87}$$

3.4.4 Resonant and non-resonant transmission

From the fundamental theory of SEA the transfer of power is considered between resonant modes. However regarding two rooms, that are separated by a wall, it is necessary to consider a direct transmission path between the two volume spaces that by passes the wall as a subsystem which represents non-resonant transmission. Although power is transmitted across the wall, the energy flow is not determined by the damping of the wall. This means that the response of the wall is forced by the airborne sound field in the source room.

Non-resonant transmission is also referred to as mass law transmission for infinite plates. For finite plates there will be modes, which do not radiate efficiently below the critical frequency [e. g. see Craik 1996; Hopkins 2007]. Therefore non-resonant transmission is often important

at frequencies below f_c. Above the critical frequency the non-resonant transmission can be neglected [Craik 1996].

Below the critical frequency Leppington et al. [1987] defines a non-resonant transmission coefficient, τ_{nr}, as follows.

$$\tau_{nr} = \left[\frac{2\,\rho_0}{m''\,k_0\,(1-\mu^{-}4)}\right]^2 \left\{ \ln\left(k_0\sqrt{S}\right) + 0.16 - U\left(\frac{L_x}{L_y}\right) + \frac{1}{4\,\mu^6}\left[\left(2\mu^2-1\right)\left(\mu^2+1\right)^2 \ln\left(\mu^2-1\right) + \left(2\mu^2+1\right)\left(\mu^2-1\right)^2 \ln\left(\mu^2+1\right) - 4\mu^2 - 8\mu^6 \ln\left(\mu\right)\right]\right\} \quad (3.88)$$

where μ is given in equation (3.37). The function $U(L_x/L_y)$ is given as

$$U\left(\frac{L_x}{L_y}\right) = \frac{1}{2\pi}\left(\frac{L_x}{L_y}+\frac{L_y}{L_x}\right)\ln\left[1+\left(\frac{L_x}{L_y}\right)^2\right] - \left(\frac{1}{2}+\frac{L_x}{\pi L_y}\right)\ln\left(\frac{L_x}{L_y}\right) - \frac{\ln 2}{\pi} - \frac{2}{\pi}\int_{L_x/L_y}^{1}\frac{\arctan t}{t}\,\mathrm{d}t \quad (3.89)$$

For plates with similar dimensions, $U(L_x/L_y)$ can be neglected in equation (3.88). However, for small aspect ratios that can occur with narrow plate strips on cavities of timber-frame walls, it has to be considered.

3.4.5 Loss factors

In the following sections internal, coupling and total loss factors which are relevant to describe timber-frame constructions using SEA are defined. The CLFs are given for the transfer of power in one direction. The reverse direction can be determined using the consistency relationship according to equation (3.80).

3.4.5.1 Internal loss factor for cavities

As wall cavities are typically narrow volume spaces there are no modes across the depth at low and mid frequencies. Hence assumptions for

diffuse fields of three-dimensional spaces can not be applied. Price and Crocker [1970] therefore distinguish between Two-dimensional (2D) and Three-dimensional (3D) sound fields to estimate the ILF for cavities. In the following a cavity with a width, L_x, a height, L_y, and a depth, L_z, is considered.

The crossover frequency between the 2D and 3D field occurs at the first cross-cavity mode, $f_{0,0,1}$, given by

$$f_{0,0,1} = \frac{c_0}{2\,L_z} \tag{3.90}$$

Below this frequency, the ILF for a cavity is

$$\eta_{\text{int}} = \frac{1}{\omega}\,\frac{c_0\,S_{\text{p}}\,\bar{\alpha}_{\text{p}}}{V\,\pi} \qquad\qquad f < f_{0,0,1} \tag{3.91}$$

where S_{p} is the surface of the cavity perimeter given by

$$S_{\text{p}} = 2\,(L_x\,L_z + L_y\,L_z) \tag{3.92}$$

$\bar{\alpha}_{\text{p}}$ is the average absorption coefficient for all angles of incidence of the cavity perimeter (timber studs and bars).

Above the first cross-cavity mode, the ILF is

$$\eta_{\text{int}} = \frac{1}{\omega}\,\frac{c_0\,S_{\text{cav}}\,\bar{\alpha}_{\text{cav}}}{4\,V} \qquad\qquad f > f_{0,0,1} \tag{3.93}$$

where S_{cav} is the total surface of the cavity given by

$$S_{\text{cav}} = 2\,(L_x\,L_z + L_y\,L_z + L_x\,L_y) \tag{3.94}$$

and $\bar{\alpha}_{\text{cav}}$ is the average absorption coefficient for all angles of incidence averaged and weighted according to the partial areas, S_k, of the total cavity surface.

$$\bar{\alpha}_{\text{cav}} = \sum_{k=1}^{6} \frac{S_k\,\alpha_k}{S_{\text{cav}}} \tag{3.95}$$

3.4.5.2 Coupling loss factor for structural point connections

Point connections occur for example between plates and timber studs that are connected with screws or nails. These can be described based on the mobility of the point-connection [e. g. Cremer and Heckl 1967]. Assuming only forces, Craik [1996] defines the CLF for N point connections as

$$\eta_{ij} = \frac{N}{\omega\, m_i} \frac{\mathrm{Re}\left\{Y_j\right\}}{\left|Y_i + Y_j + Y_c\right|^2} \tag{3.96}$$

where m_i is the mass of subsystem i, Y_i and Y_j the driving point mobilities of the subsystems i and j and Y_c the mobility of the point connection. Y_c can be a spring for example. However for rigid connections, $Y_c = 0$, can be assumed.

3.4.5.3 Coupling loss factor from a plate to a room

The resonant coupling between the bending modes of a plate and the room modes can be determined using the frequency-average radiation efficiency, σ, according to section 3.2.8.3. The coupling loss factor from a plate to a room is given as [Craik 1996]

$$\eta_{ij} = \frac{\rho_0\, c_0\, \sigma}{\omega\, m''} \tag{3.97}$$

where $(\rho_0\, c_0)$ is the characteristic impedance of air and m'' the mass per unit area of the plate.

3.4.5.4 Non-resonant coupling loss factor between volume spaces

As mentioned in section 3.4.4 there is direct coupling between two spaces that are separated by a plate. For a timber-frame wall this can be the coupling between the rooms that are separated by this wall or the coupling between the cavity and the rooms. Using the non-resonant transmission

coefficient, τ_{nr}, according to equation (3.88) the CLF is defined as [Price and Crocker 1970; Craik 1996]

$$\eta_{ij} = \frac{c_0\, S}{4\,\omega\, V_i}\,\tau_{\mathrm{nr}} \tag{3.98}$$

Regarding the sound transmission into and out of cavities this can not be directly be applied as cavities are narrow spaces and therefore the sound field is one- or two-dimensional (see section 3.4.5.1) with wave motion parallel to plate surfaces. An approach to predict the non-resonant transmission for this situation below the first cross cavity mode is given by Craik [2003]. The CLF from the cavity to the room is given as

$$\eta_{ij} = \frac{\rho_0^2\, c_0^3\, S\, \sigma_{fc}}{\omega^3\, V_i\, m''^2} \qquad\qquad f < f_{0,0,1} \tag{3.99}$$

where σ_{fc} is the radiation efficiency of the plate at the critical frequency. Above the first cross cavity mode equation (3.98) can be used.

3.4.5.5 Total loss factor of plates

The TLF is the sum of the ILF and the CLFs. From Craik [1981] the TLF of a plate that is connected on all sides, is

$$\eta_{\mathrm{tot},situ} = \eta_{\mathrm{int}} + \frac{C}{\sqrt{f}} \tag{3.100}$$

where the constant C depends on the element type. For masonry or concrete buildings $C = 1$ in combination with an ILF, $\eta_{\mathrm{int}} = 0.01$, gives a reasonable estimate [Craik 1981]. For lightweight buildings, Hopkins [2007] suggests $C = 0.4$ for timber-frame walls with empty cavities.

3.4.6 Modal density and mode count

The modal density, $n(f)$, can be determined either by calculating the mode frequencies and dividing the number for each band by the band-

width, or by using a statistical approach. The statistical mode count, N_s, for a frequency band with the bandwidth, B, is

$$N_\mathrm{s} = n(f)\,B \tag{3.101}$$

3.4.6.1 Rooms

The mode frequencies of box-shaped rooms can be calculated using

$$f_{p,q,r} = \frac{c_0}{2}\sqrt{\left(\frac{p}{Lx}\right)^2 + \left(\frac{q}{Ly}\right)^2 + \left(\frac{r}{Lz}\right)^2} \tag{3.102}$$

where L_x, L_y and L_z are the dimension of the room.

The statistical descriptor the modal density, $n(f)$, for box-shaped rooms is given by [Kuttruff 1979]

$$n(f) = \frac{4\,\pi\,f^2\,V}{c_0^3} + \frac{\pi\,f\,2(L_xL_y + L_xL_z + L_yL_z)}{2\,c_0^2} + \frac{4(L_x + L_y + L_z)}{8\,c_0} \tag{3.103}$$

3.4.6.2 Cavities

In the narrow, thin cavities of timber-frame constructions, one-, two- or three-dimensional sound fields can occur. At low frequencies there are only axial modes in the long dimension of the cavity and therefore the sound field is one-dimensional. Starting from the frequency where half a bending wavelength fits into the cavity width, a 2D sound field can be assumed. A 3D sound field occurs above the first cross cavity mode (across the cavity depth). Although these frequencies mark the transition between the three regimes, the cross-over is normally in a frequency region than at distinct frequencies.

As with rooms it is possible to determine the mode frequencies using equation (3.102) and count the modes in each band. However a statistical modal density can be determined for one-, two- and three dimensional sound fields separately.

Considering a cavity with a width, L_x, a height, L_y, and a depth, L_z, the modal density for 1D is given by equation (3.104)

$$n_{1\mathrm{D}}(f) = \frac{2\,L_y}{c_0} \tag{3.104}$$

and for 2D sound fields by equation (3.105)

$$n_{2\mathrm{D}}(f) = \frac{2\,\pi\,f\,L_x\,L_y}{c_0^2} + \frac{L_x + L_y}{c_0} \tag{3.105}$$

For 3D sound field in cavities the modal density can be calculated according to equation (3.103).

3.4.6.3 Plates and beams

The determination of the mode frequencies and the modal density for beams and plates is given in section 3.2.5.

3.4.7 Modal overlap factor

The modal overlap factor describes the number of modes that fall within the half-power bandwidth and is defined as

$$M = f\,\eta\,n(f) \tag{3.106}$$

This means that when $M \gg 1$ the response is smooth with no troughs, whereas for $M \ll 1$ the modes are separated with troughs in-between.

3.4.8 Energy from velocity or sound pressure

As energy is the primary variable in the SEA framework, it is required to transfer velocity or sound pressure to energy. The required relationships are given in the following sections.

3.4.8.1 Vibrational energy from velocity

For a modal resonator, such as a mass-spring-mass-damper system, the time average kinetic energy equals the time-average potential energy, and each are equal to half the total energy [Lyon and DeJong 1995].

$$E_{\mathrm{vib}} = E_{\mathrm{kin}} + E_{\mathrm{pot}} = 2\,E_{\mathrm{kin}} \tag{3.107}$$

As the time average of the kinetic energy is

$$\langle E_{\mathrm{kin}} \rangle_t = \frac{1}{4}\,m\,\hat{v}^2 \tag{3.108}$$

the vibrational energy can be written in terms of the peak velocity $\hat{v}$ as

$$E_{\mathrm{vib}} = \frac{1}{2}\,m\,\hat{v}^2 \tag{3.109}$$

Using mean square velocities, given by

$$\langle v^2 \rangle_t = \tilde{v}^2 = \frac{\hat{v}^2}{2} \tag{3.110}$$

the vibrational energy, which is simply denoted as E in the following, can be written as

$$E = m\,\langle v^2 \rangle_{t,s} = m\,\langle \tilde{v}^2 \rangle_s \tag{3.111}$$

As the out-of-plane velocity describes the motion of bending waves, the measurement of velocities perpendicular to the surface of plates are used to describe the energy associated with bending waves.

3.4.8.2 Energy from sound pressure level

Using the spatial and temporal average sound pressure, the energy contained in a volume can be determined as follows.

$$E = \frac{\langle p^2 \rangle_{t,s}\,V}{\rho_0\,c_0^2} = \frac{\langle \tilde{p}^2 \rangle_s\,V}{\rho_0\,c_0^2} \tag{3.112}$$

3.5 Summary

In this chapter the theory that is applied in later chapters of the thesis was presented. Consideration was given to bending wave vibrations on beams and plates including equivalent orthotropic plates to describe the properties of framed structures. The sound radiation from bending waves was described. The definition of mobility was given and analytic models for infinite and finite structures were shown. Concerning the characterization of SBS sources on a power basis, the main equations were given and methods to determine the installed SBS power were described. In addition an introduction to SEA was given by describing the main assumptions, the basic underlying equations as well as the relevant loss factors that are applied in later chapters to model a timber-frame structure.

4 Test structure and experimental procedures

4.1 Introduction

Machinery noise in buildings involves mechanical excitation, the propagation and radiation of structure-borne sound as well as the sound field in a remote room. In this thesis, experimental investigations were carried out on a laboratory test structure as well as in the field in seven timber-frame buildings. This required the application of different procedures to measure vibration as well as sound pressure which are described in this chapter. Section 4.2 describes the laboratory test mock-up. Section 4.3 shows typical characteristics of the test structures that were found in the field. Section 4.4 gives an overview of the instrumentation that is necessary for the experimental procedures described in the following section 4.5. The basic principles of the chosen measurement techniques and the application for the specific situation are described as well as limitations and reasons for the particular choice of a procedure. However, specific details on the application of the individual procedures are given in chapters 5, 6 and 8.

4.2 Laboratory test structure

Experimental investigations in the laboratory provide control of construction details, easy access, low background noise and flexible scheduling of measurements. These investigations were carried out on a laboratory test construction in the facilities of the Laboratory for Sound Measurement (LaSM) at the Technical University of Applied Sciences Rosenheim in Germany.

4.2.1 Design of the test structure

In apartment buildings, requirements on maximum sound pressure levels due to service equipment in adjacent apartments have to be met. In typical layouts of apartment buildings, bathrooms or similar rooms that contain service equipment, are often diagonally adjacent. Hence diagonal transmission is an important path that was considered in the design.

The test structure is a full scale two-storey mock-up comprising a timber-joist floor and two timber-frame walls that form a T-junction as shown in Figure 4.1. Detailed drawings of the test structure are given in Figures 4.2 and 4.3. The upper wall is accessible from both sides, and therefore this test structure provides the possibility to measure diagonal and vertical and transmission across the wall-floor-wall junction as well as horizontal transmission in the basement.

The framework of the walls and the floor was designed by the German timber house manufacturer Regnauer Fertigbau GmbH & Co. KG. It represents a common construction in terms of stud spacing and cross sections, but the structure has consciously been simplified. This means that only a single layer of sheeting and no insulation material in the cavities was used as shown in Figure 4.4a. Chipboard was chosen for sheeting as this material can be regarded as an isotropic plate due to the random arrangement of the small wood chips. OSB-boards or plasterboards are orthotropic and therefore more complicated to model.

Normally there are multiple layers of plates and absorbent material in typical timber-frame constructions as this is potentially beneficial be-

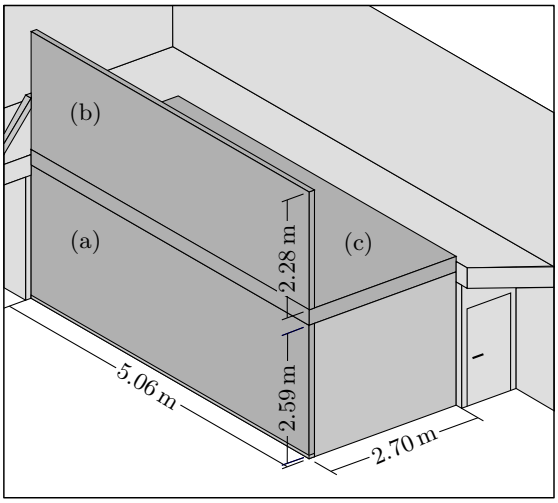

Figure 4.1: Sketch of the laboratory test structure. In the following the walls and the floor are denoted as: (a) Lower (timber-frame) wall, (b) upper (timber-frame) wall and (c) (timber-joist) floor.

cause the coincidence dip can be reduced [Matsumoto et al. 2006] or the damping of the structure increased [Trochidis 1982; Schoenwald 2008]. However a major purpose of the laboratory study was to gain insight into the vibrational behaviour of a timber-frame wall. Therefore this basic inhomogeneous construction was chosen to investigate typical aspects of framed structures. As there are only a few models that can deal with multi-layered sheeting [e. g. Sharp and Beauchamp 1969], a single layer of chipboard was chosen to simplify the modelling in SEA.

4.2.2 Construction details of the test structure

As indicated in Figure 4.1, the dimensions of the test structure resemble typical building dimensions. The spacing of the timber studs and the floor joists is 625 mm on centres. A circumferential frame with vertical studs is used for the walls, whereas only parallel aligned joists are used for the floor. The floor joists are perpendicular to the T-junction. All connections within the framework are screwed and no glue is used. The

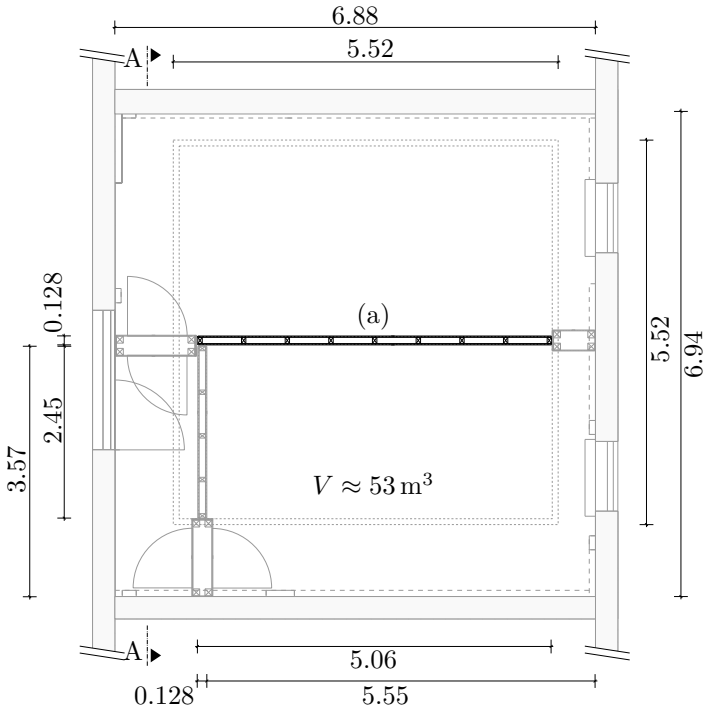

Figure 4.2: Floor plan of basement (dimensions in metres). Dark lines indicate the test structure.

cross sections of the solid spruce beams used for the frame elements are $90\,\mathrm{mm} \times 60\,\mathrm{mm}$ for the wall studs and $240\,\mathrm{mm} \times 60\,\mathrm{mm}$ for the floor joists.

On both sides of the wall, the chipboard plates are screwed to the framework with a separation of 350 mm. For the covering of the timber joist floor, the same plates are used and identical screw spacings of 350 mm are applied. No ceiling is installed underneath the joists. The boards are arranged such that their longer dimension is perpendicular to the studs or joists, respectively. Hence there are additional horizontal junctions across the wall. As the plates are arranged randomly, the vertical junctions are staggered and do not necessarily occur above studs. All chipboard joints are tongue and grooved without any glue (Figure 4.4b).

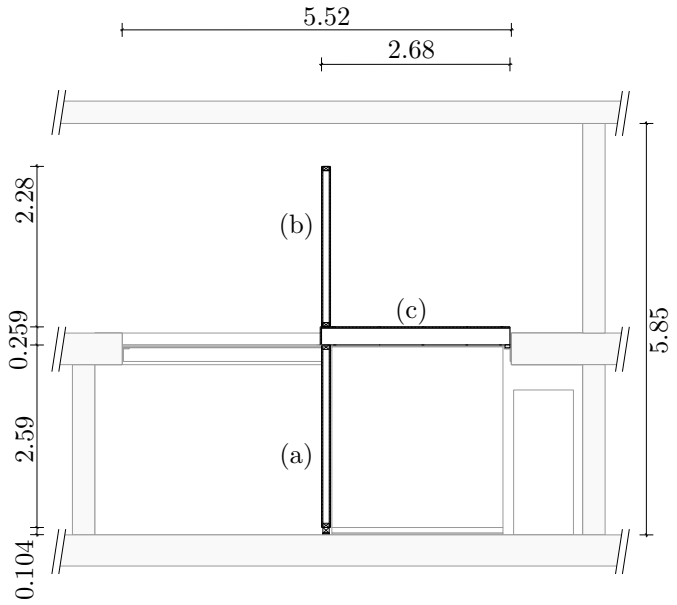

Figure 4.3: Section A-A (see Figure 4.2, dimensions in metre). Dark lines indicate the test structure.

By using elastic layers underneath the lower wall and floor joists, the whole test structure is decoupled from the rest of the building. The walls rest on line supports, the free ends of the floor joists rest on point supports. A resonance frequency of approximately 20 Hz has been estimated as the frequency above which the structure will be isolated from any vibration of the ground floor.

Using the corner of the laboratory, formed by a concrete wall, a drywall, and a segment drywall of approximately 1 m length, the two studwork walls in the basement and the timber-joist floor form a room with an enclosed volume of approximately 53 m^3. This room can be entered by a double door that is installed in the drywall segment (see Figure 4.2). The two timber-frame walls in the basement are not coupled to each other, or the building at their vertical boundaries. To avoid airborne sound transmission through the gaps, they are sealed with elastic material. At the T-junction, the floor joists, which are perpendicular to the longer

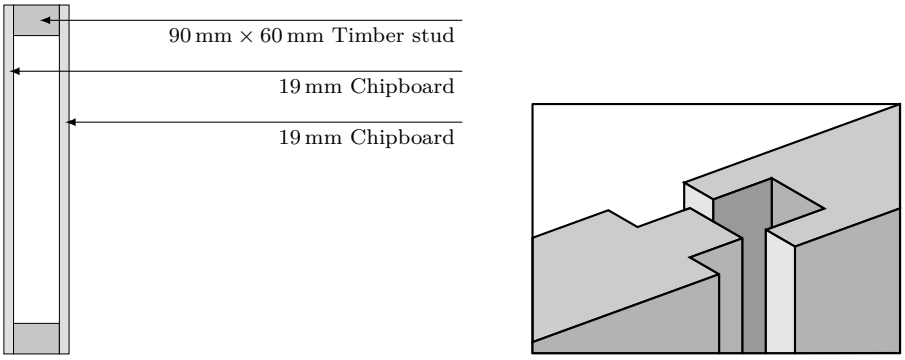

(a) Section (b) Tongue and groove joint

Figure 4.4: Construction of the basic timber-frame wall in the laboratory lightweight test structure.

wall, are rigidly connected to the framework of the long basement wall using wood screws with a length of 320 mm. The small lower wall is not connected to the timber-joist floor at its upper boundary. The gap is also sealed with elastic material.

The upper wall is placed on top of the sheeting of the floor and fixed with screws connecting the framework of the wall and the floor joists. Although the construction is stable, additional battens are installed at each end of the upper wall for safety reasons. These are also supported on elastic mounts to decouple the test structure from the laboratory building. Hence the upper wall has free boundary conditions at three edges and the wall-floor-wall junction in this test structure can be regarded as an isolated T-junction.

4.3 Field test structures

Field measurements were carried out to obtain data in lightweight building structures in-situ. The focus in the field was on walls, as all buildings had a floating concrete screed which would reduce the injected power into the bare floor. The wall constructions in the buildings have similar cross sections and stud spacings to the laboratory test structure. However

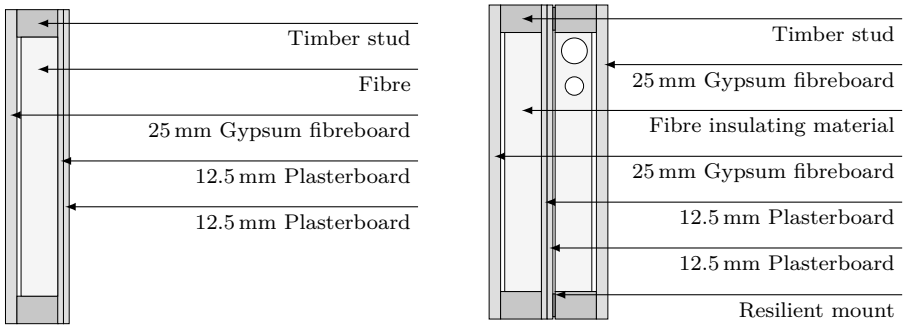

(a) Typical interior wall

(b) Typical interior wall with lining

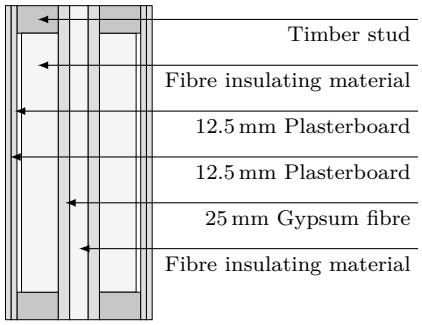

(c) Typical separating wall

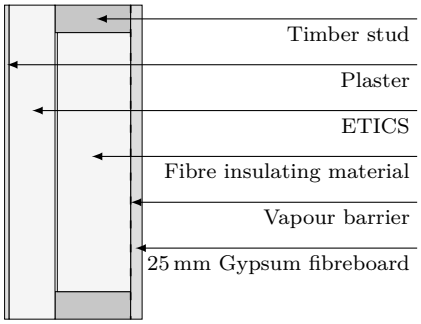

(d) Typical exterior wall

Figure 4.5: Field test structures. Examples of typical wall constructions in timber-frame buildings.

typically gypsum boards in combination with OSB-boards or gypsum fibreboards are used as sheeting material. These are necessary for the bracing of the framed construction. Typically a single layer of 25 mm boards or multiple layers of 12.5 mm or 15 mm boards are used.

For the construction of the framework of interior walls three groups can be identified: a) single framework walls, b) single framework walls with additional lining that contains pipework and c) double framework walls. Examples that represent typical construction details for these three groups are shown in Figures 4.5a, 4.5b and 4.5c. However details like the cross sections of the wall studs, the type of absorbent material in the cavity, the type of sheeting material or additional layers like tiles in bathrooms vary in different buildings. Measurements were also carried

out on exterior walls. Their framework and the inner leaf is very similar to typical interior or separating walls as shown in Figure 4.5d.

4.4 Instrumentation and Software

For the experimental investigations the equipment listed in Table 4.1 was used. Data acquisition and FFT operations were carried out with the PAK Software that is part of the PAK MKII data acquisition system listed in Table 4.1.

Narrow band FFT data was exported for further processing in MATLAB. For the measurement of room and structural reverberation times the software m|reverb developed by Müller-BBM GmbH was used. However in the field, reverberation times were also measured with the Norsonic 140.

4.5 Experimental procedures

4.5.1 Mechanical excitation techniques on structures

Three different types of mechanical excitation are used in this thesis: a) transient excitation with an instrumented hammer b) steady-state or swept sine excitation with a shaker that is attached to the structure and c) excitation with real or artificial structure-borne sound sources. With transient and steady-state excitation, the applied force is recorded with a force transducer in the hammer head or in-line with the shaker, respectively.

To avoid rotational excitation components, a stinger was used in shaker measurements. The choice of the stinger and the shaker support follows the guidelines given by Mitchell and Elliott [1984] to achieve a low transmissibility of inertial moments. The applied stinger is a steel rod with a length of 160 mm and a diameter of 2 mm. The shaker was suspended by cords to provide a low natural frequency of the shaker support. The trade-off is that above the mass-spring resonance of the shaker-stinger-

Table 4.1: Equipment

	Make	Type
Accelerometer	MMF[a]	KS76C100[b]
Accelerometer	MMF	KS77C100[b]
Accelerometer	MMF	KS95B100[c]
Force sensor	MMF	KF24
Microphone	Norsonic	112
Pre-amplifier	Norsonic	1201
Microphone	G.R.A.S.	40HL
Intensity probe	Norsonic	240
Probe microphones	Norsonic	1234
LDV	Polytec	PDV 100
Modal hammer	Endevco	2302-10
Shaker	Data Physics	IV-40
Shaker	Brüel & Kjær	4810
Analyser	MBBM VAS[d]	PAK MKII
Analyser	Norsonic	840
Analyser	Norsonic	140

[a] Metra Mess- und Frequenztechnik
[b] Weight: 23 g
[c] Weight: 3.2 g
[d] Müller-BBM VibroAkustik Systeme GmbH

system, the input force drops rapidly. As the axial stiffness of the stinger decreases with increasing length, the stinger has to be short enough to provide a flat force spectrum across a wide frequency range, but long enough to suppress rotatory components.

With the chosen set-up a flat force-spectrum could be achieved up to approximately 1 kHz. However vibration measurements were also processed above this frequency provided that the signal-to-noise ratio of the response was sufficient.

To connect the shaker to the structure, a metal washer with a threaded hole was glued and in some cases additionally screwed to the surface. To record the force, a transducer was added in-line as shown in Figure 4.6. For vibration measurements a white or pink noise signal was used in

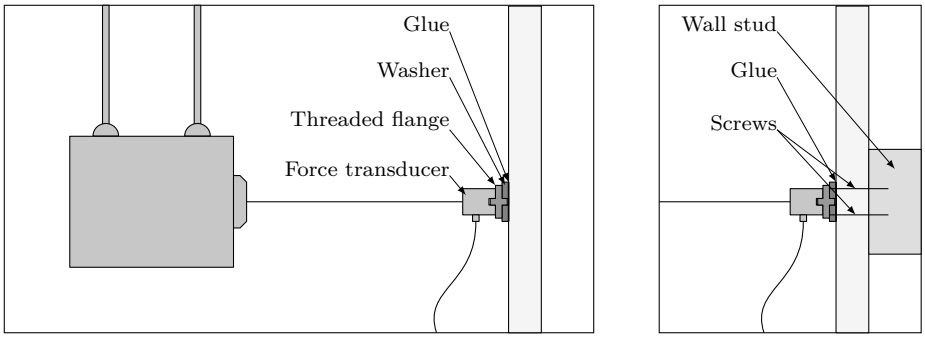

Figure 4.6: Set-up for shaker excitation in-line with a force transducer. The washer is glued to the surface using cyanoacryalate glue. For positions, where a stud is behind the sheathing, as shown in the right sketch, the washer was additionally screwed to this stud through the chipboard plate.

this study. If necessary, specific frequency bands were amplified with a graphical equalizer to provide sufficient level above background noise.

4.5.2 Vibration measurements

Vibration measurements are used to determine time and spatial average surface velocities. The out-of plane acceleration due to bending wave motion is measured with accelerometers. Although in-plane waves might also be generated in the measurements, these motions are not recorded. The measured accelerations are integrated to give velocities by dividing the complex FFT-spectra of the acceleration by $\mathrm{i}\omega$. Using the Laser Doppler Vibrometer (LDV), velocities are directly determined.

As the squared velocity is directly proportional to the kinetic energy, E_{kin}, the measurement results can be interpreted in terms of vibrational energy (section 3.4.8.1). This is used to investigate the distribution of energy across a building element, particularly attenuation with distance from a local source, or to determine the average vibrational energy over a specific area.

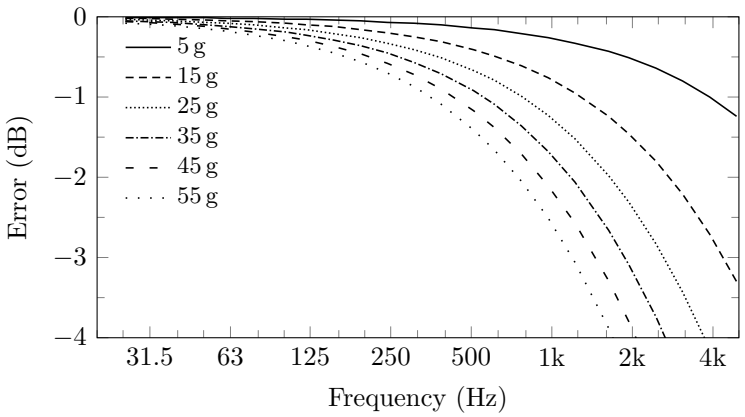

Figure 4.7: Error due to mass loading by an accelerometer on 19 mm chipboard.

4.5.2.1 Mass loading

When fixing accelerometers to a structure, the additional sensor mass can alter its response. This is particularly important when measuring on light structures like timber-frame walls. The valid frequency range can be increased to higher frequencies by using transducers (transducer mass, m_{acc}) with a mobility that is much higher than the driving point mobility, Y_{dp}, of the structure [Hopkins 2007] (equation (4.1)).

$$\frac{1}{\mathrm{i}\,\omega\,m_{\mathrm{acc}}} \gg Y_{\mathrm{dp}} \tag{4.1}$$

Figure 4.7 gives the error, $e(L_v)$ in the measured velocity level due to mass loading for a structure with a driving-point mobility, $Y_{\mathrm{dp}} = 1 \times 10^{-3}\,\mathrm{m/(N\,s)}$ according to equation (4.2) [Hopkins 2007]. This mobility corresponds approximately to an infinite plate with the properties of 19 mm chipboard.

$$e(L_v) = 20\,\mathrm{lg}\left(\frac{Z_{\mathrm{dp}}}{Z_{\mathrm{dp}} + \omega\,m_{\mathrm{acc}}}\right) \tag{4.2}$$

In this thesis accelerometers with a mass of 23 g (MMF, Type KS76C100 and Type KS77C100, Table 4.1) and 3 g (MMF, Types KS95B100, Table 4.1) were used.

4.5.2.2 Transducer mounting

In this thesis, accelerometers were mounted to the structure either using a thin layer of bees wax or a magnet that is attached to a thin metal washer glued to the surface of the structure. The advantage of using magnets is that positioning is quick once the metal washers are glued to the surface. However the additional weight reduces the upper frequency limit due to mass loading as described in section 4.5.2.1. The use of bees wax is less flexible, but no additional mass is applied and this mounting works well for most surfaces of building material (wood, plaster, concrete). An upper frequency limit due to the mounting resonance was tested with a 23 g accelerometer mounted on a small plate that was directly attached to a shaker driven with broadband noise. The accelerometers were attached to this plate using either a magnet or a thin layer of bees wax and the velocity level measured. Figure 4.8 shows the results for the mountings used in this thesis. The measured velocities are normalized to the level of line (a) at 6.3 kHz. For all three mountings the useful frequency range is up to at least 5 kHz. However as the magnet and the washer add additional mass (see limitations in section 4.5.2.1), the method using a thin layer of bees wax was preferred.

4.5.3 Structural intensity measurement

From equations (3.32) to (3.34) the displacement and its spatial and time derivatives are required to determine the structural intensity. This can be achieved experimentally using finite difference approximations [e. g. Pavic 1976] or a combination of translational and rotational transducers [e. g. Noiseux 1970].

Bauman [1994] gives a survey of five methods to estimate the structural intensity focusing on the practical application of the methods. He

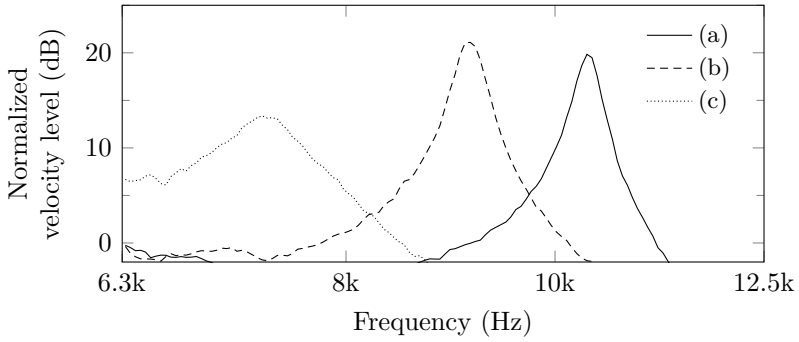

Figure 4.8: Accelerometer mounting resonances. (a) thin layer of bees wax, (b) magnet on washer glued with two-component adhesive and (c) magnet on washer glued with hot melt adhesive

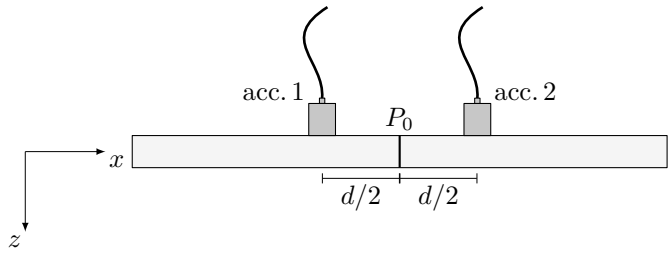

Figure 4.9: Structural intensity measurements using an a-a probe in the x-direction.

showed that a single pair of transducers provides a reasonable trade-off between practicability and accuracy [e. g. Kruppa 1986]. Although the required assumptions formulated by Noiseux [1970] are technically only valid in the far field, Baumann showed that the two accelerometer method gives reasonable results even when a point is regarded, that is influenced by nearfield wave components. Approaches that use an array of four transducers (eight for two dimensional waves in plates) overcome the problems with nearfields. However Bauman shows that these methods are very sensitive to sensor positioning and therefore of limited practical use.

4.5.3.1 Experimental set-up

For the above reasons a pair of accelerometers aligned in the direction of power flow is used in this thesis. This technique implies the following simplifications formulated by Noiseux [1970]. The first simplification is to assume that $I_{\mathrm{s},x,\mathrm{F}} = I_{\mathrm{s},x,\mathrm{M}}$ in the farfield of a plane bending wave field. Hence the structural intensity can be determined using twice the moment component ($I_{\mathrm{s},x} = 2\, I_{\mathrm{s},x,\mathrm{M}}$). This prevents third and partial derivatives contained in the force component (equation (3.32)). However this still requires the partial derivative in the twisting moment component (equation (3.34)). To reduce the set-up to two transducers, the second simplification of Noiseux is to use a modified moment component, $I'_{x\mathrm{M}}$, which is given as

$$I_{\mathrm{s},x,\mathrm{M}} \approx I'_{x\mathrm{M}} = \left\langle \frac{M_{xy} + M_{yx}}{(1+\nu)}\, \alpha_y \right\rangle_t \tag{4.3}$$

Following the derivation given in [Hopkins 2007], the structural intensity in the x-direction is approximated using

$$I_{\mathrm{s},x} \approx \frac{\mathrm{i}\sqrt{B_\mathrm{p}\, m''}}{d}\, \langle (v_1 + v_2)\,(v_2 - v_1) \rangle_t \tag{4.4}$$

In this thesis the structural intensity was obtained from complex FFT data in the frequency range. Concerning the active component (i. e. the real part) only, the structural intensity is given as

$$I_{\mathrm{s},x} \approx \frac{\sqrt{B_\mathrm{p}\, m''}}{d}\, \mathrm{Im}\{\underline{\hat{v}}_1^*\, \underline{\hat{v}}_2\} = -\frac{\sqrt{B_\mathrm{p}\, m''}}{d}\, \mathrm{Im}\{G_{v,12}\} \tag{4.5}$$

The narrow band intensity was summed to give one-third octave bands.

To determine the resulting magnitude and angle of the intensity vector, two a-a probes are used as shown in Figure 4.10. The magnitude of the resulting intensity vector is then

$$I_\mathrm{s} = \sqrt{I_{s,x}^2 + I_{s,y}^2} \tag{4.6}$$

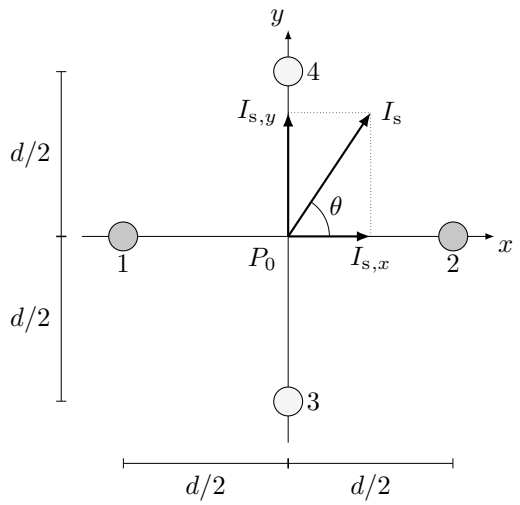

Figure 4.10: Two a-a structural intensity probes to determine a resulting intensity vector I_s in a two-dimensional plane wave field from x- and y-components.

and the angle with respect to the x-axis is given by

$$\theta = \arctan \frac{I_{s,y}}{I_{s,x}} \tag{4.7}$$

4.5.3.2 Error analysis

Although the a-a probe provides a comparatively robust technique to estimate the structural intensity, it involves two errors that limit its application. Limitations to high frequencies are given by the finite difference approximation because the bending wavelength decreases with increasing frequency and is therefore small compared to the spacing, d. Limitations to low frequencies are given by the phase match of the applied accelerometer pair because a good match is required when the spacing, d, is small in relation to the bending wavelength.

The normalized errors are estimated similar to sound intensity [Fahy 1995a; Hopkins 2007]. The normalized finite difference error for the x-

component of the structural intensity is

$$e_{\mathrm{FD}}(I_{\mathrm{s},x}) \approx -\frac{1}{6}\left(k_{\mathrm{B}}\, d\, \cos\theta\right)^2 \tag{4.8}$$

where θ is the propagation angle according to Figure 4.10. The normalized error due to phase mismatch for the x-component of the structural intensity is

$$e_{\mathrm{PM}}(I_{\mathrm{s},x}) \approx -\frac{\pm\phi_{\mathrm{PM}}}{k_{\mathrm{B}}\, d\, \cos\theta} \tag{4.9}$$

For the y-component $\sin\theta$ is used in equations (4.8) and (4.9). Normalized errors in decibels are determined using

$$10\lg\left(1 + e(I_{\mathrm{s},x})\right) \tag{4.10}$$

For the two-dimensional intensity vector the absolute error, $\varepsilon(\theta)$, for the propagation angle in radians, θ, is [Hopkins 2007]

$$\varepsilon(\theta) = \left[\arctan\left(\frac{\sin\theta\left(1 + \dfrac{\pm\phi_{\mathrm{PM}}}{k_{\mathrm{B}}\, d\, \sin\theta} - \dfrac{1}{6}\left(k_{\mathrm{B}}\, d\, \sin\theta\right)^2\right)}{\cos\theta\left(1 + \dfrac{\pm\phi_{\mathrm{PM}}}{k_{\mathrm{B}}\, d\, \cos\theta} - \dfrac{1}{6}\left(k_{\mathrm{B}}\, d\, \cos\theta\right)^2\right)}\right)\right] - \theta \tag{4.11}$$

The absolute error for the propagation angle according to equation (4.11) is shown in Figure 4.13 for five selected angles from 5° to 85° and using the phase mismatch given in Figure 4.11. In this thesis a probe spacing, $d = 33\,\mathrm{mm}$ was used. For this spacing the normalized errors are shown in Figure 4.12 for different angles of the propagating wave. These errors are shown up to the 1000 Hz one-third octave band as the results were not processed for higher frequencies. The absolute error for the propagation angle is shown in Figure 4.13 for five selected angles from 5° to 85°.

4.5.4 Driving-point mobility measurements

The driving-point mobility is required to calculate the power input as described in section 2.2.2. Additionally it can be used to identify mode

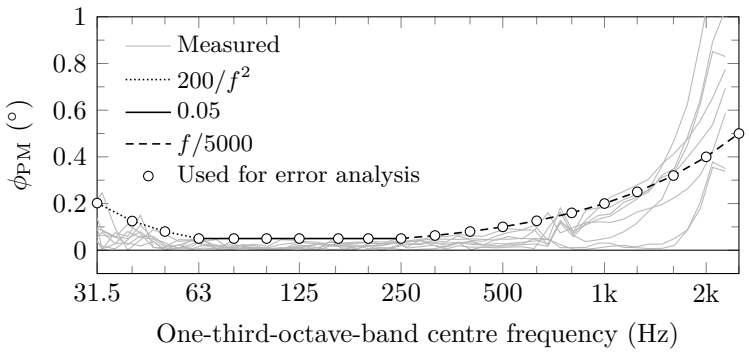

Figure 4.11: Phase mismatch of accelerometer pairs. Upper limit from $200/f^2$, 0.05 and $f/5000$ (corresponds to a Class 1 p-p probe acc. to [IEC 1043:1993]) used for the error analysis.

frequencies or to determine the modal damping from the 3 dB down bandwidth of the modal peaks. Furthermore it can be used to estimate the modal density.

To measure the complex driving-point mobility, the Frequency Response Function (FRF) between velocity and force is determined with a multi-channel FFT-analyser. As described in section 4.5.1, excitation can be performed using an instrumented hammer [ISO 7626-5:1994-07] or a shaker [ISO 7626-2:1990-02]. Using an instrumented hammer, the driving-point mobility can be measured without attaching a shaker to the structure. This can be advantageous for light structures with brittle materials like plasterboard where it can be difficult to properly attach a shaker. Using a shaker, the mobility can be measured with an impedance head to determine the force and the velocity at exactly the same position. However there can be limitations due to the stiffness of the transducer, especially for heavy and stiff receiving structures [Bietz and Wittstock 2003].

Using a force transducer, either with hammer or shaker excitation, the velocity needs to be measured with a separate transducer, typically an accelerometer. For thin plates the accelerometer can be placed on the opposite side to the excitation. For cavity walls or thick plates, where

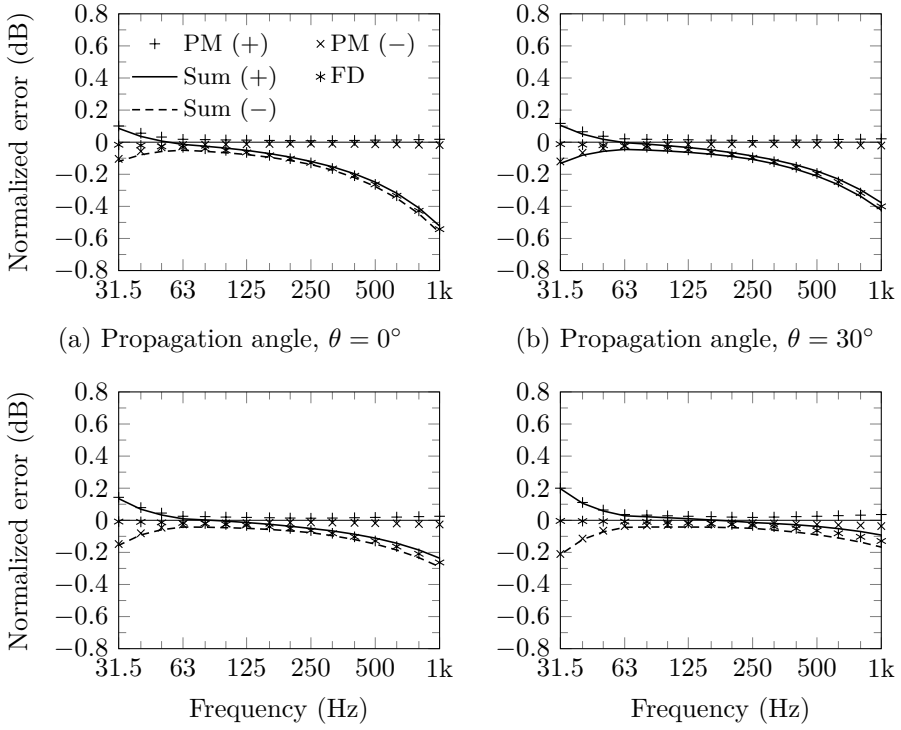

(a) Propagation angle, $\theta = 0°$

(b) Propagation angle, $\theta = 30°$

(c) Propagation angle, $\theta = 45°$

(d) Propagation angle, $\theta = 60°$

Figure 4.12: Normalized Phase Mismatch errors (PM), for $\pm\phi_{\mathrm{PM}}$, Finite Difference error (FD) and combined (Sum) errors, for $\pm\phi_{\mathrm{PM}}$ for structural intensity x-component, I_{sx}, for the probe spacing $d = 33\,\mathrm{mm}$. Phase mismatch from Figure 4.11.

there is limited (or no) access to the opposite side, the velocity can only be determined by placing the transducer as close as possible next to the excitation point. As long as the area required for the excitation and the accelerometers is small compared to the bending wavelength of the plate this method gives a good approximation of the driving-point mobility. A rule of thumb is to use a spacing between the force transducer and the accelerometer that is $< 0.1\,\lambda_{\mathrm{B}}$ [Hopkins 2007].

Using impact excitation on light structures, less sensitive accelerometers are sometimes required as they are prone to be overloaded by the

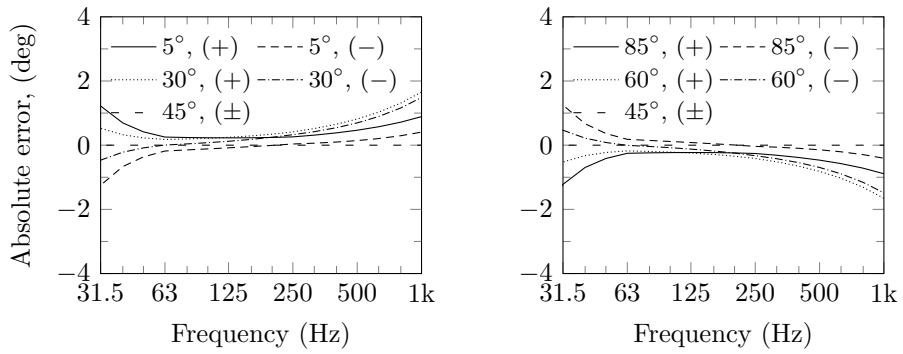

(a) Propagation angle, $\theta \leq 45°$

(b) Propagation angle, $\theta \geq 45°$

Figure 4.13: Absolute error for propagation angle of the structural intensity according to equation (4.11). The sign in brackets indicates the sign of the phase mismatch, ϕ_{PM}.

high transients. This is especially critical for driving-point mobility measurements where the transducers need to be placed very close to the excitation point.

In this work both an instrumented hammer and a shaker in-line with a force transducer were used to determine driving-point mobilities. However most measurements were carried out with the hammer. For both methods a pair of accelerometers next to the excitation point, P_0, is used to estimate the driving point mobility from the average.

As the bandwidth of the flat spectrum that can be obtained with the hammer depends on the stiffness of the hammer tip, these were varied depending on the required frequency range and Signal-to-noise (S/N) ratio. However in most cases a hard metal tip or a soft rubber tip were used. If necessary the spectra of the FRFs were assembled from results using both tips, as the soft tip provides a better S/N ratio at low frequencies and the hard tip at high frequencies.

At least five FFT-spectra were averaged when measuring the driving-point mobility with hammer excitation. However normally more hits were performed as bad hits were immediately rejected.

When using shaker excitation, random noise signals were used. To determine the FRFs at least 50 FFT-spectra from a gliding Hanning window were averaged. For the FRFs, H_1 estimates were used.

4.5.5 Moment mobility measurements

Moment mobilities were introduced in section 3.2.9.2. As a moment can not be measured directly, an indirect method is necessary which is described in the following.

4.5.5.1 Experimental set-up

To measure moment mobilities, the finite-difference approximation described by Elliott et al. [2012] was used in this work. The basic principle and the notations are given in Figure 4.14, where the point of interest is denoted as P_0.

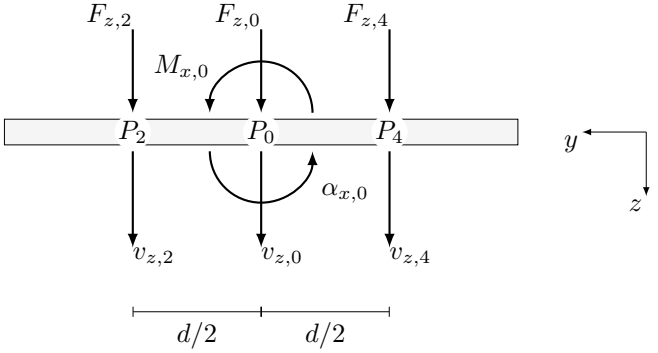

Figure 4.14: Sketch of finite difference approach according to [Elliott et al. 2012] to determine moment mobilities at a point P_0 about the x-axis in this example.

In this study the set-up was applied to measure both out-of-plane moment mobilities, $Y_{\mathrm{M}x}$ and $Y_{\mathrm{M}y}$. By using two accelerometers to approximate the point mobilities as described in section 4.5.4, in total, at least three accelerometers and one instrumented hammer are required to determine a moment mobility. However in this work, all elements of the

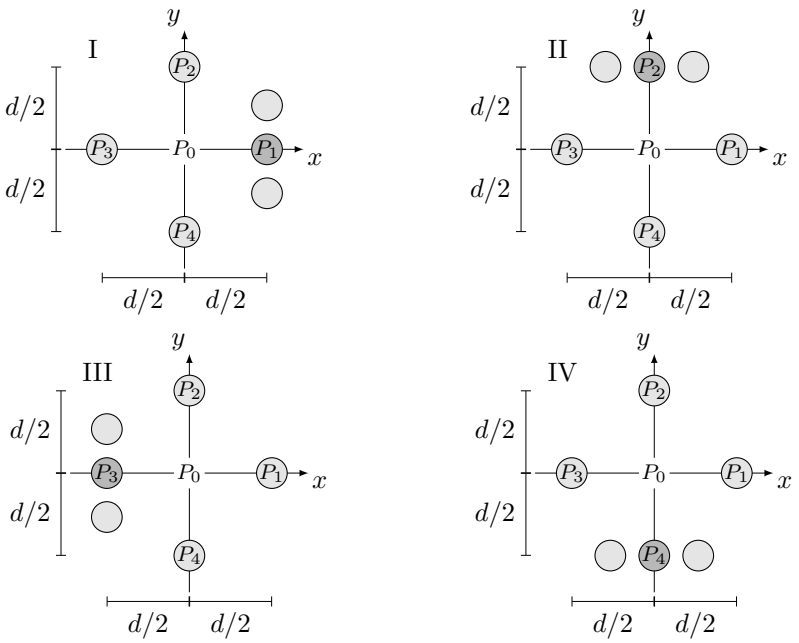

Figure 4.15: Set-up to approximate all mobilities for out-of-plane components. The light shaded circles indicate accelerometers to determine velocities, the dark shaded indicate excitation with an instrumented hammer. Four measurements, I to IV, are necessary to determine all terms necessary in equations (4.15) and (4.16). Further processing, [Elliott et al. 2012], allows the determination of the full matrix given in equation (4.12).

3×3 mobility matrix (equation (4.12)) for out-of-plane components were determined in each measurement.

$$\mathbf{Y} = \begin{pmatrix} \underline{Y}_{ii}^{v_z F_z} & \underline{Y}_{ii}^{v_z M_x} & \underline{Y}_{ii}^{v_z M_y} \\ \underline{Y}_{ii}^{\alpha_x F_z} & \underline{Y}_{ii}^{\alpha_x M_x} & \underline{Y}_{ii}^{\alpha_x M_y} \\ \underline{Y}_{ii}^{\alpha_y F_z} & \underline{Y}_{ii}^{\alpha_y M_x} & \underline{Y}_{ii}^{v_y M_y} \end{pmatrix} \tag{4.12}$$

For a detailed derivation of the approximation the reader is referred to [Elliott et al. 2012]. However the main equations to approximate the

moment mobilities at position P_0 are given in the following, using the numbering of positions P_1 to P_4 from Figure 4.15. The advantage of this finite difference approach is that only out-of-plane velocities, v_z, and forces, F_z, need to measured. The moment mobilities $Y_{\mathrm{M}x}$ and $Y_{\mathrm{M}y}$ can be approximated as

$$Y_{\mathrm{M}x} \approx \frac{1}{d^2}\left(\frac{\underline{v}_{z,2}}{\underline{F}_{z,2}} - \frac{\underline{v}_{z,4}}{\underline{F}_{z,2}} - \frac{\underline{v}_{z,2}}{\underline{F}_{z,4}} + \frac{\underline{v}_{z,4}}{\underline{F}_{z,4}}\right) \tag{4.13}$$

$$Y_{\mathrm{M}y} \approx \frac{1}{d^2}\left(\frac{\underline{v}_{z,1}}{\underline{F}_{z,1}} - \frac{\underline{v}_{z,3}}{\underline{F}_{z,1}} - \frac{\underline{v}_{z,1}}{\underline{F}_{z,3}} + \frac{\underline{v}_{z,3}}{\underline{F}_{z,3}}\right) \tag{4.14}$$

which can be rewritten in terms of mobilities.

$$Y_{\mathrm{M}x} \approx \frac{\underline{Y}_{22}^{v_z F_z} - \underline{Y}_{42}^{v_z F_z} - \underline{Y}_{24}^{v_z F_z} + \underline{Y}_{44}^{v_z F_z}}{d^2} \tag{4.15}$$

$$Y_{\mathrm{M}y} \approx \frac{\underline{Y}_{11}^{v_z F_z} - \underline{Y}_{31}^{v_z F_z} - \underline{Y}_{13}^{v_z F_z} + \underline{Y}_{33}^{v_z F_z}}{d^2} \tag{4.16}$$

Using this set-up the driving-point-mobility at the point P_0 can also be estimated by

$$Y_{\mathrm{dp}} \approx \frac{\underline{Y}_{11}^{v_z F_z} - \underline{Y}_{22}^{v_z F_z} - \underline{Y}_{33}^{v_z F_z} + \underline{Y}_{44}^{v_z F_z}}{4} \tag{4.17}$$

The set-up sketched in Figure 4.15 also allows additional processing of the three out-of-plane cross mobilities, $\underline{Y}_{ii}^{\alpha_x F_z}$, $\underline{Y}_{ii}^{\alpha_y F_z}$, $\underline{Y}_{ii}^{\alpha_y M_x}$ and their reciprocals.

However some limitations have to be considered. As described in section 4.5.2, low mass transducers are required to avoid mass loading effects on lightweight structures.

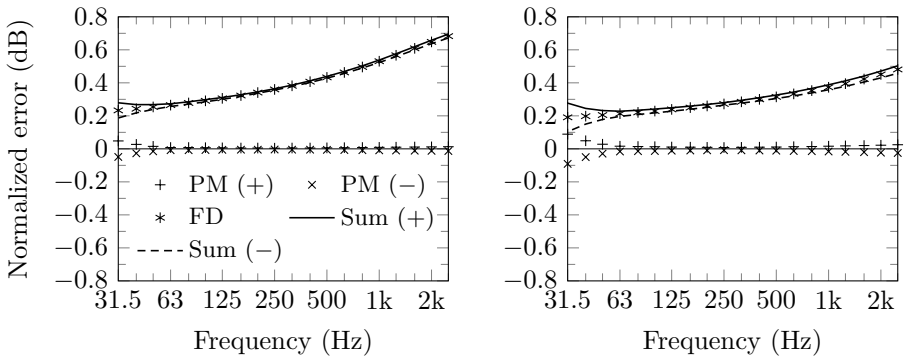

(a) Chipboard (b) Ribbed plate (Wall)

Figure 4.16: Normalized Phase Mismatch (PM), Finite Difference (FD) and combined (Sum) errors for measured moment mobilities according to section 4.5.5.2 for the properties of the 19 mm chipboard (left) and the properties of an equivalent ribbed plate (right). Phase mismatch from Figure 4.11.

4.5.5.2 Error analysis

Similar to the measurement of structural intensity, there is an error inherent in the finite difference approximation and an error due to phase mismatch of the accelerometers. The normalized error due to phase mismatch of the accelerometers can be estimated using equation (4.9) with $\theta = 0°$ as the excitation is on the axis between the accelerometers. From Elliott et al. [2012], the normalized error related with the finite difference approximation is

$$e_{\mathrm{FD}}(Y_{\mathrm{M}}) = \left| \frac{\mathrm{i}\,\omega\, d}{3\, B\, Y_{\mathrm{M}}} \right| \tag{4.18}$$

In this thesis a transducer spacing of 70 mm was used. Estimates for the normalized errors of this set-up applied in thesis are shown in Figure 4.16 for the properties of the 19 mm chipboard and the properties of an equivalent orthotropic plate (see section 3.2.4).

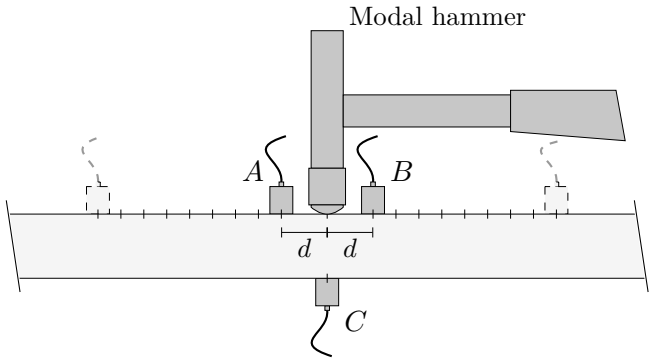

Figure 4.17: Set-up to assess the errors involved in using a pair of accelerometers for the power input using the direct method.

4.5.6 Structure-borne sound power input

4.5.6.1 Direct method

By measuring the force and the velocity, the power input can be determined using equation (3.70). This can be achieved by using an impedance head or a force transducer with a pair of accelerometers next to the excitation point. In this thesis the latter was applied by averaging the results obtained with both accelerometers similar to the measurement of the driving-point mobility as described in section 4.5.4.

The errors involved in using accelerometers and a force transducer, were assessed regarding the power input into a free-hanging 19 mm chipboard panel from a modal hammer (see Table 4.1). As reference, the power input was determined using an accelerometer (MMF, Type KS95B100, Table 4.1) directly opposite the excitation point on the reverse side of the chipboard as shown in Figure 4.17. Accelerometers A and B (MMF, Type KS95B100, Table 4.1) are positioned equidistant from the excitation point. Using these accelerometers the power input was determined for increasing distances, d, between 2 cm to 10 cm using 1 cm steps to the excitation point to avoid spatial summation of the response over too large an area.

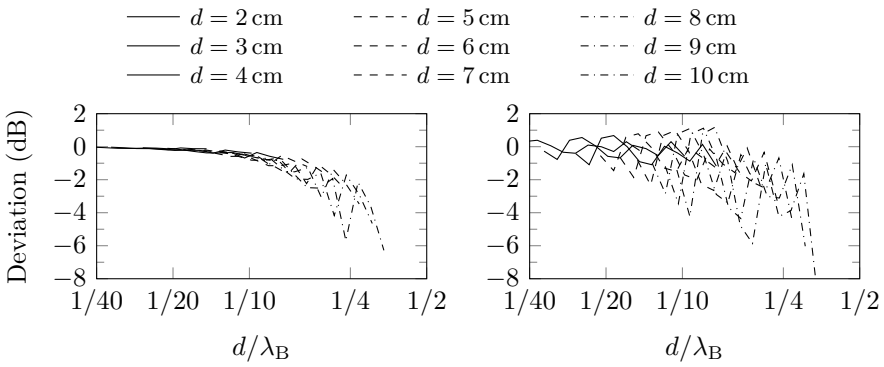

(a) Accelerometer pair

(b) Single accelerometer

Figure 4.18: Power input normalized to the power input using the accelerometer directly opposite the excitation point on the reverse side of the chipboard.

Figure 4.18 shows the power input for a pair of accelerometers and a single accelerometer on the excited surface next to the excitation point for different distances normalized to the power input determined using accelerometer C. The normalized power in shown in terms of d/λ_B, as this is a more practical descriptor than the bending wavenumber, k_B. It can be seen that the errors are significantly reduced with a pair of accelerometers. For a pair of accelerometers, the error is $\leq 1\,\mathrm{dB}$ when $d/\lambda_\mathrm{B} \leq 1/10$ (and $\leq 3\,\mathrm{dB}$ when $d/\lambda_\mathrm{B} \leq 1/6$). For a 19 mm chipboard plate $d/\lambda_\mathrm{B} = 1/10$ corresponds to a frequency of $\approx 1.7\,\mathrm{kHz}$ when $d = 2\,\mathrm{cm}$. This also applies when excitation is applied using an electrodynamic shaker. However, this procedure is only applicable to determine the power input of the force. Rotational components can not be measured directly and therefore indirect procedures were applied.

4.5.6.2 Mobility method using full mobility matrices

Concerning the out-of-plane translational excitation component the following source parameters are required to calculate the complex power input according to equation (3.75). The active component, i. e. the free

velocity, v_{Sf}, is required for each foot of a source with i feet, given by the vector in equation (4.19).

$$\mathbf{v}_{\mathrm{Sf}} = \begin{pmatrix} \underline{\hat{v}}_{\mathrm{Sf},1} \\ \underline{\hat{v}}_{\mathrm{Sf},2} \\ \vdots \\ \underline{\hat{v}}_{\mathrm{Sf},i} \end{pmatrix} \tag{4.19}$$

In addition, the passive property, i. e. the mobility of the source and the receiving structure is required. As multi-point sources are considered, the point-mobilities, $\underline{Y}_{ii}^{v_z F_z}$, as well as all transfer mobilities, are required to obtain the full mobility matrix given in equation (4.20).

$$\mathbf{Y} = \begin{pmatrix} \underline{Y}_{11}^{v_z F_z} & \underline{Y}_{12}^{v_z F_z} & \cdots & \underline{Y}_{1i}^{v_z F_z} \\ \underline{Y}_{21}^{v_z F_z} & \underline{Y}_{22}^{v_z F_z} & \cdots & \underline{Y}_{2i}^{v_z F_z} \\ \vdots & \vdots & \ddots & \vdots \\ \underline{Y}_{i1}^{v_z F_z} & \underline{Y}_{i2}^{v_z F_z} & \cdots & \underline{Y}_{ii}^{v_z F_z} \end{pmatrix} \tag{4.20}$$

Using these parameters, the active power, W, can be determined from equation (3.75), using $W = \mathrm{Re}\left\{\underline{Q}\right\}$. The narrow band active power is summed to give a one-third octave band power spectrum, that is used as reference for the simplification steps described in the following.

4.5.6.3 Mobility method applying simplifications

a) **Neglect transfer terms:** This simplification step considers only the point mobilities and potential interactions between individual contact points that are described by the transfer mobilities are neglected. This yields the mobility matrix given in equation (4.21).

$$\mathbf{Y} = \begin{pmatrix} \underline{Y}_{11}^{v_z F_z} & 0 & \cdots & 0 \\ 0 & \underline{Y}_{22}^{v_z F_z} & \cdots & 0 \\ \vdots & \vdots & \ddots & \vdots \\ 0 & 0 & \cdots & \underline{Y}_{ii}^{v_z F_z} \end{pmatrix} \tag{4.21}$$

This implies that all feet of the source act individually. This is a reasonable assumption for frequency ranges where the bending wavelength of the receiving structure is short compared to the spacing of the point contacts.

The motivation for this approach is to reduce the experimental effort in determining the source and receiver parameters.

b) **Using only one point on the receiving structure:** This simplification also neglects the transfer mobilities and only one point of the receiving structure is considered. This yields the mobility matrix for the receiving structure given in equation (4.22).

$$\mathbf{Y}_{\mathrm{R}} = \begin{pmatrix} \underline{Y}_{11}^{v_z F_z} & 0 & \cdots & 0 \\ 0 & \underline{Y}_{11}^{v_z F_z} & \cdots & 0 \\ \vdots & \vdots & \ddots & \vdots \\ 0 & 0 & \cdots & \underline{Y}_{11}^{v_z F_z} \end{pmatrix} \tag{4.22}$$

For the source mobility matrix, $\mathbf{Y}_{\mathrm{S}}$, the individual point mobilities of each foot are used as given in equation (4.21). For the free velocity of the source, equation (4.19), is used.

The motivation for this approach is to further reduce the experimental effort in determining the receiver parameters.

c) **Using the sum of individual power for each contact:** A further simplification calculates the active input power for each foot individually using equation (3.72). This assumes independent

point sources. The total input power is then calculated by the sum of the power from the individual points according to equation (4.23) Hence it is another writing for simplification (a).

$$W \approx \sum_{i=1}^{N} W_i \tag{4.23}$$

where N is the number of contact points.

d) **Using average data of the contact points:** This simplification has recently been included in [EN 15657:2017] and approximates one equivalent contact point for the multi-point source. Therefore the magnitudes of the source and the receiver mobilities are averaged according to equation (4.24).

$$|\underline{Y}_{\mathrm{R,eq}}| = \frac{1}{N} \sum_{i=1}^{N} |\underline{Y}_{\mathrm{R},i}| \quad \text{and} \quad |\underline{Y}_{\mathrm{S,eq}}| = \frac{1}{N} \sum_{i=1}^{N} |\underline{Y}_{\mathrm{S},i}| \tag{4.24}$$

The real part of the receiver mobility is averaged for all contact points using

$$\mathrm{Re}\left\{\underline{Y}_{\mathrm{R,eq}}\right\} = \frac{1}{N} \sum_{i=1}^{N} \mathrm{Re}\left\{\underline{Y}_{\mathrm{R},i}\right\} \tag{4.25}$$

where N is the number of contact points. For the free velocities at each foot of the source the sum according to equation (4.26) is used.

$$|\underline{\hat{v}}_{\mathrm{Sf,eq}}|^2 = \sum_{i=1}^{N} |\underline{\hat{v}}_{\mathrm{Sf},i}|^2 \tag{4.26}$$

The active power input is then approximated using

$$W \approx \frac{1}{2} |\underline{\hat{v}}_{\mathrm{Sf,eq}}|^2 \frac{\mathrm{Re}\left\{\underline{Y}_{\mathrm{R,eq}}\right\}}{|\underline{Y}_{\mathrm{S,eq}}|^2 + |\underline{Y}_{\mathrm{R,eq}}|^2} \tag{4.27}$$

e) **Using a constant value for the mobility of the receiving structure:** This approach is similar to d), except that for the mobility of the receiving structure a constant value is used. Hence $\underline{Y}_{\mathrm{R,eq}}$ in equation (4.27) is a frequency invariant value that represents the mobility of the receiving structure. For this purpose infinite plate mobilities according to equation (3.55) can be used. A typical value for timber-frame constructions is in the range between $1 \times 10^{-4}\,\mathrm{m/(N\,s)}$ to $1 \times 10^{-3}\,\mathrm{m/(N\,s)}$ [e. g. Mayr and Gibbs 2016].

The motivation for this approximation is that no measurements are required on the receiving structure. Only the source parameters need to be determined which can be done in the laboratory.

4.5.6.4 Reception plate method

This method is described in section 3.3.3.3 in a general way. For the particular application in this thesis, a 19 mm chipboard plate with the dimensions $2.05\,\mathrm{m} \times 0.93\,\mathrm{m}$ was used as reception plate. This plate was freely suspended from the ceiling using rubber cords. In addition absorbent material was added to the room to suppress the response of the airborne sound field.

The total loss factor was measured using the decay method. The arrangement of the transducers was validated with the directly measured power input of a shaker. The spatial-average-mean square velocity was determined with 20 accelerometers.

4.5.6.5 Inverse method

The reception plate allows determination of the power input of an unknown source. This includes force and potentially rotational excitation components that excite bending waves in the plate. Reciprocal relationships [Ten Wolde 1973; Fahy 1995b; Scheck 2011] can be applied to determine the individual components separately.

For point excitation at a position, P_0, the following relationships with a reference position, P_r are used. For the situation shown in Figure 4.19a these are

$$\frac{\underline{v}_\mathrm{r}}{\underline{F}_0} = \frac{\underline{v}_0}{\underline{F}_\mathrm{r}} \quad i.\,e. \quad \underline{Y}_{r0}^{vF} = \underline{Y}_{0r}^{vF} \tag{4.28}$$

and for Figure 4.19b.

$$\frac{\underline{v}_\mathrm{r}}{\underline{M}_0} = \frac{\underline{\alpha}_0}{\underline{F}_\mathrm{r}} \quad i.\,e. \quad \underline{Y}_{r0}^{vM} = \underline{Y}_{0r}^{\alpha F} \tag{4.29}$$

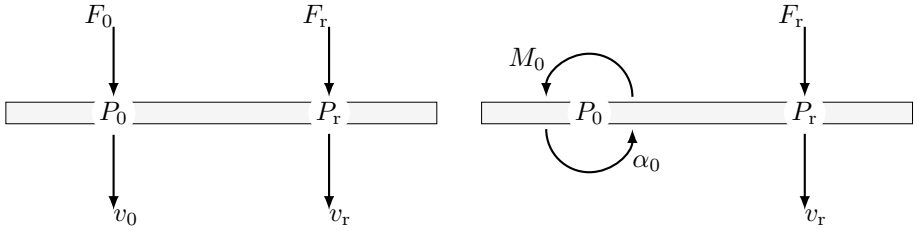

(a) Translational component (b) Rotational component

Figure 4.19: Reciprocity relationships.

By applying the set-up described in section 4.5.5, the complex transfer and cross-transfer mobilities for the positions indicated in Figure 4.20 are determined experimentally using an instrumented hammer and the 3 g accelerometers (see Table 4.1). Using these mobilities, the three excitation components, $F_{0,z}$, $M_{0,x}$ and $M_{0,y}$, can be determined from translational velocities at three reference positions as follows.

$$\begin{pmatrix} \underline{F}_{0,z} \\ \underline{M}_{0,x} \\ \underline{M}_{0,y} \end{pmatrix} = \begin{pmatrix} \underline{Y}_{0\mathrm{r}_1}^{v_z F_z} & \underline{Y}_{0\mathrm{r}_1}^{\alpha_x F_z} & \underline{Y}_{0\mathrm{r}_1}^{\alpha_y F_z} \\ \underline{Y}_{0\mathrm{r}_2}^{v_z F_z} & \underline{Y}_{0\mathrm{r}_2}^{\alpha_x F_z} & \underline{Y}_{0\mathrm{r}_1}^{\alpha_y F_z} \\ \underline{Y}_{0\mathrm{r}_3}^{v_z F_z} & \underline{Y}_{0\mathrm{r}_3}^{\alpha_x F_z} & \underline{Y}_{0\mathrm{r}_1}^{\alpha_y F_z} \end{pmatrix}^{-1} \begin{pmatrix} \underline{v}_{\mathrm{r}_1,z} \\ \underline{v}_{\mathrm{r}_2,z} \\ \underline{v}_{\mathrm{r}_3,z} \end{pmatrix} \tag{4.30}$$

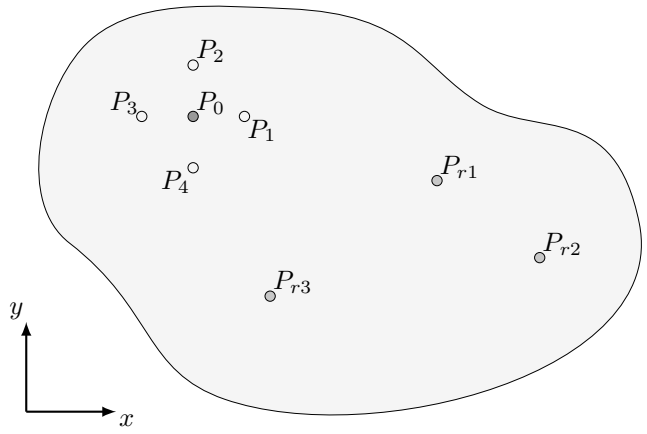

Figure 4.20: Set-up to determine the out-of-plane excitation components at a position P_0 using the inverse method.

To obtain complex velocities, the following velocity transfer functions are used

$$\underline{H}^{v_z v_z}_{\mathrm{r_2 r_1}} = \frac{\underline{v}_{\mathrm{r_2},z}}{\underline{v}_{\mathrm{r_1},z}} \quad \text{and} \quad \underline{H}^{v_z v_z}_{\mathrm{r_3 r_1}} = \frac{\underline{v}_{\mathrm{r_3},z}}{\underline{v}_{\mathrm{r_1},z}} \tag{4.31}$$

Using these, equation (4.30) is rewritten in terms of normalized velocities.

$$\begin{pmatrix} \underline{F}_{0,z} \\ \underline{M}_{0,x} \\ \underline{M}_{0,y} \end{pmatrix} = \begin{pmatrix} \underline{Y}^{v_z F_z}_{0\mathrm{r_1}} & \underline{Y}^{\alpha_x F_z}_{0\mathrm{r_1}} & \underline{Y}^{\alpha_y F_z}_{0\mathrm{r_1}} \\ \underline{Y}^{v_z F_z}_{0\mathrm{r_2}} & \underline{Y}^{\alpha_x F_z}_{0\mathrm{r_2}} & \underline{Y}^{\alpha_y F_z}_{0\mathrm{r_2}} \\ \underline{Y}^{v_z F_z}_{0\mathrm{r_3}} & \underline{Y}^{\alpha_x F_z}_{0\mathrm{r_3}} & \underline{Y}^{\alpha_y F_z}_{0\mathrm{r_3}} \end{pmatrix}^{-1} \begin{pmatrix} 1 \\ \underline{H}^{v_z v_z}_{\mathrm{r_2 r_1}} \\ \underline{H}^{v_z v_z}_{\mathrm{r_3 r_1}} \end{pmatrix} \left| \underline{v}_{\mathrm{r_1},z} \right| \tag{4.32}$$

With the source in operation, additionally the velocities at positions P_1 to P_4 indicated in Figure 4.20 are measured to determine the translational and angular velocities at P_0 using the following approximations by Elliott et al. [2012]

$$\underline{v}_{0,z} = \frac{1}{4} \left(\underline{v}_{1,z} + \underline{v}_{2,z} + \underline{v}_{3,z} + \underline{v}_{4,z} \right) \tag{4.33}$$

$$\underline{\alpha}_{0,x} = \frac{1}{d}\left(\underline{v}_{4,z} - \underline{v}_{2,z}\right) \quad \text{and} \quad \underline{\alpha}_{0,y} = \frac{1}{d}\left(\underline{v}_{3,z} - \underline{v}_{1,z}\right) \tag{4.34}$$

To account for the correct phase, the velocities are also normalized to the reference position P_{r1} using complex velocity transfer functions.

$$\begin{aligned} \underline{v}_{1,z} &= \underline{H}_{\mathrm{P_1r_1}}^{v_z v_z} \left|\underline{v}_{\mathrm{r_1},z}\right|, \quad \underline{v}_{2,z} = \underline{H}_{\mathrm{P_2r_1}}^{v_z v_z} \left|\underline{v}_{\mathrm{r_1},z}\right|, \\ \underline{v}_{3,z} &= \underline{H}_{\mathrm{P_3r_1}}^{v_z v_z} \left|\underline{v}_{\mathrm{r_1},z}\right|, \quad \underline{v}_{4,z} = \underline{H}_{\mathrm{P_4r_1}}^{v_z v_z} \left|\underline{v}_{\mathrm{r_1},z}\right| \end{aligned} \tag{4.35}$$

Finally the components of the input power can be determined using equation (3.69) for the translational component and

$$\underline{Q} = \frac{1}{2}\,\hat{\underline{M}}\,\hat{\underline{\alpha}}^* \tag{4.36}$$

for the rotational components.

4.5.7 Experimental determination of sound radiation

The radiated sound power was determined using sound intensity which comprises an active and a reactive component. Only the active component, I_a, is of interest as it efficiently radiates sound (e. g. [Cremer and Heckl 1967] or [Fahy 1995a]).

$$I_\mathrm{a} = \frac{1}{2}\,\mathrm{Re}\{\hat{\underline{p}}\,\hat{\underline{u}}^*\} \tag{4.37}$$

Similar to structural intensity measurements with an a-a probe (section 4.5.3), the active component of the sound intensity (positive direction) perpendicular to the structure of interest, I_z, (in this case denoted as z-direction) is approximated in the frequency domain from FFT data of the two microphones using

$$I_z \approx \frac{1}{2\,\omega\,\rho_0\,d}\,\mathrm{Im}\{\hat{\underline{p}}_1^*\,\hat{\underline{p}}_2\} = -\frac{1}{2\,\omega\,\rho_0\,d}\,\mathrm{Im}\{G_{p,12}\} \tag{4.38}$$

where, d, is the spacing between the two microphones of the p-p-probe.

In this thesis the p-p probe listed in Table 4.1 was used. The sound pressure signals were sent to the FFT-analyser listed in Table 4.1 and the Cross Spectrum $G_{p,12}$ exported to MATLAB to process the sound intensity as described above. The narrow band sound intensity was finally summed to one-third octave bands.

To determine the radiation efficiency, σ, the surface velocity of the structure is measured at the same point as the sound intensity. In this thesis the LDV listed in Table 4.1 was used for this purpose. The intensity probe and the LDV were mounted on a device that can be moved in two dimensions, which is practical to measure all positions of the measurement grid and keep the focus and distance to the structure for both [Grünewald 2016].

As with the a-a structural intensity probe, there are limitations due to the finite difference approximation and the phase mismatch of the microphones. To cover a wide frequency range, the sound radiation was determined by combining the results from measurements with two different microphone spacings (12.5 mm and 100 mm). As shown by Hopkins [2007] the finite difference error with a 12.5 mm space is within ± 0.2 dB up to 2000 Hz. To account for errors due to phase mismatch, the pressure-residual intensity index, δ_{pI0}, was determined by exposing the two microphones of the p-p-probe to the same sound pressure level. For each measurement of the sound intensity, the pressure-intensity index, F_{pI}, was determined by

$$F_{\mathrm{pI}} = L_p - |L_I| \tag{4.39}$$

If $\delta_{\mathrm{pI0}} - F_{\mathrm{pI}} < 10\,\mathrm{dB}$ the measured value was rejected, as the error is within ± 0.5 dB when $\delta_{\mathrm{pI0}} - F_{\mathrm{pI}} > 10\,\mathrm{dB}$ [e. g. Hopkins 2007]. The one-third octave band results from the two spacer lengths were averaged in the overlap of the reliable frequency ranges.

The sound intensity and the velocity, measured at discrete points are spatially averaged to determine the radiation efficiency. The grid spacing was 20 cm and therefore the spacing between the p-p probe and the

surface was set to 20 cm as well. Investigations by Grünewald [2016] on the test structure showed that a more narrow grid spacing gives the same results.

4.5.8 Sound pressure measurements

To quantify the sound energy in a volume, the spatial-average sound pressure that represents the reverberant sound field is measured. Fixed microphone positions were used in this study for the following reasons: Moving microphones can only be used for steady-state signals. As transient excitation was used in some measurements, fixed microphone positions were necessary. Low frequency procedures [Hopkins and Turner 2005] require additional sound pressure levels in the corners of a room. Fixed microphone positions allow the calculation of standard deviations and confidence intervals of the spatial average.

To obtain uncorrelated sample positions, the spacing between the individual microphones, d, must be chosen such, that $k\,d \geq \pi$ (i. e. $d \geq \lambda/2$) [Hopkins 2007]. Although a sufficient number of samples is required to obtain an average value that represents the reverberant sound field, correlated positions can increase uncertainty [Hopkins 2007]. In this study, the spatial sampling was carried out based on the guidelines given in [ISO 16283-1:2014-06] for the measurement of sound insulation in the field.

4.5.8.1 Measurements in cavities

To determine the spatial-average sound pressure level in the cavities of the timber-frame wall, microphones were inserted. Therefore holes were drilled into the chipboard that were large enough to allow an air gap that avoids contact to the structure which was sealed with elastic material.

4.5.9 Reverberation time measurements

The reverberation time T as well as the structural reverberation time T_s are defined as the required time for a 60 dB decay of an initial energy

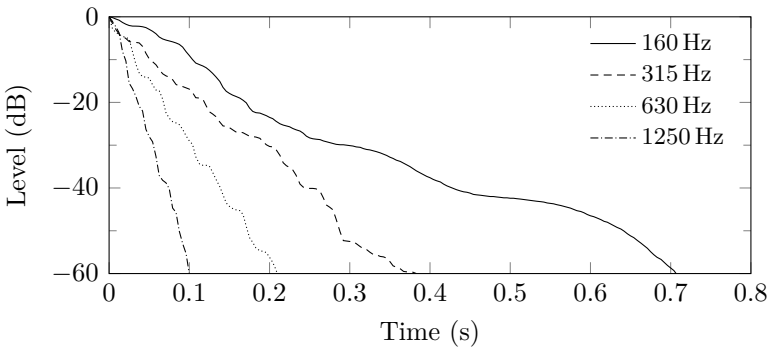

Figure 4.21: Example decay curves for selected one-third octave bands for measurements of the structural reverberation time on a free 19 mm chipboard plate.

level. It is therefore sometimes also denoted as T_{60}. The reverberation time is linked to the loss factor η as follows

$$T = \frac{2.2}{\eta f} \tag{4.40}$$

The experimental procedure to determine the reverberation time is described in [ISO 3382-2:2008]. Additional details for the structural reverberation can be found in [ISO/DIS 10848-1:2016]. According to these standards, two procedures, the interrupted noise method and the integrated impulse response method [Schroeder 1965] are possible. In this thesis, the integrated impulse response method was used with swept sine excitation provided by the measurement software m|reverb.

The obtained decay curves rarely provide a 60 dB decay in practice. Hence the reverberation time is extrapolated from 10 dB, 15 dB, 20 dB or 30 dB decays. The corresponding notation is then T_{10}, T_{15}, T_{20} and T_{30}. The starting point is normally chosen 5 dB below the level at the beginning to omit the curvature in the initial part of the decay [Jacobsen and Rindel 1987]. For structural reverberation time measurements T_{10} was used in this thesis. For reverberation time measurements of sound fields in rooms T_{20} was used.

As the reverberation times are typically determined in one-third octave bands, a filter analysis of the signal is required. However, band-pass filters have their own impulse response, and can alter the measurements. This is a limitation inherent in this method, as the decay time of the system (room, or structure) that is regarded, must be long compared to the filter decay time. This is a particular issue for structural reverberation times, as these are typically very short. As the impulse response of one-third octave band filters is asymmetric, with a faster response than decay, reverse filter analysis can be used to measure shorter reverberation times [Jacobsen and Rindel 1987]. Using the bandwidth for one-third octave bands

$$B = 0.23\, f_{\mathrm{tob,c}} \tag{4.41}$$

where $f_{\mathrm{tob,c}}$ is the band centre frequency for one-third octave bands. The limitation can be expressed in terms of the product of the bandwidth B and the reverberation time T.

If short reverberation times need to be determined and measurements are taken at low frequencies, octave bands can be used rather than one-third octave bands to increase the measurable frequency range. The bandwidth for octave bands is

$$B = 0.707\, f_{\mathrm{oct,c}} \tag{4.42}$$

where $f_{\mathrm{oct,c}}$ is the band centre frequency. Using equations (4.40) in combination with (4.41) and (4.42), respectively, the maximum measurable loss factors, η, can be estimated for different $B\,T$ limits. These are listed in Table 4.2 for forward- and reverse-filter analysis.

In terms of spatial averaging of excitation and response positions, Mecking et al. [2012] propose using the median rather than the arithmetic mean as this is a more robust estimator since large outliers, that potentially occur in reverberation time measurements, have less effect than with arithmetic averaging. In addition measured reverberation times are often

Table 4.2: Maximum measurable loss factors η for forward and reverse filter analysis.

	forward-filter analysis		reverse-filter analysis
	$BT \geq 16$[a]	$BT \geq 8$[a]	$BT \geq 4$
one-third octave bands	0.032	0.063	0.126
octave bands	0.097	0.194	0.389

[a] For sound insulation measurements with forward filter analysis, the accuracy of $BT \geq 8$ is normally sufficient [Hopkins 2007].

asymmetrically distributed rather than in a normal distribution. Therefore the median was used to determine average reverberation times.

4.5.10 Quasi-longitudinal phase velocity

Quasi-longitudinal phase velocities, c_L, are required because material properties, such as the Young's modulus for example, can be derived from it for beams (equation (3.2)) and plates (equation (3.7)).

Quasi-longitudinal waves have in-plane displacements which can be measured with accelerometers orientated along the propagation direction of the wave. The structure under test is excited with a short impulse provided by a hammer on one end and the response measured with two transducers spaced at a distance, d. In the processing, for both signals the starting point in time of the initial slope is found [Craik 1982]. It is only the initial slope that is of interest, as everything that follows includes reflected waves and potentially other wave types. The quasi-longitudinal phase velocity can be determined from the time difference, Δt, between the two points in time and the sensor spacing.

$$c_\mathrm{L} = \frac{d}{\Delta t} \tag{4.43}$$

To reduce the uncertainties a high time resolution must be chosen in the analyser, as well as sufficiently large samples to allow a preferably large sensor spacing.

4.6 Summary

The constructions, set-ups and procedures described in this chapter form the basis for the work described in the following chapters. Chapter 5 uses all procedures described in section 4.5 to investigate the vibrational behaviour and sound radiation of the laboratory timber-frame test structure. Chapter 6 uses the excitation techniques and the procedures for vibration and mobility measurements as well as the procedure to determine the SBS power. The experimental work presented in chapter 8 uses the excitation techniques and the procedures to determine the power input and to measure sound pressure that have been described in this chapter.

5 Experimental investigation of a timber-frame structure

5.1 Introduction

As the dynamic response of lightweight inhomogeneous constructions is complex, experimental work was carried out to investigate the vibrational behaviour of a timber-frame laboratory test structure. Based on the procedures described in chapter 4, measurements and results are presented and discussed in this chapter. Section 5.2 describes the determination of material properties for the laboratory test structure. Furthermore the experimental determination of total and coupling loss factors is described. In section 5.3 experimental investigations on the vibrational behaviour of the specific structure are presented. As knowledge about the receiver mobility is required to describe the structure-borne sound power input, measured mobilities are presented and discussed in section 5.4. Finally measurements of the SPL in the empty cavities as well as the experimental determination of the radiation efficiency are described. The results and findings in this chapter form the basis for the investigations in chapters 6, 7 and 8.

5.2 Material properties and transmission parameters for the laboratory test structure

Material properties for the laboratory test structure were obtained experimentally: density, quasi-longitudinal phase velocity and ILFs of the the timber-joists, timber-studs and chipboard plates.

The TLFs of the chipboard leaves forming the the timber-frame wall in the basement of the test structure, a cavity inside the wall and the receiving room of the test structure were also determined from reverberation time measurements. The TLF of the chipboard plates were required to determine the CLF of tongue and groove junctions in-situ as described in section 5.2.3.2. The TLF of an empty cavity in the timber-frame wall was needed to assess the SEA prediction in chapter 7. Measurements of the reverberation time in the receiving room are required for the normalization of SPLs to obtain data that is independent of the receiving room. Furthermore the TLFs of the rooms in the test structure are used as input data for modelling in chapter 7.

As there are no models available to predict the CLF across the tongue and groove joint of chipboard plates, it was measured to provide input data for the SEA models in chapter 7.

5.2.1 Material properties

The lightweight test-rig described in section 4.2 comprises three building elements, wall studs, floor joists and chipboard plates. For these three elements the material properties were determined experimentally. Different numbers of samples of each element were available, and are listed in Table 5.1. A final summary of the material properties derived from them is given in Table 5.2. The results are in good agreement with similar materials mentioned in literature [e. g. see Hopkins 2007].

Table 5.1: Dimensions of samples of chipboard plates, wall studs and floor joists for the determination of material properties.

	Plates	Wall studs				Floor joists					Unit
	1-4	1	2	3	4	1	2	3	4	5	
L_x	2.05	2.67	3.01	2.15	2.47	5.50	5.36	5.37	5.31	5.38	m
L_y	0.93			0.06				0.06			m
L_z	0.019			0.09				0.24			m

5.2.1.1 Density

The mass of each sample was measured using a crane scale with a precision of 10 g. From the dimensions of the samples given in Table 5.1 their density was calculated and is given in Table 5.2.

5.2.1.2 Quasi-longitudinal phase velocity

The quasi-longitudinal phase velocity was determined for the beams and plates following the procedure described in section 4.5.10. Figures 5.1 and 5.2 show the set-up for the measurements on the beams and the plates, which were suspended vertically by cords. As the particles in the chipboard plates are arranged randomly, they can be regarded as isotropic and the quasi-longitudinal phase velocity was only measured across the longer dimension.

In this study a sampling rate of 102 400 Hz was used. Assuming a quasi-longitudinal phase velocity for soft wood of 5000 m/s [e. g. see Hopkins 2007], Δt is approximately 4.3×10^{-4} s on the shortest sample stud ($L_x = 2.15$ m). This corresponds to approximately 44 time samples, giving an accuracy of at least $\pm 2.3\,\%$.

The starting point of the initial slope was found using a threshold slightly above noise. To reduce uncertainties two sensors at each end of the sample were used to obtain an average for the starting point of the rising slope. The average results are given in Table 5.2.

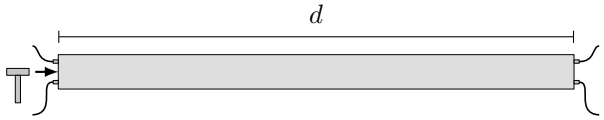

Figure 5.1: Measurement set-up to determine quasi-longitudinal wave velocity, $c_{\mathrm{L,b}}$ for the wall studs and floor joists.

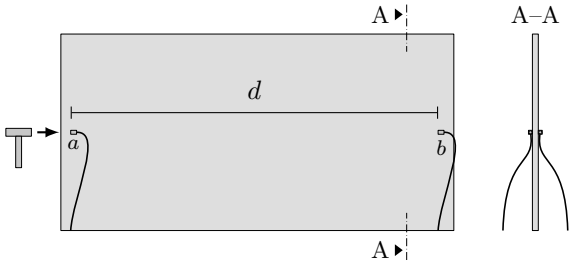

Figure 5.2: Measurement set-up to determine quasi-longitudinal wave velocity, $c_{\mathrm{L,p}}$ for the chipboard plates.

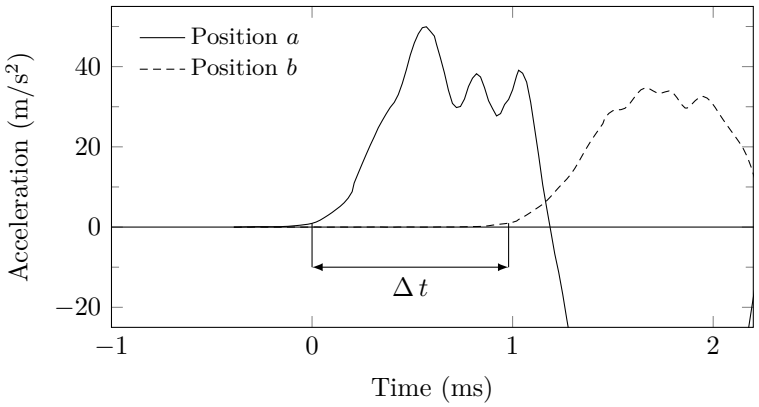

Figure 5.3: Example of measured time signals for two accelerometers at positions a and b (indicated in Figure 5.2) on a chipboard plate.

Table 5.2: Experimentally determined material properties of the building elements used in the lightweight test-rig. Values are given with 95 % confidence limits.

Parameter	Chipboard plates	Wall studs (spruce)	Floor joists (spruce)	Factor	Unit
Samples	4	4	5	–	–
Height	19	90	240	10^{-3}	m
Width	–	60	60	10^{-3}	m
Moisture	–	11.2 ± 1.8	11.9 ± 0.7	1	%
ρ	6.15 ± 0.10	4.97 ± 0.56	4.72 ± 0.35	10^{2}	kg/m^3
c_L	2.02 ± 0.07	5.46 ± 0.33[a]	5.36 ± 0.30[a]	10^{3}	m/s
ν	0.3[b]	–	–	1	–
E	2.29 ± 0.18[c]	14.5 ± 3.4[c]	13.6 ± 1.7[c]	10^{9}	N/m^2
$f_{\mathrm{B,thin}}$[d]	5.31	3.03	1.12	1	kHz
η_int	1.7 ± 0.1[e]	1.6 ± 0.2[f]	1.2 ± 0.2[g]	10^{-2}	–

[a] Measured along grain
[b] Estimate
[c] Determined from ρ and c_L of individual samples using equation (3.2) respectively (3.7) before averaging. Rounding causes slight variations in the decimal places if E is calculated from the average values of c_L and ρ given in this table.
[d] Corresponds to $\lambda_\mathrm{B} = 6\,h$, see equation (3.11)
[e] Arithmetic average of median for one-third octave bands 160 Hz to 1250 Hz
[f] Arithmetic average of median for one-third octave bands 160 Hz to 2500 Hz
[g] Arithmetic average of median for one-third octave bands 100 Hz to 1000 Hz

5.2.1.3 Internal loss factor

The ILF, η_int, was estimated from measured reverberation times using equation (4.40) in one-third octave bands. As this method only gives the TLF, η_tot, this procedure can only be used in frequency ranges where it is reasonable to assume that the internal losses dominate, i. e. below the coincidence frequency [Hopkins 2007]. For the measurements, the elements were resiliently suspended to approximate free boundary conditions. The chipboard was excited perpendicular to the surface and the studs and joists were excited on axis. As the free chipboard plate exchanges energy with the surrounding airborne sound field, especially at and above the coincidence frequency, additional absorbent material was

added to the room were the measurements took place, to avoid any influence of the sound field. The majority of absorbent material (polyester fibre) was placed in front of the walls that were parallel to the chipboard surface with a thickness of approximately 0.5 m to 1 m.

As described in section 4.5.9, shaker excitation with a swept sine signal was used for these measurements. For each element two excitation positions were used. The response positions were chosen, such that the direct field in the vicinity of the excitation position and the boundaries was excluded. As the remaining space was limited, only three response positions for each excitation position were chosen for the studs to avoid measuring correlated positions. This resulted in 2×3 combinations for each of the four samples, to give 24 decay curves in total. For the chipboard plates and the floor joists more space was available, hence four response positions were used. This resulted in a total number of 32 decay curves for the four available chipboard samples. Since five samples were available for the floor joists, 40 decay curves could be used.

The decay curves were determined using reverse-time integration of the impulse responses and evaluated in one-third octave bands. The TLF was calculated from $T_{\mathrm{s},10}$ for the chipboard plates, the wall studs and the floor joists. Since the median was used to find a representative estimate, the results are presented as boxplots. The box represents the upper and lower quartile and the horizontal line in the box the median (50 % quantile) of the data. The whiskers represent the upper or lower quartile plus or minus 1.5 times the height of the box. For normally distributed data this corresponds to $\pm 2.7\ \sigma$ (99.3 %-coverage). If the most extreme outlier is within the whisker, its length is set to this value.

Chipboard plates Figure 5.4 shows the TLF for the chipboard plates. However, as described in section 4.5.9, the low number of modes at low frequencies can affect the uncertainty in the obtained values. To find a lower frequency limit for the obtained data, the statistical mode count for the chipboard samples under test was estimated using equations (3.28) and (3.101).

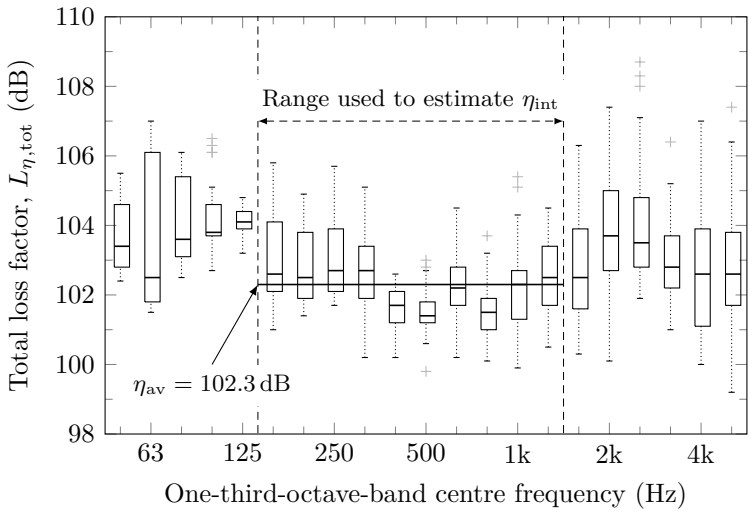

Figure 5.4: Total loss factor of chipboard determined from $T_{\mathrm{s},10}$ using equation (4.40). Four chipboard plates were measured with 2×4 combinations of excitation and response position on each, giving a total number of $n = 32$ samples for the boxplot.

Additionally the mode frequencies were calculated according to section 3.2.5 (assuming free boundary conditions) and the number of modes counted in each one-third octave band. Figure 5.5 shows the mode count from the mode frequencies and the statistical mode count for a chipboard plate with the same dimensions used for the loss factor measurement.

For the chipboard plates, the actual mode count is higher than the statistical mode count at low frequencies. The small number of modes is likely to be the cause of the high variation in the loss factors at low frequencies. In the 63 Hz one-third octave band there are no predicted modes which could be the cause of the high variation for the TLF in this band. Based on Figures 5.4 and 5.5, the lower frequency limit was qualitatively set to 160 Hz because above this frequency, the median of the loss factor starts to converge to a constant value which is expected for the ILF.

Additionally an upper frequency limit for the data is necessary to determine the ILF, as the measured TLF also includes radiation losses at

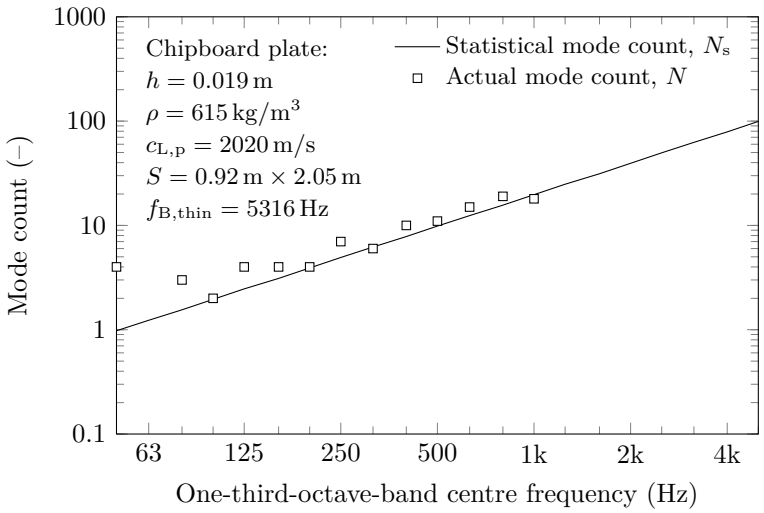

Figure 5.5: Mode count for one-third-octave-bands of a free chipboard plate. As the results converge at high frequencies, the actual mode count is shown only up to 1000 Hz

and above the coincidence frequency, f_c. Hence this provides the upper limit for the determination of the ILF. For thin isotropic plates the coincidence frequency is given in equation (3.36).

Using $c_{\mathrm{L,p}}$ from the measurements described in the previous section, the coincidence frequency for the chipboard is approximately 1693 Hz which is within in the 1600 Hz one-third octave band. The influence of the radiation loss can be observed with the increasing TLF in Figure 5.4 at and above the 1600 Hz one-third octave band. Hence the upper frequency limit was set to the 1250 Hz one-third octave band. This also avoids possible mass loading of the sensors (see section 4.5.2.1) as 23 g transducers were used.

The measured TLF was averaged in the frequency range from 160 Hz to 1250 Hz as indicated in Figure 5.4. As the internal losses are constant with frequency it is assumed that the results apply over the entire buildings acoustics frequency range from 50 Hz to 5000 Hz.

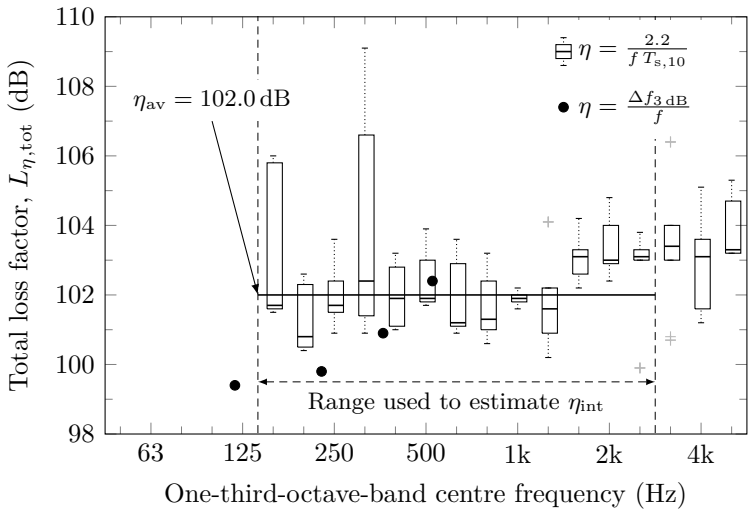

Figure 5.6: Total loss factor and estimate for internal loss factor of the freely suspended wall studs. Four sample studs with 2×3 combinations of excitation and response position on each, giving a total number of $n = 24$ samples for the boxplot.

Wall studs and floor joists Figures 5.6 and 5.7 show the TLFs for the wall studs and the floor joists, respectively; these were determined from measurements of the structural reverberation time and the 3 dB bandwidths. Similar to the chipboard plates the ILF can be determined directly from the TLF only in a limited frequency range. Hence frequency limits are needed to calculate a frequency average ILF. As for the chipboard plates, the statistical mode count was obtained from the modal density for bending waves on thin beams using equation (3.27).

Using equation (3.101) the statistical mode count can be obtained for the samples of the wall studs and the floor joists. The available samples have the same cross sectional area but different lengths, L_x, hence the statistical mode count, N_{s}, shown in Figures 5.8 and 5.9 differs slightly.

Similar to the chipboard plates, free boundary conditions are approximated, which allows a calculation of the mode frequencies, f_p, for a finite Euler-Bernoulli beam given by equation (3.24). Again the modes are counted in each one-third octave band to give the mode count, N which

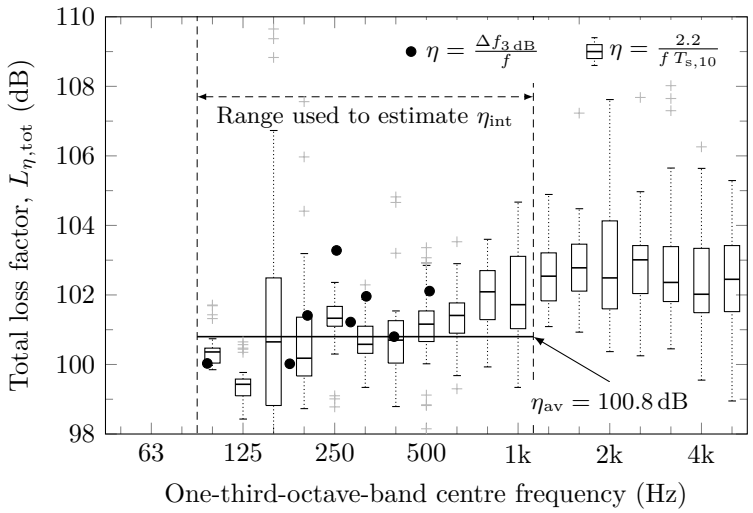

Figure 5.7: Total loss factor and estimate for internal loss factor of the freely suspended floor joists. Five sample joists with 2×4 combinations of excitation and response position on each, giving a total number of $n = 40$ samples for the boxplot.

is added to Figures 5.8 and 5.9. As the lengths of the samples vary, the mode count also differs slightly. However there is only one marker used for all samples, as the loss factor is determined from the median of measurements on all samples.

Figures 5.8 and 5.9 show that for the samples of wall studs and floor joists there are up to 3 modes in each one-third octave band. For bands without a mode the application of the decay method is questionable. However as the sample beams have different lengths, the mode frequencies vary and therefore at least one of the samples provides a mode for each one-third octave band. Nevertheless the uncertainty is high for bands where for example only one of the samples has a mode. As this is more likely at low frequencies a lower frequency limit was introduced.

To support the results determined from the measured reverberation times, the half-power bandwidth method was also applied. Driving point mobilities were measured, and the bandwidth at the peaks of the mode frequencies f_p was evaluated at the 3 dB-down points, $\Delta f_{3\,\mathrm{dB},p}$.

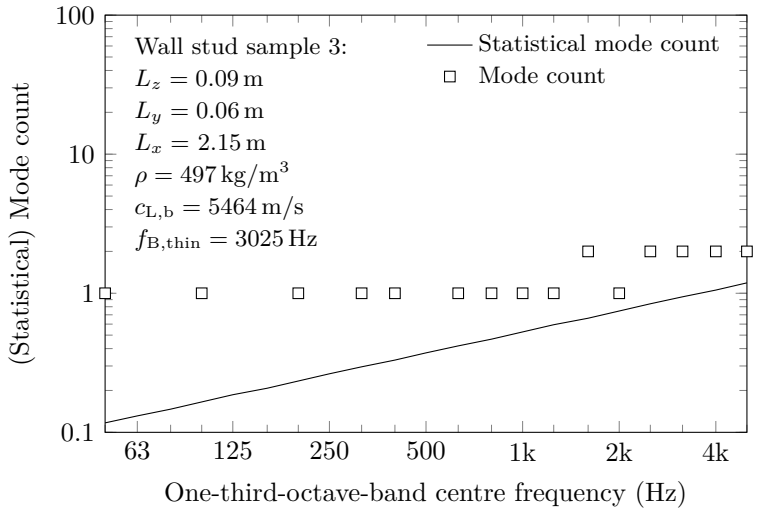

Figure 5.8: Mode count for one-third-octave-bands of the shortest wall stud (sample 3) with free boundary conditions.

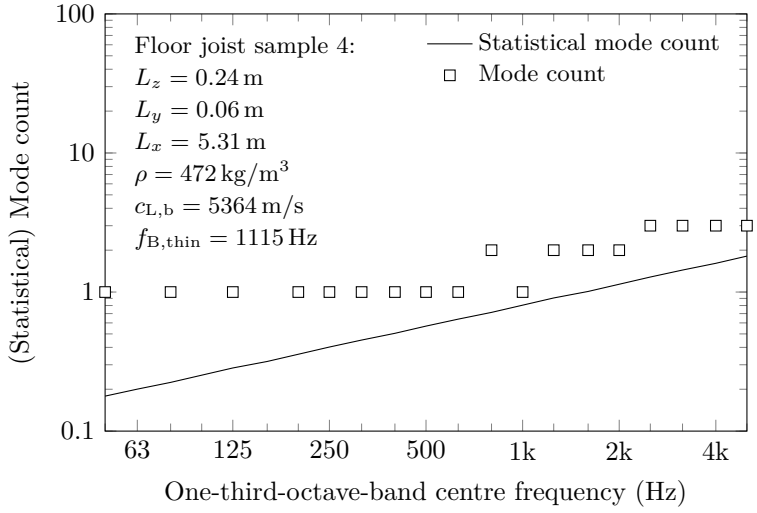

Figure 5.9: Mode count for one-third-octave-bands of the shortest floor joist (sample 4) with free boundary conditions.

The ILF can then be determined from

$$\eta_{\mathrm{int},p} = \frac{\Delta f_{3\,\mathrm{dB},p}}{f_p} \tag{5.1}$$

The driving point mobility was measured at three positions on one sample wall stud and one sample floor joist. These loss factors were averaged for these three positions and added to Figures 5.6 and 5.7. They show good agreement with the results obtained from reverberation times. However, as the decay method gives continuous data, these results were used to obtain an ILF from an arithmetic frequency average.

As the bending wavelength, λ_{B}, gets smaller compared to the dimension of bending displacement, L_z, with increasing frequency, pure bending waves no longer occur (see section 3.2.3). Hence the loss factors determined from measured reverberation times do not exclusively describe the decay of bending modes.

Towards high frequencies the experimentally determined TLFs increase for the wall studs and the floor joists, which might be caused by thick plate behaviour. Hence for the wall studs, $f_{\mathrm{B,thin}} = 3025\,\mathrm{Hz}$ can be set as upper limit for the determination of ILFs of bending modes, η_{int}, from the experimentally determined TLFs, η_{tot}. Therefore the 2500 Hz one-third octave band was the last band included in the average as indicated in Figure 5.6. For the floor joists, $f_{\mathrm{B,thin}}$ is 1115 Hz which is at the transition between the 1000 Hz and 1250 Hz one-third octave band. Hence the upper limit was set above the 1000 Hz one-third octave band as indicated in Figure 5.7. The final results for all elements under test are given in Table 5.2.

5.2.2 Total loss factors

5.2.2.1 Timber-frame wall

To gain knowledge about the overall losses of a timber-frame structure, the TLF of the chipboard plates that form the lower wall in the test structure was determined experimentally using the decay method.

To determine the TLF according to equation (4.40), the structural reverberation time was measured with shaker excitation and a swept-sine signal as described in section 4.5.9. The measurement was carried out based on the procedure described in [ISO/DIS 10848-1:2016] for the determination of the structural reverberation time of building elements for which the TLF is governed by the coupling losses. This is not the case for lightweight timber-frame structures especially towards high frequencies as mentioned in section 2.3.1. However at low frequencies lightweight structures such as the timber-frame wall tend to behave like a single plate, with no significant decrease of vibration across its surface [Nightingale and Bosmans 1999].

Similar work was done by Mecking [2012] who measured the TLF of a timber-joist floor. Mecking proposed using less excitation and measurement positions above ribs compared to bay positions as the percentage surface area of the ribs is typically lower. Hence two out of six excitation positions were chosen above timber studs for the measurements. For each excitation position six response positions were measured with one out of these six above a timber stud. To avoid correlated positions the distance between individual response positions was at least 1 m which is half the bending wavelength of 19 mm chipboard at approximately 20 Hz. The minimum distance between the excitation position and the response positions was also 1 m which equals the reverberation distance, r_{rd} (equation (5.2)) at approximately 1600 Hz for a 19 mm chipboard plate with the dimensions of the wall (5.06 m × 2.59 m) and the TLF estimated according to equation (3.100) (with $C = 0.4$ timber-frame walls acc. to [Hopkins 2007]).

$$r_{\mathrm{rd}} = \frac{\omega\,\eta\,S}{4\,\pi\,c_{\mathrm{B,p}}} \tag{5.2}$$

The response was measured with the 23 g accelerometers listed in Table 4.1 that were fixed with magnets (24.5 g) to metal washers that are screwed to the surface of the chipboard plates. To reduce the influence of the excited airborne sound field in the adjacent rooms, a thick layer

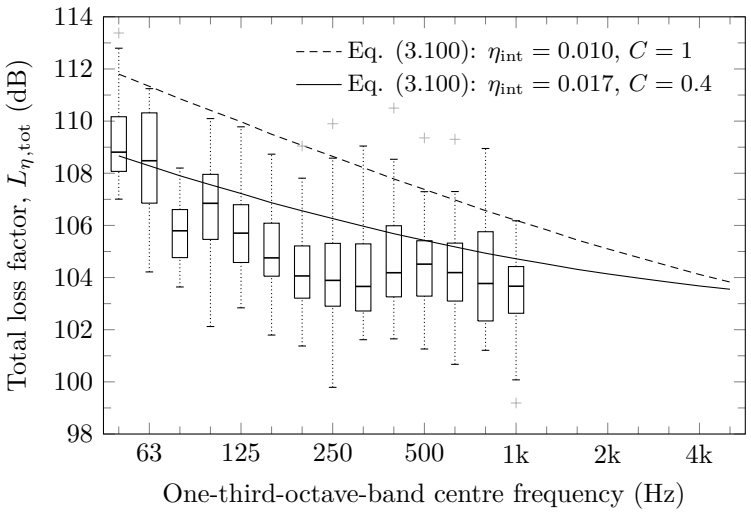

Figure 5.10: Total loss factor of timber-frame wall determined from $T_{\text{s},10}$ using equation (4.40).

(≈0.7 m) of absorbent fibre material was placed in front of the walls, parallel to the timber-frame wall under test.

The results are shown in Figure 5.10 using the median and the boxplot to visualize the data (6×6 combinations of excitation and response). As the use of the TLF is questionable for timber-frame walls at higher frequencies due to limitations in the experimental procedure (reverberation distance, mass loading) the results are only processed and shown up to the 1000 Hz one-third octave band.

Additionally the TLF can be estimated according to equation (3.100). In Figure 5.10 constants for heavyweight and lightweight buildings are included to allow comparison of the measured results against those estimates.

In the 50 Hz and the 63 Hz one-third octave bands, there is reasonable agreement between the measurement and the prediction according to equation (3.100) with $C = 0.4$. Between 80 Hz and 1000 Hz the measured TLF is up to 2.5 dB lower than the prediction. As the attenuation of vibration with distance increases with frequency, the losses due

to structural coupling at the boundaries, described by the factor $\frac{C}{\sqrt{f}}$ in equation (3.100), has less influence and therefore the prediction is higher.

5.2.2.2 Cavities

The timber-frame wall has empty cavities. For modelling of the sound propagation and transmission using SEA, the TLF of the cavities is needed. This requires knowledge about the sound absorption of the surfaces in the cavity. However, the absorption coefficients of chipboard plates and the timber studs and bars were not measured. The values given in [DIN 18041:2016-03] or [EN 13986:2004+A1:2015] indicate that the absorption coefficients range roughly from 0.03 to 0.25. The issue is that absorption coefficients are normally determined for random incidence but the cavity has one-, two-, or three-dimensional sound fields over the frequency range from 50 Hz to 5000 Hz; hence the TLF of one empty cavity was determined experimentally using the decay method (see section 4.5.9) to give a better estimate.

To excite the sound field in the cavity, a sheet of chipboard was removed to insert a small loudspeaker in the cavity. For the measurements, the chipboard plate was replaced in its original position. Microphones were inserted through drilled holes in the chipboard that were large enough to keep a small gap that was sealed with elastic material as shown in Figure 5.11. To avoid correlated microphone positions, only four were chosen in the cavity. However at each position the reverberation time measurement was repeated and two depths of the inserted microphone were chosen to obtain an averaged reverberation time for each to increase the accuracy at each position. The holes were drilled with a minimum distance of 0.5 m to the loudspeaker, 0.13 m to the cavity perimeter and 0.02 m to the inner chipboard surfaces.

The TLF from measurements is shown in Figure 5.12 for comparison with ILFs, η_{int}, (based on section 3.4.5.1) for absorption coefficients ranging from 0.03 to 0.25.

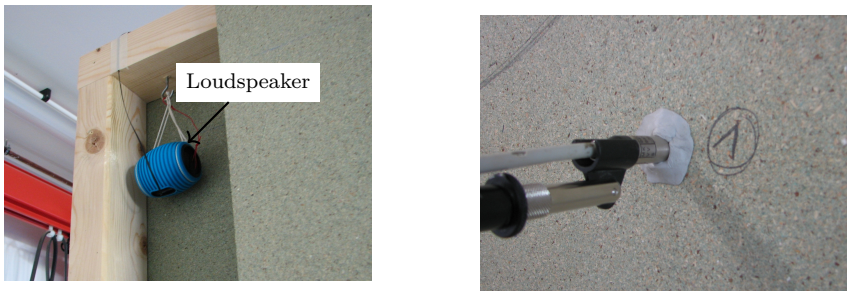

(a) Small loudspeaker in cavity

(b) Microphone inserted into the cavity

Figure 5.11: Set-up to measure reverberation times in the empty cavity.

As the measured TLF of the cavity includes coupling losses there are some deviations compared to the estimated ILF. Compared to the estimated transition at $f_{0,0,1}$ the measured data only has a slight step change in the TLF. The results indicate a feasible range for the sound absorption of the cavity surfaces, as the ILF must be equal to, or smaller than the TLF that includes coupling. Hence it seems that the absorption coefficient for the chipboard plates and the wall studs tends to be towards the lower limit of the range that is shown in Figure 5.12. Below the first cross-cavity mode, only the absorption of the studs is relevant, which is approximately 0.1 below 500 Hz according to [EN 13986:2004+A1:2015]. Above $f_{0,0,1}$, the absorption of the chipboard dominates due to the high percentage of area it covers. Although [EN 13986:2004+A1:2015] gives a value of 0.25 for chipboard at high frequencies, it might be lower for the material used in this particular situation. Especially as [DIN 18041:2016-03] gives values of 0.06 above 1000 Hz for veneered chipboard directly in front of a solid structure.

5.2.2.3 Receiving room

The measurement procedure described in section 4.5.9 was applied using two excitation positions with four response positions. The results are shown in Figure 5.13 in terms of the TLF using equation (4.40).

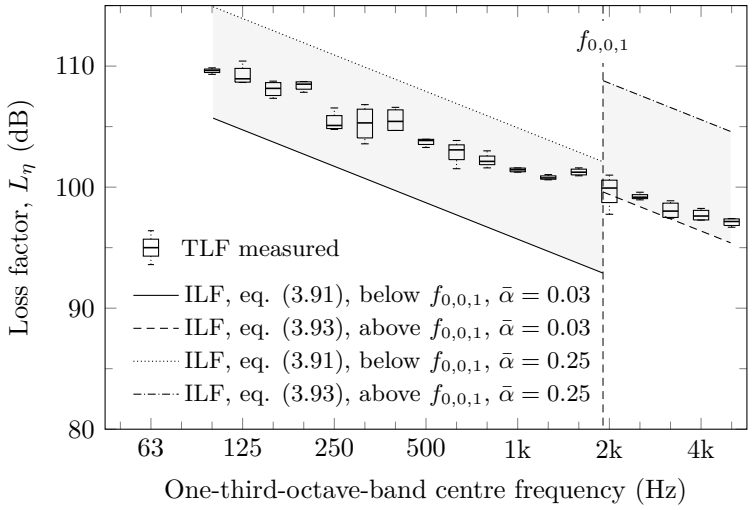

Figure 5.12: Comparison of measured total loss factors and predicted internal loss factors for the empty cavity.

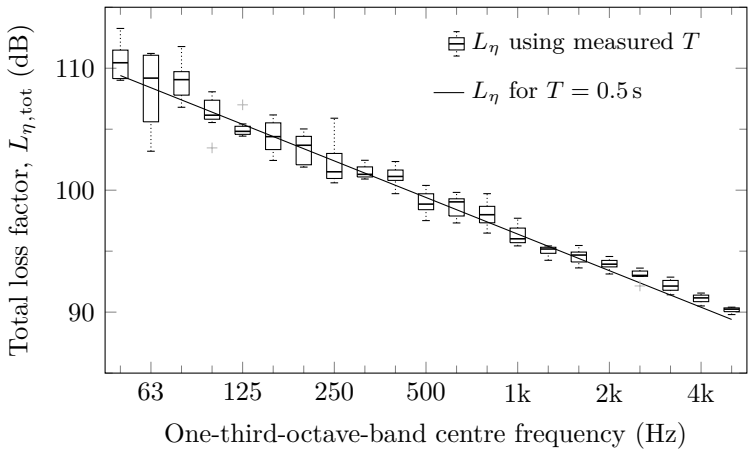

Figure 5.13: Total loss factor obtained from T_{10} in the receiving room of the lightweight test-rig

5.2.3 Coupling loss factor for the tongue and grooved chipboard plates

For tongue and groove joints, no analytical models are available to estimate the coupling of the chipboard plates; hence they were determined experimentally.

5.2.3.1 Free chipboard plates

To assess an isolated, single joint, two chipboard plates (from the samples listed in Table 5.1) were suspended vertically and connected along the shorter edges. To describe the quantities that are necessary to determine the CLF, the simple two-subsystem SEA-model sketched in Figure 3.12 is used. From equation (3.85), the TLF of plate 2 is

$$\eta_{\mathrm{tot},2} = \eta_{21} + \eta_{\mathrm{d},2} \tag{5.3}$$

Assuming negligible power flow back to plate 1, the CLF can be written in terms of energies using equation (3.84)

$$\eta_{12} = \frac{E_2}{E_1}\,\eta_{\mathrm{tot},2} \tag{5.4}$$

As the two plates used are identical ($m_1 = m_2$), this can be written as

$$\eta_{12} = \frac{\langle v_2^2\rangle_{t,s}}{\langle v_1^2\rangle_{t,s}}\,\eta_{\mathrm{tot},2} \tag{5.5}$$

where $\langle v_1^2\rangle_{t,s}$ and $\langle v_2^2\rangle_{t,s}$ are the spatially averaged mean square velocities of plate 1 and 2, respectively. This can also be expressed in decibels using the velocity levels of plate 1, $L_{v,1}$ and plate 2, $L_{v,2}$ as well as the TLF of plate 2 in decibels, $L_{\eta,\mathrm{tot},2}$.

$$\begin{aligned} L_{\eta,12} &= L_{v,2} - L_{v,1} + L_{\eta,\mathrm{tot},2} \\ &= -(L_{v,1} - L_{v,2}) + L_{\eta,\mathrm{tot},2} \\ &= L_{\eta,\mathrm{tot},2} - D_{v,12} \end{aligned} \tag{5.6}$$

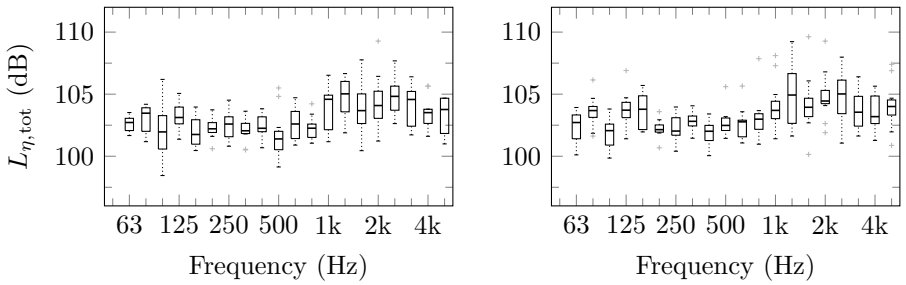

(a) Plate a, chipboard sample 1 (b) Plate b, chipboard sample 2

Figure 5.14: TLF of coupled chipboard plates.

where $D_{v,12}$ is the velocity level difference between the excited source subsystem, 1, and the receiving subsystem, 2. Hence the TLF can be determined from measured spatial-average velocity levels and the TLF of one of the two plates.

The TLF was determined in the actual experimental set-up with the chipboard plates coupled. However the measurement was carried out for plate a as well as plate b. Therefore the same procedure was applied as for the determination of the ILFs of chipboard plates, described in section 5.2.1.3. The results for both plates are shown in Figure 5.14. The plates are identical and the boundary conditions are the same, hence the TLF can be assumed to be nominally identical.

The spatial-average velocity level was measured on each plate using structural excitation with a shaker driven with broadband noise. The measurements were carried out in both directions; meaning that either plate a or plate b was excited. The two excitation positions were chosen towards the free end of the plate to avoid nearfields incident on the junction. Preliminary investigations ensured that, the signal-to-noise ratio was sufficient and that flanking transmission via the airborne sound field or the suspensions was negligible for the frequency range of interest. This was assessed by disconnecting the plates whilst suspended in nominally the same position. To suppress airborne flanking, absorptive material was placed around the receiving plate.

The vibration level difference was determined in both directions and arithmetically averaged similar to the procedure for flanking measurements according to [ISO/DIS 10848-1:2016]. An average value was determined using three joints from four different chipboard samples, giving three level differences which were arithmetically averaged to give the average level difference, $\overline{D_{v,12}}$.

As the TLF of plate 1 and 2 can be assumed to be nominally identical, an averaged CLF for the tongue and groove joint, $L_{\eta,\mathrm{TG}}$, was determined using the average TLF shown in Figure 5.14.

$$L_{\eta,\mathrm{TG}} = L_{\eta,\mathrm{tot}} - \overline{D_{v,12}} \tag{5.7}$$

Figure 5.15 shows the CLF and the TLF. Between 63 Hz and 200 Hz the CLFs and TLFs are similar, however, above 200 Hz the coupling significantly decreases with increasing frequency. Hence the individual chipboard plates can be regarded as weakly coupled SEA-subsystems at mid and high frequencies.

Figure 5.15 also gives an exponential fit for the measured CLF that can be used for an estimate for the CLF across a tongue and groove joint. This fit function is given by

$$L_{\eta,\mathrm{TG,fit}} = 10\,\mathrm{lg}\left(\frac{0.02\,e^{0.002\,f}}{1\times 10^{-12}}\right) \tag{5.8}$$

5.2.3.2 Measurement in-situ

To compare the coupling measured on plates with free boundaries with plates with in-situ boundary conditions, measurements were additionally carried out on chipboard junctions on the test wall. This required measurements using structural intensity (described in section 4.5.3).

Figure 5.16 shows the set-up for the measurement. The CLF was determined for the two horizontal chipboard junctions in the far left bay of the timber-frame wall in the basement of the test structure (see Figure 5.16a). The chipboard in the middle of the wall was excited with

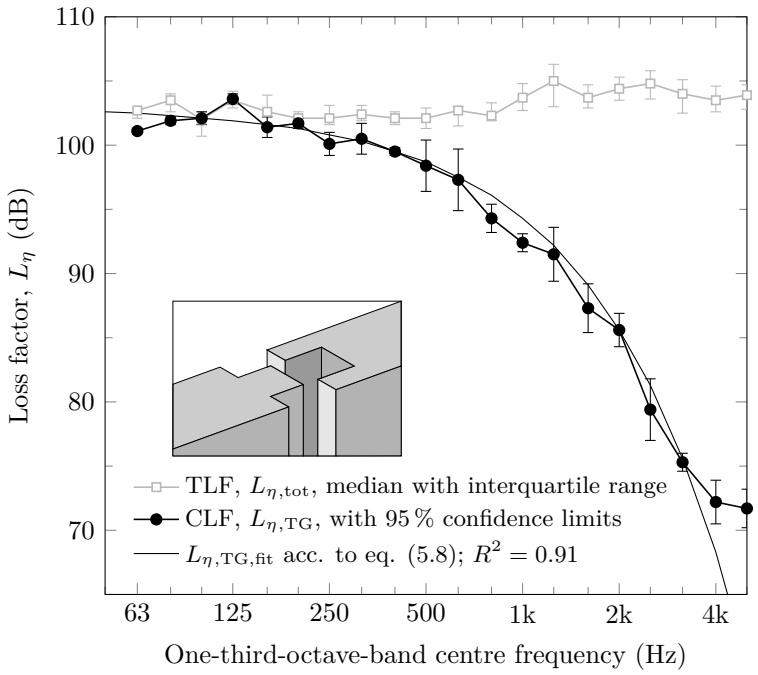

Figure 5.15: Coupling loss factor for tongue and groove joint, $L_{\eta,\mathrm{TG}}$, measured with two free chipboard plates. For comparison the TLF from Figure 5.14 is also shown. Additionally an exponential fit is given for the measured CLF.

a point force applied by a shaker using the set-up in Figure 4.6. For these investigations two excitation positions were used. The structural intensity was then measured with a set of six a-a probes behind the junctions. To extend the frequency range to high frequencies, a probe spacing, $d = 30\,\mathrm{mm}$ was used with small accelerometers (weight of 3 g – see Table 4.1). From Figure 4.12 it can be seen that this gives a maximum normalized error of approximately $-0.5\,\mathrm{dB}$ at 1000 Hz.

The net power, W_{net}, transmitted across the junction is determined from the measured structural intensities using

$$W_{\mathrm{net}} = \frac{L}{N} \sum_{i=1}^{N} I_{\mathrm{s},i} \tag{5.9}$$

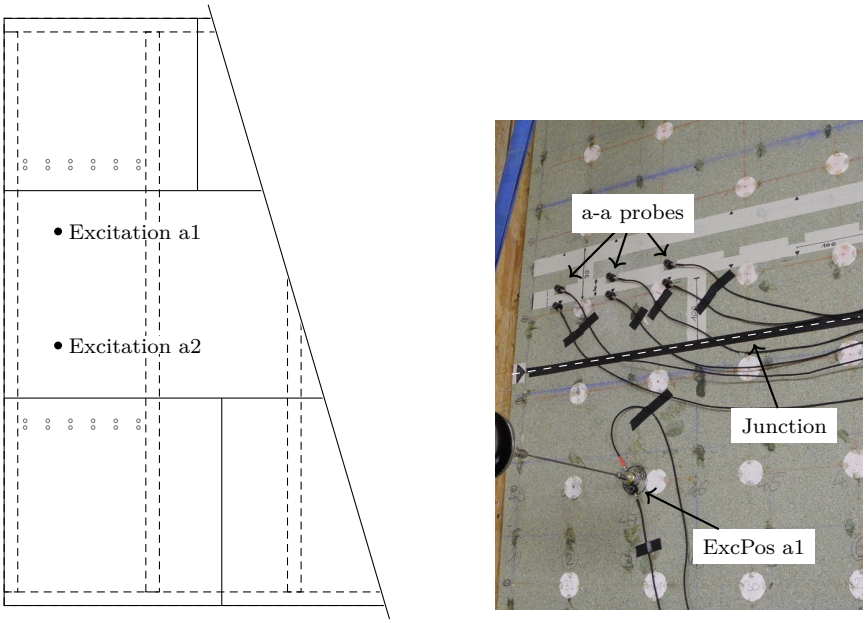

(a) Sketch of set-up (b) Photograph of set-up

Figure 5.16: Experimental set-up on the timber-frame wall in the basement of the test structure to determine the CLF of the tongue and groove chipboard joints with structural intensity.

where L is the length of the junction for which the stud spacing is 625 mm. N is the number of a-a probes along the junction line (in this case six).

The measured net power across the junction can then be used to determine the CLF. Based on the two-subsystem model shown in Figure 3.12, the net power transmitted from subsystem a to b is [e. g. see Craik et al. 1995; Hopkins 2007]

$$W_{\mathrm{net},ab} = W_{ab} - W_{ba} = \omega\,\eta_{ab}\,E_a - \omega\,\eta_{ba}\,E_b \tag{5.10}$$

This gives the CLF as

$$\eta_{ab} = \frac{W_{\mathrm{net},ab} + \omega\,\eta_{ba}\,E_b}{\omega\,E_a} \tag{5.11}$$

where the denominator is estimated from the power input, $W_{\mathrm{in},a}$, obtained from the force and velocity measured at the excitation point according to equation (3.70) as follows

$$\omega \, E_a = \frac{W_{\mathrm{in},a}}{\eta_a} \tag{5.12}$$

Additionally the power returning from subsystem b to a was neglected, which gives the following approximation for the CLF

$$\eta_{ab} \approx \frac{W_{\mathrm{net},ab}}{W_{\mathrm{in},a}} \, \eta_a \tag{5.13}$$

For the TLF, η_a, the measured data described in section 5.2.2.1 was used.

As two excitation positions and two junctions were measured, four CLFs were determined. The averaged CLF is shown in Figure 5.17 for comparison with the data obtained with free chipboard plates as described in section 5.2.3.1.

The 95 % confidence intervals overlap over most of the frequency range, indicating that the two measurements are in agreement. Towards higher frequencies the data is not shown as the results for the TLF from section 5.2.2.1 were only valid up to 1000 Hz due to mass loading effects at higher frequencies.

Due to the limited frequency range from the in-situ structural intensity measurements, the CLF used in the SEA model was taken from the free chipboard plates.

5.3 Vibrational behaviour of a timber-frame structure

The vibration field over the chipboard surface of the wall is expected to be complex due to the combination of individual chipboard plates, point connections and proximity to studs. Therefore, measurements were carried out on the double leaf timber-frame wall in the basement of the test

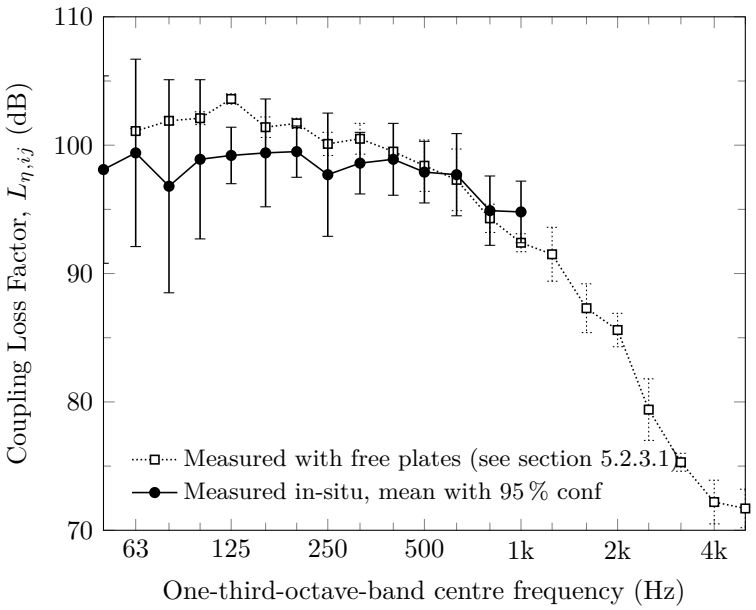

Figure 5.17: Coupling loss factor for tongue and groove joint, $L_{\eta,\mathrm{TG}}$, measured in-situ on the test structure. Additionally the TLF from Figure 5.15 is shown.

structure described in section 4.2. As machinery locally injects structure-borne sound power, point excitation was used in this study.

5.3.1 Surface velocities with force excitation

5.3.1.1 Experimental set-up

For the experimental investigations a single point excitation was applied using the electrodynamic shaker IV-40 (see Table 4.1) at one end of the wall. To investigate structure-borne sound power input and propagation, the source was first attached to the chipboard in a bay (position 1, Figure 5.18) and then above a stud at a screw position (position 2, Figure 5.18). In the bay the shaker was connected to the wall as shown in Figure 4.6. On the stud the aluminium plate was screwed through the chipboard into the studs (Figure 4.6).

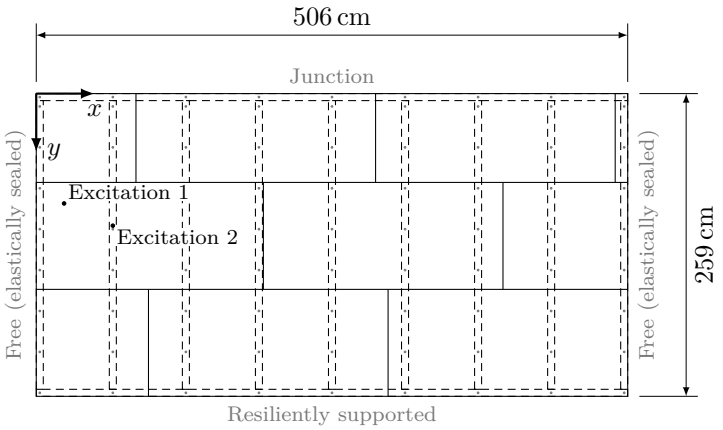

(a) Source surface

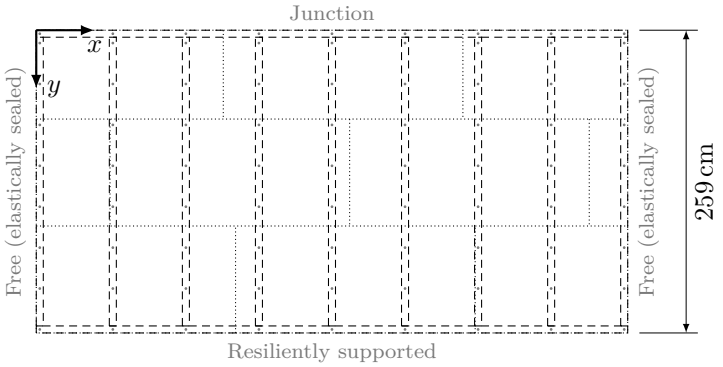

(b) Receiving surface

Figure 5.18: Construction details of the lower timber-frame wall in the test structure: Timber studs and bars (----), chipboard plates on source (——) and receiving surface (·····). Screws are indicated by dots above the wall studs. The receiving surface is visualized using the same point of a view as for the source surface (see coordinate system). Details on the boundary conditions are shown in Figure 5.19.

The vibrational response of the wall was measured with 23 g accelerometers (see Table 4.1) at the intersection points of a regular grid across the whole wall. The data was collected up to the 2500 Hz one-third oc-

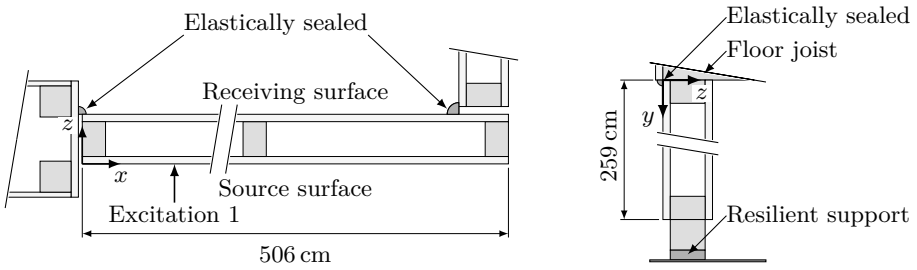

(a) Horizontal section (b) Vertical section

Figure 5.19: Sections of lower timber-frame wall of the test structure indicating details on the boundary conditions.

tave band. However from Figure 4.7 the 23 g accelerometers have an estimated error of ≈3 dB at ≈2500 Hz and a ≈1 dB error at ≈800 Hz. For the investigation of relative levels across the surface of a structure this error was tolerable because the same accelerometers were used across the surface and it is the spatial variation (rather than absolute values) that is of interest.

The same grid was used on both surfaces (source surface, Figure 5.18a and receiver surface, Figure 5.18b) of the structure. Across the length of the wall the grid spacing was 10.4 cm, hence every sixth position is above a stud as the stud spacing is 62.5 cm on centres. Across the height of the wall the positions were equally spaced with a similar distance of 11.0 cm. This results in 49×24 measurement positions for each surface. 24 accelerometers were used, so the surface velocity levels were determined in a series of measurements with a set of 12 accelerometers being moved along each wall leaf.

At the excitation point the input force was measured with a force transducer, along with the acceleration by averaging the signal from two accelerometers on either side of the force transducer. The excitation signal was white noise in order to ensure sufficient vibration level above background at all points. The S/N ratio for bay excitation is shown in Figure 5.20 for the set of accelerometers furthest from the driving point (i. e. positions vertically aligned on the far right end on the receiving

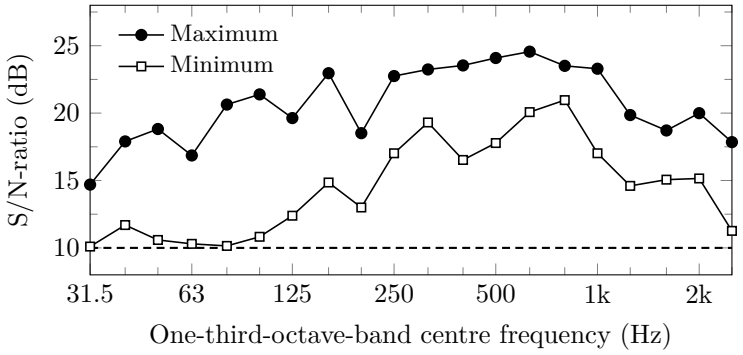

Figure 5.20: S/N ratio for the column of positions with the longest distance to the excitation position. This is the furthest right column of positions ($n = 24$) of the measured grid on the surface opposite to the excitation (receiving room). The minimum corresponds to the upper right position at 4.92 m

surface). Throughout the frequency range from 31.5 Hz to 2500 Hz the S/N ratio is >10 dB. The minimum S/N corresponds to the position at the upper end of the wall at the wall-floor-wall junction. The majority of positions were well-above 10 dB.

For this measurement the multi-channel FFT-analyser listed in Table 4.1 was used and the narrow band FFT-spectra of the accelerations were integrated to output velocities for further processing in MATLAB.

5.3.1.2 Velocity level distribution

The measured velocity levels are shown in Figure 5.21 for excitation between two studs (excitation position 1) and in Figure 5.23 for excitation above a stud. In these contour plots the velocity levels are normalized to the maximum on the source leaf, close to excitation position which was set to 0 dB. Results are shown for the 31.5 Hz, 100 Hz, 800 Hz and 2500 Hz one-third octave bands to indicate the main trends.

In the 31.5 Hz band, the velocity levels are uniformly distributed across the wall for both excitation positions. However there is a local gradient in the vicinity of the excitation in the bay (see Figure 5.21a) due to

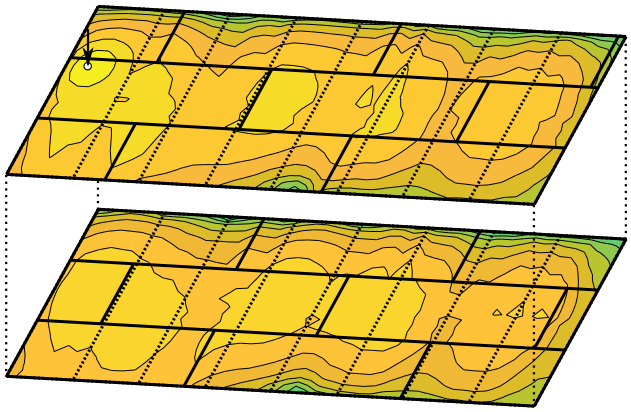

(a) 31.5 Hz

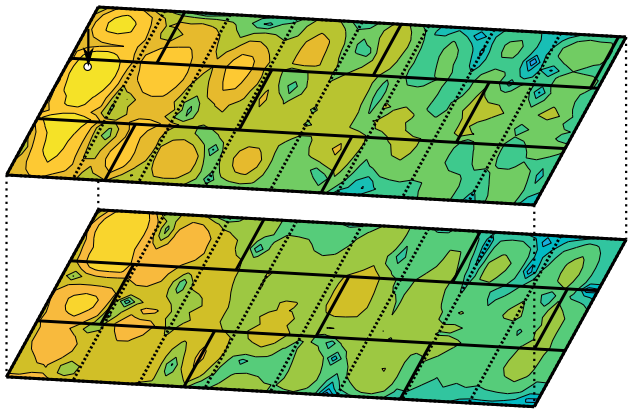

(b) 100 Hz

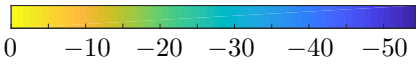

Figure 5.21: Distribution of velocity levels on both leaves of the timber-frame wall (see Figure 5.18) for 31.5 Hz and 100 Hz. The point force excitation in a bay is highlighted by the arrow in the plots. The solid lines indicate the chipboard plates, the dashed lines indicate the wall studs. For each one-third octave band the upper plot is the source surface and the lower plot is the receiving surface of the wall.

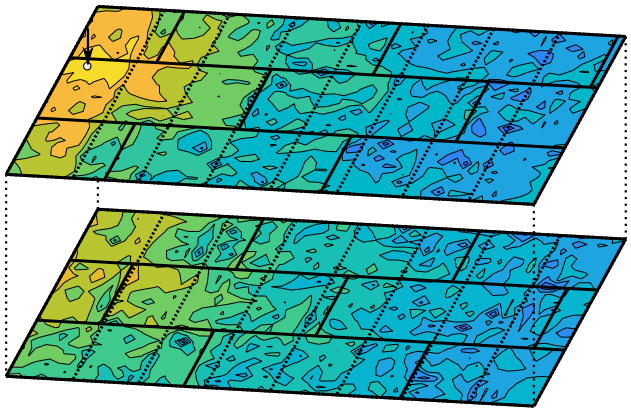

(a) 800 Hz

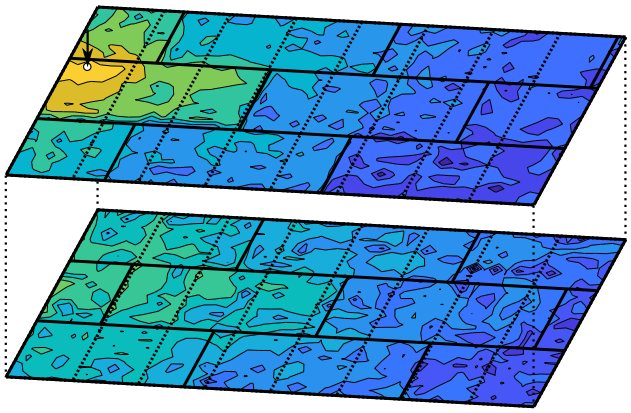

(b) 2500 Hz

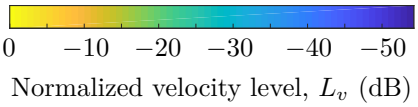

Figure 5.22: As Figure 5.21 but for the 800 Hz and 2500 Hz one-third octave bands.

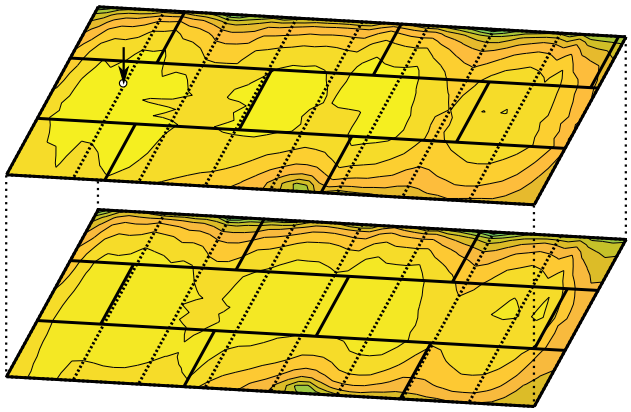

(a) 31.5 Hz

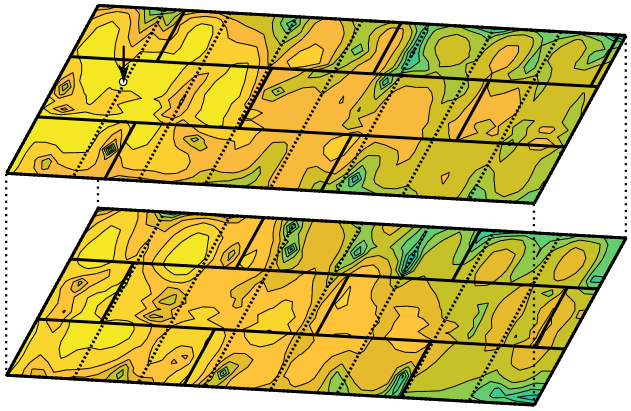

(b) 100 Hz

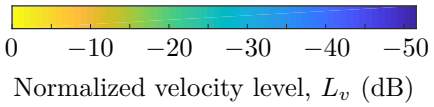

Figure 5.23: As Figure 5.21 but with excitation on a stud at a screw, indicated by the black arrow.

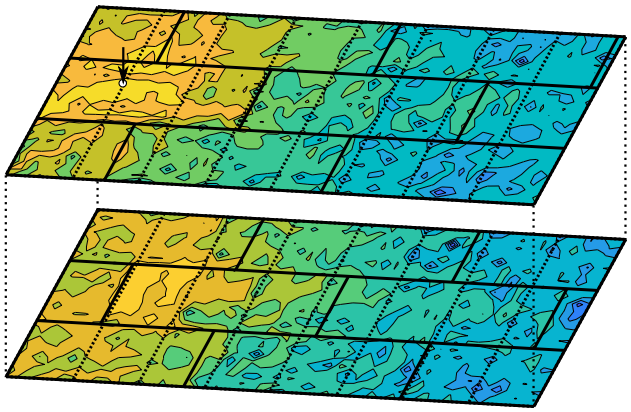

(a) 800 Hz

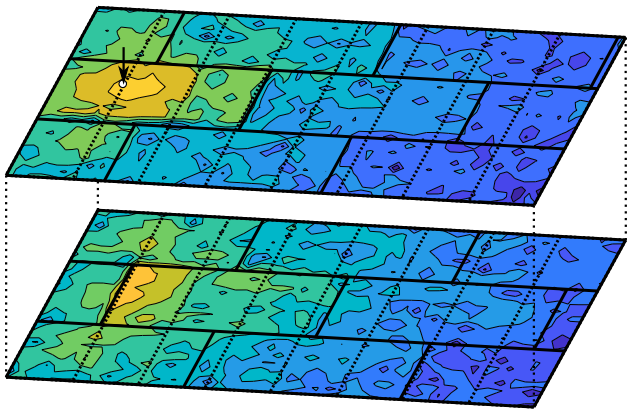

(b) 2500 Hz

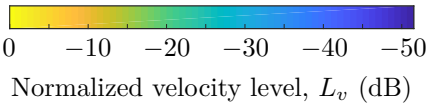

Figure 5.24: As Figure 5.23 but for the 800 Hz and 2500 Hz one-third octave bands

the direct field (see section 3.2.6). For stud excitation (Figure 5.23a), the velocity level close to the excitation point is not significantly higher compared to the rest of the wall. At the top of the wall the lowest velocity levels occur, because the displacement is constrained by the rigid T-junction (see Figure 5.19b). As the wall is free at both sides and resiliently supported at the bottom (see Figure 5.18), the velocity levels are higher at these boundaries compared to the upper end of the wall. For bay and stud excitation, there is no relation between the pattern of the contour plot and the position of the studs or the arrangement of the chipboard plates in this frequency range. Apart from the maximum in the vicinity of the excitation position, maxima occur at the same positions on the source and the receiver surface, which results in a uniform velocity level difference of approximately 0 dB. Hence the timber-frame wall behaves as a single plate at low frequencies.

For bay excitation (see Figure 5.21b) in the 100 Hz band a significant decrease of velocity levels up to ≈20 dB occurs across eight wall studs. Although a decrease is also present for stud excitation, it is not as pronounced (≈10 dB, see Figure 5.23b). From the source to the receiving surface there is a slight decrease in velocity levels, but the pattern of the contour plot differs between the source and receiving surface. For both excitation positions, low velocity levels tend to occur at stud positions. Hence the chipboard sheeting could be considered as being line-connected to the timber studs in the 100 Hz one-third octave band as noted by Nightingale and Bosmans [1999].

In the 800 Hz band (Figures 5.22a and 5.24a) there is a strong attenuation of velocity levels between 25 dB and 30 dB across the length of the wall for bay and stud excitation (see also Figures 5.25 and 5.26). For bay excitation a stronger initial decrease can be observed on the contour plots as the point force on the stud excites the framework directly and therefore the vibrational energy can travel further. Furthermore the coupling of the tongue and groove joints becomes weaker towards higher frequencies (see section 5.14); hence there are significant level differences between adjacent sheets. At 800 Hz there is no influence of the wall studs on the

velocity level distribution. Regarding the decrease of velocity levels from the source to the receiver surface, there is a significant difference between the results observed for bay or stud excitation, because the direct excitation of the stud is more efficient in terms of exciting the receiving surface as well. Therefore these velocity level differences are larger for bay excitation, especially close to the excitation position (see also Figures 5.31a and 5.32a).

With increasing losses across the tongue and groove joints, the individual chipboard sheets become clearly visible in the contour plots of the 2500 Hz band. Across the longest dimension of the wall the velocity levels are attenuated by approximately 45 dB with respect to the maximum in the vicinity of the excitation position. The velocity level distribution close to the excitation shows a direct field (see section 3.2.6). For stud excitation this local gradient is visible on the source and receiving surfaces due to the efficient coupling across the stud. On the receiving surface, the chipboard joint close to the excitation is clearly visible because the plate to the left of the excited wall stud is not screwed to the stud and therefore only excited across the tongue and groove joint.

5.3.1.3 Decay perpendicular to the timber studs

To quantify the vibrational decrease with distance perpendicular to the timber studs, normalized velocity levels are shown in Figure 5.25 for excitation in a bay and Figure 5.26 for excitation above a stud at a screw position. In these figures, vertical columns of grid positions were averaged to give 49 average velocity levels as function of the x-dimension of the test structure shown in Figure 5.18. As the vertical chipboard joints of the individual rows of plates are irregular (see Figure 5.18), only positions on the middle row were averaged as indicated in the sketch included in these figures. Additionally the corresponding chipboard joints as well as the positions of the studs are indicated.

For the 31.5 Hz band there is no significant attenuation with distance. In the 100 Hz band the minima at or close to the stud positions can be

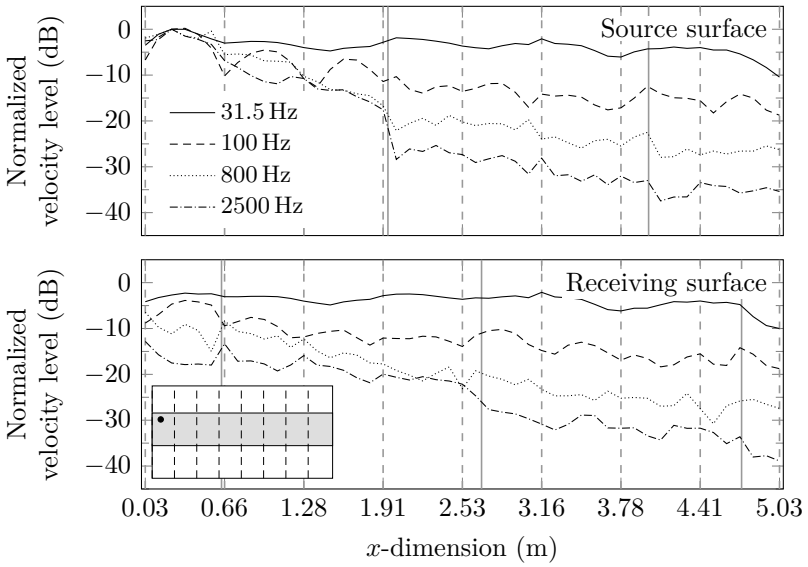

Figure 5.25: Vibration level decay perpendicular to the timber studs for the selected one-third octave bands with point excitation in a bay (black dot). The normalized velocity levels are averaged for vertical columns of grid positions across the middle row of chipboard plates (see sketch) and normalized to the column close to the excitation position. Vertical lines indicate the position of the wall studs (- - -) and tongue and groove joints (——).

observed. Towards higher frequencies the attenuation increases up to −40 dB for the positions at the far right end of the wall. The decrease in the vibration levels at the tongue and groove joints is clearly seen in the 800 Hz and the 2500 Hz bands. Close to the excitation point it can be seen that the difference between the source and receiving surface is significantly higher for bay excitation.

In the 2500 Hz band the velocity levels on the source surface tend towards a constant value in the far right area of the wall. The reason for this is not insufficient signal because the S/N ratio is >10 dB (Figure 5.20). A monotonous decrease that becomes shallower with distance is a feature of periodic structures as bending waves are converted to in-plane

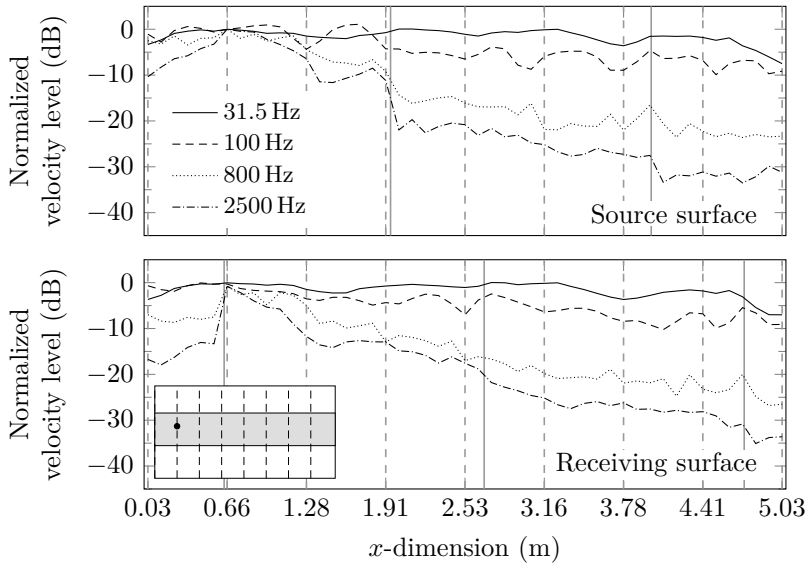

Figure 5.26: As Figure 5.25 but with point excitation on a stud at a screw (black dot).

waves and vice-versa at plate-beam junctions, as described by Mead and Markuš [1983] for semi-infinite periodic structures or Nightingale and Bosmans [1999] for a timber-frame floor assembly.

However at 2500 Hz there are point connections rather than line connections and the structure under test is finite and this behaviour can only be observed on the source surface, whereas on the receiving surface there is a continuous decrease across the whole length in the x-dimension of the wall. Hence it is likely to be a different reason than wave conversion. As the chipboard plates behave independently of the framework, the plates on the source surface can be regarded to have a free boundary condition at the far right end of the wall. The reflection of bending waves at this free edge can be a possible reason for the cessation of the continuous decrease. On the receiving surface, the elastic material is attached to the chipboard plates at the end of the wall to seal the gap (see Figure 5.19). Hence there is damping at the edge and the velocity levels continuously

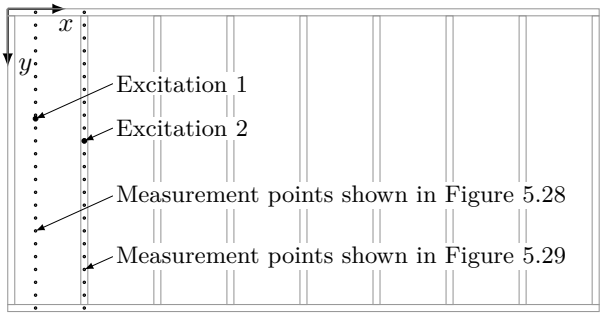

Figure 5.27: Measurement points used to investigate the attenuation of velocity levels parallel to the timber studs.

decrease towards this end of the wall. This can also be observed in the 800 Hz one-third octave band.

5.3.1.4 Decay parallel to the timber studs

Further investigations of the grid data now use lines of measurement points parallel to the timber studs. As shown in Figure 5.27 two lines are considered. One in the first bay that includes excitation position 1 and the other along the second stud where excitation position 2 was applied. The velocity levels along these lines are shown in Figures 5.28 and 5.29. Again normalized levels are used with the measurement line close to the excitation as reference.

For both excitation positions, the lower levels at the top of the wall caused by the constraint at the T-junction can be seen. Apart from the upper end of the wall, there is no significant decrease of the velocity levels for the stud excitation in the 31.5 Hz band. However, for the bay positions where only the chipboard was excited, an attenuation can be observed. In the 100 Hz band fluctuations due to modal behaviour can be observed for bay excitation, which are not as pronounced above the timber stud. Towards higher frequencies the attenuation towards the upper and lower end of the wall increases for both excitation positions. Again a drop of vibration levels across the tongue and groove joints can

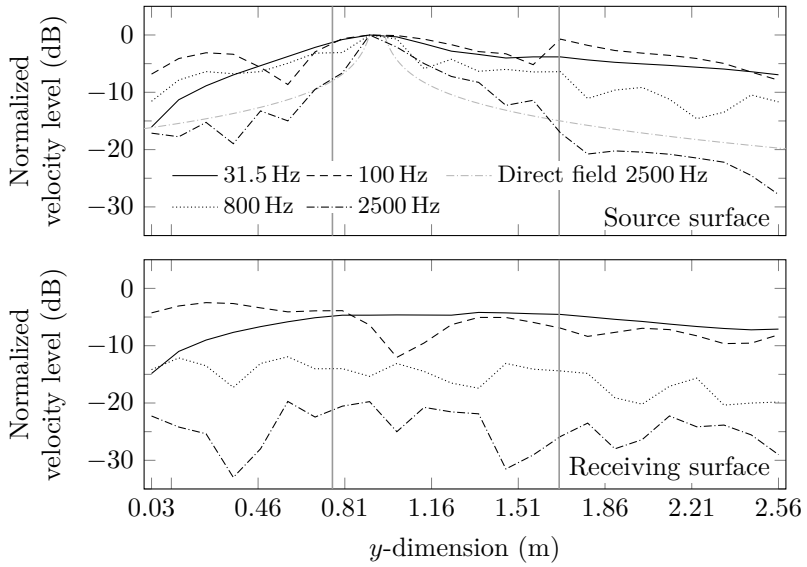

Figure 5.28: Velocity level decay parallel to the timber studs for the selected one-third octave bands and excitation in a bay. Levels for one vertical row of measurement positions in the bay with point excitation. Additionally the direct field according to equation (3.29) is shown for the 2500 Hz one-third octave band. Vertical lines (——) indicate the position of the tongue and groove joints.

be seen in the 2500 Hz band. However, the measured data in the 2500 Hz indicates the direct field of a chipboard plate.

The decrease in vibration from the source to the receiving surface is significantly higher for bay excitation especially towards higher frequencies as the the transmission path across the cavity is less efficient compared to the structural transmission path across the stud.

5.3.1.5 Discussion

The influence of the framework and the screw fixing of the chipboard panels on the vibrational behaviour can be interpreted by considering three frequency regions [see Nightingale and Bosmans 1999; Craik and Smith 2000b; Schoenwald 2008]. These can be defined by the relation of

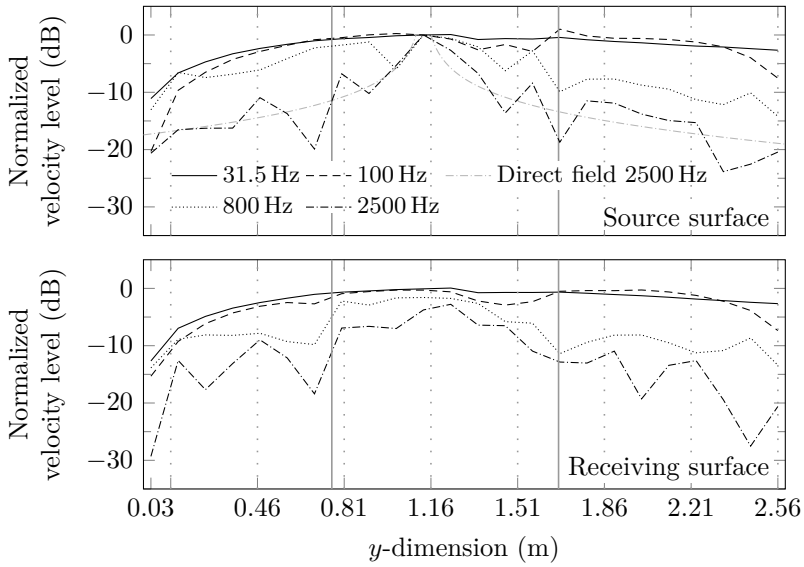

Figure 5.29: Velocity level decay parallel to the timber studs for the selected one-third octave bands and excitation on a stud. Levels for the vertical row of measurement positions on the stud with point excitation. Additionally the direct field according to equation (3.29) is shown for the 2500 Hz one-third octave band. Vertical lines indicate the tongue and groove joints (——) and the screw fixing points on the stud (· · · ·).

the bending wavelength of the 19 mm chipboard plates to the stud and screw spacing as shown in Figure 5.30

I) $\lambda_{B,p}/2 >$ Stud spacing (62.5 cm)
At very low frequencies (below the 50 Hz band) the velocity levels are distributed uniformly across each leaf that forms the surface of the framework wall. The framework underneath the sheeting can not be identified in the contour plots of the velocity level distribution (see Figures 5.21a and 5.23a). In this lower frequency range, the timber-frame wall can be regarded as an equivalent orthotropic plate.

II) Stud spacing (62.5 cm) > $\lambda_{B,p}/2$ > screw spacing (35 cm)
In the one-third octave bands from approximately 50 Hz to 160 Hz, low velocity levels tend to occur above the studs. Hence there is only a local influence of the timber studs on the stiffness of the construction in a region where they can be considered to be line-connected to the chipboard plates. At line-connected junctions, wave conversion from bending to in-plane waves and vice-versa can potentially occur [Nightingale and Bosmans 1999]. This typically causes a significant decrease across the first stud that levels out with increasing distance as observed by Nightingale and Bosmans [1999] and Schoenwald [2008] because the accelerometers are orientated to measure out-of-plane displacements caused by bending waves.

III) Screw spacing (35 cm) > $\lambda_{B,p}/2$
As the chipboard is fixed to the studs with screws there is an upper limit for these approximately periodic point connections to act as line connections, which can be estimated as $\lambda_{B,p}/2$ [Nightingale and Bosmans 1999; Craik and Smith 2000b; Schoenwald 2008]. The screw spacing is 35 cm which relates to $\lambda_{B,p}/2$ on the chipboard at approximately 140 Hz. Hence above this frequency, no significant differences occur between levels in a bay or above the studs. The vibration field on the chipboard can be considered to be independent of the timber framework underneath.

These frequency regions approximately describe the vibrational behaviour, although the cross-over frequencies between the regions are not precise. The cross-over frequency between region II and III is typically higher for real building structures, as the screws do not represent an ideal point connection but a local area connection [Nightingale and Bosmans 1999]. Therefore the screw distance needs to be regarded as being smaller than the actual measure. However the type of screw or craftsmanship will influence the size of this local area, hence it is difficult to quantify a radius for the local constraint.

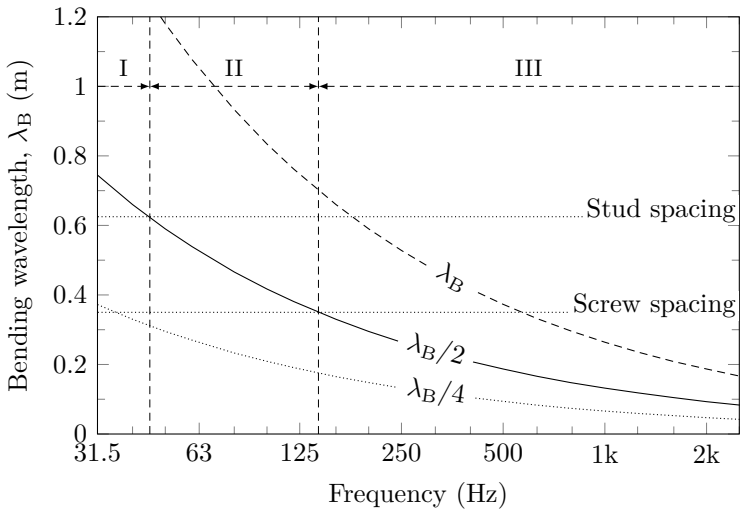

Figure 5.30: Bending wavelength of 19 mm chipboard in relation to the geometrical properties of the timber-frame test structure.

Although the observed vibrational behaviour shows some features that are typical for exactly periodic structures, these characteristics are not clearly pronounced and other features such as an increase of levels in remote bays due to conversion from in-plane to bending waves do not occur. Hence this timber-frame wall tends to behave like a non-periodic structure as there are some inherent irregularities.

Although the stud and screw spacing is meant to be the same across the structure, there are variations due to craftsmanship (i. e. tightening torque of the screws). Furthermore there are tongue and groove joints which means that the periodic structure is interrupted after every two or three studs. In addition it can not be assumed that there are exactly the same material properties for the repeating studs and plates as there are slight variations that can be seen in the 95 % confidence intervals given in Table 5.2.

5.3.2 Coupling between both leaves of the wall

5.3.2.1 Velocity level difference

Besides the attenuation with distance perpendicular to the studs, the coupling of both leaves is of particular interest in terms of sound transmission to adjacent rooms but also for the definition of subsystems when modelling the sound transmission using SEA.

The measured velocities from the previous section are now used to investigate the coupling between both leaves. Figures 5.31 and 5.32 show the difference of the measured velocity levels on the source and receiving surface. As the same grid was used on both sides of the wall the difference was calculated for each opposite pair of velocities and visualized using contour plots. The differences are shown for the same selected one-third octave bands as in Figures 5.21 and 5.23.

In the 31.5 Hz band the velocity level difference is ≈0 dB across the whole wall. For bay excitation there is a local gradient caused by the direct field on the source leaf, which results in a circular pattern of higher level differences in the vicinity of the excitation position. As there is strong structural coupling across the stud this can not be seen for the excitation above a stud.

In the 100 Hz band the level difference spatially varies across the wall. Hence the vibration pattern differs between the source and receiving surface, indicating that the wall does not behave as one single plate any more.

In the 800 Hz band a higher difference can be observed in the far left bay. However, for the rest of the wall surface the velocity level differences are ≈0 dB. For stud excitation this holds for the whole wall as the structural transmission path across the excited stud is very efficient because it is additionally at a fixing point and therefore provides similar power input to both leaves.

At high frequencies, in this case represented by the 2500 Hz band, the chipboard plate boundaries on both leaves can be identified in the contour plot of the velocity level differences. Again significant differences

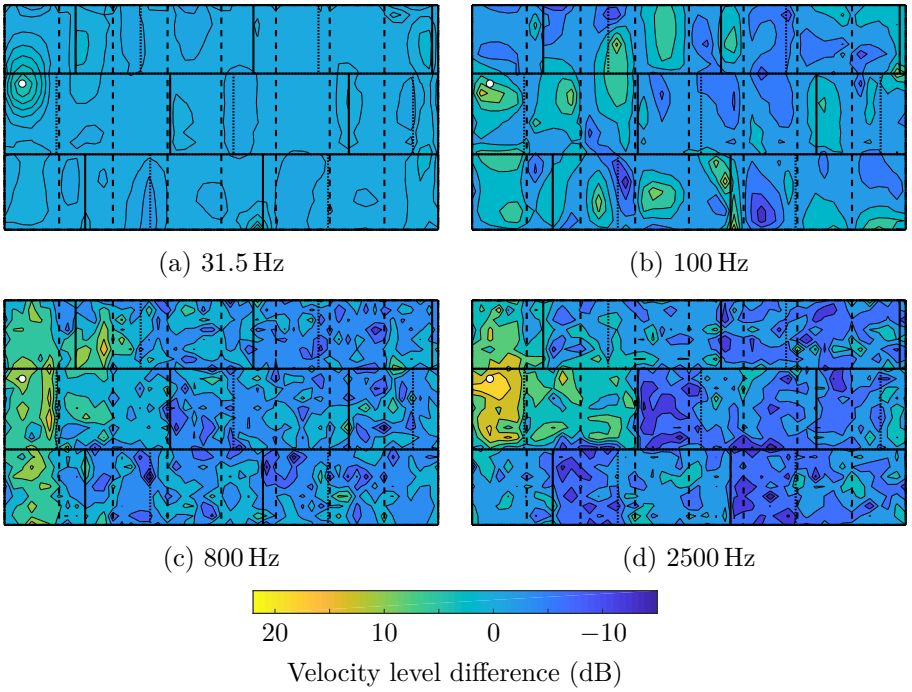

Figure 5.31: Velocity level difference between the source and the receiving surface of the test structure for bay excitation. Dashed lines indicate the wall studs. Solid lines show the tongue and groove joints on the source surface the dotted lines for the receiving surface. The excitation point is indicated as small white circle.

can be observed for bay excitation close to the excitation point which is not as pronounced with stud excitation. For both excitation positions, some areas described by boundaries of chipboard plates show higher levels on the receiving leaf (negative velocity level difference). To explain this, Figure 5.33 shows four possible transmission paths from the local point excitation to a pair of accelerometers. This example shows that transmission paths to the accelerometer on the receiving surface include no tongue and groove joint and are therefore potentially more efficient at high frequencies where the coupling of the plates is weak. Hence to any remote pair of accelerometers there are many transmission paths and

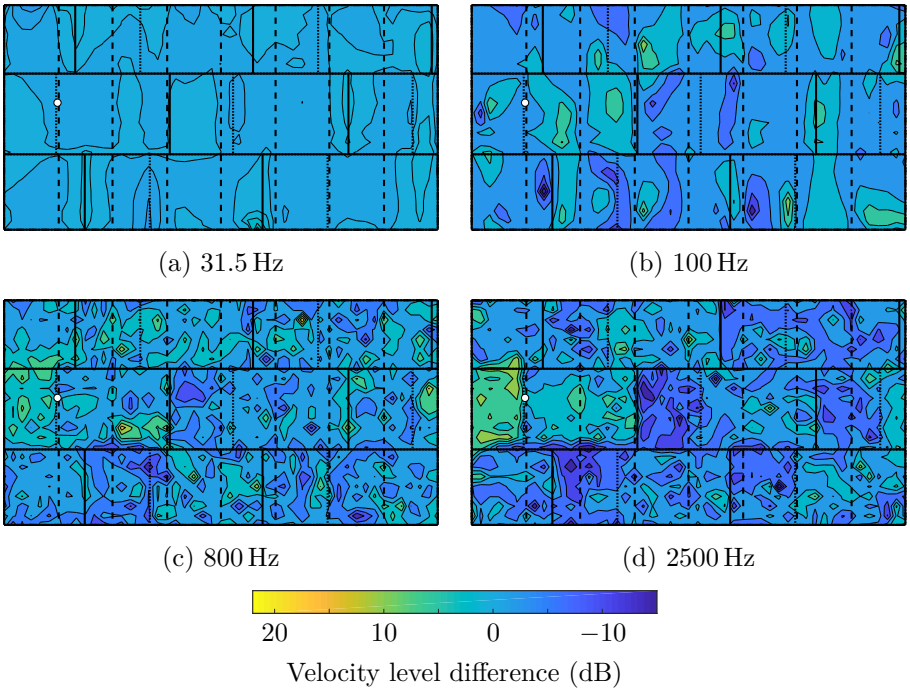

Figure 5.32: As Figure 5.31 but for excitation on a stud at a screw.

therefore the velocity level difference tends to fluctuate about 0 dB across the whole wall except close to the excitation point.

The leaves of double walls are strongly coupled at the mass-spring-mass resonance frequency, f_{msm}. For empty cavities it can be calculated using [e. g. see Hopkins 2007] by assuming adiabatic compression, $\gamma = 1.4$ and a temperature of 20 °C.

$$f_{\mathrm{msm}} = 60 \sqrt{\frac{m''_1 + m''_2}{m''_1 \, m''_2 \, L_z}} = 60 \sqrt{\frac{2 \, m''_{\mathrm{chip}}}{m''^2_{\mathrm{chip}} \, L_z}} \tag{5.14}$$

where m''_{chip} is the mass per unit area of the 19 mm chipboard plates and L_z the cavity depth. Using the properties given in Table 5.2 and the cavity width of 90 mm, this results in a mass-spring-mass resonance frequency of 83 Hz for the test structure. Above f_{msm}, direct coupling

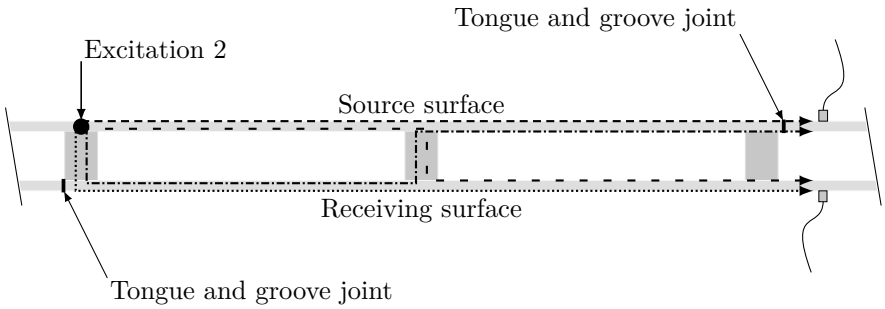

Figure 5.33: Four possible structural transmission paths on the timber-frame wall from excitation position 2 (see Figure 5.18) to a remote pair of accelerometers.

across the cavities is weak. Therefore the contour plot of the level differences in the 100 Hz one-third octave band is not as uniform as in the 31.5 Hz band. This is also the reason for the increasing level difference with increasing frequency in the first bay for excitation between timber studs.

5.3.2.2 Correlation analysis

In the previous section the coupling was investigated using the velocity level difference. This gives information about the attenuation of vibrational energy across the constructions. But there is no information about the correlation of both wall surfaces. Hence further processing used complex narrow band data to investigate the phase relationship between the source and receiving surfaces.

In the grid measurements the input force was used as reference to determine a set of complex FRFs. Using this data, opposite pairs of measurement positions on the source and receiving surface can be considered in terms of their phase relation. This allows the Frequency Response Assurance Criterion (FRAC) to be used to quantify the correlation of both leaves based on the complex FRFs. The FRAC is described by Allemang [2003] and is calculated using

$$FRAC_{ab}(f) = \frac{\left| \sum_{x=1}^{N_x} \sum_{y=1}^{N_y} Y_a(x,y,f)\, Y_b{}^*(x,y,f) \right|^2}{\left[\sum_{x=1}^{N_x} \sum_{y=1}^{N_y} Y_a(x,y,f)\, Y_a{}^*(x,y,f) \right] \left[\sum_{x=1}^{N_x} \sum_{y=1}^{N_y} Y_b(x,y,f)\, Y_b{}^*(x,y,f) \right]} \tag{5.15}$$

where the complex transfer mobilities $Y_a(x,y,f)$ and $Y_b(x,y,f)$ of the measurement grid (x,y) represent the (a) source surface and (b) receiving surface respectively. A value of exactly unity means that all pairs of measurement positions are in phase whereas zero implies that the vibrational behaviour of both leaves is uncorrelated.

Figure 5.34 shows the FRAC for bay and stud excitation including all positions on the measured grid of the source and receiving surface. The uniform vibrational behaviour of the whole wall at low frequencies is evident where the FRAC has values close to unity, which implies correlation of both wall surfaces. For bay excitation the value is slightly lower than for stud excitation due to the direct field of the point force that dominates the response in the first bay. Above the mass-spring-mass resonance frequency (83 Hz), the FRAC values drop down below 0.2. Hence the modal response becomes increasingly incoherent towards higher frequencies. When modelling the wall using SEA, this means that above the 80 Hz band, both wall surfaces can be considered as individual subsystems.

5.3.3 Structural intensity with force excitation

The time-average surface velocity levels give information about the distribution of vibrational energy. To visualize net-power flow across the test structure, the structural intensity was measured following the procedure described in section 4.5.3.

A set of twelve a-a structural intensity probes was used with the multichannel FFT-analyser listed in Table 4.1. For the measurements, the 23 g

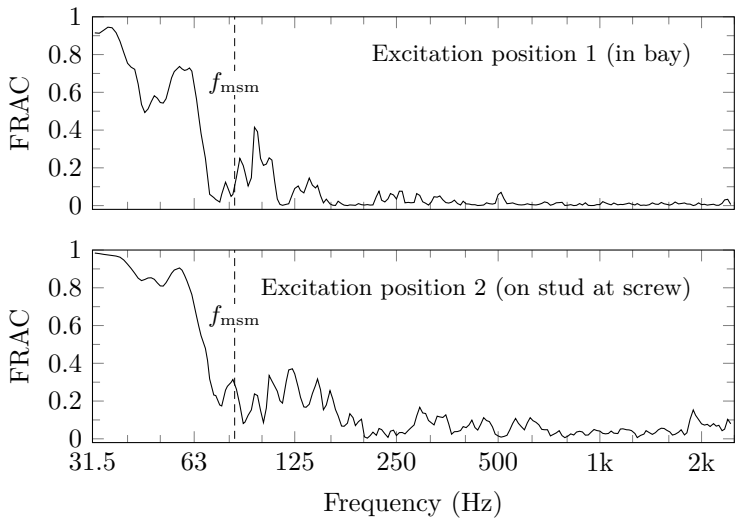

Figure 5.34: Frequency Response Assurance Criterion (FRAC) for both leaves of the wall.

accelerometers were used. Due to mass loading at high frequencies the data was valid up to the 800 Hz one-third octave band.

Using these a-a probes, the two dimensional structural intensity was determined on a grid of 32×18 positions across the source surface of the timber-frame wall shown in Figure 5.18a. Therefore two probes were mounted at each position as sketched in Figure 4.10. As the procedure described in section 4.5.3 is only valid in the free-field, positions above studs were omitted. Hence in each bay there were 4×18 positions where the nearest distance to wall studs was 10 cm. The probe spacing, d was 3.3 cm to allow the processing of data to higher frequencies. The wall was excited the same way as described in section 5.3.1.1 in a bay (excitation position 1 in Figure 5.18a).

The results are presented in Figure 5.35 for the same one-third octave bands as in Figures 5.21, 5.23, 5.31 and 5.32. The 2500 Hz band is not shown as the grid of the structural intensity probes is too coarse to interpret the pattern of intensity vectors and mass loading might affect the results. The figures show the intensity vectors to indicate the direction

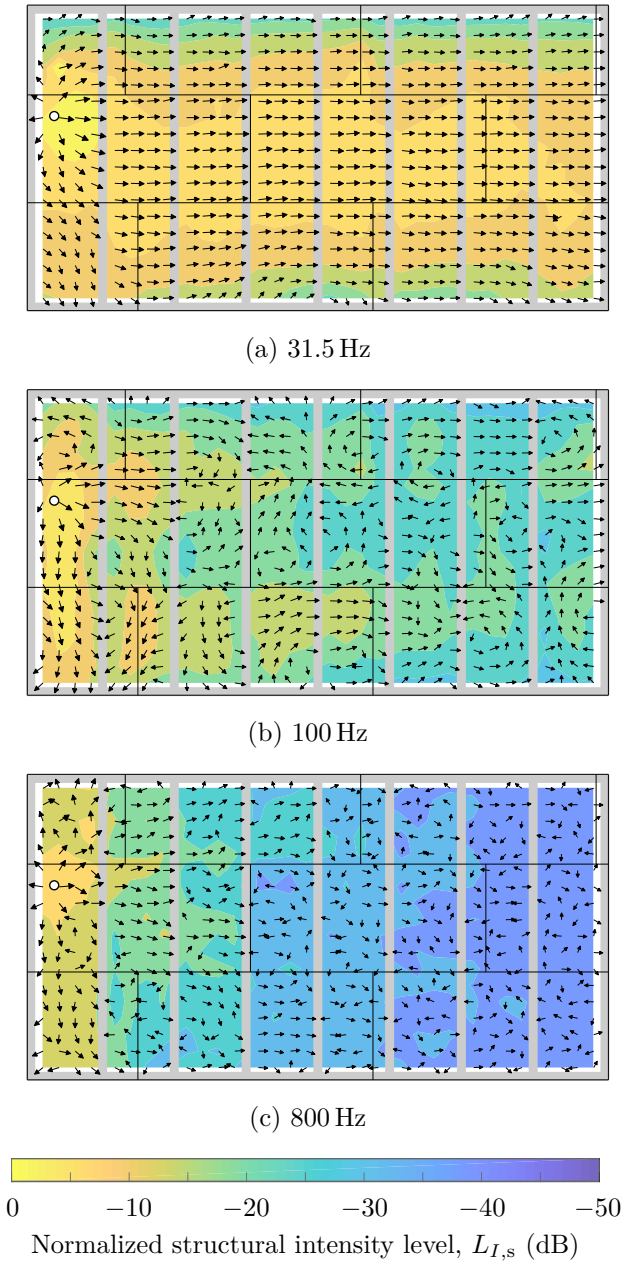

(a) 31.5 Hz

(b) 100 Hz

(c) 800 Hz

Figure 5.35: Measured structural intensity vectors on the test structure. The point excitation is indicated by the white circle. The thick grey lines indicate the wall studs. The thin black lines indicate the the tongue and groove joints.

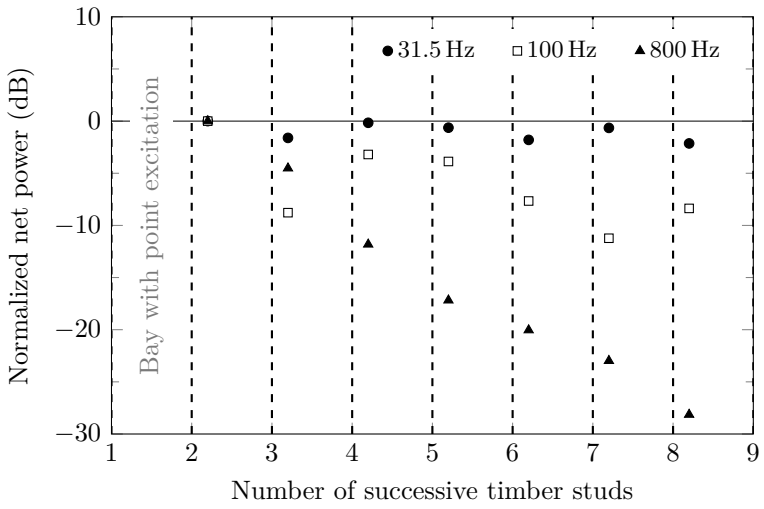

Figure 5.36: Power input into successive bays of the test structure using the sum of the one-third octave band x-components to the right of each stud from Figure 5.35.

of the net-power flow. Although the length of the vectors represents the magnitude, a contour plot of the normalized intensity level was added behind the vectors to clarify the strength of the power flow.

The structural intensity data was also used to quantify the power input into each successive bay. Therefore the x-components of the structural intensity (perpendicular to the wall studs) at positions to the right of wall studs were integrated (summed) over the height of the wall. The results are shown in Figure 5.36, normalized to power input in the second bay. The first bay was omitted as the point excitation was applied there.

In the 31.5 Hz band, all vectors shown in Figure 5.35a are oriented perpendicular to the wall studs beginning in the second bay with maximum power flow towards the middle axis of the wall. There is no significant decrease of the net power flow across the studs as also indicated in Figure 5.36.

In the 100 Hz band, circulating vectors indicate a vibrational behaviour dominated by standing waves (modes) [Tanaka et al. 1994]. The magnitude of the intensity vectors decreases by ≈20 dB across the wall.

In the 800 Hz band, the chosen grid spacing is too coarse to allow a proper interpretation of direction of the structural intensity vectors. However the magnitudes indicate a strong and continuous decrease across the length of the wall. In Figure 5.36 it can be seen that the decrease of the power input into each successive bay is ≈5 dB on average.

The results indicate that at low frequencies the whole wall can be considered as a single SEA subsystem. Whereas towards high frequencies the wall needs to be subdivided into several subsystems; these subsystems could be individual bays as indicated by the results for the 800 Hz band in Figure 5.36.

5.3.4 Discussion

The investigations on the vibrational behaviour of the timber-frame wall of the test structure show the typical characteristics of an inhomogeneous ribbed structure. For local mechanical excitation the propagation of vibrational energy is strongly attenuated caused by internal damping of the materials and at structural discontinuities such as junctions between plates and timber studs and the tongue and groove chipboard joints. As reported in previous work [e. g. Nightingale and Bosmans 1999; Craik and Smith 2000b; Schoenwald 2008], three frequency regions can be identified to interpret the vibrational behaviour. At very low frequencies a single orthotropic plate can be assumed followed by a regime that resembles the behaviour of line connected plates. The majority of the frequency range however indicates the behaviour of line-connected chipboard plates.

In the line-connected regime, wave conversion from bending to in-plane waves and vice versa can potentially occur [Nightingale and Bosmans 1999]. There is however no strong evidence for this behaviour from the presented results. Furthermore the structure does not distinctly show typical characteristics of perfectly periodic structures described by Mead and Markuš [1983] for example. This is potentially due to irregularities

inherent in normal building structures caused by craftsmanship and a variation in material parameters.

For local point excitation, the level difference between the excited leaf and the opposite leaf is not significant except in the area close to excitation point for bay excitation. The structural path across a position where the sheeting plates are fixed to the framework is very efficient. Therefore the power input to the receiving surface is similar as to the source surface for excitation positions above a stud at a screw. However both surfaces have uncorrelated vibration fields above the mass-spring-mass resonance as shown by the FRAC.

These results give indications about the choice of SEA-subsystems to model the dynamic response of this wall. At low frequencies the whole wall can be considered as a single subsystem. As both wall surfaces are uncorrelated above the mass-spring-mass resonance, they need to be modelled as individual subsystems. Furthermore the results indicate, that the individual leaves can not be modelled as one subsystem. In the mid frequency range, the individual bays could be used as subsystems based on the findings from the structural intensity measurements. However at high frequencies, there is a weak coupling across the tongue and groove joints and therefore it might be necessary to treat each chipboard sheet as an individual SEA subsystem.

5.4 Mobility of the test structure

The mobility (or impedance respectively) is an important quantity to determine the power input of a mechanical source to a receiving structure. As the framework of the regarded timber-frame structures causes a spatial variation of the structural properties, the mobility of the test structure is determined experimentally at various positions to investigate its range.

Structure-borne sound sources potentially excite the structure not only by a force component perpendicular to the surface but also by in-plane forces or by moments for three degrees of freedom. In this thesis only out-of-plane components are considered. Hence the experimental inves-

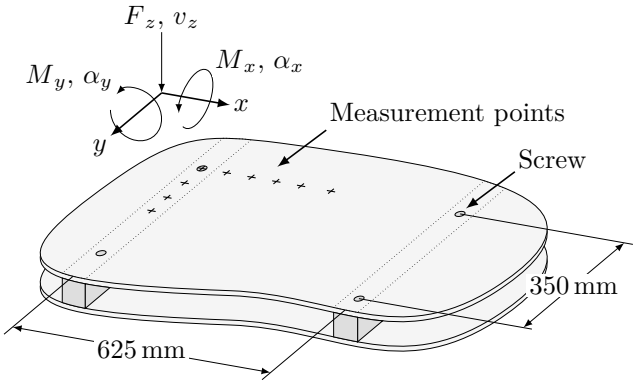

Figure 5.37: Measurement points and direction conventions for investigations of the spatial variation of point mobilities on the timber-frame wall.

tigations concerning the driving point mobility, Y_{dp}, as well as the out-of-plane moment mobilities, $Y_{\mathrm{M}x}$ and $Y_{\mathrm{M}y}$, are presented in the following sections. To model the mobility of the structure at these frequencies the properties of an equivalent orthotropic plate can be used, that accounts for the different bending stiffness parallel and perpendicular to the studs. For the equivalent orthotropic plate the mobility can then be calculated according to equation (3.55).

5.4.1 Driving-point mobility (force)

To investigate its spatial variation, the driving-point mobility was measured at various positions on the test structure following the procedure described in section 4.5.4 with the instrumented hammer listed in Table 4.1. Therefore the mobility was determined at positions above a wall stud and at positions towards the centre of a bay as indicated in Figure 5.37. Although this drawing shows the timber-frame wall, the measurements points on the timber-joist floor were chosen in the same way.

To interpret the results, infinite beam and plate mobilities according to sections 3.2.9.3 and 3.2.4 are compared with the measurements. The following infinite beam and plate mobilities were considered:

a) Infinite plate according to equation (3.55) for 19 mm chipboard (material properties given in Table 5.2).

b) Infinite beam according to equation (3.57) for the wall studs with a cross section of 60 mm × 90 mm and floor joists with a cross section of 60 mm × 240 mm (material properties given in Table 5.2).

c) Infinite plate according to equation (3.55) using the properties of the equivalent orthotropic plate described in section 3.2.4.

Figure 5.38 shows the measured driving point mobility for one position above a stud and at a screw as well as for one position right in the middle of two studs. The results for similar positions on the timber-joist floor are shown in Figure 5.39.

At low frequencies, below the 63 Hz one-third octave band, the measured mobilities are similar for the stud and the bay position. This is in-line with the findings from section 5.3.1 which showed that the test structure behaves like a single plate at low frequencies. Mayr [2009] noted that above or close to a stiffening rib the mobility can be approximated by the infinite beam mobility of the rib at low frequencies.

For the timber-frame wall the measured mobility lies between the mobility for an infinite equivalent orthotropic plate and the infinite beam mobility for the wall stud below the 63 Hz band. As mentioned in section 3.2.4 the properties of the equivalent orthotropic plate must be regarded as an upper limit due to the potentially small shear deformation allowed by the screw connections. Hence the mobility of this infinite equivalent orthotropic plate is expected to be lower than the actual value and as indicated by the results in Figure 5.38 it can be regarded as a lower limit. The infinite beam mobility only represents the wall stud, neglecting the influence of the chipboard above it; hence it should be regarded as an upper limit for the mobility. For the timber-frame wall

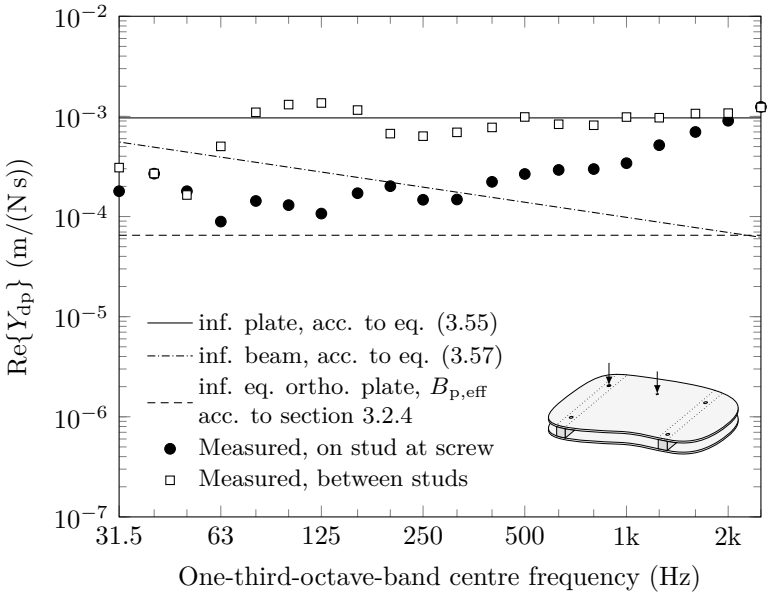

Figure 5.38: Real part of driving point mobility of the timber-frame wall for one position above a stud at a screw and one position in-between two studs.

with narrow 90 mm studs and 19 mm plates on both sides, the true value is expected to be significantly lower than the infinite beam mobility of the wall stud. Additionally it should be noted that although the results are shown in one-third octave bands the number of modes in each band is low at low frequencies. Hence there are modal fluctuations in the measured data that potentially causes discrepancies when comparing it with infinite beam/plate theory.

For frequencies above the 63 Hz band the mobility between the studs has similar values to an infinite 19 mm chipboard plate. The position above a stud at a screw fluctuates about 1×10^{-4} m/(N s) up to ≈315 Hz. Towards higher frequencies it also tends towards the values for the infinite 19 mm chipboard plate. This is also supported by the findings from section 3.2.4 that showed point-connected behaviour of the sheeting at high frequencies.

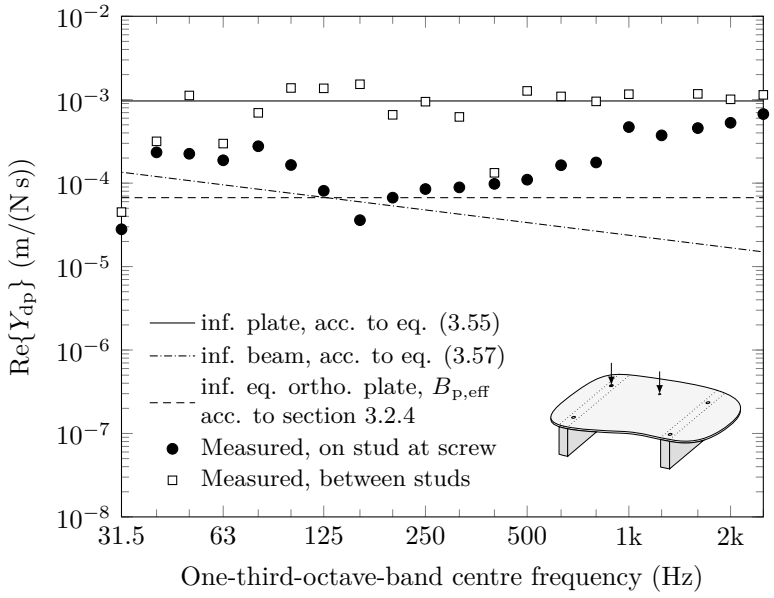

Figure 5.39: Real part of driving point mobility of the timber-joist floor for one position above a stud at a screw and one position in-between two studs.

For the timber-joist floor (Figure 5.39), the mobility of the infinite beam is significantly lower, because the depth of the floor joists is large compared to the wall studs. The influence of the chipboard on the bending stiffness is smaller as only one layer is screwed on top of the joists. Hence the value for the mobility of an infinite equivalent orthotropic plate is in the same range as the infinite beam mobility for the 240 mm floor joist. The trend of the measured data follows the infinite beam mobility in the low frequency range. This is similar to findings from Hammer and Brunskog [2002], Hopkins [2007], and Mayr [2009] on ribbed timber structures or Nightingale and Bosmans [2007] for a ribbed perspex structure.

As for the timber-frame wall, the position in the bay shows values in the range of the infinite 19 mm chipboard plate at mid and high frequencies. The position on the stud at a screw is in the range of the equivalent

orthotropic plate in the mid-frequency range up to about 500 Hz and tends towards the infinite 19 mm chipboard plate at high frequencies.

Figure 5.40a shows the measured mobilities for different distances to the wall stud at the measurement points indicated in Figure 5.37. At low frequencies all positions are similar and tend towards the mobility of an infinite 19 mm chipboard plate at high frequencies. For positions that are further away from the wall stud, the mobility starts increasing at lower frequencies. Similar findings were observed by Mayr [2009] for a timber-joist floor. Therefore the same non-dimensional plot as used by Mayr is shown in Figure 5.40b for the measured data. The measured mobilities are normalized to the value for an infinite 19 mm chipboard plate and plotted as a function of the ratio of the distance to the bending wavelength of the 19 mm chipboard.

This shows that positions with a distance, $d > \lambda_B/4$, follow the behaviour of an infinite plate with the properties of the sheeting material which confirms theoretical work by Lin and Pan [2006]. Mayr [2009] showed for a timber-joist joist floor, that the same behaviour can be observed for positions above a stud with varying distance to a screw. Similar measured data is shown for the timber-frame wall of the test structure in Figure 5.41a (measurement positions given in Figure 5.37). Again there is a logical rank order of the data in the mid and high frequency range with values increasing with the distance from the screw. However the relationship with the d/λ_B ratio, shown in Figure 5.41b, does not show the same clustering as for the positions in the bay.

This is potentially due to the assumption of an ideal point connection. However on the building structure, there are variations in the type of the screw or the tightening torque, which have an influence on the behaviour of the sheeting plate in the vicinity of the fixing point. Hence the area of the local constraint is prone to vary depending on these parameters Therefore it is difficult to identify one specific value for the distance, d, between the observation point and the fixing point as this is more a local area than a defined point [see Nightingale and Bosmans 1999]. This might explain the difficulties in the interpretation of the measured mobilities

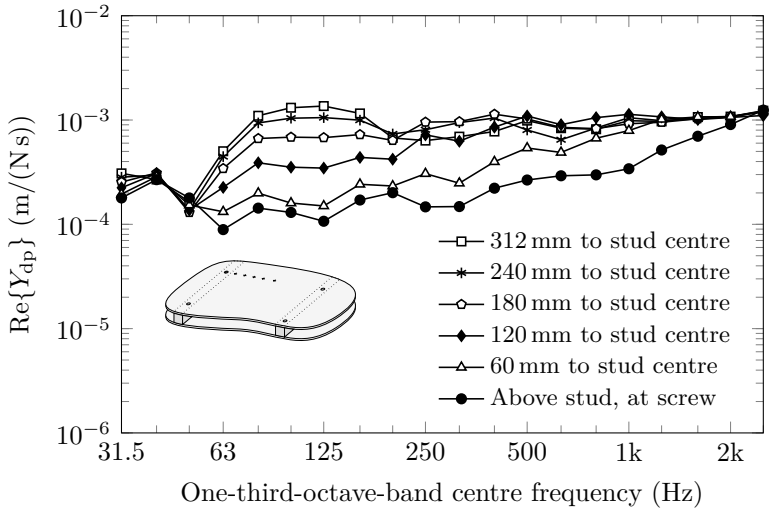

(a) Real part of driving point mobility.

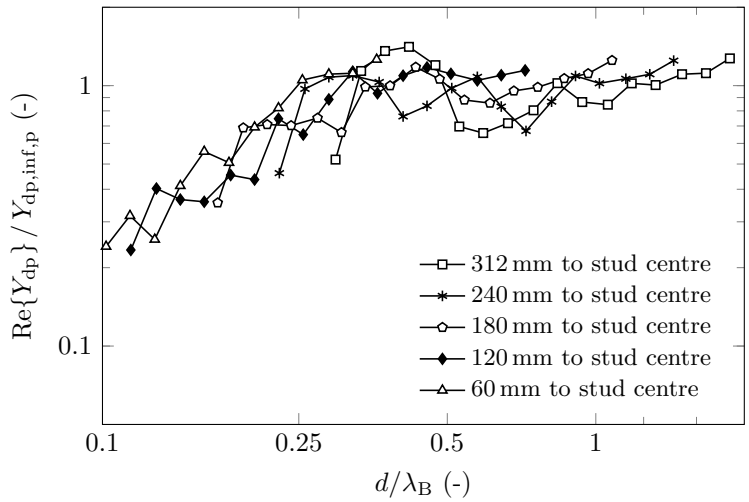

(b) Non-dimensional diagram for one-third octave bands from 63 Hz to 2.5 kHz. For $Y_{\mathrm{dp,inf,p}}$ and λ_{B} the properties of 19 mm chipboard (see Table 5.2) were used.

Figure 5.40: Spatial variation of driving point mobility along a line perpendicular to the stud. Positions between studs. Variation of the distance to the closest stud centre line.

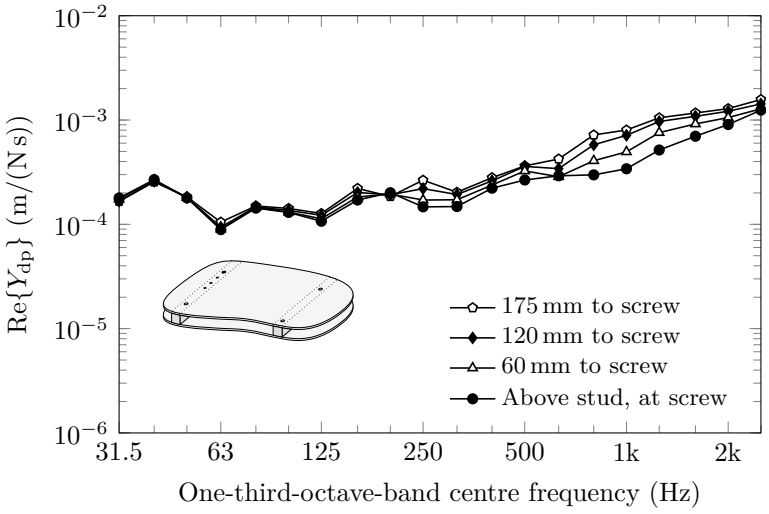

(a) Real part of driving point mobility.

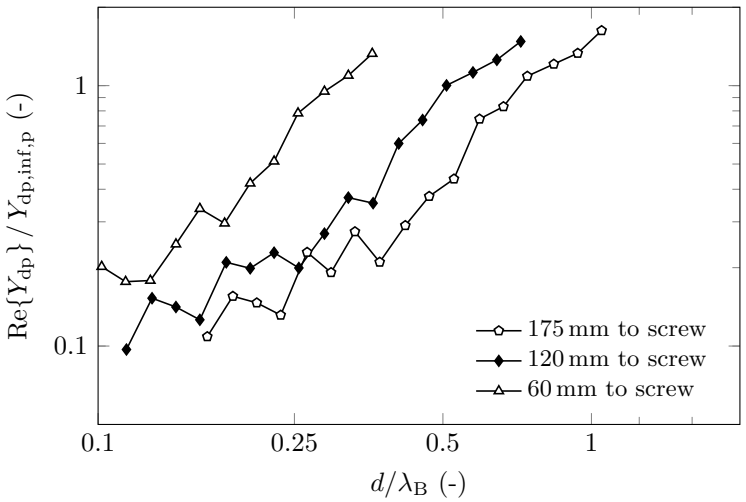

(b) Non-dimensional diagram for one-third octave bands from 63 Hz to 2.5 kHz. For $Y_{\mathrm{dp,inf,p}}$ and λ_{B} the properties of 19 mm chipboard (see Table 5.2) were used.

Figure 5.41: Spatial variation of driving point mobility on a line on top of the stud. Positions above stud. Variation of the distance to the closest screw.

as a function of the d/λ_B ratio for positions above a stud, shown in Figure 5.41b for the data obtained on the test structure regarded in this thesis. On the other hand, positions in the bay are not as dependent on the stud. Therefore the position of the fixing point and the distance, d, are well defined, with half the stud width being the maximum uncertainty. Hence the interpretation based on the d/λ_B ratio is more robust as shown in Figure 5.40b. This was not investigated further in this work, however future work could look at the variation of tightening torque of the screw on the spatial variation of the mobility.

5.4.2 Moment mobility

Typically only perpendicular force excitation is considered in building acoustics. However, in lightweight building structures moment excitation potentially needs to be considered as well. Therefore the moment mobility of the test structure was determined experimentally following the procedure described in section 4.5.5.

Various positions on the timber-frame wall and floor of the test structure were used as shown in Figure 5.37 (this figure also shows the direction conventions for the moment mobilities). The measured results were compared with infinite plate and beam mobilities using the three cases described in section 5.4.1.

Figure 5.42 and Figure 5.43 show the results for the timber frame-frame wall for the moment about the x- and y-axis respectively. For the moment about the x-axis, there is a significant difference between the position above a stud and in the middle of a bay at mid and high frequencies, similar to the driving-point mobilities shown in Figure 5.38. At low frequencies both positions have similar values and are in the range of the mobility for an infinite beam with the properties of the wall stud. Above 100 Hz, the position between the studs tends towards the mobility of an infinite plate with the properties of the 19 mm chipboard plate. However, the position on the stud has values in the range of an infinite equivalent orthotropic plate from 80 Hz to 200 Hz. Above 200 Hz the

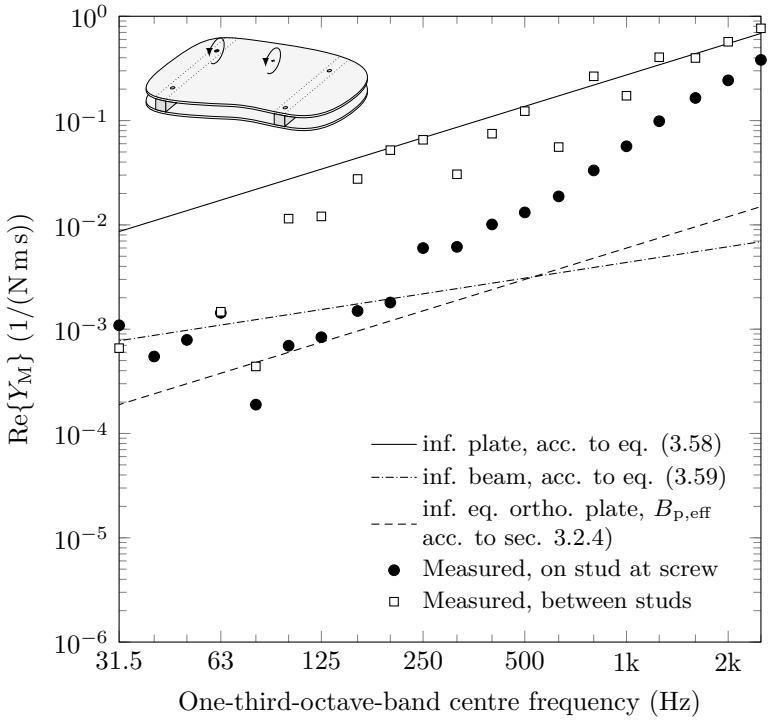

Figure 5.42: Real part of moment mobility about the x-axis for a position above a stud at a screw and in-between two studs on the timber-frame wall. Direction conventions according to Figure 5.37.

mobility above the stud also increases and is similar to the bay position at high frequencies.

For the moment about the y-axis the values are also in the range of the infinite beam with the stud properties and the infinite equivalent orthotropic plate at frequencies below 50 Hz. Above 63 Hz the measured values for both positions increase towards the infinite 19 mm chipboard plate. As the y-axis is parallel to the timber studs, the moment mobility is not influenced by the stiffness of the stud and therefore shows a similar behaviour to that in the middle of a bay.

Figure 5.44 shows the moment mobility about the x-axis for a position above a stud and one in a bay on the timber-joist floor. As the procedure

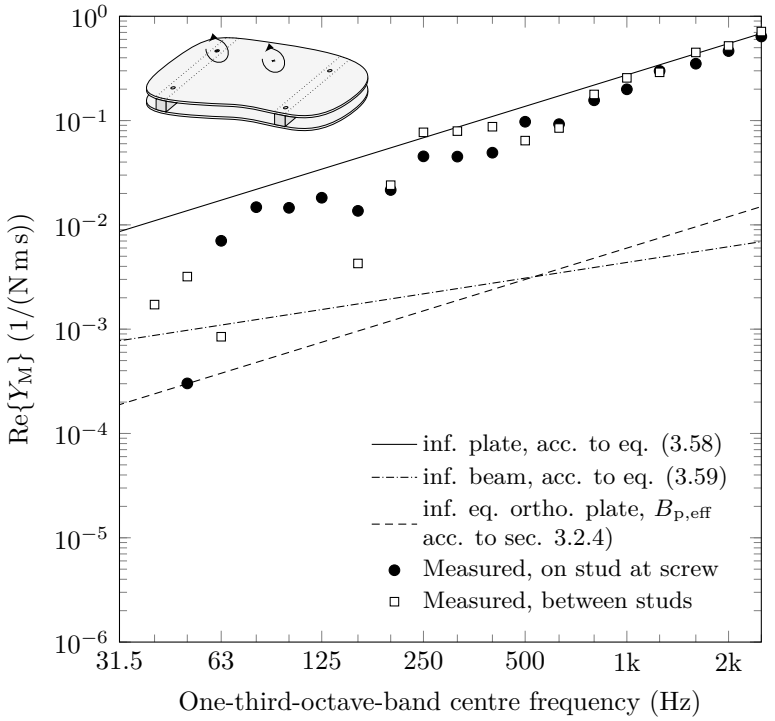

Figure 5.43: Real part of moment mobility about the y-axis for a position above a stud at a screw and in-between two studs on the timber-frame wall. Direction conventions according to Figure 5.37.

is sensitive to phase errors, some FFT lines in the low frequency range had negative real parts and therefore the one-third octave bands were rejected. However the trend shows the same results as for the timber-frame wall, whereas the infinite beam and infinite equivalent orthotropic plate moment mobility seem to underestimate the result at very low frequencies. Towards high frequencies both positions have values in the range of the infinite 19 mm chipboard plate, whereas the bay position reaches these values at a lower frequency.

Figure 5.45 shows the moment mobility about the y-axis for the timber-joist floor. As with the timber-frame wall, both positions show results in

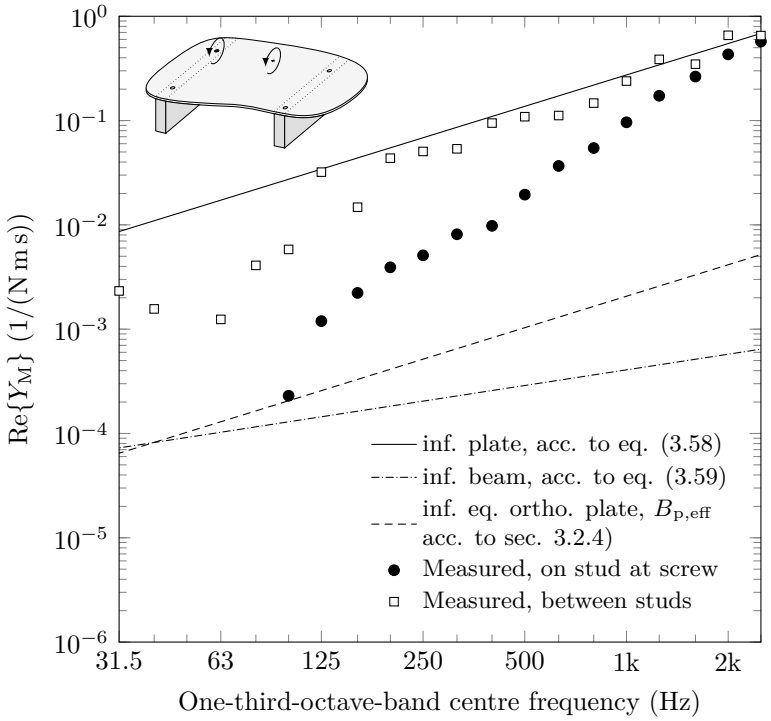

Figure 5.44: Real part of moment mobility about the x-axis for a position above a stud at a screw and in-between two studs on the timber-joist floor. Direction conventions according to Figure 5.37.

the range of the infinite 19 mm chipboard plate as the y-axis is parallel to the floor joist.

5.4.3 Discussion

At low frequencies the driving-point mobility does not vary significantly across the wall surface and can be approximated using the properties of an equivalent orthotropic plate. This was valid as long as the bending wavelength of the sheeting was large compared to the stud spacing. Positions that are at least a quarter of a wavelength to the nearest wall stud

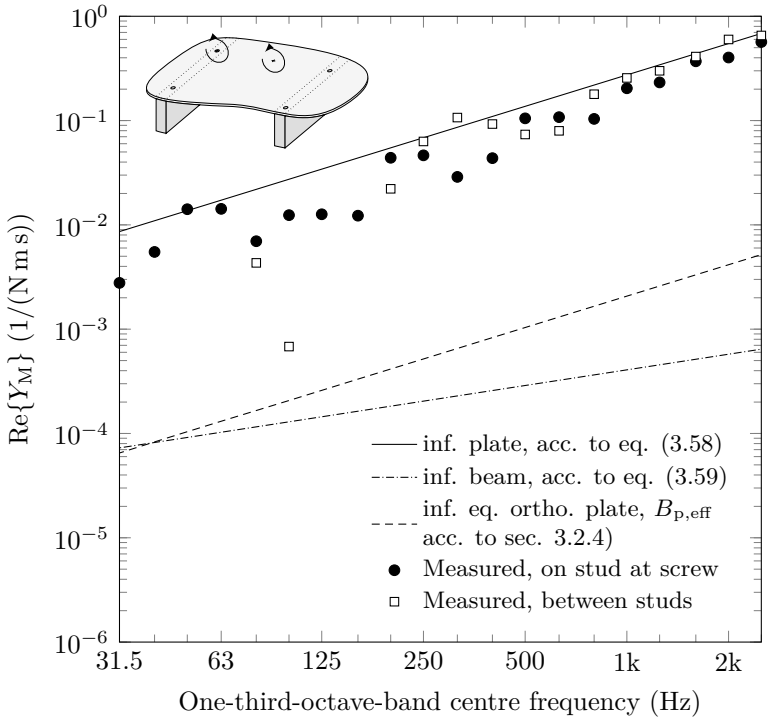

Figure 5.45: Real part of moment mobility about the x-axis for a position above a stud at a screw and in-between two studs on the timber-joist floor. Direction conventions according to Figure 5.37.

or floor joist can be approximated by the mobility of an infinite plate with the properties of the sheeting material.

The spatial variation of moment mobilities had similar findings to the driving-point mobilities. However for positions above a stud or joist there was a significant difference between the two moments about the x- and y-axis respectively. The moment rotating about the axis of the stud or joist was similar to positions in-between the stud or joist.

5.5 Sound fields and sound radiation

Additionally to the measurement of vibrations and mechanical mobilities, the sound field in the empty cavities and the sound radiation of the test structure was investigated experimentally.

5.5.1 Cavity sound pressure levels

The spatial average sound pressure levels were measured in the empty cavities. Three random microphone positions were used in each cavity inserted as described in section 4.5.8.1. At each position, the different depths of the microphone showed almost identical results because the positions were highly correlated due to the limited range of possible depths (see section 4.5.8). Hence only one depth was used in the spatial average. In the x-y-plane of the cavity a spacing of at least 0.7 m was used for the individual positions and the minimum distance to the cavity boundaries was 0.1 m. In the far left bay where the mechanical point force was applied, the minimum distance to the excitation position was set to 0.7 m to avoid the influence of a direct field. Mechanical point excitation was applied at the same positions, one in a bay and one above a stud, as shown in Figure 5.18.

Figure 5.46 shows the spatial-average SPL for mechanical point excitation in the far left bay of the timber-frame wall. The results are normalized to the cavity where the excitation was applied as this had the highest SPL. At low frequencies the SPL in cavities 2 to 8 is similar and the maximum difference between them is about 10 dB. This is similar to the results of the measured surface velocity level distribution shown in section 5.3.1. Towards higher frequencies there is a logical rank order of the average SPLs for cavities that decreases with increasing distance from cavity 1. In the 2500 Hz one-third octave band the difference is about 35 dB between the far left and the far right cavity. The 95 % confidence limits of the averaged levels are not added in this plot for the sake of clarity, but are given in Figure 5.48.

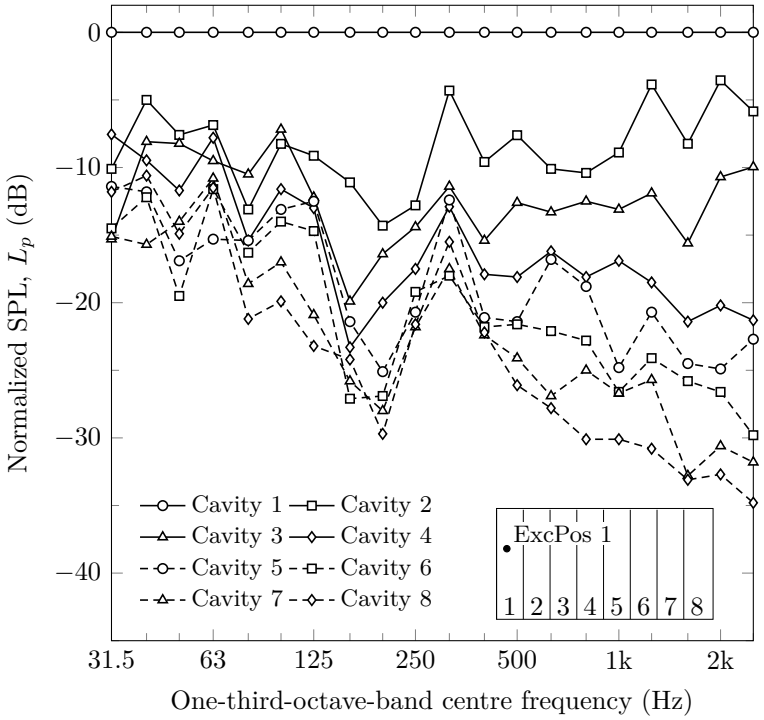

Figure 5.46: Cavity sound pressure levels for bay excitation (excitation position 1, indicated in Figure 5.18). Average values for three microphone positions in each bay. Results are normalized to the cavity where the excitation was applied.

Following the findings from section 5.3.1, the results for excitation above a stud are shown in Figure 5.47. For this excitation position the results are normalized to cavity 2. At low frequencies the average SPLs are in the same range because the wall behaves like a single plate with little attenuation in this frequency range. As the excitation is not in a bay, the SPL in all cavities are within 10 dB of each other up to 125 Hz. Towards high frequencies, again the attenuation increases and the rank corresponds to the distance of successive cavities. For cavity 8 the spatial average SPL in the 2500 Hz one-third octave band is about 35 dB below cavity 1 which is near to where the point force was applied.

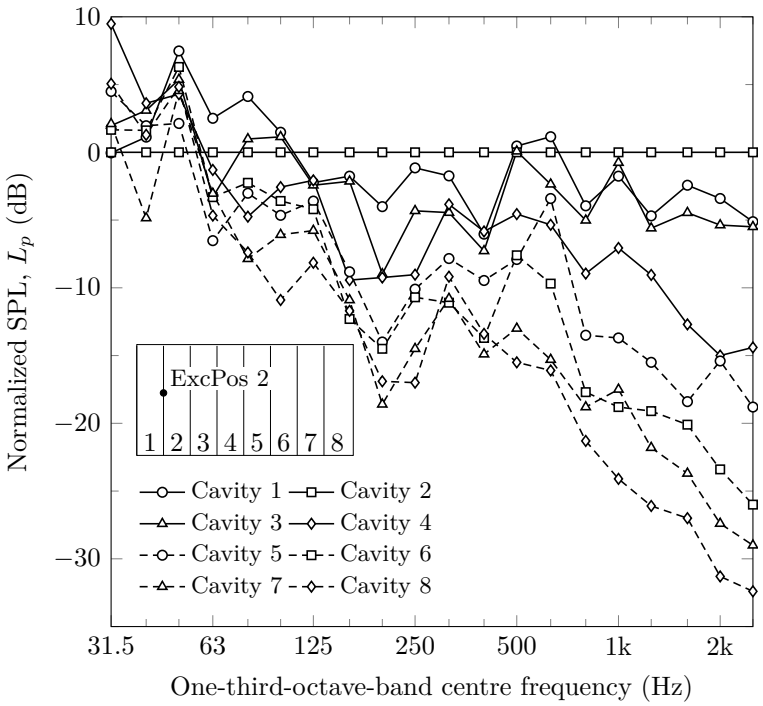

Figure 5.47: Cavity sound pressure levels for stud excitation (excitation position 2, indicated in 5.18). Average values for three microphone positions in each bay. Results are normalized to cavity 2.

5.5.2 Radiation efficiency of the laboratory test structure

To describe the coupling of bending waves to the sound field in the cavities or rooms and vice versa, knowledge about the radiation of bending waves is required. Therefore the sound radiation of the timber-frame test structure was investigated experimentally and the results compared with the model described by Leppington et al. [1982; 1986].

To measure the radiation efficiency, the procedure described in section 4.5.7 was applied. The measurements were part of the Bachelor Thesis by Grünewald [2016] at the Technical University of Applied Sciences Rosenheim which was supervised by the author. In these experiments the frequency-average radiation efficiency was determined in one-third

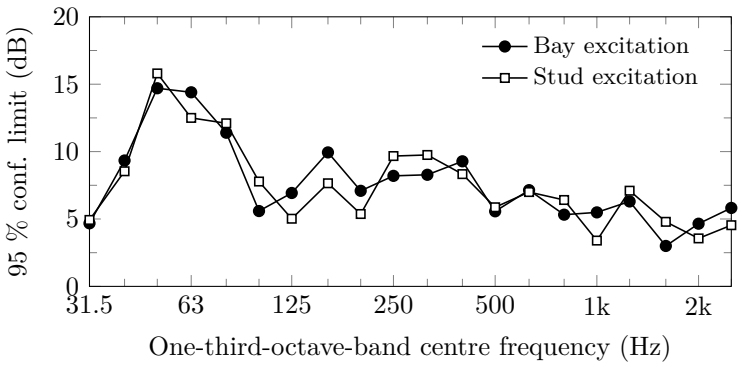

Figure 5.48: Arithmetic mean of 95 % confidence limits for spatial average cavity SPL determined in eight bays.

octave bands for mechanical point excitation either above a stud or in a bay on the source surface as indicated in Figure 5.19. The excitation positions are shown in Figure 5.49. On the receiving surface, the velocity levels and the sound intensity were measured on a 20.8 cm × 20 cm grid across the wall giving 24 × 12 positions. The grid spacing was chosen, such that every fourth grid intersection in the x-direction was above a timber-stud. To cover a wide frequency range, two spacers, 12 mm and 100 mm were used and the two resulting one-third octave band spectra assembled.

The experimental results described in section 5.3.1 showed that the vibrational behaviour of a timber-frame wall is frequency dependent and can be divided into three regimes. In the low frequency range the vibrational behaviour is strongly influenced by the stiffness of the framework. At mid and high frequencies, it is affected by the properties of the sheeting plates only. This knowledge is now applied to investigate the measured radiation efficiency by taking into account either the whole plate surface or only positions between studs.

To compare the measured data with theory, the radiation efficiency was calculated as described in section 3.2.8.3 using three sets of parameters. The measured results and the calculation variations are shown in Figure 5.50 for excitation position 3 (above a stud) and in Figure 5.51

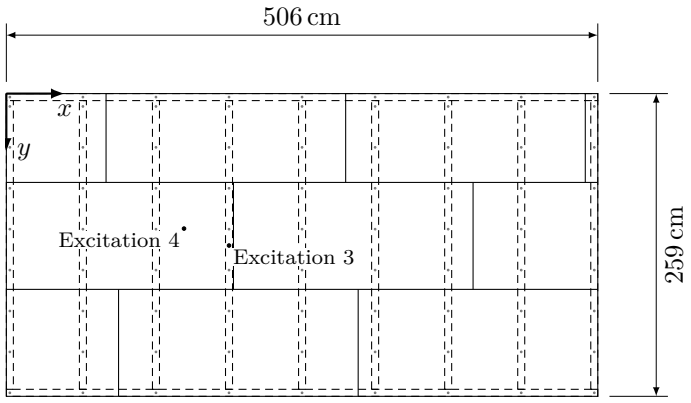

Figure 5.49: Chosen mechanical excitation position on the source surface of the timber-frame wall for the experimental determination of the radiation efficiency.

for excitation position 4 (in a bay). In these figures the radiation index for the definition of levels in decibels is shown. The measured grid data was processed differently for two cases: A) Using the spatial average of all points of the measurement grid across the timber-frame wall and B) Using the spatial average of only positions between studs. It has to be noted however, that although the velocity can be measured at discrete points the sound intensity represents radiation from an area on the structure rather than a discrete point. Nevertheless the influence of the stud on the measured data for the radiation efficiency is reduced by omitting positions directly above the studs.

The measured radiation index shown in Figures 5.50 and 5.51 is similar for the stud and bay excitation. At high frequencies it agrees well with the theory for a plate with the properties of 19 mm chipboard. The calculated radiation index using the dimensions of the whole wall overestimates the radiation index slightly in the 2000 Hz one-third octave band near the coincidence frequency. At high frequencies there is no difference if positions above the stud are included or not; this is in accordance with the findings from section 5.3.1 which showed that the point-connected chipboard sheeting vibrates independently of the studs.

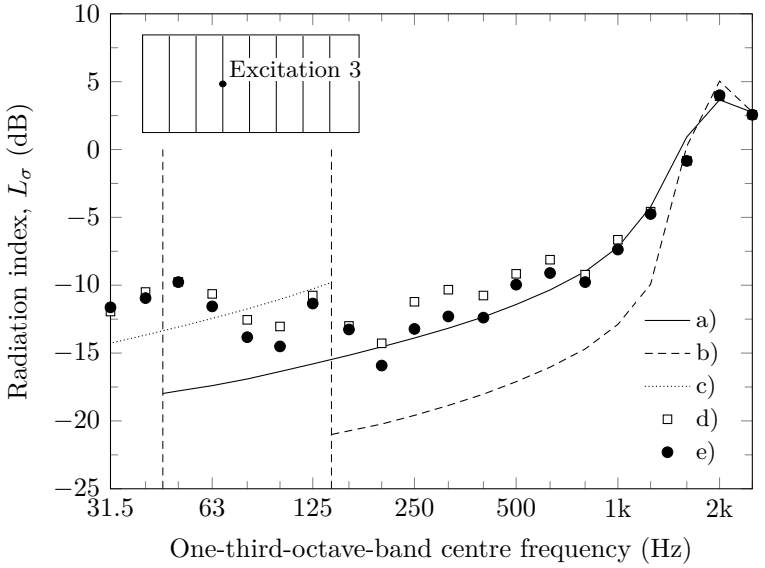

Figure 5.50: Radiation index of the timber-frame wall for stud excitation. a) Predicted using material properties of the 19 mm chipboard plates and the dimensions of the bays. b) Predicted using material properties of the 19 mm chipboard plates and the dimensions of the whole wall. c) Predicted using properties of the equivalent orthotropic plate, described in section 3.2.4 and the dimensions of the whole wall, d) Measured using only positions between studs. e) Measured using all positions including positions above wall studs. Vertical dashed lines indicate the transition frequencies shown in Figure 5.30.

In the mid-frequency range the measured data agrees well with the model that assumes individual simply supported rectangular plates with the bay dimensions. Similar findings were observed by Schoenwald [2008] for example. At these frequencies, the data set that includes the positions above studs is slightly higher than the results obtained for bay positions that fits well with theory.

In the low-frequency range the wall behaves like an equivalent orthotropic plate (see sections 5.3.1 and 5.4). Therefore the measured radia-

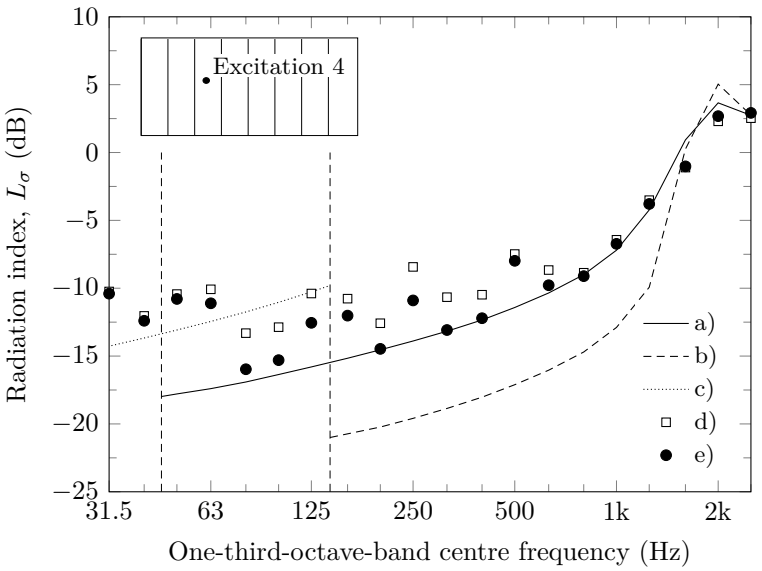

Figure 5.51: As Figure 5.50 but for bay excitation.

tion index is in the range of the model that uses the properties of the equivalent orthotropic plate, particularly for the one-third octave bands below 80 Hz and there is no difference between the measurement with or without stud positions. These results indicate that above ≈100 Hz, the radiation of the wall can be modelled by assuming individual rectangular plates with the dimensions of the bays and the properties of the 19 mm chipboard.

5.6 Summary

In this chapter, experimental investigations, based on the procedures given in chapter 4, on individual building elements and a laboratory test structure were described and the results discussed.

For the individual chipboard plates and the timber studs and joists, the most relevant material properties to describe the dynamic behaviour were determined experimentally and serve as input data for models described in chapters 6, 7 and 8.

The cavity TLF was measured and compared with predicted ILFs of empty cavities [Price and Crocker 1970]. This indicates reasonable estimates for absorption coefficients [e. g. see DIN 18041:2016-03; EN 13986:2004+A1:2015].

A special feature of the test structure are the tongue and groove joints of the chipboard plates. As no model is available to calculate the CLF across this joint, measurements were carried out on two coupled plates with free boundary conditions and at two joints on the test structure using structural intensity. The measured CLF decreases with increasing frequency and is used in the SEA models in chapter 7.

To gain knowledge about the dynamic response of the test structure, the distribution of surface velocity levels was investigated experimentally for a local mechanical point excitation. Three main frequency regimes were confirmed [see also Nightingale and Bosmans 1999; Schoenwald 2008]. In the low frequency range, where the bending wavelength of the sheeting material is large compared to the spacing of the studs, the whole wall can be regarded as a single plate with orthotropic material properties. When half a bending wavelength fits into the stud spacing, the point-connected plates act as being line-connected to the studs. Towards high frequencies, strong attenuation with distance can be observed.

Further investigations used structural intensity to visualize the net-power flow across the structure for point force excitation. The results confirm the findings obtained from the surface velocity levels that at low frequencies the wall can be considered as a single SEA subsystem but at higher frequencies it might be necessary to subdivide it into several subsystems.

To quantify the coupling between both sides of the double wall, the level differences as well as the phase relationship were investigated. Since a point force was applied, the level differences were only significant in the vicinity of this position. In distant parts of the wall the existence of several transmission paths caused a level difference of $\approx 0\,\mathrm{dB}$ across the wall. The phase relationship, quantified using the FRAC, showed that the vibrational response of both wall surfaces are uncorrelated above the

mass-spring-mass resonance frequency of the plate-cavity-plate system, which indicates that an SEA model could reasonably be considered.

To provide the basis for the calculation of the power input from machinery, measurements of the receiver mobility were carried out. As moment excitation can not be neglected a-priori, moment mobilities were measured in addition to the driving point mobility. The obtained results resemble the findings from the measurement of the surface velocity levels. At low frequencies the whole wall acts as a single plate and no spatial variation is apparent. The measured mobilities are in the range of an infinite plate with the properties of an equivalent orthotropic plate. In the mid-frequency range there is a strong spatial variation between positions above studs and in-between studs. However positions that are a quarter of a bending wavelength away from a stud show the behaviour of an infinite plate with the properties of the sheeting material [see also Lin and Pan 2006; Mayr 2009]. Hence at high frequencies all positions are determined by the sheeting plate. This applies for the driving point and the moment mobilities. However for the moment mobility above studs there is a difference concerning the direction of the moment. Moment mobilities above a stud parallel to the axis of the beam are similar to positions in-between studs. Perpendicular to the beam, theory for an infinite beam and an infinite equivalent orthotropic plate give a reasonable estimate at frequencies $<250\,\mathrm{Hz}$. Where infinite beam theory tends to give an upper limit and infinite plate theory for an equivalent orthotropic plate tends to give a lower limit. Towards high frequencies the measured mobility tends to infinite plate theory for 19 mm chipboard.

To gain insight into the sound field in the empty cavities, the SPL was measured for mechanical point excitation. This indicated a decrease in SPL as the distance of the cavity from the excitation position was increased.

The sound radiation of bending waves was investigated by experimentally determining the radiation efficiency of the test structure for mechanical point excitation. Results were compared with the model of Leppington et al. [1982] for thin rectangular plates. Again the three frequency

regimes can be identified and need to be considered when modelling the sound radiation.

The measurements give insight into the behaviour of a basic inhomogeneous structure. Real building structures are more complex in terms of their assembly (e. g. multiple layers of sheeting). However knowledge about the behaviour of this specific test structure provides the necessary background for the work presented in the following chapters.

6 Structure-borne sound power of mechanical sources on timber-frame constructions

6.1 Introduction

This chapter describes the determination of the power input from SBS sources into timber-frame structures. It describes approaches to simplify the determination of the power input for force excitation from machinery. Only out-of-plane excitation components are considered which primarily excite bending waves. To investigative the importance of out-of-plane moment excitation, inverse methods are used to determine the power input.

Section 6.2 describes the excitation sources that were used for the investigations. Section 6.3 applies inverse methods to determine a moment power about a single point. Section 6.4 focuses on force excitation perpendicular to the surface for multi-point sources.

6.2 Excitation sources

6.2.1 Force excitation using a shaker acting in direction perpendicular to the surface of the structure

To excite the structure with a force perpendicular to the surface, a shaker in-line with a thin steel rod (stinger) is used as described in section 4.5.1.

6.2.2 Moment excitation using a shaker parallel to the surface of the structure

For the excitation of moments, various experimental approaches can be found in literature. Petersson [1987] used a magnetostrictive device with two rods acting with inverse phase. The author showed that the pair of magnetostrictive rods can easily be matched in terms of phase, however drawbacks are the stability of the device and problems with heat due to the required high current. Another approach can be found in a paper by Sanderson [1995] who used two shakers attached to levers (T- and I-like) to excite a moment in order to measure moment mobilities. The advantage of this approach is that ordinary laboratory equipment can be used. However the resonance frequency of the lever is an upper frequency limit for the measurement and the two individual forces delivered by the two shakers must be matched. Another approach is given by Champoux et al. [2003] that used two synchronized impact hammers that apply a pair of forces to excite a moment. The advantage of this approach is that no mass is attached to the structure. However a tailor-made device to synchronize the two hammers is required. Elliott et al. [2012] proposed a finite difference method for moment excitation, however with the main aim to determine moment excited FRFs (i. e. mobilities).

In this thesis a similar approach to Sanderson [1995] is applied by using a shaker parallel to the surface, that is attached to a lever as shown in Figure 6.1. With this set-up a moment is predominantly excited. However all three out-of-plane excitation components, F_z, M_x and M_y, were determined to assess experimental procedures to quantify the power

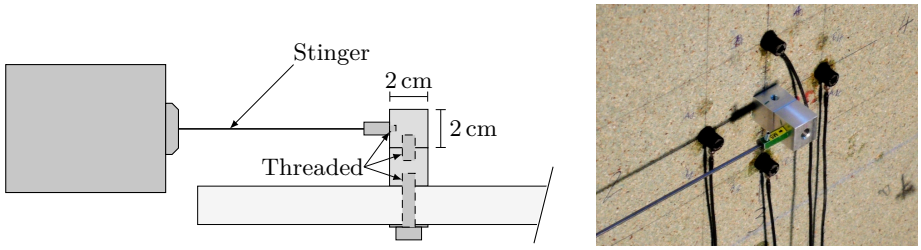

(a) Sketch (b) Photo

Figure 6.1: Experimental set-up for moment excitation.

input of these components individually. The aim of this set-up is – in contrast to the three approaches described above – not to inject a pure moment but to imitate a source that predominantly excites rotational components.

To make the lever, two aluminium cubes with an edge length of 2 cm are used which are connected with threaded rods as shown in Figure 6.1. For the excitation, a shaker is attached to the upper cube via a stinger parallel to the surface of the receiving structure.

6.2.3 Artificial source

To investigate the power input from compact multi-point sources, an artificial source was designed and constructed. This source is made of steel profiles that form a frame, see Figure 6.2. It is designed to imitate box-shaped service equipment with four contact points and an internal excitation source. Parts of the experimental work on this artificial source were carried out by a Bachelor student [Betz 2015] that was supervised by the author.

6.2.3.1 Description

The artificial source comprises two metal frames that are connected with cross bars to form a box shape. The outer dimensions are 84 cm × 57 cm × 18 cm. The frame is made from steel profiles that are used for sanitary pre-wall-installation systems. An inertial shaker (see Table 4.1) is atta-

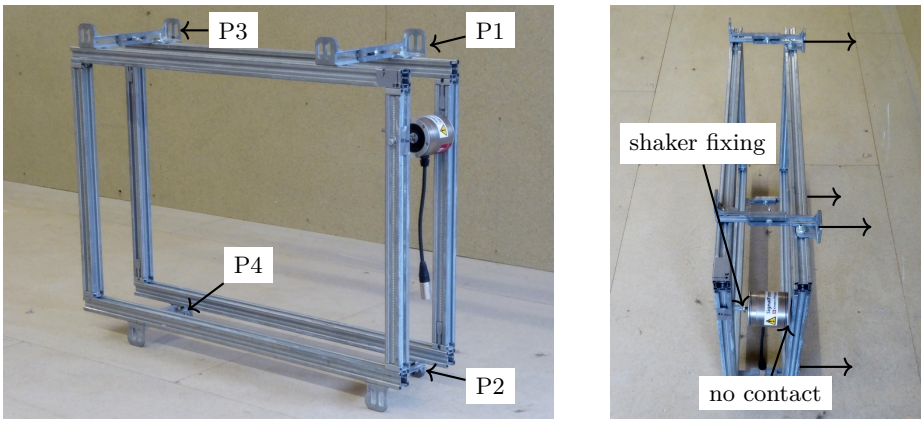

(a) (b)

Figure 6.2: Photos of the artificial source. (a) shows the notation for the four contact points; (b) shows the mounting points and the position of the shaker excitation inside the metal frame.

ched to the frame as an internal excitation source. The shaker is attached to the frame opposite the mounting points as indicated in Figure 6.2a. This represents a compact SBS source with an internal excitation source. The contact points are spaced at 62 cm centres in the vertical and horizontal directions. This corresponds to a typical spacing of studs and joists in timber constructions. By using a shaker, this artificial source can be fed with any excitation signal. To provide broadband excitation, pink noise was used for the investigations that are presented in this thesis. For reproducibility, the excitation signal was prepared and stored as an audio file that was used for each measurement. In addition the same hardware with identical configuration was used for the experiments.

6.2.3.2 Source free velocity

The out-of plane free velocity was measured with accelerometers (Type KS95B100, see Table 4.1) at each of the four contact points on the source which was suspended using rubber cords. The measured free velocities at the four contact points, (P1 to P4) are shown in Figure 6.3. It can be seen

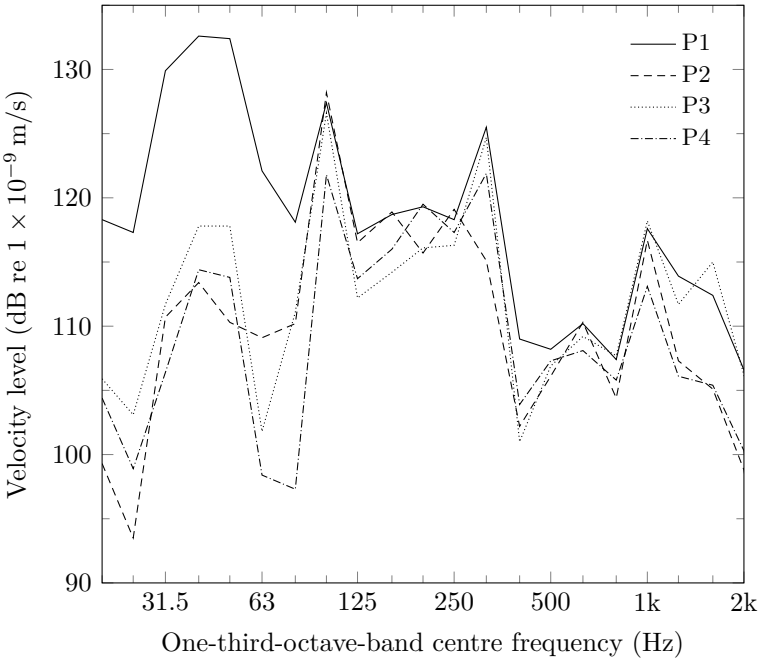

Figure 6.3: Artificial source: Measured free velocity of the artificial source at the four contact points indicated in Figure 6.2.

that P1 is dominant at low frequencies up to the 80 Hz one-third octave band because of its proximity to the internal source (shaker). Above 80 Hz this position has slightly higher velocity levels in most one-third octave bands, but is similar to the other three positions.

6.2.3.3 Source mobility

The source mobility was measured with the artificial source elastically supported with rubber cords (similar to the measurement of the free velocities). The measurement was carried out with the instrumented hammer listed in Table 4.1 and four accelerometers (Type KS95B100, see Table 4.1). By using four accelerometers, the cross mobilities were also measured to determine the full 4×4 mobility matrix for the out-of-plane force component.

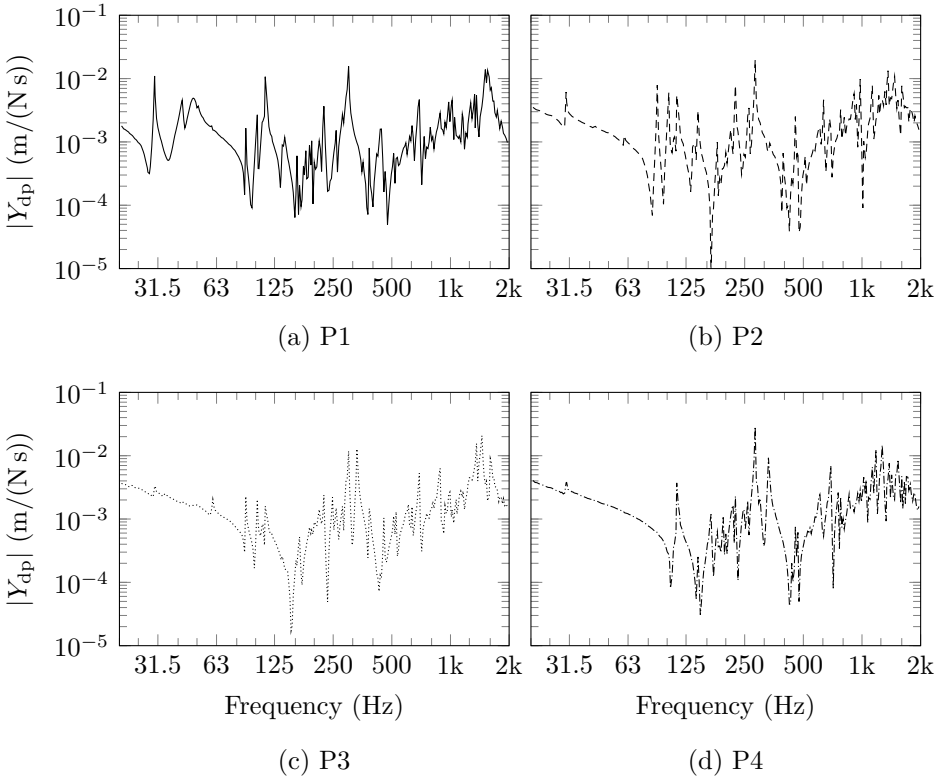

Figure 6.4: Artificial source: Measured driving-point mobilities in narrow bands at the four contact points, P1 to P4.

Figure 6.4 shows the narrow band magnitude of the driving point mobilities at each of the four contact points. All four points are similar except the mobility at P1 in the low frequency range. This difference is caused by the shaker as this position is close to it.

The measured driving point mobilities of all four contact points are shown in Figure 6.5 averaged into one-third octave bands. As the power input to lightweight timber structures is of interest, the mobility of an infinite 19 mm chipboard plate is also shown in this figure. It can be seen that the mobility of the artificial source is in the same range as the chipboard. Therefore the two simplifications for the installed structure-borne sound power given in equations (3.73) and (3.74) can not be applied.

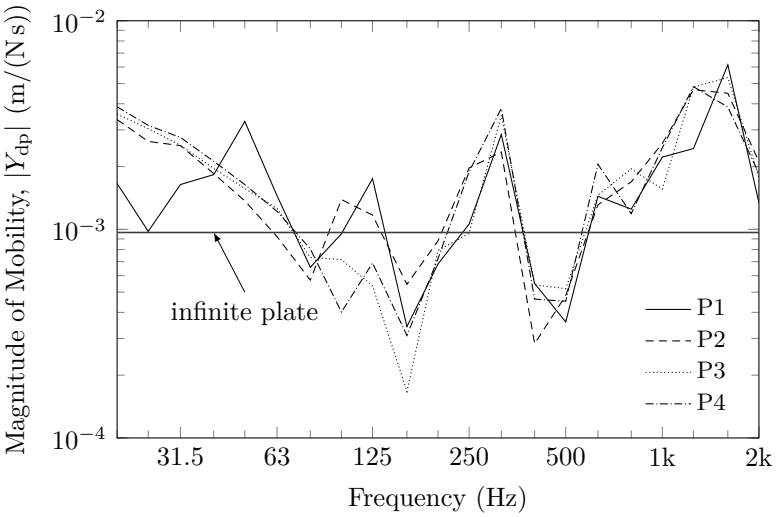

Figure 6.5: Artificial source: Driving-point mobility in one-third octave bands compared to the infinite plate mobility of 19 mm chipboard (see section 5.4.1).

6.2.4 Ventilation system

The artificial source described in section 6.2.3 allows investigations of the power input using any excitation signal for which the strength and the spectral shape can be modified. Although the artificial source was designed to imitate typical appliances, a real source was additionally investigated, a ventilation unit.

6.2.4.1 Description of the source

The real source is a compact ventilation unit with the dimensions 60 cm × 78 cm × 38 cm. The total weight of this unit is 42.5 kg. Figure 6.6a shows the whole unit mounted on a wall. The air inputs and outputs are short-circuited for the operating conditions in the laboratory. The ventilation system is hung on a wall using a mounting rail that is connected to the structure (see Figure 6.6b). The fixing to the mounting rail is a turned-up metal sheet at the top edge on the back of the body housing – see

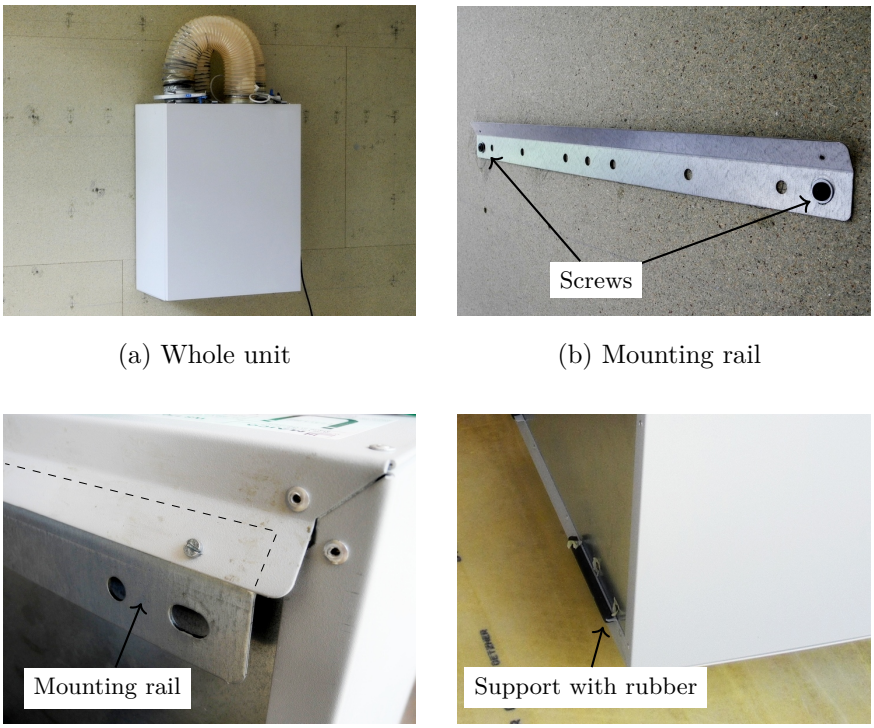

(a) Whole unit

(b) Mounting rail

(c) Detail of contact at top

(d) Detail of contact at bottom

Figure 6.6: Ventilation system.

Figure 6.6c. At the bottom, the box is supported via a sheet turned up 90° at the bottom left and right corner. This sheet is covered with a thin U-shaped rubber profile (see detail of one corner in Figure 6.6d). These complex fixings support the choice for investigations on a real source in addition to the artificial source, for which the contact points are well defined. In this study the power input of this ventilation system is estimated using the same approach as for the artificial source. However this requires approximations that are described in the following section.

6.2.4.2 Approximations for the definition of the contact points

Although this source is attached via a mounting rail at the top and two flanges at the bottom, four point contacts were assumed for this source.

When attached to the wall, the mounting rail is connected at two points using screws (see Figure 6.6b). To determine the source parameters, this mounting rail is considered as part of the source. Normally the ventilation unit is hung onto the mounting rail that has been attached to the receiving structure. For the source characterization, the mounting rail was connected to the isolated source in the same position as it would rest when the unit was attached to a wall (see Figure 6.6c). The rail was temporarily fixed with screws at the position close to the holes in the metal that are provided to fix it to the structure. Additionally the rail was temporarily glued to the metal strip on the source.

The chosen contact points are shown on the photos in Figure 6.7. At the top of the housing two sets of of positions were considered. P1(a) and P2(a) on the mounting rail and P1(b) and P2(b) on the housing of the unit.

The first set, P1(a) and P2(a) are on the mounting rail as these are the points that are actually connected to the receiving structure when the source is attached to a wall. However in the free condition, the mounting rail is basically a cantilever which is not constrained at its free end as it would be in the installed condition. Hence it is necessary to apply an approximation for the measurement. In this case resilient material was clamped between the mounting rail and the unit housing (see detail in Figure 6.7) as a compromise between the free and rigid connection of the unit housing to the free end of the mounting rail.

The second set, P1(b) and P2(b) is on the unit housing above the mounting rail. In this case the measurement positions are defined, but the positions are not those which are connected to the structure.

6.2.4.3 Source free velocity

To measure the source free velocity, the ventilation unit is suspended using a spring that provides a low resonance frequency in combination with the source ($<$10 Hz) to approximate free conditions. To ensure

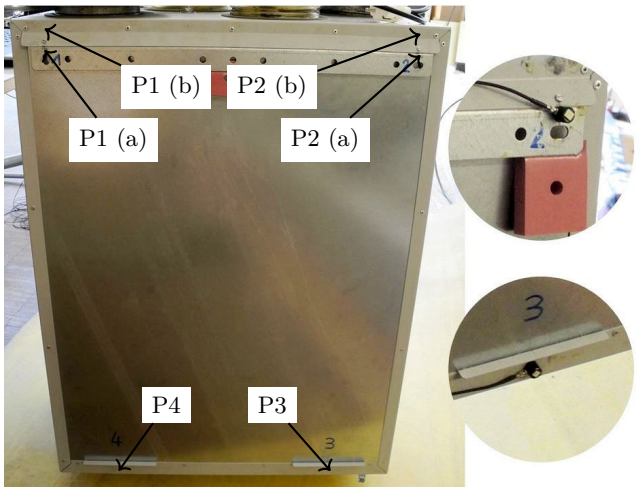

Figure 6.7: Measurement positions on the back of the ventilation system. P1 (a) and P2 (a) indicate positions on the mounting rail (see detail on top). P1 (b) and P2 (b) indicate positions on the housing of the unit.

reproducible operation conditions the airflow was monitored in addition to the settings in the ventilation system.

Using the Type KS95B100 accelerometers (see Table 4.1), the free velocity was measured on the positions indicated in Figure 6.7. The results for positions P1(a) and P2(a) (on the mounting rail) and positions P3 and P4 are shown in Figure 6.8a. The source free velocities measured on the housing (P1(b) and P2(b)) are shown together with the same data for P3 and P4 in Figure 6.8b.

All six measured positions show a high peak in the 50 Hz one-third octave band, caused by rotating components inside the source. The measured free velocities decrease with increasing frequency. The measurement positions on the mounting rail (P1(a) and P2(a), Figure 6.8a) show higher velocity levels in the mid-frequency range from 100 Hz to 630 Hz, whereas the positions on the housing (P1(b) and P2(b), Figure 6.8b) are in the same range as P3 and P4 on the housing at the bottom of the source.

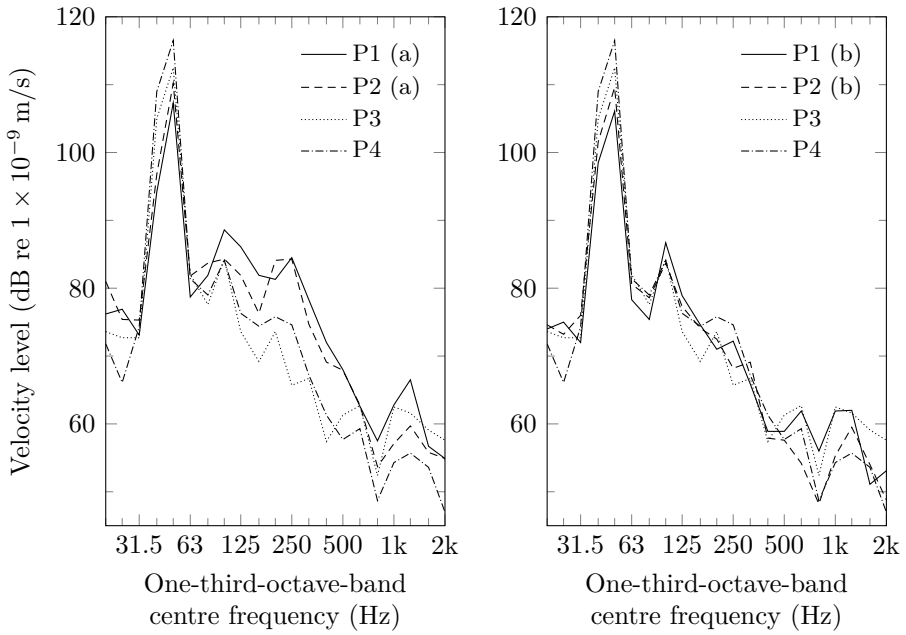

(a) P1 (a) and P2 (a) measured on the mounting rail

(b) P1 (b) and P2 (b) measured on housing

Figure 6.8: Ventilation system: Measured free velocity.

6.2.4.4 Source mobility

The source mobility was measured at the same positions as the free velocity using the same set-up to approximate free conditions. The measurements were carried with the instrumented hammer and the Type KS95B100 accelerometers (see Table 4.1). As for the artificial source the full mobility matrix for the out-of-plane force component was determined.

Figure 6.9 shows the driving-point mobility at position P1(a) on the mounting rail and P1(b) on the unit housing. As P1(a) is on the light cantilever mounting rail, the driving-point mobility differs to position P1(b) on the solid unit housing. For P1(a) the same set-up as for the free velocity measurement with resilient material clamped between the mounting rail and the housing was applied. The cantilever (P1(a)) behaves as a spring in the range 20 Hz to 160 Hz, whereas mass behaviour

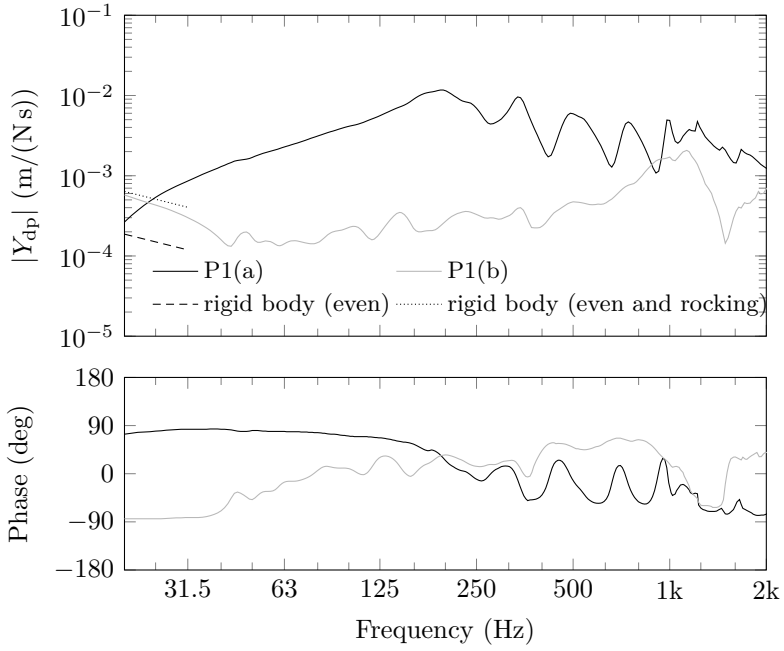

Figure 6.9: Ventilation system: Comparison of the driving-point mobility of contact P1(a) on the mounting rail and P1(b) on the housing. Additionally the rigid body modes are shown. For the rocking mode, only rocking about the vertical axis was taken into account.

can be observed for P1(b) on the housing. Note that the position is not at the centre of gravity and therefore the mobility of the rocking body modes add up to the mobility of the rigid body mode given by $(\mathrm{i}\,\omega\,m)^{-1}$. The rocking body mode can be calculated as described in section 3.2.9.5. In this case only rocking about the vertical axis was taken into account as the source was hung at one point in the centre for the measurements. Therefore rocking about the vertical axis was possible, whereas rocking about the horizontal axis is potentially suppressed. The sum of the rigid and rocking (vertical axis) mode gives a good estimate of the measured mobility.

Figure 6.10 shows the source mobility for the positions P1(a), P1(b), P3 and P4. It can be seen that P1(a) and P2(a), both on the mounting

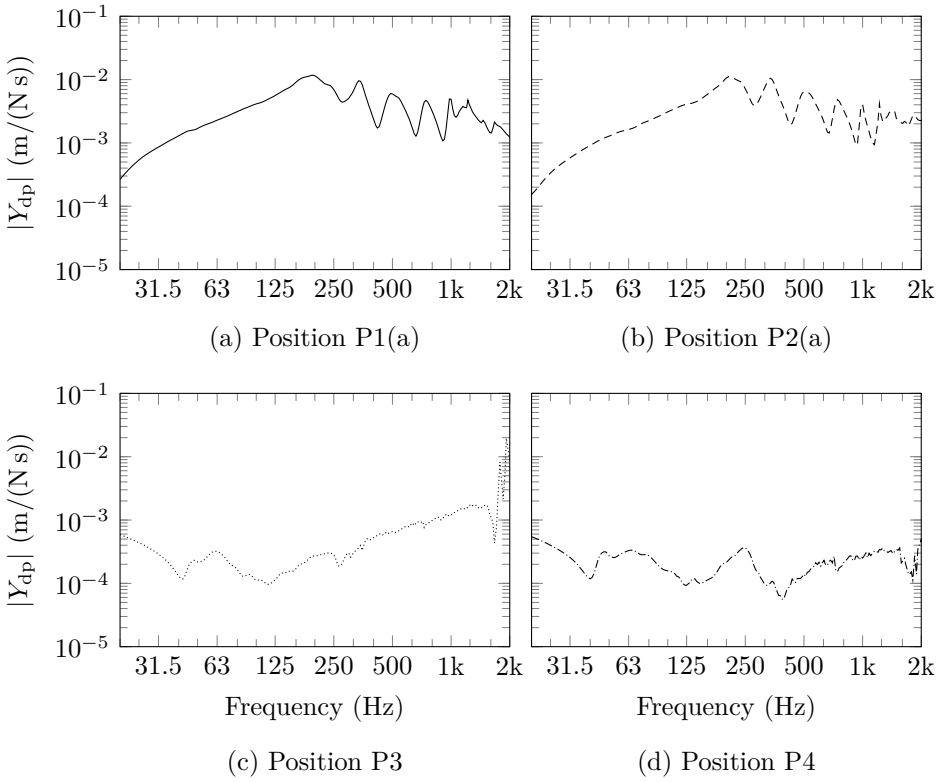

(a) Position P1(a) (b) Position P2(a)

(c) Position P3 (d) Position P4

Figure 6.10: Ventilation system: Measured driving-point mobilities at the four chosen positions, P1(a), P2(a), P3 and P4.

rail, are very similar. Compared to position P1(b), P3 and P4 are lower and show different spectral shape because they are on the housing.

6.2.4.5 Discussion

This ventilation system reveals problems that can arise with real sources in terms of the definition and choice of the actual contact position on system boundaries to measure the source parameters. In this case, point contacts for the mounting rail are assumed. For all four contact points approximations are necessary to obtain the source parameters.

Gibbs and Mayr [2012] described possibilities to estimate the source mobility based on characteristic dynamic properties. In this case mea-

sured data were used because the dynamic properties of this source are difficult to model. Although the rigid body behaviour could be described at low frequencies.

To calculate the power input from this source, the measurement positions on the mounting rail are considered as these are the points that are actually attached to the receiving structure.

6.3 Investigation into using inverse methods to obtain moment power about a single point

In addition to the excitation of a force perpendicular to the surface, the two out-of-plane moments can potentially excite bending waves on building structures. To assess the relative importance of these rotatory components in relation to the force component, it is necessary to determine the power input of all three out-of-plane excitation components experimentally. The power input of a point force is determined as described in section 4.5.6.1. However for the rotational components, there is no way to directly measure their power input; hence as described in section 4.5.6.5, inverse methods are used to determine all out-of-plane components separately.

This section describes the application of this method to obtain the moment power about a single point for the moment source described in section 6.2.2 when attached to a free chipboard plate and the test structure. Additionally the moment power of the artificial source (described in section 6.2.3.1) is determined with one contact point attached to a free chipboard plate.

6.3.1 Using an isolated chipboard panel as receiver

As a reference for the power determined with the inverse method the plate power is determined using the reception plate method described in sections 3.3.3.3 and 4.5.6.4.

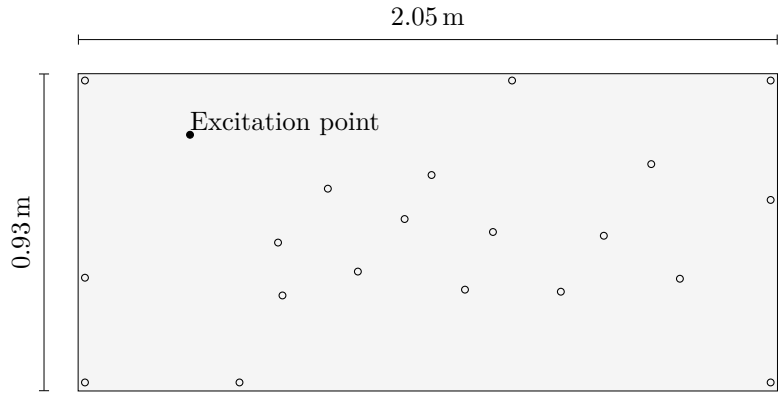

Figure 6.11: Excitation and measurements points on the chipboard reception plate to determine the spatial-average mean-square velocity.

6.3.1.1 Experimental set-up

A 19 mm chipboard plate with dimensions 2.05 m × 0.93 m is suspended with rubber cords from the ceiling in the laboratory to approximate free boundary conditions. A point force was applied with a shaker perpendicular to the surface and the input power was determined directly using a force transducer and a pair of accelerometers as described in section 4.5.6.1. The spatial-average mean-square velocity was measured on the plate to determine the reception plate power according to equations (3.76) and (3.111). The measurement points and the position of the point force excitation are shown in Figure 6.11.

Figure 6.12 shows the comparison of the directly measured input power and the reception plate power. It can be seen that the reception plate method closely approximates the input power. The deviations are less than 2 dB in the majority of the one-third octave bands from 20 Hz to 2000 Hz, with differences up to 3 dB in the 25 Hz, 40 Hz and 1000 Hz bands. For the inverse method described in the following, this procedure is therefore used as reference.

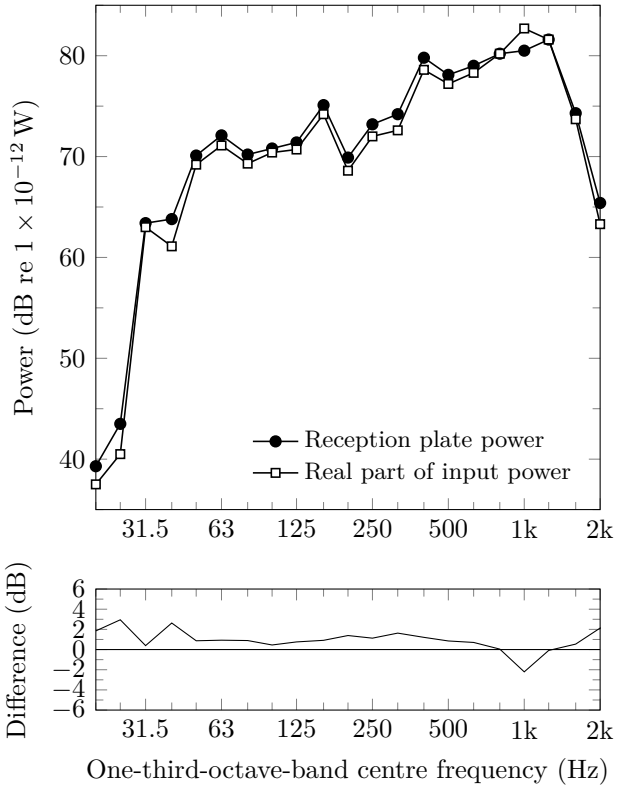

Figure 6.12: Force excitation from shaker: Direct input power and reception plate power on chipboard reception plate.

6.3.1.2 Moment excitation from a shaker

Using the set-up described in section 6.2.2, the free chipboard plate was excited at the excitation position shown in Figure 6.11. The set-up and the coordinate system used for the notation is shown in Figure 6.13. In this experiment the aim was to excite a moment component, M_x. The accelerometer spacing at the excitation position is 100 mm to determine the angular velocity that is required to calculate the active moment power. The accelerometers distributed across the plate are used to determine the reception plate power as reference. In addition three of these accelerometers are used as reference positions for the inverse method. These three were selected based on the closest phase matching (see Fi-

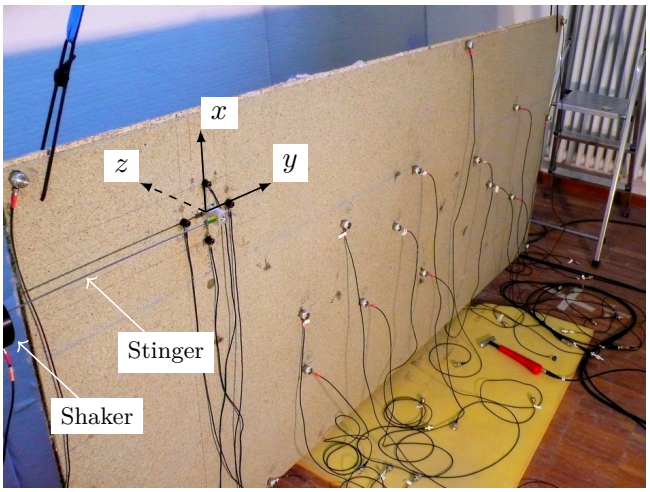

Figure 6.13: Set-up using chipboard as reception plate for moment excitation with a shaker attached parallel to the plate surface as described in section 6.2.2. The relevant coordinate system is additionally indicated on this photo.

gure 4.11) with the four accelerometers at the excitation positions that are used to determine the rotational components.

Figure 6.14 shows the active power for the moment about the x-axis, M_x according to equation (4.36). It can be seen that due to negative real parts of the power there are gaps in the narrow band spectrum.

The phase shows the expected behaviour of a finite rectangular plate as described in section 3.2.9.5. However the phase exceeds the range from $\pm$ 90° for some FFT-lines. This explains the gaps in the real part of the power. These problems tend to occur for troughs in the active power where there is a low signal-to-noise ratio as there a no modes. At these frequencies, the inverse method is prone to error.

However as these problems only tend to occur where there is low input power, these narrow bands can potentially be neglected when the power is summed into one-third octave bands. Hence two strategies were applied to determine one-third octave band power. This was compared to the reception plate power. The first approach was to set all negative real

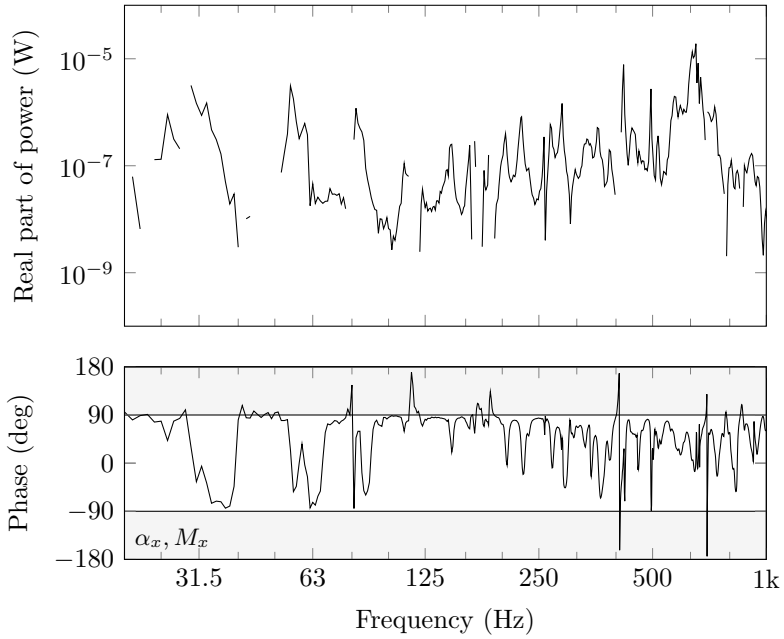

Figure 6.14: Moment excitation from shaker: Active moment input power determined using the inverse method for the moment about the x-axis on the free chipboard plate with excitation using a shaker parallel to the surface.

parts to zero before summing the narrow band data into one-third octave bands. The second approach was to close the gaps by using the lower of the two adjacent narrow band data points with positive values as indicated in Figure 6.15.

The one-third octave band active moment power using the two approaches is shown in Figure 6.16 for comparison with the reception plate method. It should be noted that the reception plate power includes other components of excitation. However it is assumed that the set-up predominantly excites the M_x component. Figure 6.16 shows that both approaches are within 0.1 dB except in the 20 Hz one-third octave band. In the 20 Hz band the second approach to close the gaps has slightly better agreement with the reception plate. However, for practical purposes

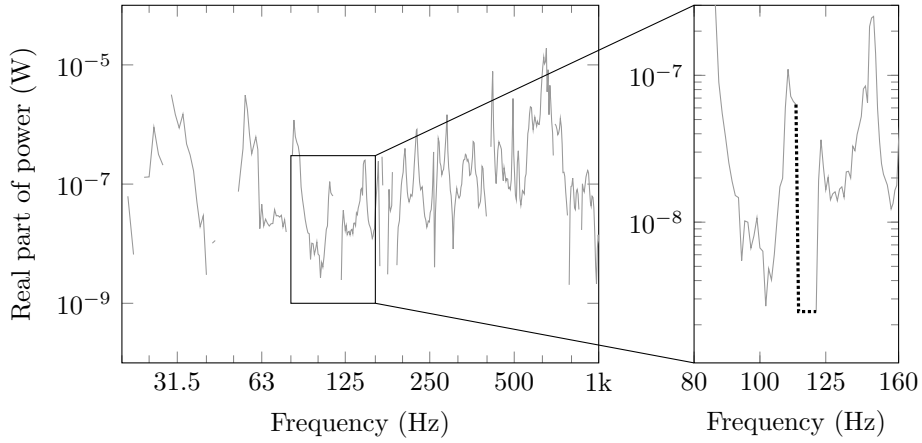

Figure 6.15: Approach to close gaps due to negative real parts of the complex power using the lower of the two adjacent narrow band data points with positive values

it is concluded that both approaches can be used when the narrow band spectrum has some negative real parts.

These investigations concerned the component that was predominantly excited with the set-up using a shaker parallel to the plate surface. The experimental set-up used four accelerometers at the excitation point to process the additional out-of plane components, F_z and M_y in addition to the predominately excited component M_x.

The results show that the active power of F_z and M_y were contaminated by noise and that the majority of the power is delivered by M_x. The phase for M_x, M_y and F_z is shown in Figure 6.17.

It is concluded that the inverse method can be applied to determine the input power of individual out-of-plane excitation components if there is enough signal for this component. Further it has been shown, that with a shaker perpendicular to the surface it is feasible to predominately excite a moment.

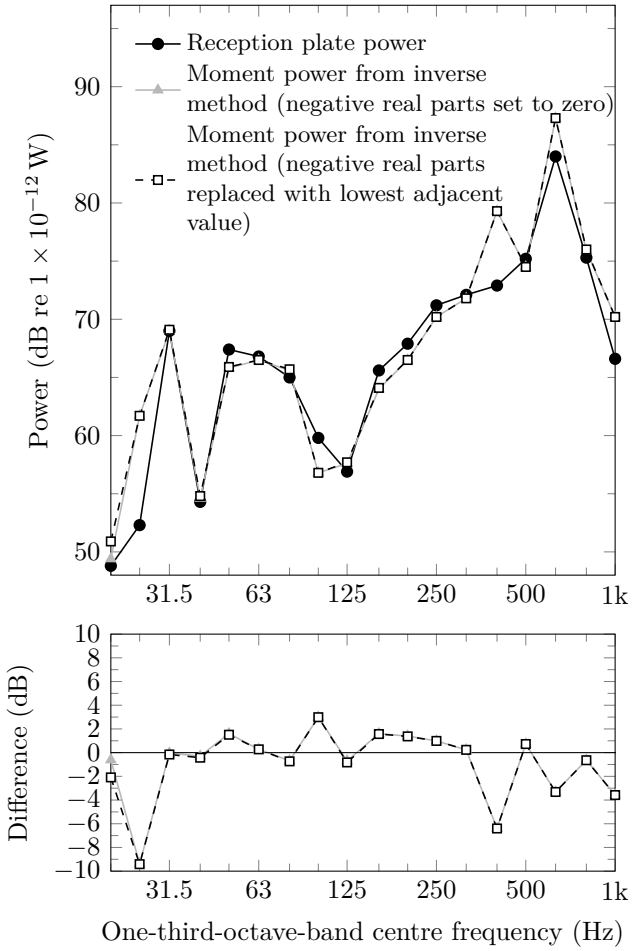

Figure 6.16: Moment excitation from shaker: Moment power on a free chipboard plate from the inverse method and the reception plate method.

6.3.1.3 Artificial source

In the previous section the inverse method was applied and validated using a shaker to predominantly excite a moment. However for most sources it is not known which component will dominate. This section investigates the excitation components of the artificial source.

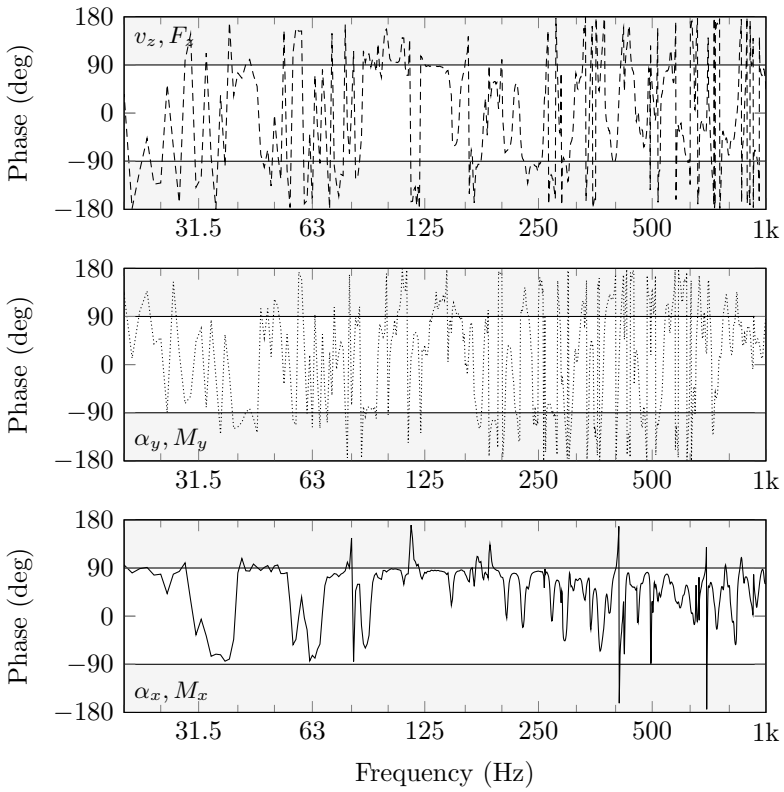

Figure 6.17: Moment excitation from shaker: Phase between the response (v_z, α_y and α_y) and the excitation (F_z, M_y and M_y) on a free chipboard plate determined using the inverse method.

To investigate the individual excitation components of the artificial source it was resiliently supported and attached to the free chipboard plate with only one contact point at the the same position (opposite surface) used for the moment excitation with a shaker (see Figure 6.11). The experimental set-up is shown in Figure 6.18. The transducer spacing at the excitation position is 70 mm.

The individual excitation components were determined using the inverse method. As discussed in the previous section problems can arise when there is negligible signal. In this case all three components were

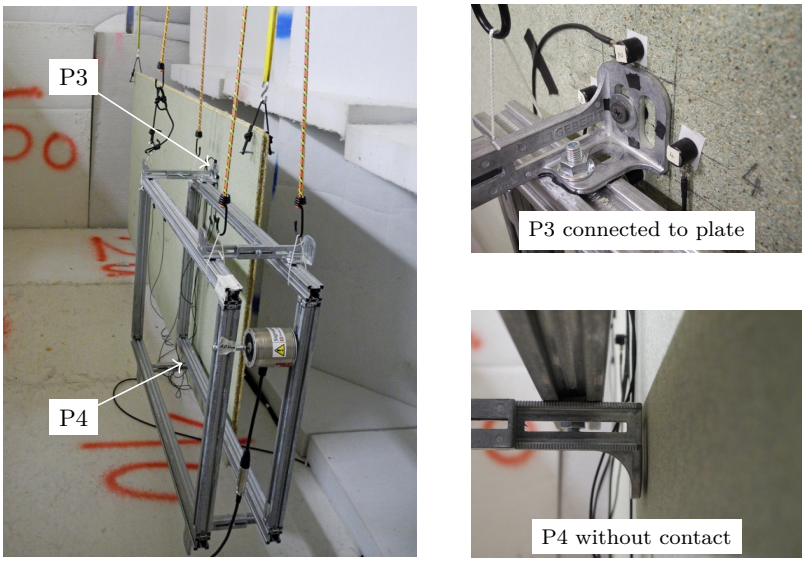

Figure 6.18: Experimental set-up to investigate the excitation components from one contact point on the artificial source when connected to the free chipboard plate using the inverse method.

affected by noise as indicated by the phase in Figure 6.19, although the force components are least affected.

As the data is noisy, the procedure to close gaps with negative real parts was not applied here because it is not clear that the gaps appear at troughs of the active power. Nevertheless the available data, including all gaps, was used to investigate the relative importance of moments in relation to the force. Therefore the narrow band data of the active power was normalized to the active power of the force component, F_z, as shown in Figure 6.20.

Although there are a lot of negative FFT-lines, the moment components tend to be lower than the force component between 100 Hz and 300 Hz.

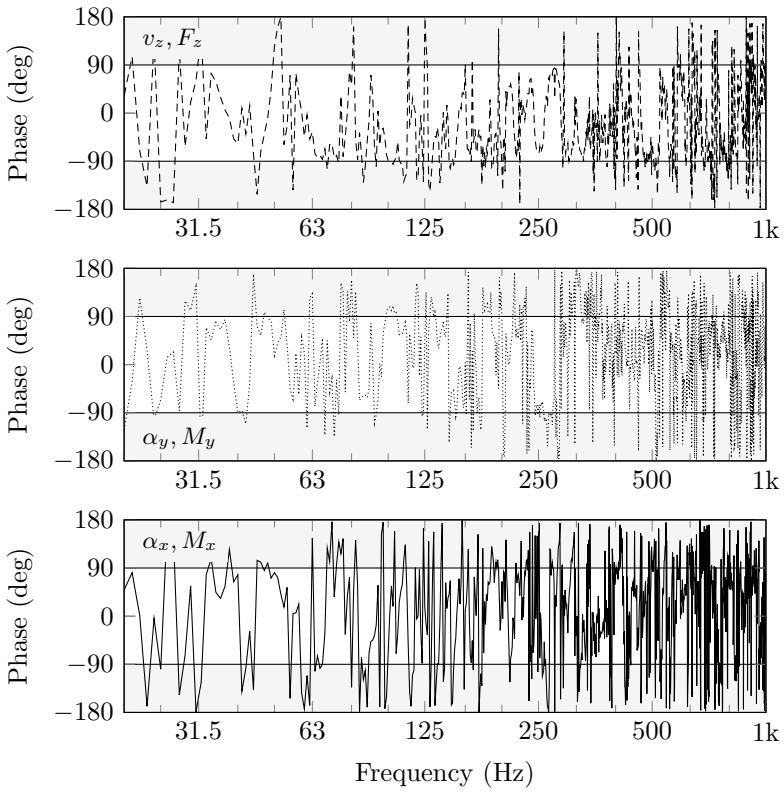

Figure 6.19: Artificial source: Phase of mobility for each out-of-plane excitation component on the free chipboard plate determined using inverse method.

6.3.1.4 Discussion

Using a shaker to inject moment power, M_x, into the chipboard plate showed that the inverse method gives a reasonable estimate of M_x when compared to the reception plate power. However there are gaps in the data due to negative real parts. These can be closed by using either zeros or the lower of the available adjacent values of the gap. For other power components the procedure is very sensitive to noise and gives unreliable results. For the artificial source with one contact point, all three components of power are noisy; hence none of them clearly dominates, although the moment components tend to be lower than the force component.

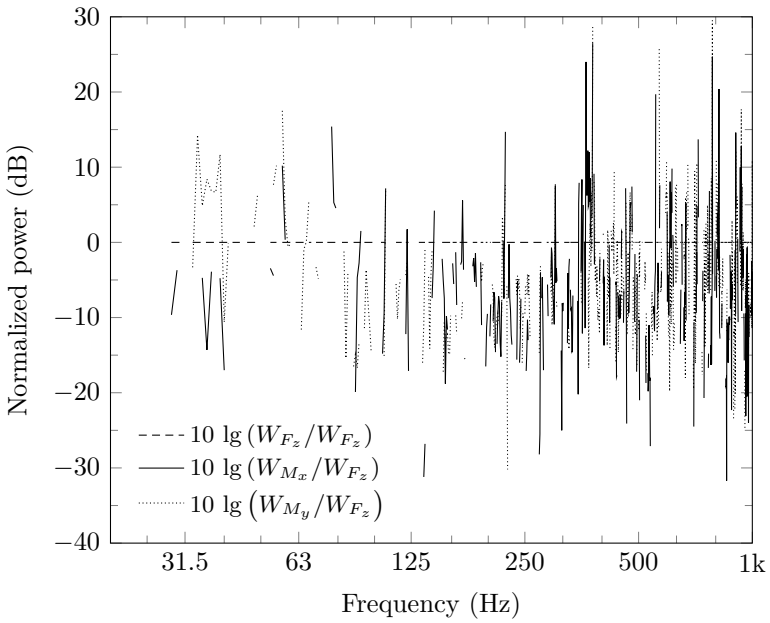

Figure 6.20: Artificial source: Force and moment power components normalized to the force component.

The next step is to use the test structure because the presence of the timber stud frame could affect the injection of moment power. The shaker parallel to the surface is used because there were clearer results from the chipboard using this source rather than the artificial source.

6.3.2 Using a timber-frame wall as receiver

Using the shaker parallel to the surface as shown in Figure 6.1 a moment about the x- and y-axis was injected into the timber-frame wall in two separate measurements where the shaker was orientated as required.

6.3.2.1 Experimental set-up

The moments, M_x and M_y as well as the angular velocities, α_x and α_y were determined using the inverse method. The experimental set-up is shown in Figure 6.21. The excitation position was chosen to be in a bay of

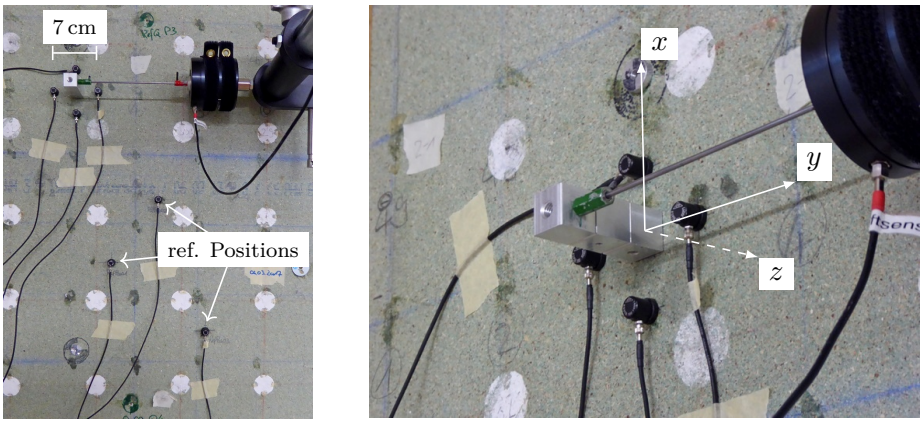

Figure 6.21: Experimental set-up that was used to excite a moment on the timber-frame structure and to measure power using the inverse method.

the timber-frame structure close to the position used in section 5.3.1.1. To obtain the required transfer functions described in section 4.5.6.5, all positions for the inverse method were chosen in one bay and on one chipboard plate to avoid transfer paths across chipboard boundaries or wall studs.

The inverse method was also applied for a shaker exciting a force perpendicular to the wall surface. Hence the test structure was excited with all three out-of-plane excitation components in three individual measurements, where the force and the moments were estimated using the inverse method.

6.3.2.2 Results

Figures 6.22, 6.23 and 6.24 show the phase of the mobility determined with the inverse method for excitation with F_z, M_y and M_x respectively. Only the phase is shown because this gives a continuous line whereas gaps occur in the real part of the power when the phase exceeds $\pm 90°$.

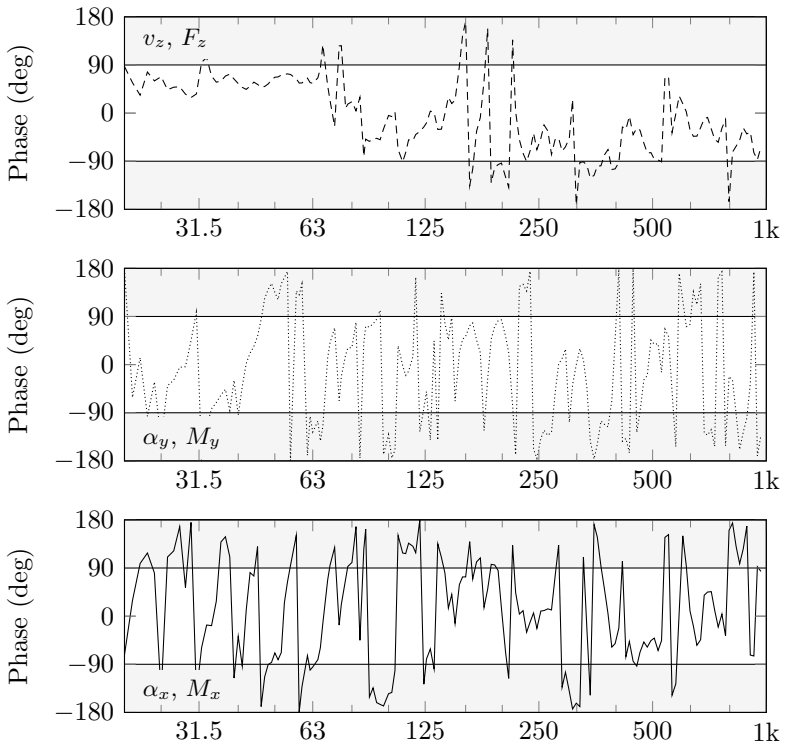

Figure 6.22: Phase of mobility for each out-of-plane component for excitation with F_z on the timber-frame structure determined using inverse method.

Similar to the results on the free chipboard plate, only the predominantly excited component gives reasonable results because the phase of the other power components is affected by noise.

However, the method described in section 6.3.1.2 to close gaps of negative real parts of the predominantly excited component can be used to determine a continuous one-third octave band spectrum of the active power that can serve as input data for models that describe the transmission across the structure.

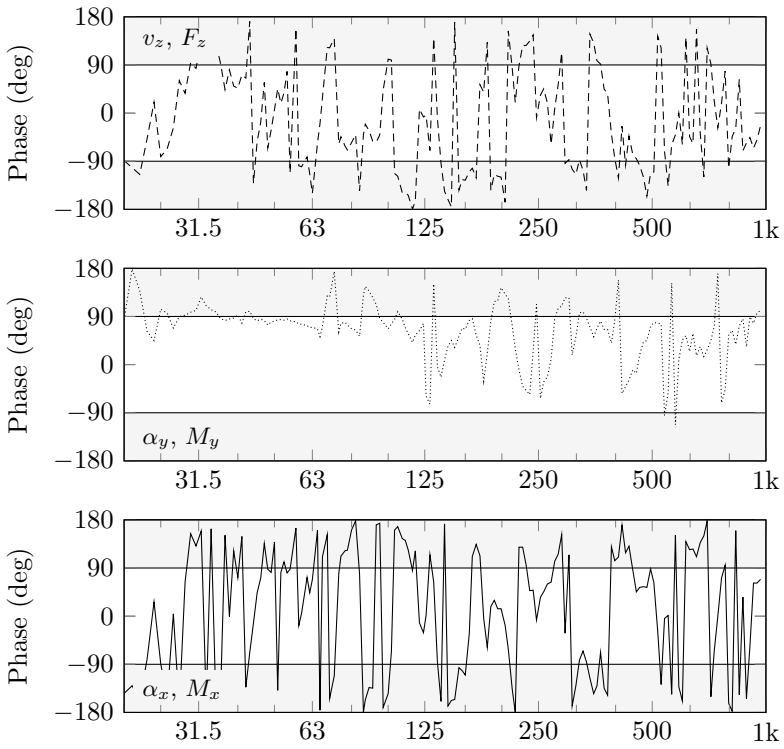

Figure 6.23: As Figure 6.22 but for excitation of M_y.

6.4 Investigation into the determination of the power input for multi-point sources

This section investigates the power input for multi-point sources using the mobility method described in section 3.3.3.2. Only the out-of-plane translational excitation component is considered. In building acoustics practical methods are preferred, hence starting from the detailed calculation described in section 4.5.6.2, five simplified approaches are applied (see section 4.5.6.3). Using the detailed calculation as reference these simplifications (briefly described in sections 6.4.1 and 6.4.2) are applied in two case studies regarding the artificial source and the real source attached to a timber-frame structure (sections 6.4.3 and 6.4.4). As the artificial source and the real source have four point contacts, the calcula-

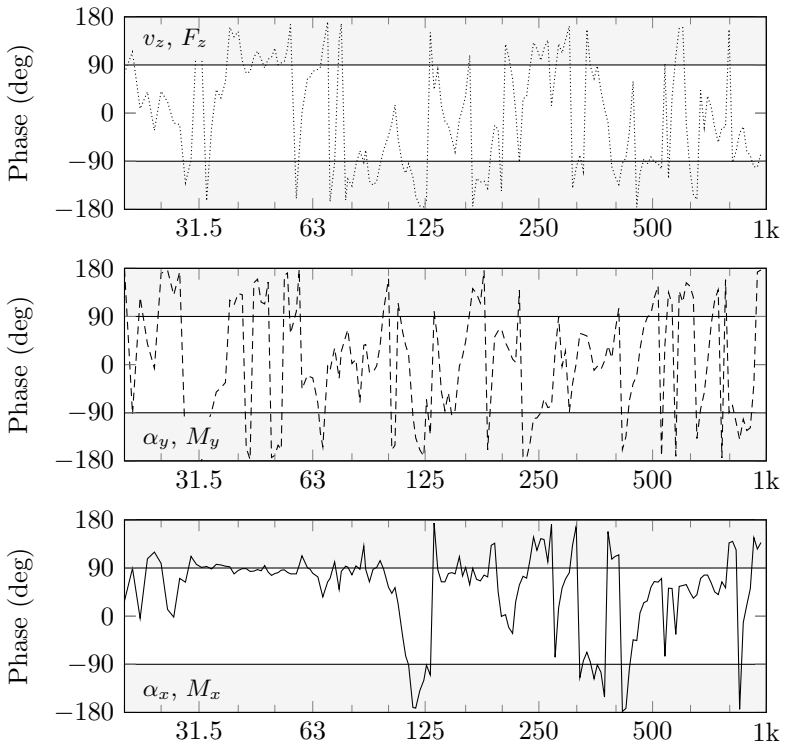

Figure 6.24: As Figure 6.22 but for excitation of M_x.

tion methods in sections 4.5.6.2 and 4.5.6.3 are described for these four points.

6.4.1 Determination of the power input using the mobility method with full mobility matrices

This method is described in detail in section 6.4.1. It uses all point and transfer mobilities for the out-of-plane translational excitation component to determine the input power. Hence a 4×4 mobility matrix is required for the source and receiver mobility. The source activity is described by the 4×1 free velocity vector. This method is denoted as "exact method".

6.4.2 Simplifications in the determination of the power input

Based on the exact method, five simplified approaches (a) to (e) are applied which are described in detail in section 4.5.6.3 and briefly summarized here:

(a) uses only point mobilities and neglects any transfer terms.

(b) also neglects transfer terms. For the point mobilities of the receiver, only one (P1) of the four contact points is used.

(c) regards each contact point as an individual point contact. The total power is then calculated by the sum of the power transmitted at each of the four contact points.

(d) uses an equivalent single contact point. Therefore the magnitudes of the source and receiver mobility as well as the real part of the receiver mobility are averaged. For the free velocities the sum of all four contacts is used. Based on that the power is calculated for an equivalent single contact point.

(e) is very similar to d), but for the receiver mobility a frequency invariant value of $1 \times 10^{-3}\,\mathrm{m/(N\,s)}$ is used.

6.4.3 Results for the artificial source on a timber-frame structure

Using the approaches described in sections 6.4.1 and 6.4.2 the power input for the artificial source attached to the timber-frame structure was calculated. For the source parameters the data described in section 6.2.3 was used. The artificial source was attached to the test structure using positions in the bay between the studs. At these positions, the receiver mobility was measured including all transfer mobilities between these four positions. The magnitudes of the measured point mobilities at these four positions are shown in Figure 6.25. It can be seen that all four

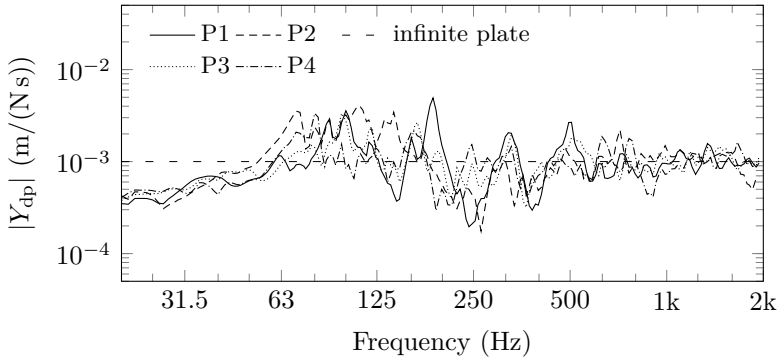

Figure 6.25: Magnitude of the receiver mobilities on the test structure to calculate the power input of the artificial source. All four positions are located between studs for comparison with the infinite plate mobility of 19 mm chipboard.

positions are similar and tend towards a value of 1×10^{-3} m/(N s) at high frequencies.

The input power for the artificial source attached to these four points is shown in Figure 6.26 in one-third octave bands. All simplifications are compared with the exact method as described in section 6.4.1. The highest differences between the simplifications (a) to (e) and the exact method occur at lower frequencies. Above 500 Hz all calculation methods tend to give similar results.

Simplified approaches (a) to (c) give similar results with <1 dB difference from the exact method above the 1000 Hz band. All three account for individual contact points but neglect any transfer terms between them. A similar study by Mayr and Gibbs [2012] showed, that neglecting transfer terms tends to overestimate the power at low frequencies. Towards higher frequencies, the contribution of the transfer terms are less and therefore the deviation is lower.

As the receiver mobility is very similar for all four points, the simplified approach (b) that uses one position which is representative for all four (P1 in this case) gives reasonable agreement with less than 5 dB difference from the exact method. As described in section 6.2.3, the spacing bet-

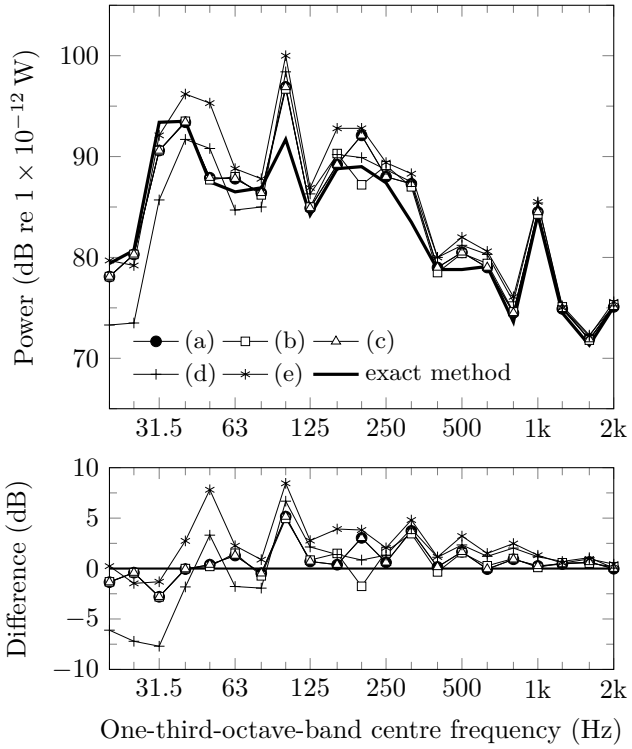

Figure 6.26: Artificial source on timber-frame structure: Calculated power input. For the estimate (e), $Y_{\mathrm{R,eq}} = 1 \times 10^{-3}\,(\mathrm{m/s})/\mathrm{N}$ was used. Simplified approaches (a) to (e) are normalized to the exact method.

ween the contact points is 62 cm on centres. This distance corresponds to one bending wavelength on the chipboard at ≈180 Hz (see Figure 5.30). Above ≈180 Hz the differences between the simplified approaches (see Figure 6.26) decrease.

Simplified approaches (d) and (e), that use one equivalent contact point show the highest deviations especially at low frequencies. However the estimates are still within ± 5 dB at and above the 125 Hz band and within ± 10 dB at lower frequencies. Although (e) uses a frequency invariant value for the receiving mobility, this estimate gives reasonable results.

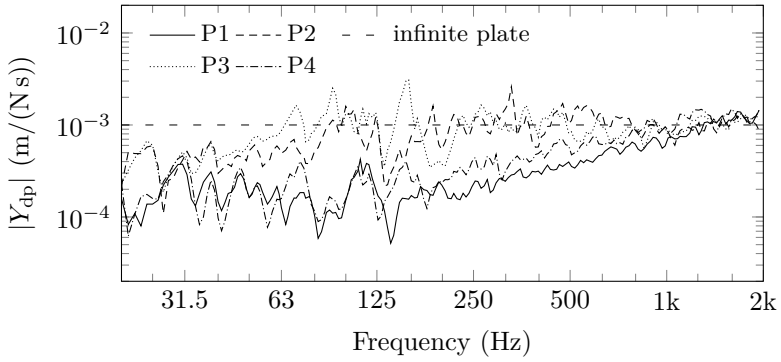

Figure 6.27: Magnitude of the receiver mobilities on the test structure to calculate the power input of the ventilation unit. Positions P2 and P3 are located between studs for comparison with the infinite plate mobility of 19 mm chipboard.

6.4.4 Results for the ventilation system on a timber-frame structure

The power input for the real source described in section 6.2.4 attached to the test structure was calculated using the approaches described in sections 6.4.1 and 6.4.2. In this case however, two contact points (P1 and P4) were above a wall stud and the other two (P2 and P3) were in a bay. The measured receiver mobilities at these positions are shown on Figure 6.27 for comparison with the infinite plate mobility of 19 mm chipboard.

Figure 6.28 shows the calculated power input using the simplified approaches and the exact method. Similarly to the artificial source, simplifications (a) to (c) that neglect transfer terms give reasonable results with deviations less than ± 3 dB except one outlier in the 400 Hz band with up to 9 dB difference to the exact method. Except this outlier at 400 Hz and adjacent bands, the simplified approaches that neglect transfer terms tend to result in an overestimate.

Simplification (b), that uses only position P1 for the receiver mobility shows larger differences from the exact method. In this case P1 has a lower mobility at low frequencies and therefore the power is underesti-

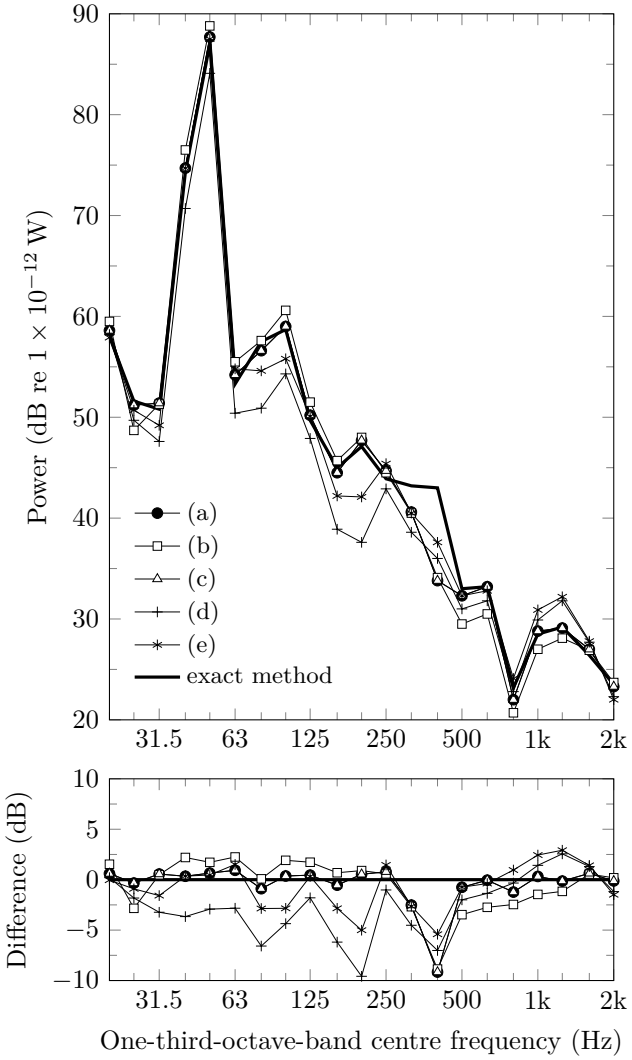

Figure 6.28: Ventilation system on timber-frame structure: Calculated power input. For the estimate e), $Y_{\mathrm{R,eq}} = 1 \times 10^{-3}\,(\mathrm{m/s})/\mathrm{N}$ was used. The simplifications (a) to (e) are normalized to the exact method.

mated because the higher mobilities of P2 and P3 are not considered. With increasing frequency all four positions tend towards infinite plate-like behaviour and therefore the differences decrease.

Simplifications (d) and (e), that approximate one equivalent contact point show the highest differences although the deviation is within ±5 dB for simplification (e).

6.4.5 Discussion

The two case studies show that for practical purposes the proposed simplification approaches to calculate the power input are reasonably close to the exact calculation using full mobility matrices, especially the approaches that only neglect the transfer terms.

Overall in practice the decision for one of the simplified approaches needs to be made based on the available data and the required accuracy. For a tonal source for example a 10 dB uncertainty in the relevant one-third octave band can be significant.

6.5 Summary

In this chapter the power input of SBS sources to timber-frame structures was investigated. This included the application of inverse methods to obtain the moment power about a single point and the determination of the power input for multi-point sources.

For experimental investigations four excitation sources were used: (a) force excitation with a shaker, (b) moment excitation using a shaker parallel to the surface of the structure in combination with a lever, (c) an artificial source with four contact points and (d) a real source (compact ventilation system).

To calculate the input power, excitation sources (c) and (d) were fully characterized experimentally. Hence the free velocities as well the source mobilities were measured on each contact point. Additionally all transfer mobilities were measured to account for interactions between the contact points. The investigations on the real source (d) indicated, that approximations for ideal point contacts have to be adopted as the contacts of real sources are often complex.

Using excitation sources (b) and (c), inverse methods were applied to quantify the moment power for the sources attached to a free chipboard plate and attached to the timber-frame structure. To verify the inverse method for the input power, the reception plate power on the free chipboard plate was used as reference.

For source (b) on a free chipboard plate it was shown, that the moment power from the inverse method gives reasonable agreement with the reception plate power. However, the inverse method is sensitive to noise at troughs of the input power, which causes negative real parts of the complex power. Therefore two approaches to overcome these problems were proposed to obtain a continuous one-third octave band spectrum of the active input power. Through comparison with the reception plate power, it was shown that it is feasible to close gaps at troughs of the power by setting negative real parts to zero. An alternative approach uses the adjacent values of a frequency range with negative real parts to close the gap but the results are similar. This experimental investigation also showed that using source (b), a moment component can predominantly be excited because the reception plate power (that contains all excitation components) resembles the moment power obtained with the inverse method.

For source (c) the input power for the three out-of-plane excitation components could not be determined properly using the inverse method. Hence source (b) was used to investigate the moment excitation on the test structure. Although the results are more noisy compared to the source attached to the free chipboard, the results can be used in combination with the approaches to close gaps of negative real parts to obtain continuous one-third octave band active power spectrum. These input data will be used for prediction of structure-borne sound transmission across the test structure in chapter 8.

The investigations concerning the determination of the input power for multi-point sources focused on the translational out-of-plane component only. Using the free velocity and the coupling conditions described by the source and receiver mobilities (mobility method, see section 3.3.3.2), the

input power for excitation sources (c) and (d) was calculated. As practical methods are required in building acoustics, five simplified approaches to the calculation of the input power were investigated and compared to the detailed model. For the prediction of the power input in building acoustic consultancy it is often not possible to measure the receiver mobility although the source parameters could be provided by the manufacturers using laboratory measurements. Hence a practical approach used a frequency-invariant value for the receiving structure that is typical for lightweight constructions. The results show promising results as the deviations were within ±10 dB in the range from 20 Hz to 2000 Hz. For intermediate simplification steps the deviations were within ±5 dB for the majority of one-third octave bands in the range from 20 Hz to 2000 Hz.

7 Prediction model based on SEA for direct transmission

7.1 Introduction

In this chapter, SEA is used to model a timber-frame wall undergoing mechanical point excitation. This concerns direct transmission across the test structure described in section 4.2, although the focus is on modelling rather than the development of a generally applicable prediction method. The aim is to assess whether predictive SEA can reproduce the decrease in vibration that was identified in chapter 5. Three SEA models were developed with an increasing degree of detail. For validation, the measured data from chapter 5 is used.

Section 7.2 identifies the test structure under consideration. In section 7.3 the different SEA models are described in terms of subsystem definition, required assumptions and CLFs and ILFs. For these models the results are given in section 7.4. In a case study that is described in section 7.5 the model with the highest degree of detail is used to predict the sound pressure level in the adjacent room for the artificial source (section 6.2.3) attached to the wall.

7.2 Test structure

Direct transmission across the lower timber-frame wall (Figure 4.1) into the adjacent room is considered. The construction details of the wall are shown in Figure 5.18, as well as excitation position 1 which is used for power injection.

7.3 Description of SEA models

This section describes three SEA models ranging from a six- to a 41-subsystem model for the timber-frame wall.

7.3.1 Six-subsystem SEA model

To model a plate-cavity-plate system with structural coupling across the timber framework as an individual subsystem, a six-subsystem SEA model is used as shown in Figure 7.1.

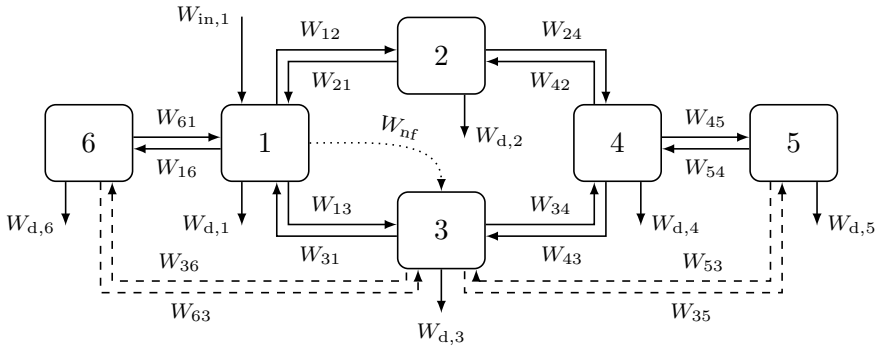

Figure 7.1: SEA model for six subsystems: (1) source leaf, (2) studs, (3) cavity, (4) receiving leaf, (5) receiving room and (6) source room (i. e. the room into which the excited leaf directly radiates). The dashed line indicates non-resonant coupling and the dotted line indicates power injection due to the nearfield.

7.3.1.1 Definition of subsystems

The source leaf is a 5.06 m × 2.59 m wall which is modelled as one subsystem; the same applies to the receiving leaf. One cavity subsystem is used to represent all cavities. It is assumed that the source and receiving leaf as well as the source and receiving room are coupled to this single cavity subsystem. Similarly one subsystem represents all wall studs. This assumes that all point connections, i. e. the screws, of the source and receiving leaf are attached to this single stud. The beam length represents that of the vertical wall studs. The horizontal studs are not included in this model.

As the source leaf is excited by mechanical point excitation, nearfield radiation, W_{nf}, into the cavity is also included as shown in Figure 7.1. The nearfield radiation according to equation (3.51) is implemented as power input from the source leaf to the cavity and is subtracted from the power injected into the source leaf. For the driving-point mobility needed to calculate W_{nf}, the infinite plate mobility was used for the source leaf. As this equation is only valid well below the coincidence frequency, the upper limit was set to $0.5\, f_{\mathrm{c}}$ [Cremer and Heckl 1967]. The radius of the washer (10 mm) used to attach the force transducer (see section 4.5.1) in the measurement was used to represent r in equation (3.51).

7.3.1.2 Loss factors

The internal loss factors of the chipboard and the timber wall studs were determined experimentally as described in section 5.2.1.3 and listed in Table 5.2. For the source and receiving room the measured reverberation time was used to determine the TLF. The ILF of the cavities was modelled as described in section 3.4.5.1 by distinguishing between the frequency range below (equation (3.91)) and above (equation (3.91)) the first cross cavity mode. Based on the findings from section 5.2.2.2 the ILF of the cavities was approximated using an absorption coefficient for the studs that linearly increases from 0.05 at 100 Hz to 0.25 at 5000 Hz and an absorption coefficient of 0.06 for the chipboard plates.

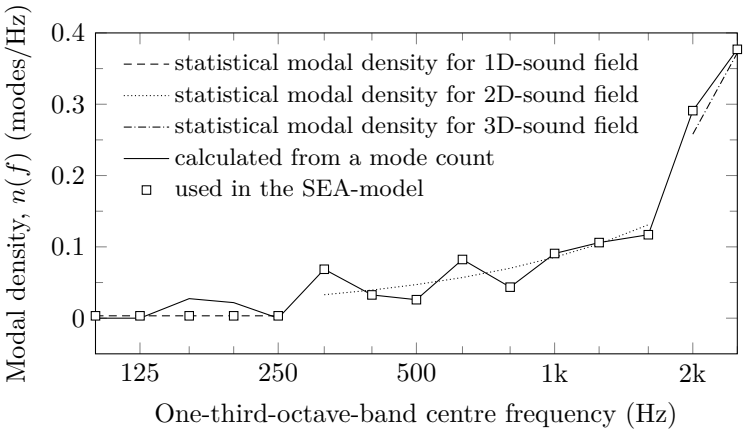

Figure 7.2: Modal density of cavity in the timber-frame wall.

The losses from the plates to the studs due to structural coupling were modelled according to section 3.4.5.2. For the plate and stud mobilities infinite plate and beam mobilities according to equations (3.57) and (3.55) were applied using the material properties given in Table 5.2. The screws were assumed to form rigid point connections. Losses due to radiation from the plates were modelled according to equation (3.97). Non-resonant coupling between the cavity and the room was modelled according to section 3.4.5.4. The consistency relationship given by equation (3.80) was used to give CLFs in the reverse direction. As the modal density is low for the studs, the statistical mode count according to equation (3.27) was used.

In the cavities one-, two- or three dimensional sound fields can occur as decsribed in section 3.4.6.2. Therefore the modal density was calculated for all three possibilities according to equations (3.104), (3.105) and (3.103). The upper limit for the 1D sound field was set to the first tangential mode, $f_{1,1,0}$. The cross over frequency from a 2D to 3D sound field was set to the first cross cavity mode $f_{0,0,1}$. The chosen modal density in the model is shown in Figure 7.2.

For the cavities, a combination of statistical mode count and mode count was used to obtain the modal density. At and below the one-

third octave band containing $f_{1,1,0}$ the statistical mode count was used. Above this frequency, the mode frequencies were calculated according to equation (3.102).

7.3.2 35-subsystem SEA model

The experimental investigations in section 5.3.1.2 showed that there is a significant decrease of vibrational energy across the wall for mechanical point excitation. To try and reproduce this decay a more detailed SEA model is used, that considers more than one subsystem for the source and receiving leaf and the cavities. This 35-subsystem SEA model considers each of the nine wall studs as an individual subsystem (horizontal studs (cross bars) are not included in the model). Hence each plate subsystem on each side is coupled to two adjacent studs as indicated in Figure 7.3. Therefore two adjacent plate subsystems share the number of point connections into each stud subsystem. Between the plate subsystems, no direct coupling is included as all transmission is assumed to occur across the studs. This gives eight plate subsystems on the source leaf, eight cavity subsystems, nine stud subsystems, eight plate subsystems on the receiving leaf and the source and receiving room subsystem, which gives 35 subsystems in total (see Figure 7.3).

7.3.3 41-subsystem SEA model

7.3.3.1 Definition of subsystems

In the 35-subsystem SEA model, the boundaries of the plate subsystems were defined along the vertical wall studs and no direct CLF was included between plate subsystems. This 41-subsystem model overcomes this approximation by considering every chipboard plate with its real dimensions as a single subsystem.

Due to complexity it was not possible to draw a comprehensive block diagram for this 41-subsystem SEA model. From Figures 7.4a and 7.4d it can be seen that this gives ten subsystems for the source and the receiving

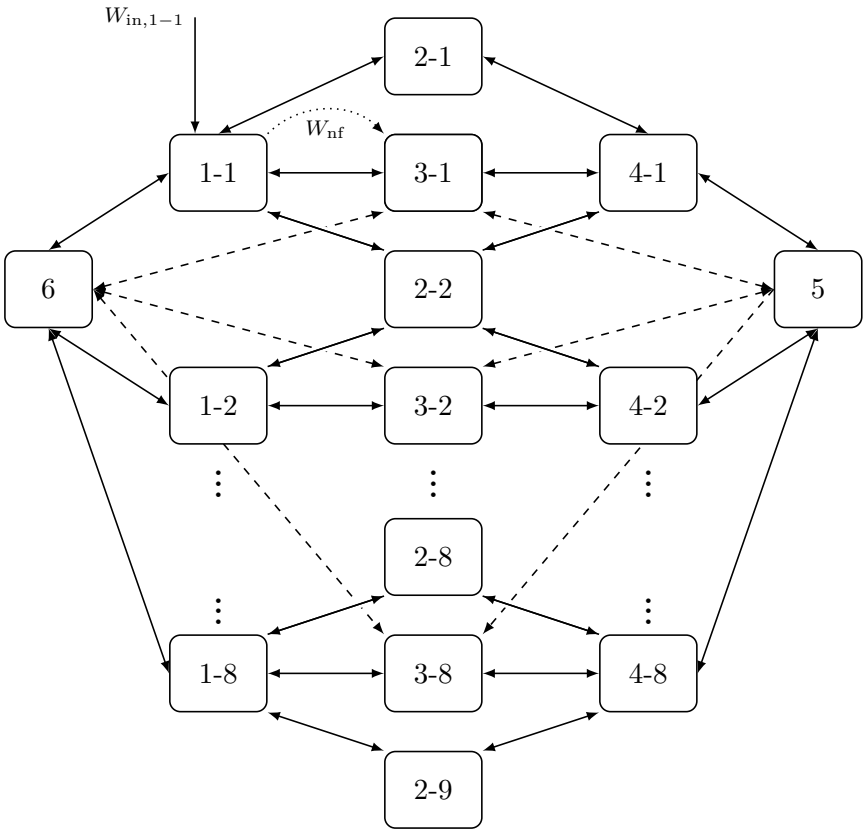

Figure 7.3: SEA model for 35 subsystems. For simplicity, ILFs are not shown and the CLFs in both directions are indicated using one double arrow. 1-1 to 1-8) Source leaf plates, 2-1 to 2-9) wall studs, 3-1 to 3-8 cavities, 4-1 to 4-8) receiving leaf plates, 5) receiving room and 6) source room. The dashed line indicates non-resonant coupling and the dotted line indicates power injection due to the nearfield.

leaves, respectively. Additionally the studs at the top and bottom of the wall are included as shown in Figure 7.4b; however, no structural coupling is incorporated between the studs.

This gives ten plate subsystems on the source leaf, eight cavity subsystems (Figure 7.4c), nine stud subsystem, ten plate subsystems on the receiving leaf, the source and receiving room subsystem and two cross bar subsystems, which gives 41 subsystems in total.

7.3.3.2 Loss factors

Across the tongue and groove joints, between individual chipoard plates a measured CLF is incorporated as described in section 5.2.3. All other CLFs are predicted.

As the plates are aligned horizontally they span across multiple cavities and fractions of cavities. This is included in the model using equation (3.97) by introducing a factor that accounts for the fractional area of the plate that covers the cavity. This yields the following form for the CLF between the plates and the cavities:

$$\eta_{ij} = \frac{\beta_{ij}\, L_{x,\mathrm{cav},j}}{L_{x,\mathrm{plate},i}} \frac{\rho_0\, c_0\, \sigma}{\omega\, m''} \tag{7.1}$$

where β_{ij} is a factor that describes the fraction of the width (x-direction) that plate i covers of the width of cavity j.

For the structural coupling, semi-infinite plate mobilities (see equation (3.56)) are used in equation (3.96) for the point connections on beams that form the perimeter of the wall (CLF of plates with subsystems 2-1, 2-8, 7-1 and 7-2, see Figure 7.4b). For the CLF of plates with wall stud subsystems 2-2 to 2-7, infinite plate mobilities are used to model the structural coupling with the plates.

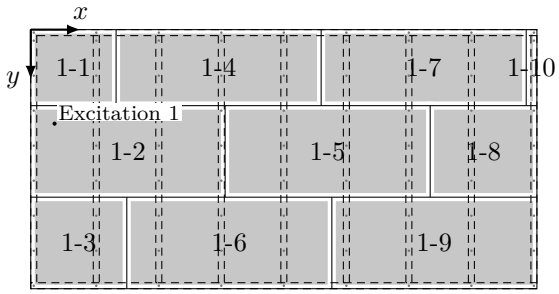

(a) Plate subsystems on source leaf

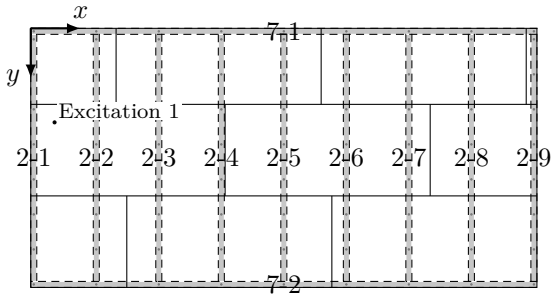

(b) Stud subsystems

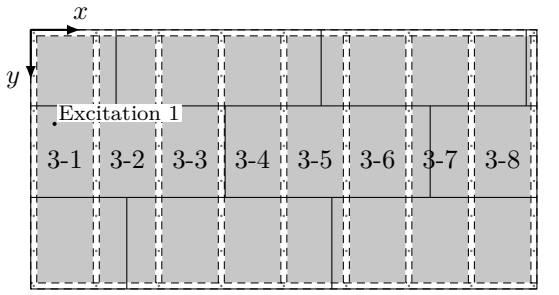

(c) Cavity subsystems

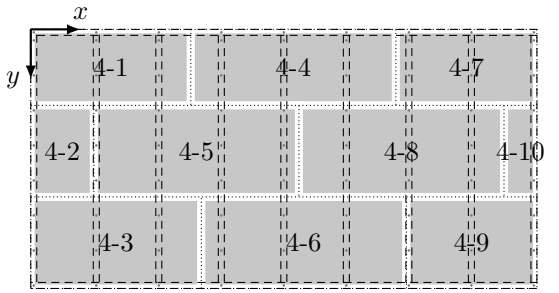

(d) Plate subsystems on receiving leaf

Figure 7.4: 41-subsystem SEA model: subsystems

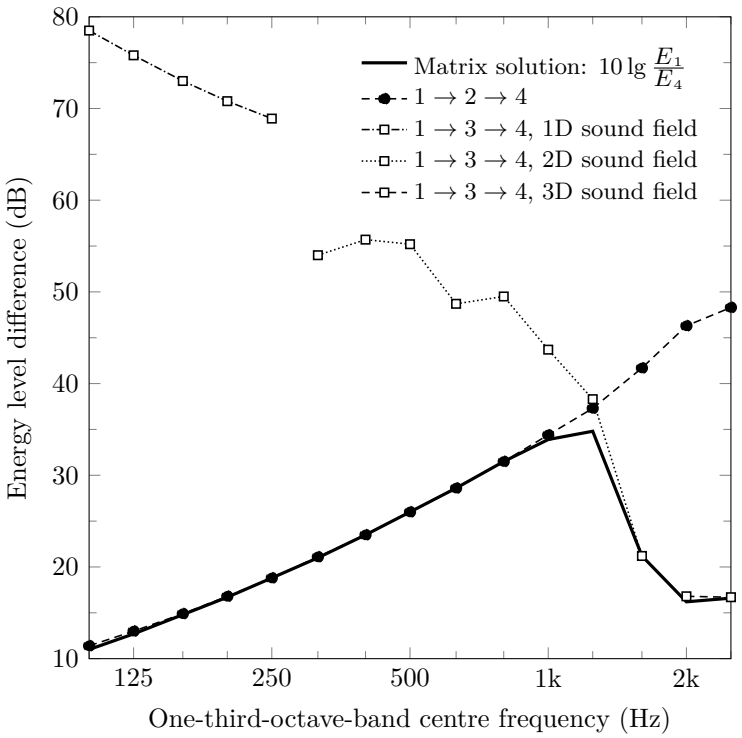

Figure 7.5: Six-subsystem SEA model: Path analysis for subsystem 1 (source leaf) to 5 (receiving room).

7.4 Results

7.4.1 Six-subsystem SEA model

Using this simple six-subsystem model, the basic features of transmission across the framework wall can be assessed using SEA path analysis (section 3.4.3). Whilst the matrix solution gives the resulting energies for each subsystem, path analysis gives the energies from an individual path. When a transmission path gives nominally the same energy level difference as the matrix solution, this path can be said to be dominant. Figure 7.5 shows the energy level difference between the source leaf (subsystem 1) and the receiving leaf (subsystem 4) for comparison with the matrix solution of the SEA model.

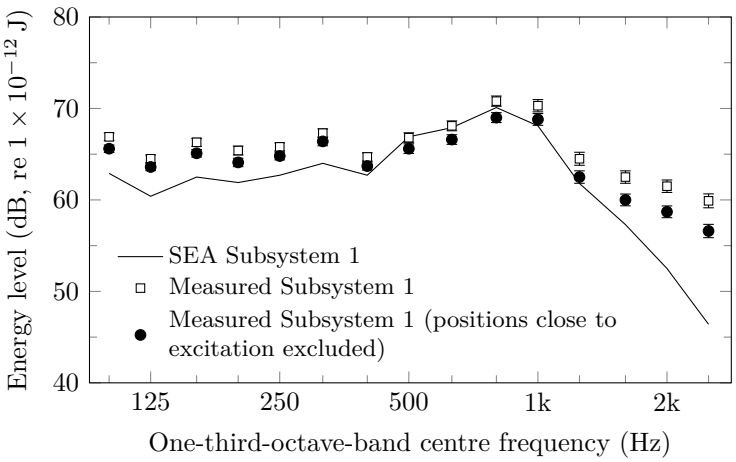

Figure 7.6: Six-subsystem SEA model: Energy in subsystem 1 (source leaf). Comparison with measured data (spatial average with 95 % confidence limits) – note that these confidence limits are very small and only just visible).

This shows that at frequencies up to 1000 Hz, the structural coupling across the timber studs (path $1 \rightarrow 2 \rightarrow 4$) dominates. Above the critical frequency, the transmission path across the sound field in the cavity is dominant. Figure 7.5 shows the three different models for the path across the cavity using the 1D, 2D and 3D assumption for the sound field in the cavity.

The energies determined from the matrix solution are compared with measured data in Figures 7.6, 7.7 and 7.8. Spatial-average velocities and sound pressure levels are converted to energies according to section 3.4.8 and are shown with 95 % confidence limits. For the measured velocities on the source leaf, accelerometer positions close to the excitation point were excluded that were within a distance of 0.5 m. This distance was chosen visually from the contour plot at 2500 Hz (Figure 5.23). An exact calculation of the reverberant distance, i. e. the distance where the direct field equals the reverberant field, is difficult as the reverberant field is dependent on the plate size and the loss factor, which are hard to identify for the tongue and grooved chipboard on the timber-framework.

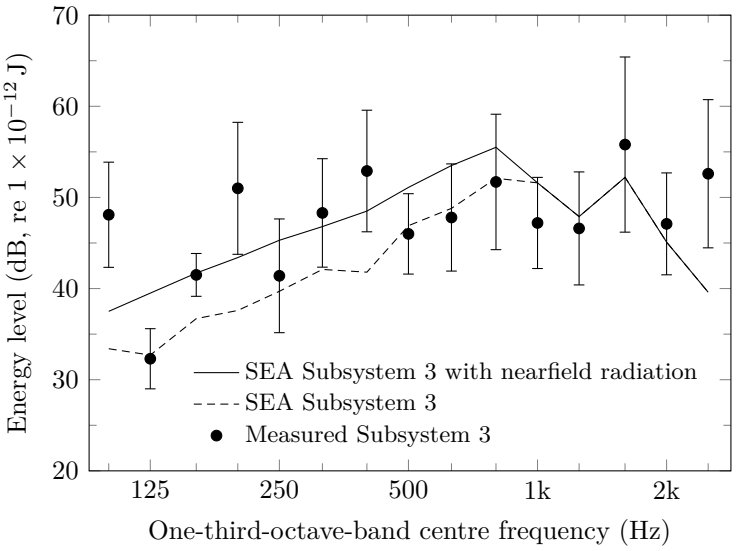

Figure 7.7: Six-subsystem SEA model: Energy in subsystem 3 (cavity). Comparison with measured data (spatial average with 95 % confidence limits).

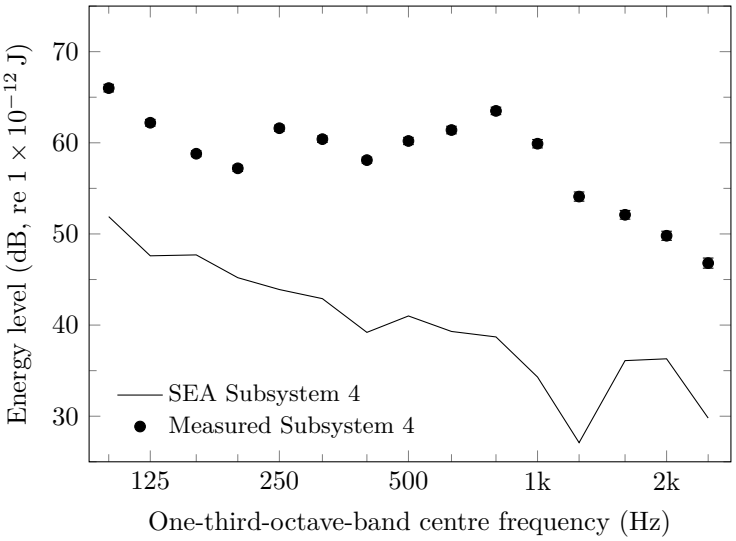

Figure 7.8: Six-subsystem SEA model: Energy in subsystem 4 (receiving leaf). Comparison with measured data (spatial average with 95 % confidence limits – note that these confidence limits are very small and only just visible).

The 95 % confidence limits of the measured velocities are narrow as 24×49 positions (excluding 32 positions close to the excitation position) were measured across the surface. For the sound pressure level in the cavities there were three measured positions in each cavity, i. e. 24 positions. This results in high 95 % confidence limits because cavities that were distant from the source had significantly lower levels (see Figure 5.46).

For the source leaf the model slightly underestimates the energy at frequencies at and below the 315 Hz one-third octave band. From 400 Hz to 1250 Hz there is close agreement with measurements, whereas at higher frequencies the model again underestimates the energy. The agreement is better towards high frequencies when measured positions close to the excitation point are neglected.

For the cavities, there is reasonable agreement between the SEA model and the measurements, however the large 95 % confidence intervals make it difficult to be definitive on the importance of the nearfield radiation in the SEA model.

Although the model gives reasonable results for the source leaf and the cavity, it significantly underestimates the energy on the receiving leaf across the entire frequency range by 10 dB to 25 dB. Therefore this simple six-subsystem model is not suitable to represent the transmission across the wall.

7.4.2 35-subsystem SEA model

To look at this model in detail, path analysis is shown for various paths between plate 1 (subsystem 1-1) and plate 2 (subsystem 1-2) on the source leaf in Figure 7.9. It can be seen that at mid and low frequencies the path along the stud (2-2) that is shared between the two plates is dominant. However at low frequencies (100 Hz to 200 Hz) the influence of longer paths including two wall studs increases. Above the coincidence frequency the path involving the airborne sound field in the source room (1-1 $\rightarrow$ 6 $\rightarrow$ 1-2) is important and therefore this room must be included in the model at high frequencies.

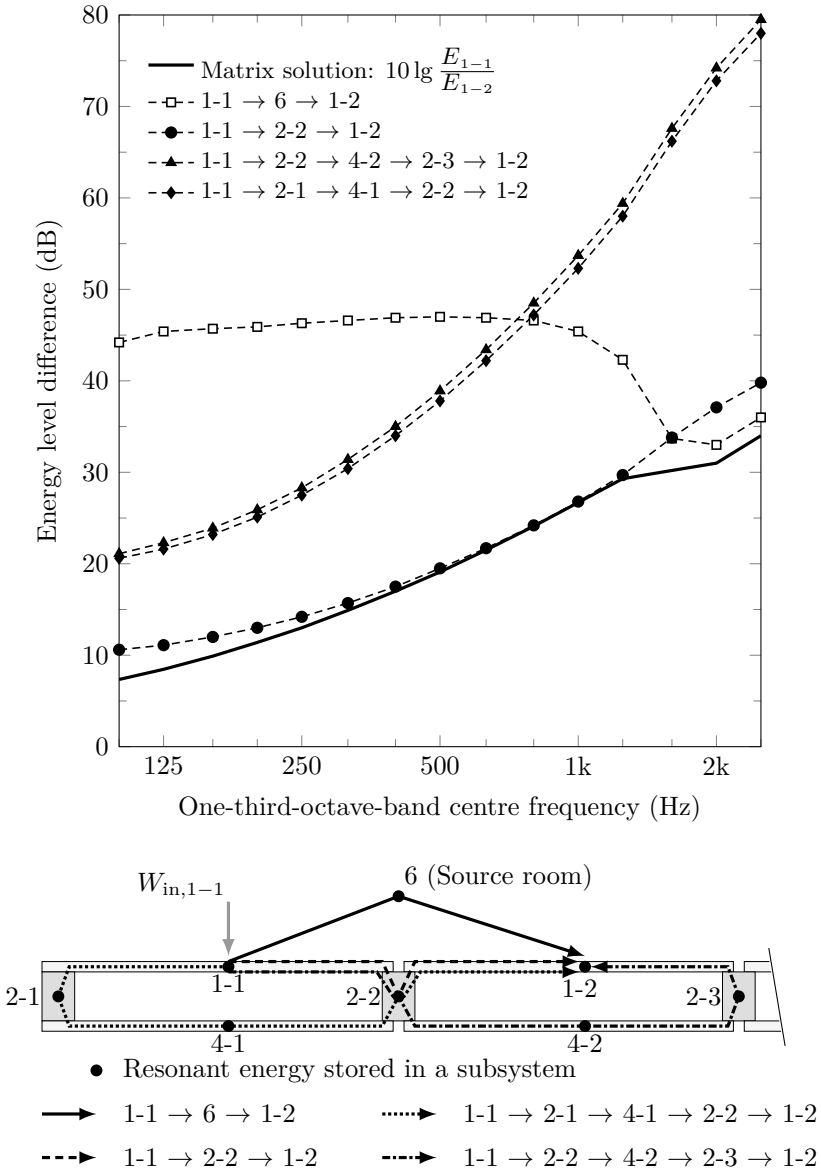

Figure 7.9: 35-subsystem SEA model: Comparison of the matrix solution with path analysis from subsystem 1-1 (source leaf, plate 1) to 1-2 (source leaf, plate 2).

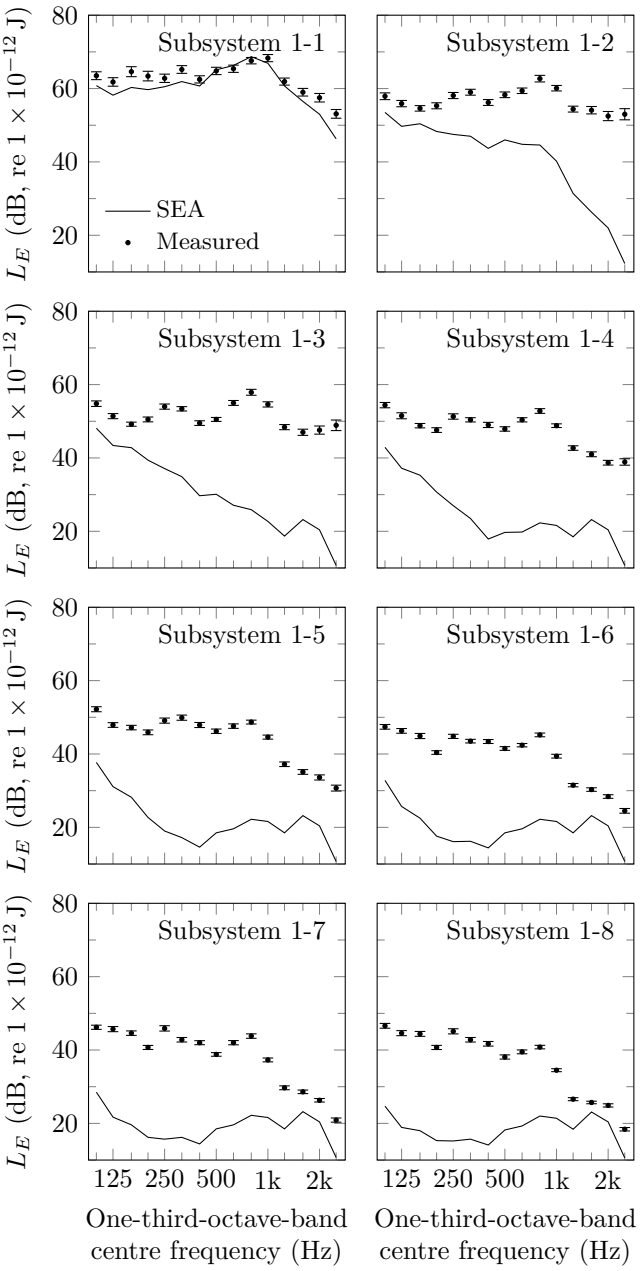

Figure 7.10: 35-subsystem SEA model: Energy in subsystems 1-1 to 1-8 (source leaf plates). Comparison with measured data.

Using the measured velocities, the energy for each plate subsystem was determined using the relevant measurement position for the spatial average. The required mass was determined from the surface density of the chipboard and the width and height of one cavity. The comparison of the measured data with SEA for the source leaf plates is shown in Figure 7.10. There is reasonable agreement for the first plate (subsystem 1-1). However, the losses across successive plates in the SEA model are too large and therefore the energy is underestimated on plates that are more distant from the source plate. This may be caused by the assumption that plate subsystems cover the individual cavities. For the plate subsystems there is no CLF between adjacent plates (see Figure 7.3). On the actual wall there are tongue and groove joints in horizontal and vertical direction between the individual plates. Hence power is transmitted more effectively in the source leaf as it is modelled in the current 35-subsystem SEA model. This leads to the consideration of a 41-subsystem SEA model, that uses plates representing chipboard sheets with their actual dimensions and a measured CLF that is incorporated for the tongue and groove joints.

7.4.3 41-subsystem SEA model

To assess the loss factors that are applied in this model, the measured TLF in the cavity (section 5.2.2.2) is compared with the predicted TLF in the SEA model (Figure 7.11).

For the CLF between the cavity and the plates, the 1D, 2D and 3D regimes can be identified by the discontinuities between the lines in Figure 7.11. The loss factors differ because of the individual fractional area of the plates that cover the cavities (equation (7.1)). For non-resonant transmission between the cavity and the rooms, two regimes below and above the first cross cavity mode can be observed following section 3.4.5.4. Although only one is visible, two identical CLFs are present for the transmission to the source and the receiving room. The sum of the ILF and the CLFs shows reasonable agreement with the measured TLF in the

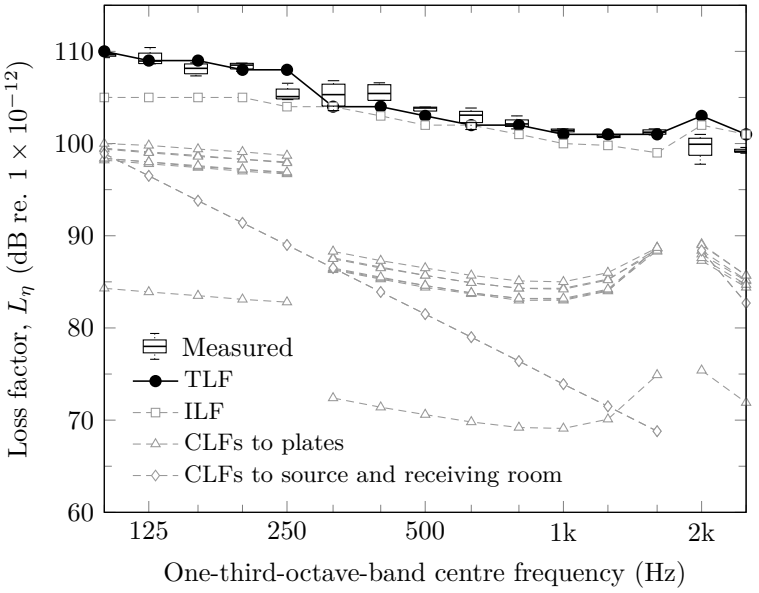

Figure 7.11: 41-subsystem SEA model: TLF of the cavity.

cavity. Slight deviations occur at the transition between the 1D and 2D sound field in the cavity which indicates some uncertainty in the cross-over frequency. At the coincidence frequency, the TLF is overestimated by about 3 dB; this is due to the difficulty in accurately predicting the radiation efficiency at the coincidence frequency [Hopkins 2007].

Using the measured surface velocities and sound pressure levels in the cavities, the predicted subsystem energies are compared with the measured energies. For the individual chipboard plates, the relevant measurement points and dimensions are used to determine the vibrational energy. Positions close to the excitation point were excluded (see section 7.4.1).

The absolute energies are shown in Figures 7.12, 7.13 and 7.14 for the source leaf subsystems, the cavity subsystems and the receiving leaf subsystems. The source leaf plate 10 (subsystem 1-10) is not shown due to its small dimensions (it is only $0.09\,\mathrm{m}^2$ compared to other boards which were at least $0.71\,\mathrm{m}^2$, see Figure 7.4a).

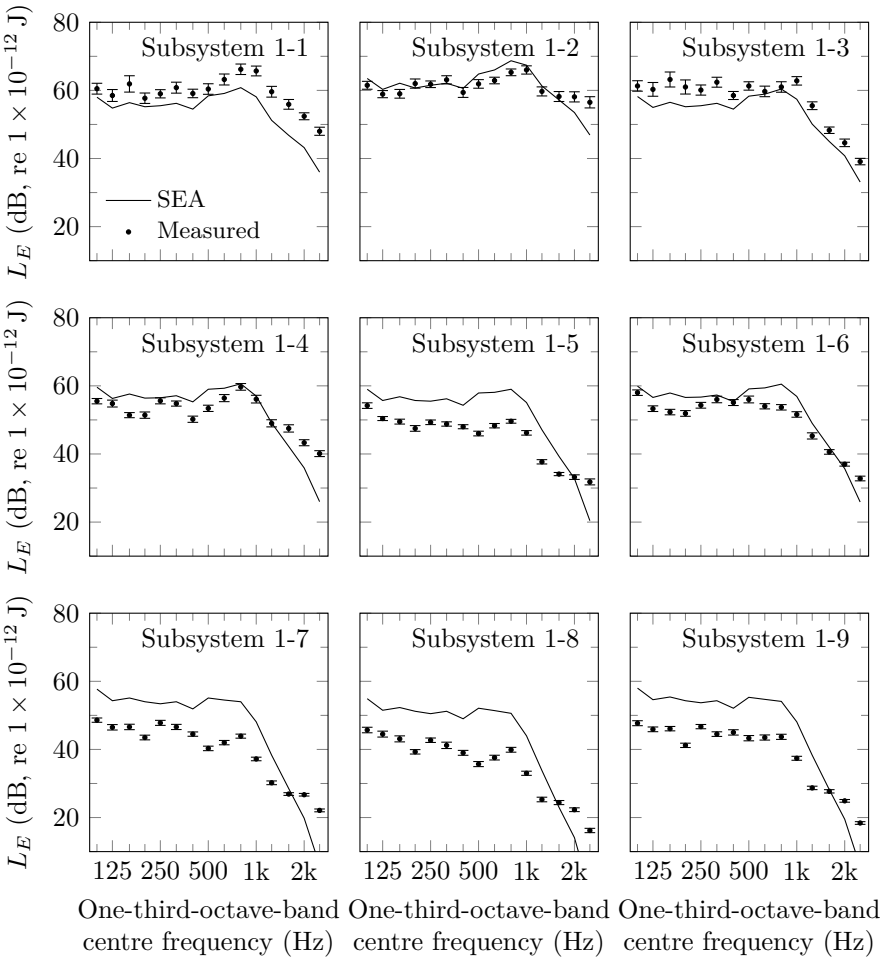

Figure 7.12: 41-subsystem SEA model: Energy in subsystems 1-1 to 1-9 (source leaf plates). Comparison with measured data.

This 41-subsystem model predicts the decrease in vibration across the x-direction from subsystem 1-2 (source) to 1-5 to 1-8 (see Figure 7.12) but the measured decrease is greater. There is close agreement for the excited subsystem 1-2; however in the other plate subsystems on the source leaf, the model overestimates the energy from 400 Hz to 1000 Hz and underestimates at and above the 2000 Hz band.

For the vertically adjacent plate subsystems 1-1 and 1-3 the model underestimates the measurement by about 5 dB to 10 dB. However the spectral shape of the predicted energy follows that of the measurement including the bands above 1250 Hz which is not the case for all other source leaf subsystems. For more distant subsystems (1-4 to 1-9) the model overestimates the energy in the range from 100 Hz to 1250 Hz. For these subsystems the agreement is closest for the vertically adjacent plates 1-4 and 1-6.

For the cavities (subsystem 3-1 to 3-8, see Figure 7.13) the model shows reasonable agreement with measurements, although only three microphone positions were used in each cavity and therefore the 95 % confidence limits are large. For cavity subsystem 3-1, which is directly behind the excitation position, the model underestimates the measurement even though nearfield radiation was included. For more distant cavities the trend indicates that the model overestimates the energy, which is consistent with the predicted energies of the source leaf plate subsystems that are distant to the excitation point.

On the receiving leaf (subsystems 4-1 to 4-10, see Figure 7.14) the trends are similar to the source leaf. The agreement is reasonable for plate subsystems that are close to the excitation point (4-1, 4-2, 4-3 and 4-5). For more distant subsystems (4-4 and 4-6 to 4-10), the model overestimates the energy and therefore underestimates the decrease with distance in the range from 100 Hz to 1250 Hz. As with the source leaf the prediction shows a significant decrease of energy with increasing frequency that is not evident in the measurement.

The difference between the measured data and the SEA model is shown in Figure 7.15, 7.16 and 7.17. To determine the difference, normalized energies were calculated for every subsystem, i, according to equation (7.2).

$$D_i = 10 \lg \frac{E_{i,\mathrm{SEA}}}{E_{1-2,\mathrm{SEA}}} - 10 \lg \frac{E_{i,\mathrm{meas}}}{E_{1-2,\mathrm{meas}}} \tag{7.2}$$

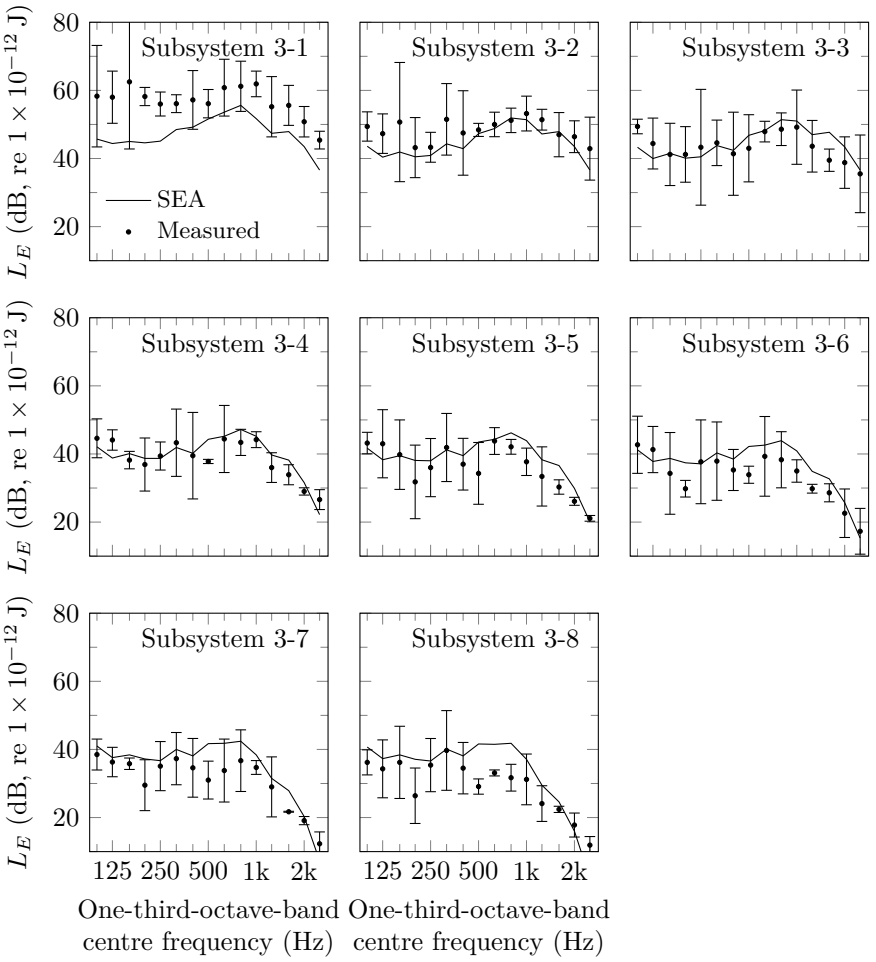

Figure 7.13: 41-subsystem SEA model: Energy in subsystems 3-1 to 3-8 (cavities). Comparison with measured data.

For the plates on the source leaf (subsystems 1-1 to 1-9), the measurements show deviations that are mainly within 10 dB. The deviations tend to increase with increasing distance from the excited plate (subsystem 1-2). The SEA model closely agrees with measurements (see Figure 7.12) for plate subsystems that are directly connected to the excited subsystem (1-1, 1-3, 1-4 and 1-6). The differences between the model and the measurements for the cavity subsystems is typically within 10 dB for cavities

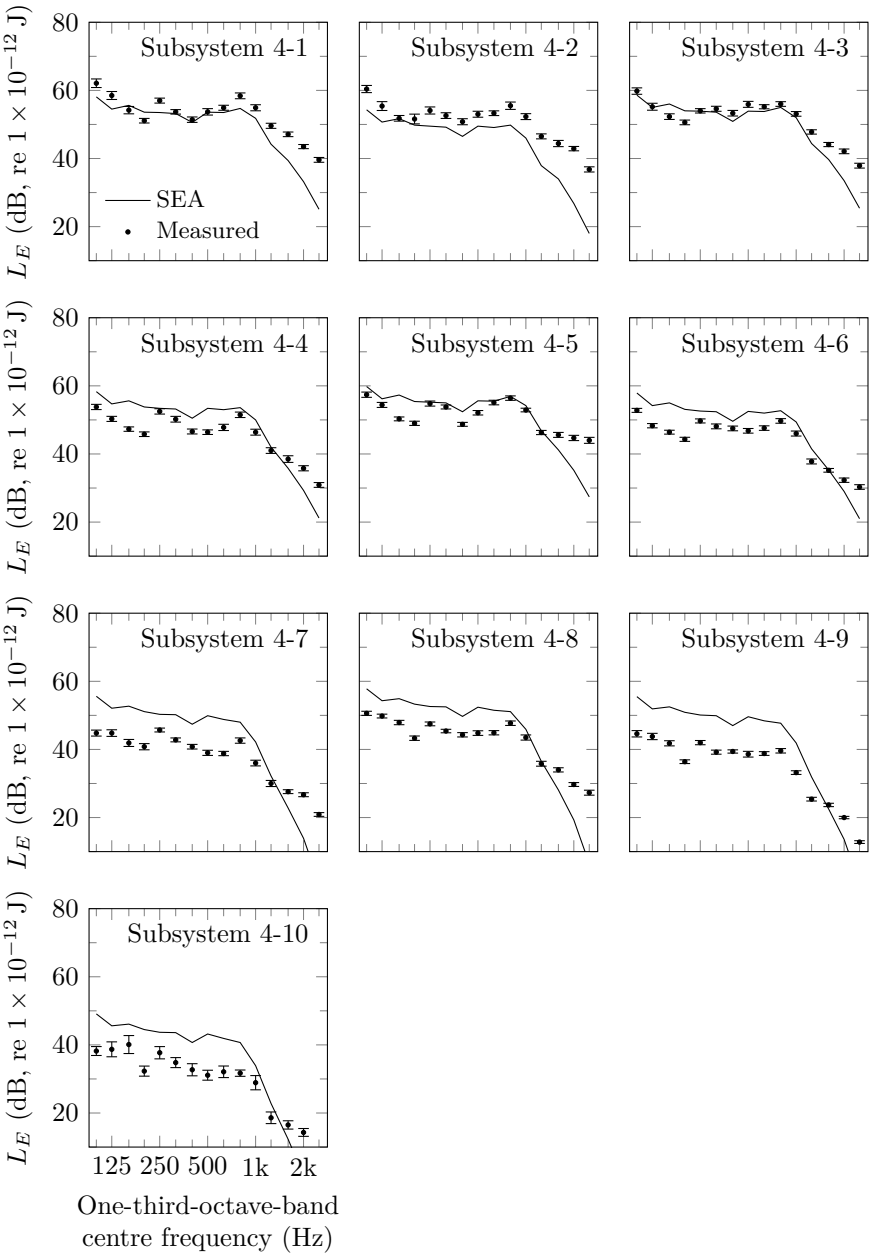

Figure 7.14: 41-subsystem SEA model: Energy in subsystems 4-1 to 4-10 (receiving leaf plates). Comparison with measured data.

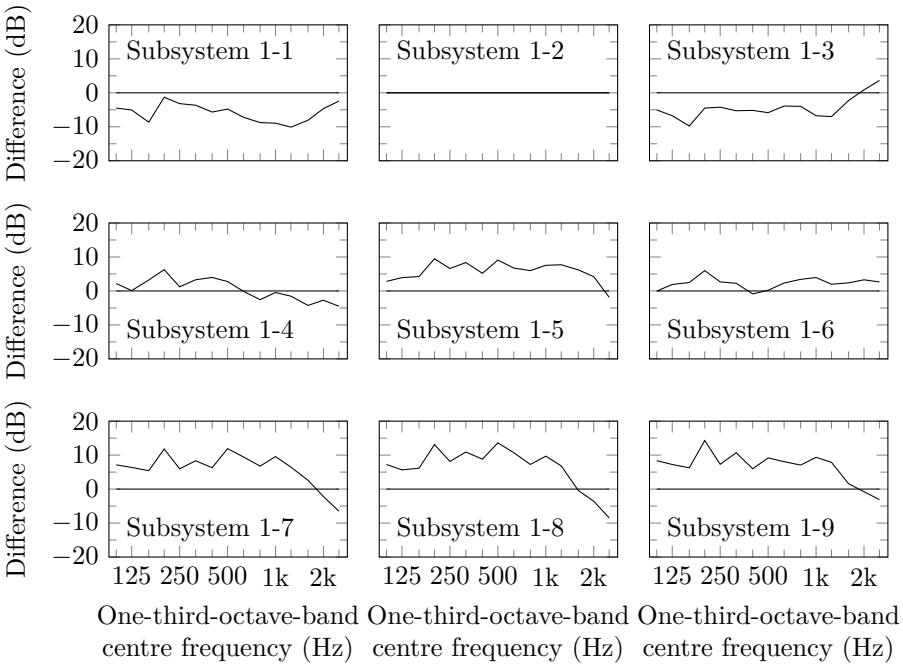

Figure 7.15: 41-subsystem SEA model: Difference between SEA and measurement for subsystem 1-1 to 1-9 (source leaf plates).

3-2 to 3-8. In cavity 3-1 which was closest to the excitation point, the differences are greater at low frequencies (up to 20 dB). On the receiving leaf the differences are mainly within 10 dB.

7.4.4 Discussion

Three SEA models with increasing complexity led from a six-subsystem model to a 41-subsystem model.

Figure 7.18 shows the modal overlap factor and the mode count for the plate, beam and cavity subsystems in the 41-subsystem SEA model. For the beams, some of the small plates and the cavities below the first tangential mode (1D sound field), the number of modes was low. The statistical mode count indicates that there are frequency ranges with values < 1 for the beams and cavities and some of the plates. As low

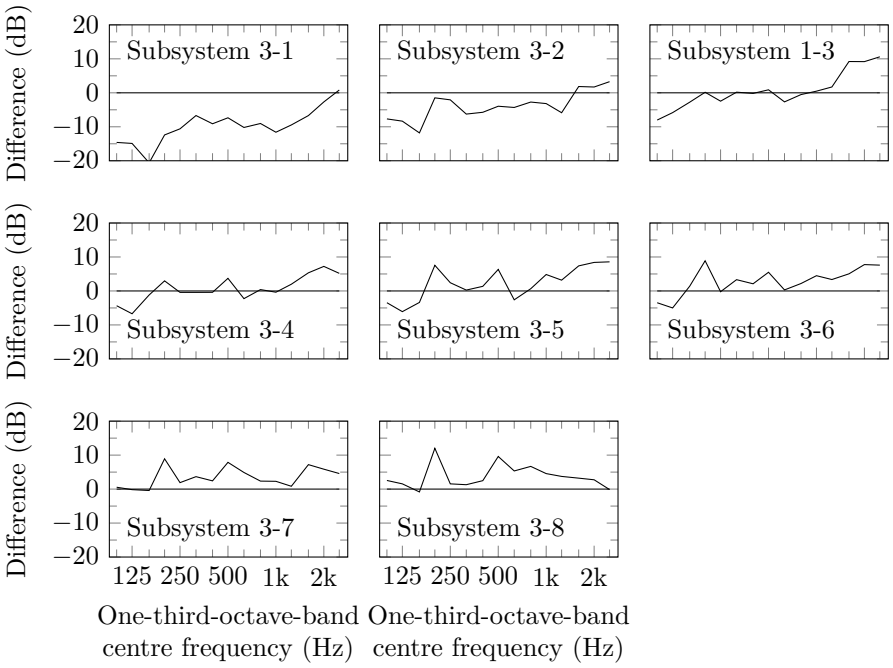

Figure 7.16: 41-subsystem SEA model: Difference between SEA and measurement for subsystem 3-1 to 3-8 (cavities).

mode counts and low modal overlap occur at low frequencies the highest uncertainties would be expected in this frequency range. However the comparison with measured data in section 7.4.3 did not show particular high deviations towards low frequencies. This is similar to what is seen with heavyweight walls and floors which can also have fractional mode counts [Hopkins 2007]. With the lightweight timber-frame wall, there will be global modes even when the local mode count is < 1, and this is likely to partly overcome issues with fractional mode counts [Hopkins 2002].

One potential uncertainty concerns the coupling at the tongue and groove chipboard joints. Although the CLF was measured on isolated chipboard plates and in-situ (section 5.2.3), it may not apply to all joints on the timber-frame wall, because the joint might behave differently when it is closer to a wall stud or aligned parallel to a stud.

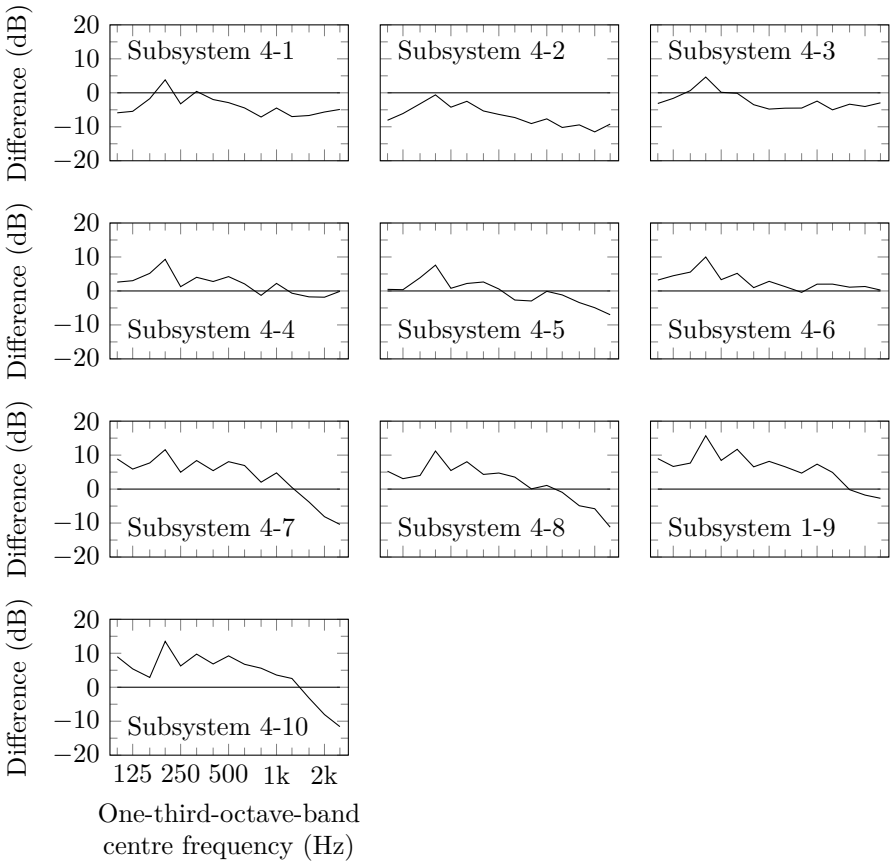

Figure 7.17: 41-subsystem SEA model: Difference between SEA and measurement for subsystem 4-1 to 4-10 (receiving leaf plates).

Another assumption is made in the coupling between the plates and the cavities. The applied model of Leppington et al. [1982] for the radiation efficiency was validated experimentally (section 5.5.2) which gave reasonable agreement. As one chipboard plate subsystem can span across two or more cavities, fractional areas have to be used in the calculation of the CLF between the plates and the cavities (equation (7.1)). However the validation of the TLF of the cavity showed that the predicted CLFs and the ILF gave reasonable agreement with the measured TLF.

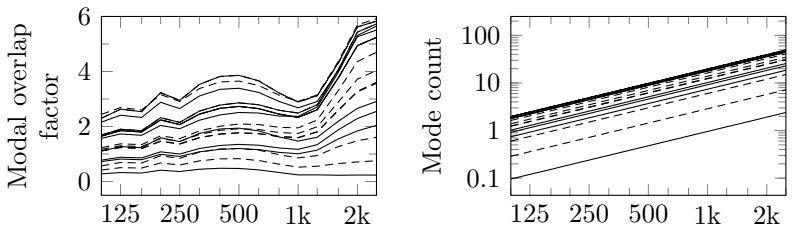

(a) Plates (solid: Source leaf subsystems, dashed: Receiving leaf subsystems)

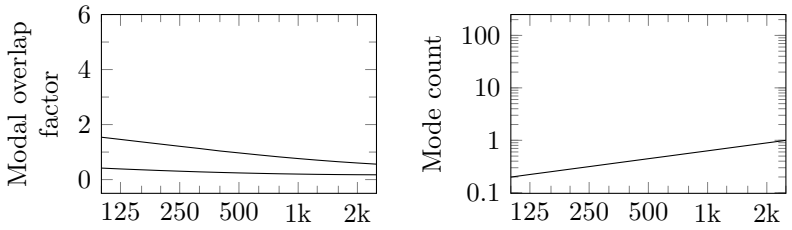

(b) Vertical wall studs

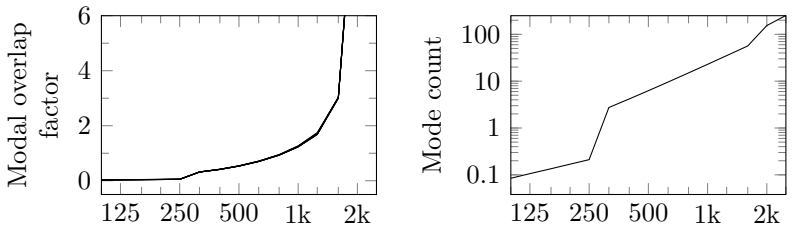

(c) Cavities

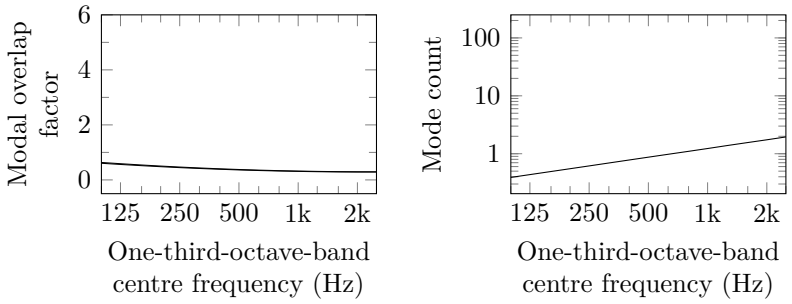

(d) Horizontal cross bars

Figure 7.18: 41-subsystem SEA model: Modal overlap factor, M and mode count, N.

The structural coupling between the plates and the timber-framework was modelled using point connections and infinite or semi-infinite mobilities for studs and plates which can potentially cause uncertainties towards low frequencies where modal behaviour is present. Galbrun [2010] observed fluctuations at low frequencies due to low number of modes in experiments that concerned the velocity level difference between two plates that were screwed to a beam. However previous experimental validations by Craik and Smith [2000b] for similar structures showed the applicability of the model with infinite beam and plate mobilities down to 80 Hz.

Craik and Smith [2000b] suggested a rule of thumb (screw spacing = $\lambda_{B,p}/2$) for the transition between modelling point-connected plates and beams as line connections or point connection (see also section 5.3.1.5). In Figure 5.30 it can be seen that this corresponds to a frequency of ≈140 Hz for the test structure that is concerned. Hence the point connection model applies for the majority of the frequency range shown in this chapter. In addition Galbrun [2010] showed that the theory is still reasonable at frequencies below the transition frequency according to this rule of thumb.

At frequencies above 2000 Hz Craik and Smith [2000b] and Galbrun [2010] found that the point connection model deviates from measurements. The comparison with measurements in Figures 7.12 and 7.14 also indicates a different behaviour at high frequencies above 1600 Hz. For the majority of the plate subsystems on the source and all plate subsystems on the receiving leaf, the model underestimates the energy above this frequency. However this is not as pronounced for plate subsystems 1-1 and 1-3, that are directly adjacent to the excited plate 1-2. For more distant plates that include paths across the timber-framework, similar deviations occur as observed by Craik and Smith [2000b] and Galbrun [2010].

Considering the energies for the validation from measured data, the direct field potentially causes uncertainties as this is not covered by the

SEA model. Hence measurement points within the reverberation distance were omitted when calculating the spatial average velocity.

In summary the model is reasonable at and below 1600 Hz for the source plate (subsystem 1-2) and adjacent plates on the source leaf (1-1, 1-3, 1-4 and 1-6). Reasonable agreement with measurement can also be observed for plates on the receiving leaf that are close to the excitation point (4-1, 4-2, 4-3 and 4-5). The trend for the cavities indicates that the model works for all cavities except the cavity closest to the excitation point (3-1).

However above the 1600 Hz one-third octave band the SEA model shows different behaviour to the measurement. As noted by Galbrun [2010] at high frequencies this could be due to the point connection model not working because of the one-dimensional modelling of the beams. Although the decrease in vibration can be modelled, the transmission is still overestimated. However the decay with distance is significant and therefore the uncertainties for the distant subsystems are potentially not important when direct transmission across the wall is considered. As the 41-subsystem model is the more accurate of the three models it is now used to assess the artificial source in a case study.

7.5 Case study using the artificial source

Using the 41-subsystem SEA-model the power input of the artificial source (section 6.2.3) was used to predict the sound pressure level in the receiving room (subsystem 5) for direct transmission. Measured data is used to assess the model.

7.5.1 Description

The artificial source was attached to chipboard plate 2 (subsystem 1-2) on the source leaf with all four feet. Two contact points were attached to the chipboard in the first bay (i. e. between vertical studs) and the two other contact points in the second bay. Hence the power input is

in the same subsystem as for the validation with point excitation from a shaker described above. Because the force at each contact point could not be measured, nearfield radiation into the cavities as described in sections 7.3.1 was not considered in this case study. The source was operated with the same signal and settings that were used to determine its free velocity (section 6.2.3.2). To obtain the input power, the full mobility matrix was measured on the receiving structure to determine the installed power according to section 6.4.1. With the source in operation, the sound pressure level was measured in the receiving room. The measured data was corrected for possible airborne flanking and background noise.

7.5.2 Results

Using the installed power, the energy in the receiving room was determined from the matrix solution of the 41-subsystem SEA model and converted to a sound pressure level according to equation (3.112). The comparison between the SEA model and the measured spatial average sound pressure level is shown in Figure 7.19. The sound pressure level predicted with the 41-subsystem SEA model is in reasonable agreement with the measurement at and below the 315 Hz one-third octave band. Near the 1000 Hz one-third octave band the model underestimates the sound pressure level by $\approx$ 10 dB and up to $\approx$ 20 dB at 2000 Hz. This underestimation of the SEA model was also observed for the energies on the plates described in section 7.4.3. On the receiving leaf (subsystems 4-1 to 4-10) the model underestimates the energy particularly for the plates close to the excitation source which are the most important in terms of the radiated power to the adjacent room. Another potential reason for the underestimation of the sound pressure level is potential flanking transmission via the timber-joist floor (see Figure 4.3) as the SEA-model only concerns direct transmission across the wall. Additionally the installed power according to section 6.4.1 considers only out-of-plane force excitation and therefore the prediction tends to underestimate although the results in section 6.3.1.3 indicated that force excitation dominates.

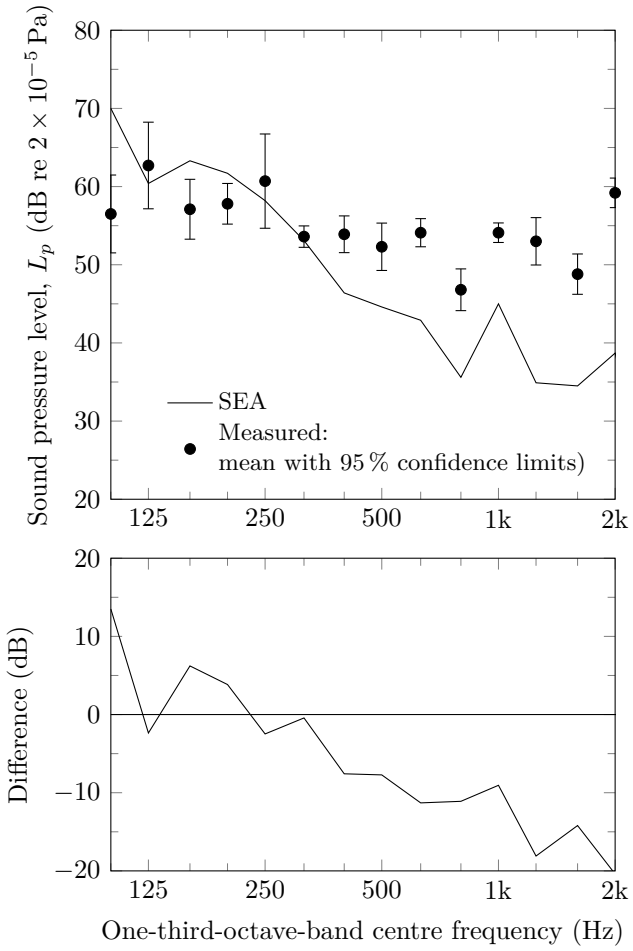

Figure 7.19: 41-subsystem SEA model: Case study with artificial source. Sound pressure level in receiving room due to direct transmission.

7.6 Summary

SEA was used to model a timber-frame wall undergoing mechanical point excitation. Predictive SEA was applied to model the structural coupling between the plates and the framework, the coupling between the plates and the rooms or cavities and the non-resonant coupling between the

rooms and cavities. A measured CLF was used on a pair of isolated plates joined by a tongue and groove joint.

To model the decrease in vibrational energy across the wall it was shown that it is necessary to use an SEA model that subdivides the wall into subsystems for each building element, i. e. plates and beams, to reproduce the decrease in vibration across the wall. Additionally assumptions are necessary to predict the CLFs coupling between the plates and the cavities as the plates can span across two or more cavities and therefore fractional areas radiate into these cavities. For the structural coupling between the chipboard and studs, point connections are assumed and infinite and semi-infinite mobilities are applied.

Three SEA models were considered using six, 35 and 41 subsystems. The 41-subsystem model was the most successful at predicting the response on individual sheets of chipboard and in each cavity although there were errors up to 10 dB in some frequency bands. In addition the model can be used to gain insight into the transmission process using path analysis.

It is concluded that predictive SEA can be used to model a timber-frame structure undergoing local mechanical excitation if errors up to 10 dB can be accepted on some subsystems. The case study using the artificial source (with four contact points) showed that the predicted sound pressure level gives close agreement with measurements below 500 Hz with a 10 dB error near 1000 Hz and a 20 dB error near 2000 Hz. For some building machinery these errors are not problematic as there will be insignificant power input above 500 Hz [e. g. see Scheck et al. 2016].

Approaches based on FEM are an alternative. However these require detailed information about the actual boundary conditions and material properties. Additionally the modelling effort is high, requires significant computational power and measurements are still necessary to identify damping parameters.

Therefore the next chapter focuses on an a practical approach for the prediction of the resulting sound pressure level from machinery.

8 Simplified model based on measured transmission functions

8.1 Introduction

The previous chapter investigated the application of SEA to model a timber-frame wall undergoing mechanical point excitation. The focus was on modelling the response of the structure rather than the prediction for specific machinery. This chapter aims to facilitate prediction by introducing an empirical approach based on measured transmission functions that relate the spatial-average sound pressure level in a room to the installed structure-borne sound power.

In general transfer functions are a useful tool in the identification of complex forms of excitation over many degrees-of-freedom and for noise control where there is a specific excitation point and a specific receiver point. However, they are less well-suited to the determination of spatial-average sound pressure levels in rooms with uncertain or undefi-

ned excitation positions for the machinery and therefore the concept of transmission functions is introduced.

The measurement protocols and the definition of a transmission function, D_{TF} were presented in [Schöpfer et al. 2017] and included in [ISO 10848-1:2017].

This approach aims to facilitate the prediction of machinery noise in lightweight timber buildings. A transmission function, D_{TF} combines all transmission paths from the power injected at one or more source positions on an element to a spatial average sound pressure level in a receiving room. For horizontal and vertical adjacent rooms this includes direct and flanking paths. For diagonally adjacent or distant rooms all flanking paths are included. As a power based descriptor is used, this approach is aligned with SEA or SEA based methods but also with descriptors such as transmission coefficients for airborne sound insulation.

Section 8.2 describes the protocols for the measurement of transmission functions. To assess these protocols, experimental investigations were carried out in the laboratory and the field, which are described in section 8.3. These included case studies in which this empirical approach is applied to estimate machinery noise using the predicted installed structure-borne sound power (see section 6.4) and measured transmission functions. Section 8.4 gives the results of the laboratory and field investigations as well as results of the case studies.

8.2 Definition and general principle

8.2.1 Definition of transmission function, D_{TF}

The fundamental assumption in this procedure is that there is a linear time invariant system. For typical machinery in buildings this can reasonably be assumed. The transmission function is given as the ratio between the spatial-average squared sound pressure in a receiving room to the injected/installed structure-borne sound power on a building element. For the power injected at a position k, the transmission function,

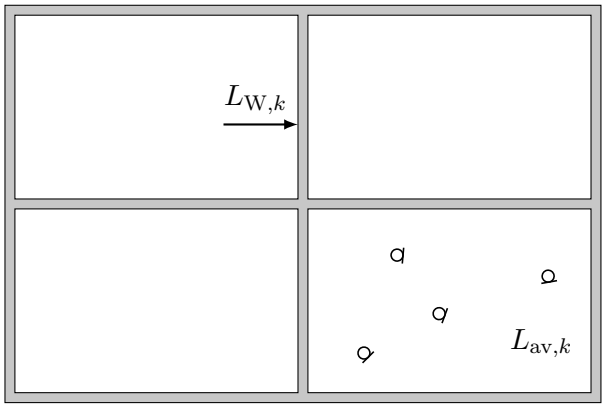

Figure 8.1: Principle to determine a transmission function $D_{\mathrm{TF},k}$ for power input at a position k on a wall.

D_{TF}, can be written in the following form using a level difference

$$D_{\mathrm{TF},k} = L_{\mathrm{av},k} - L_{W,k} \tag{8.1}$$

where $L_{W,k}$ is the injected structure-borne sound power level in one-third octave bands at position k and $L_{\mathrm{av},k}$ is the resulting spatial average sound pressure level in one-third octave bands in a receiving room (see Figure 8.1).

To obtain a spatial average of K excitation positions across the excited wall or floor, the spatial-average transmission function, $D_{\mathrm{TF,av}}$, is given by

$$D_{\mathrm{TF,av}} = 10\,\mathrm{lg}\left(\frac{\sum_{k=1}^{K} 10^{0.1\,D_{\mathrm{TF},k}}}{K}\right) \tag{8.2}$$

To allow the comparison of transmission functions for different receiving rooms, the standardized spatial-average transmission function,

$D_{\mathrm{TF,av,n}T}$, is given by

$$D_{\mathrm{TF,av,n}T} = D_{\mathrm{TF,av}} - 10\,\mathrm{lg}\left(\frac{T}{T_0}\right) \tag{8.3}$$

where T is the reverberation time in the receiving room and T_0 is the reference reverberation time of 0.5 s. Alternatively, a normalized spatial-average transmission function, $D_{\mathrm{TF,av,n}}$ can be defined using the absorption area.

8.2.2 Determination of power input

For the structure-borne sound power input any individual excitation component or the sum of forces and moments as well as out-of-plane and in-plane components can be considered. However for the experimental determination of the transmission function, the out-of-plane force component is most conveniently applied using a shaker or modal hammer and the direct method to obtain the input power, described in section 4.5.6.1.

The work presented in this chapter mainly uses the direct method. In addition, to investigate moment excitation, the data obtained the with the inverse method (see section 6.3) is used. For both methods, the narrow band data of the active power is summed to one-third octave bands to be used in equation (8.1).

8.2.3 Determination of spatial average sound pressure level

The spatial-average sound pressure level is measured using fixed microphone positions. For each position, the narrow band squared sound pressure is summed to one-third octave bands and converted to sound pressure levels. The one-third octave band sound pressure levels are corrected for background noise if necessary using the procedure described in [ISO 16283-1:2014-06].

Using these corrected sound pressure levels for M positions in the receiving room, the spatial-average sound pressure level for structure-

borne sound power input at position k is determined according to

$$L_{\mathrm{av},k} = 10\,\mathrm{lg}\left(\frac{\sum_{i=1}^{M} 10^{0.1\,L_{p,i,k,\mathrm{corr}}}}{M}\right) \tag{8.4}$$

For low frequencies, the corner measurement procedure described in [ISO 16283-1:2014-06] can be used for the 50 Hz, 63 Hz and 80 Hz one-third octave bands for receiving rooms smaller than 25 m^3. As machinery noise is a problem at low frequencies including the range below 50 Hz, the 20 Hz, 25 Hz, 31.5 Hz and 40 Hz one-third octave bands were also concerned. Therefore the same procedure was applied as it has been validated down to the 20 Hz or 25 Hz one-third octave band in room volumes ranging from 18 m^3 to 245 m^3 [Hopkins and Turner 2005; Simmons 1999]. For this procedure additional measurement positions in the corners are required. Although [ISO 16283-1:2014-06] uses four corner positions, the results presented in this chapter were determined using only two corners due to time constraints. Using the highest corner levels for each of the relevant one-third octave bands, the low-frequency energy-average sound pressure level at low frequencies is calculated according to

$$L_{\mathrm{av},k,\mathrm{LF}} = 10\,\mathrm{lg}\left(\frac{2\cdot 10^{0.1 L_{\mathrm{av},k}} + 10^{0.1 L_{\mathrm{av,corner},k}}}{3}\right) \tag{8.5}$$

If necessary the spatial-average sound pressure level can be corrected for airborne flanking transmission. Therefore the sound pressure level is also measured in the source room during structural excitation. Using a measured airborne sound level difference the airborne flanking contribution can be determined. Three cases are considered: (a) when the contribution of the airborne path is 10 dB below the total level in a band. In this case the measured total sound pressure level is used without correction for this one-third octave band. (b) when the difference between the airborne contribution and the total sound pressure level is between 0 dB to 10 dB in a band, the airborne contribution is energeti-

cally subtracted from the total level in this band. (c) when the airborne contribution in a one-third octave band is higher than the sound pressure level due to the structure-borne path, the measurement is rejected.

8.2.4 Steady-state and transient excitation

To determine the power input with steady-state excitation from a shaker, a force transducer (in combination with accelerometers) or an impedance head needs to be fixed to the receiving structure. This is possible on timber structures, however it is more difficult on brittle materials such as plaster or plasterboard.

With steady-state excitation broadband noise can be used. However when measuring sound pressure levels with microphones in distant rooms it is important to achieve sufficiently high S/N ratios. This can be an issue at high frequencies in timber-frame buildings due to isolated double-leaf constructions and relatively high internal losses. A Maximum Length Sequence (MLS) or swept-sine signal can be used to overcome this problem but this increases the measurement time.

Transient excitation with a modal hammer is a quick method that requires less time to set-up as a shaker excitation. This is well-suited to field measurements where short transients are advantageous when there is intermittent background noise from traffic or construction work. However in lightweight constructions with plasterboard surfaces the upper frequency limit using a force hammer with a metal tip tends to be around the 1 kHz one-third octave band. This is not problematic for this application as machinery noise tends to be a low-frequency issue. Other draw backs in transient excitation can be issues with non-linearity when sufficient signal is required to measure a sound pressure level in distant rooms.

In the following sections the advantages and disadvantages of steady-state and transient excitation to determine transmission functions in lightweight timber constructions are investigated and assessed experimentally.

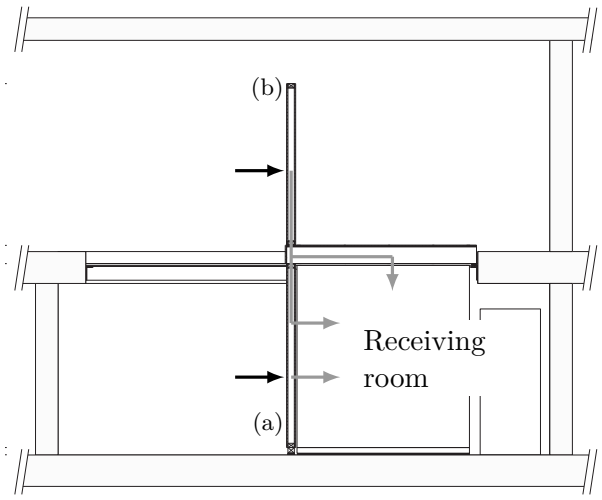

Figure 8.2: Transmission paths on the test structure. Excitation of wall (a) for direct transmission and wall (b) for diagonal transmission.

8.3 Experimental investigations

8.3.1 Laboratory measurements

8.3.1.1 Laboratory test structure

The laboratory measurements were carried on the test structure described in section 4.2. On this mock-up horizontal/direct and diagonal transmission was considered as indicated in Figure 8.2.

8.3.1.2 Comparison of steady-state and transient excitation

To compare steady-state and transient excitation three transmission paths were considered on the test structure. Horizontal transmission with excitation above a vertical wall stud, horizontal transmission with excitation in a bay and diagonal transmission with excitation above a vertical wall stud.

For horizontal transmission and steady-state excitation the set-up shown in Figure 4.6 was used. The force transducer (Type KF24, see Table 4.1) was only glued to the surface for the bay and stud excitation. The excitation signal was MLS from the Norsonic 840 (see Table 4.1) fed to the Brüel & Kjær shaker listed in Table 4.1. For transient excitation the impact hammer listed Table 4.1 with rubber and metal tips was used.

For diagonal transmission the same shaker was used but with pink noise. Additionally the force transducer was mounted to a washer that was additionally screwed to the vertical wall stud (see Figure 4.6). For transient excitation the same hammer with a metal tip was used.

For all situations, the power input was determined using the direct method (see section 4.5.6.1) with a pair of accelerometers (Type KS95B100) next to the excitation position. In the receiving room three microphones were used to sample six fixed positions in two measurements. For transient and steady-state excitation, the same microphone positions were used. All transducers were fed into the same multi channel FFT-analyser (PAK MKII, see Table 4.1). For transient excitation all channels were triggered by the force signal and processed with same FFT window length.

Correction for airborne flanking was not necessary for the spatial average sound pressure level.

8.3.1.3 Spatial variation of excitation positions

To assess whether an average transmission function, $D_{\mathrm{TF,av}}$, according to equation (8.2) can be used to represent a transmission situation globally, the influence of the excitation position and the range of transmission functions was investigated on the laboratory test structure. Therefore horizontal and diagonal transmission were considered as shown in Figure 8.2.

Measurements in the bay or above the vertical wall studs were carried out for diagonal and horizontal transmission to assess the influence of the stud distance. On the upper wall (a) (see Figure 4.2) additionally

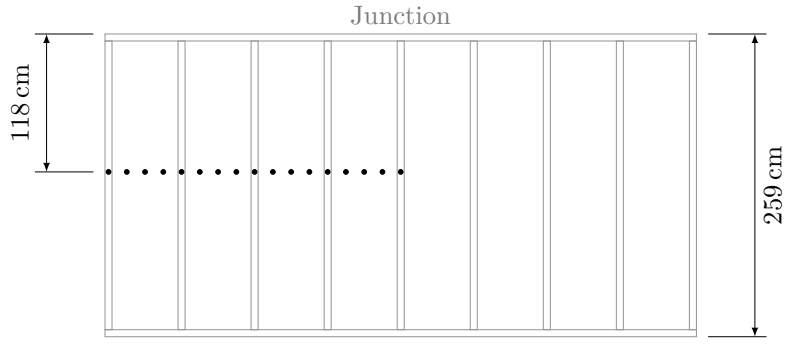

(a) 17 excitation positions on the lower wall.

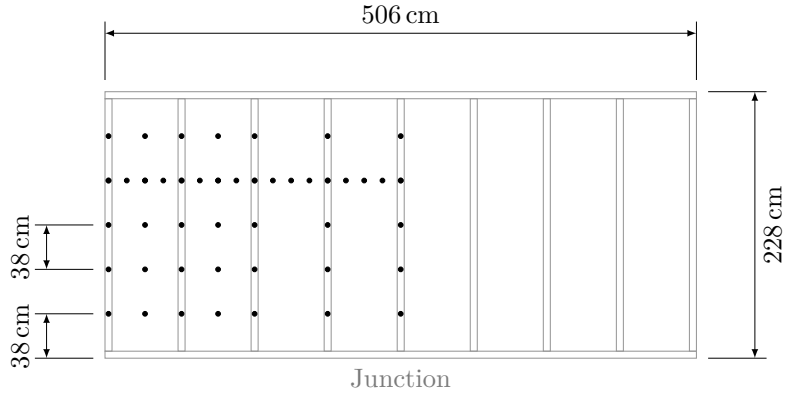

(b) 45 excitation positions on the upper wall.

Figure 8.3: Excitation positions to investigate the spatial variation on (a) horizontal/direct and (b) diagonal transmission.

the distance to the T-junction was investigated. The chosen positions for these measurements are shown in Figure 8.3.

8.3.2 Field measurements

8.3.2.1 Field test structures

Additionally to the simple laboratory test structure measurements were taken in the field with a variety of more complex constructions. Typical examples for constructions are shown in section 4.3.

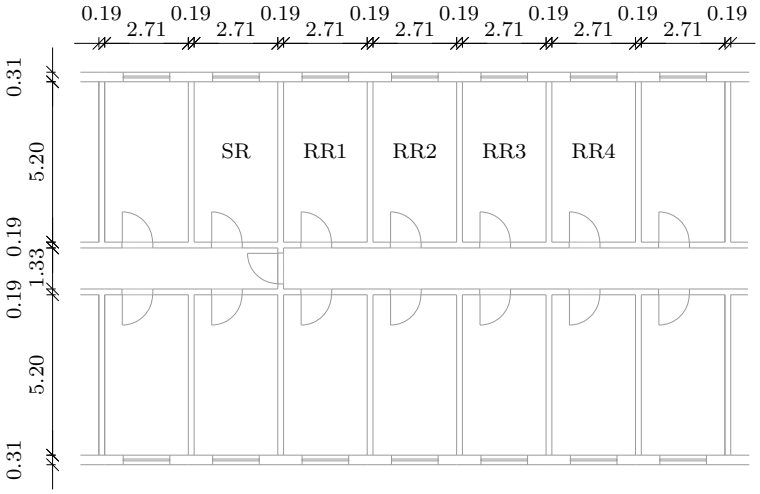

Figure 8.4: Field test construction: Ground floor plan of the timber-frame building (dimensions in metres).

8.3.2.2 Case study: Transmission to adjacent and non-adjacent rooms

In an unoccupied timber-frame building it was possible to assess the procedure to measure transmission functions in the field. This building is used as accommodation for refugees and has a regular floor plan. It is therefore well suited to investigate the transmission from a source room (SR) to an adjacent receiving room (RR1) and non-adjacent receiving rooms (RR2 – RR4) as shown in Figure 8.4. Additionally this allows identification of the limitations in measuring transmission functions in the field using either steady-state or transient excitation.

All the rooms are identical with a volume of $35.2\,\mathrm{m}^3$ and are separated by timber-frame walls. These were covered with two layers of 12.5 mm plasterboard on one side. On the opposite side timber laths are mounted on resilient channels. This side is covered with 25 mm gypsum fibre boards. This separating wall has a sound reduction index R_w of $\approx 58\,\mathrm{dB}$. In all rooms the floor is covered with a floating screed and the ceiling is suspended on hangers.

8.3.2.3 Survey for different field constructions and transmission paths

As indicated in section 4.3 there is a range of possible constructions that exist for timber-frame buildings. Therefore measurements were taken in a range of buildings including detached houses, guesthouses, apartment buildings and office buildings. In total nine buildings built by four different manufacturers were used. In each building several transmission functions were determined for horizontally, vertically or diagonally adjacent rooms. However only walls were excited as the measurements were taken at the end of the construction process were the floating screed was already built in.

To effectively determine a range of transmission functions, only transient excitation was used. In each situation at least two excitation positions were averaged; one above a stud and one in a bay. The spatial-average sound pressure level was corrected for airborne flanking transmission; however, this was negligible in most cases as the structure-borne path was usually dominant. Below the 100 Hz one-third octave band, the low-frequency procedure described in section 8.2.3 was applied.

8.3.3 Case studies: Application of transmission function for the prediction of machinery noise

In the following case studies, the application of transmission functions is assessed as empirical model to predict machinery noise. The prediction involves two stages: The first includes the calculation of the installed power, which is described in chapter 6. The second stage is covered by the measured transmission functions.

8.3.3.1 Excitation sources

Two multi-contact structure-borne sound sources are concerned: (a) The artificial source that is described in section 6.2.3 and (b) the ventilation system described in section 6.2.4). The input power is either estimated

from full mobility matrices (see section 6.4.1) or by using the simplifications described in section 6.4.2.

8.3.3.2 Transmission situations

For the case studies one transmission situation is considered in the laboratory and one in the field. In the laboratory test structure, horizontal transmission from the ventilation system is used. For the artificial source, horizontal transmission in a timber-frame building is chosen.

8.3.4 Transmission function for moment input power

The input power from a force hammer or a shaker only concerns the force perpendicular to the surface. Because machinery is potentially available to inject a moment power, the transmission function was also determined for moment excitation in the laboratory test structure. Therefore the procedure described in section 6.3 was used to obtain the installed moment power in one-third octave bands. For this set-up, the spatial-average sound pressure level was measured in the receiving room for horizontal transmission using the same microphone positions that were used for force excitation.

8.4 Results

8.4.1 Laboratory measurements

8.4.1.1 Comparison of steady-state and transient excitation

Figure 8.5 shows the comparison of transmission functions determined with transient and steady-state excitation. The corresponding differences are shown in Figure 8.6. The following cases are shown:

(a) Horizontal transmission with excitation directly above a stud (Figure 8.5a)
Steady-state excitation: washer to mount the force transducer wasglued to surface of the chipboard and additionally screwed in the

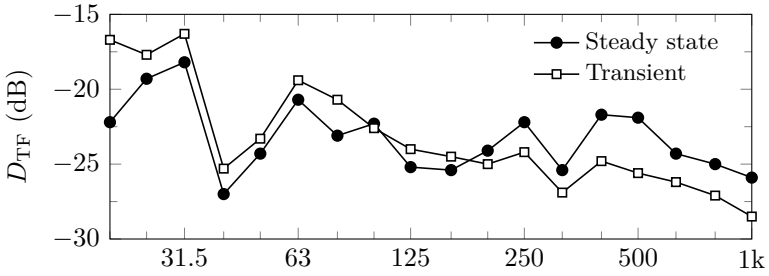

(a) Horizontal transmission with excitation on a stud.

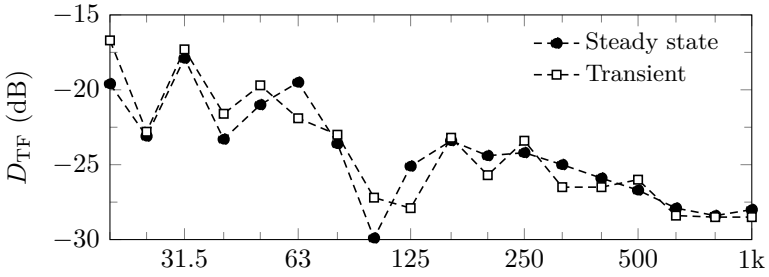

(b) Horizontal transmission with excitation in a bay.

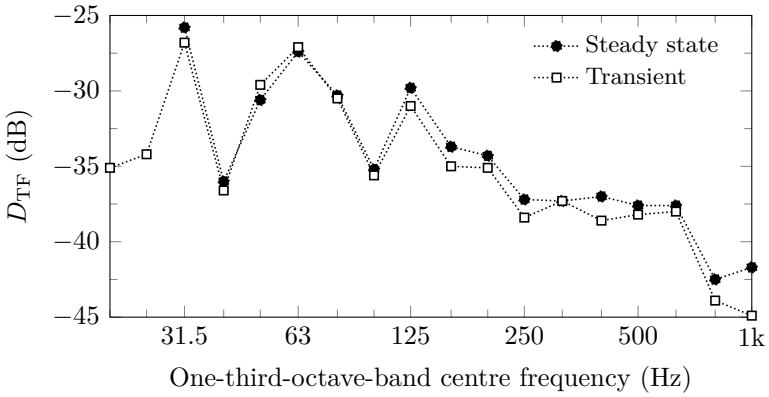

(c) Diagonal transmission with excitation on a stud.

Figure 8.5: Laboratory measurements. Comparison of transmission function for steady-state and transient excitation.

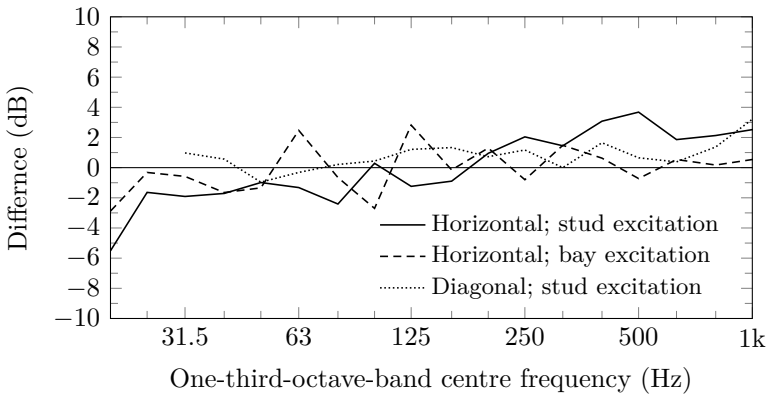

Figure 8.6: Laboratory measurements. Comparison of transmission function for steady-state and transient excitation. Differences: $D_{\mathrm{TF,steady-state}} - D_{\mathrm{TF,transient}}$ from the data in Figure 8.5.

stud (see Figure 4.6).
Transient excitation: force hammer with a rubber tip in the 20 Hz, 25 Hz and 31.5 Hz one-third octave bands and a metal tip at and above the 40 Hz one-third octave band.

(b) Horizontal transmission with excitation in a bay (Figure 8.5b).
Steady-state excitation: washer to mount the force transducer was glued to surface of the chipboard (see Figure 4.6)
Transient excitation: force hammer with a rubber tip in the 20 Hz, 25 Hz and 31.5 Hz one-third octave bands and a metal tip at and above the 40 Hz one-third octave band.

(c) Diagonal transmission with excitation on the chipboard directly above a stud (Figure 8.5c).
Steady-state excitation: washer to mount the force transducer was glued to the surface of the chipboard to mount the force transducer (NB The S/N ratio when using steady-state excitation was too low in the 20 and 25 Hz one-third octave bands to yield data)
Transient excitation: force hammer with a metal tip

The difference between steady-state and transient excitation is $< 2\,\mathrm{dB}$ for (a), (b) and (c) between 31.5 Hz to 1000 Hz. In the 20 Hz and 25 Hz bands, differences up to 5.5 dB occured. For horizontal transmission and stud excitation, the average difference above 250 Hz is $\approx 2.5\,\mathrm{dB}$. For bay excitation and horizontal transmission the average difference is $\approx 0.5\,\mathrm{dB}$ for the same frequency range. This could be due to the mounting conditions of the shaker for case (a) where additional screws were used to fix the force transducer into the stud. In comparison to transient excitation on the surface of the chipboard the power is then directly injected into the stud. However across the frequency range no systematic difference can be observed. As machinery predominately injects power at low frequencies the higher differences observed in case (a) are not important. Hence all three presented methods can be considered as equivalent and therefore transient excitation is preferred due to its practicability in the field.

To assess potential problems with non-linearity when using transient excitation, different force levels were applied in the laboratory and referred to steady-state excitation. Figure 8.7 shows the three force levels and the difference with respect to steady-state excitation for the obtained transmission function.

With the "weak" hit indicated in Figure 8.7a the signal to noise ratio was only 6 dB at and below the 25 Hz band. Hence the 20 Hz and 25 Hz bands were rejected in the transmission function shown in Figure 8.7b. For the comparison shown in Figure 8.7b only one fixed microphone position was used for both steady-state and transient excitation. The microphone was not moved between the measurements to exclude variations due to microphone positioning. The average results obtained with transient excitation using either a rubber or metal tip are $\approx$1 dB lower than steady-state excitation. The difference between the three different force levels does not show conclusive evidence of non-linearity for the "strong" hit. It can therefore be concluded that transient excitation can reasonably be used to obtain transmission functions.

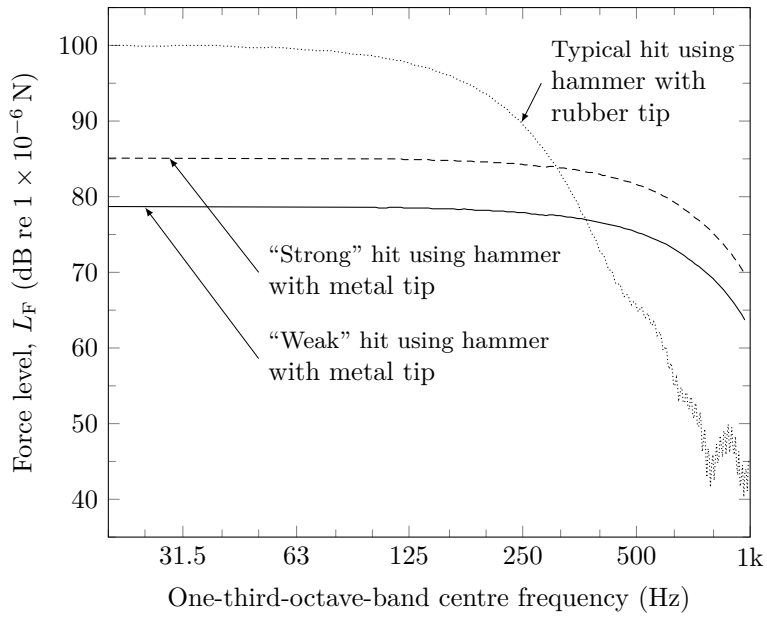

(a) Different force levels of the transient excitation with the force hammer.

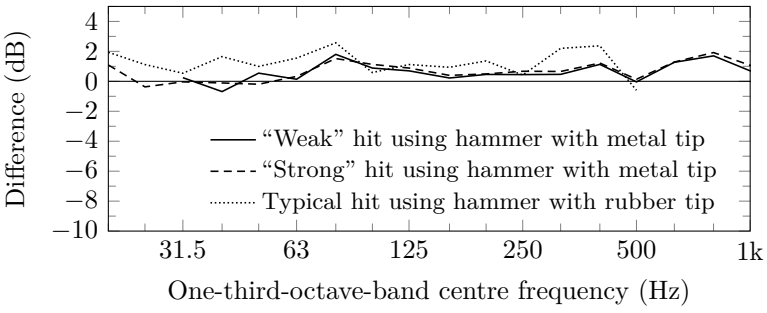

(b) Difference $D_{\mathrm{TF,steady-state}} - D_{\mathrm{TF,transient}}$ determined using transient and steady-state excitation.

Figure 8.7: Laboratory measurements. Investigation into the effect of different strength of transient excitation. (a) Applied force levels and (b) difference with respect to steady-state excitation for these three force levels.

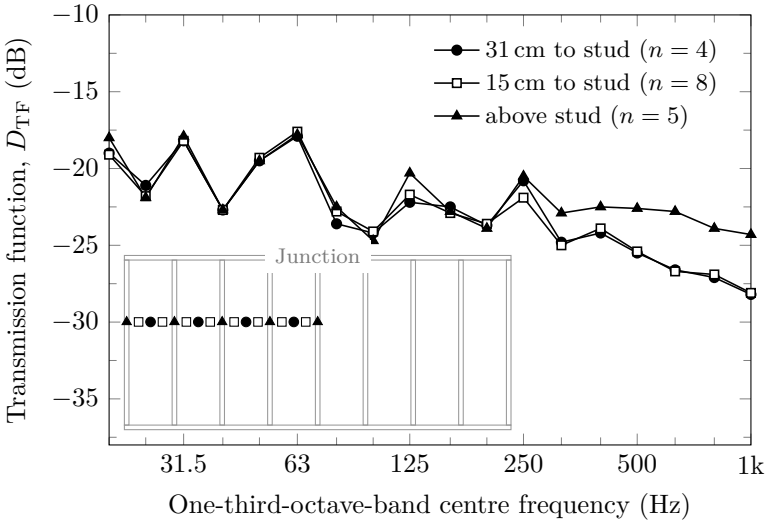

Figure 8.8: Laboratory measurements. Average transmission functions. Horizontal transmission measured above the stud and at different distances from the stud in the bay.

8.4.1.2 Spatial variation of excitation positions

To investigate the distance to the nearest stud three groups of excitation positions are used for horizontal and diagonal transmission: (1) positions above the stud, (2) positions 15 cm to the nearest stud (1/4 of stud spacing) and (3) positions in the middle of a bay. Figures 8.8 and 8.9 show average transmission functions for each of the three groups for horizontal and diagonal transmission respectively.

For each group the 95 % confidence intervals were ≈ 3 dB. For reasons of clarity the intervals are not added to the figures. It can be seen that for horizontal transmission the confidence intervals do not overlap above the 500 Hz one-third octave band.

Below this frequency and for the entire frequency range shown for diagonal transmission there is no obvious dependence of the excitation position. The higher values of the transmission function for stud excitation and horizontal transmission are potentially due to the strong structural transmission path across the stud (as indicated by SEA path analysis in

Figure 7.5). The average values for the three groups for diagonal transmission are within ±4 dB with less influence of the excitation position than for horizontal transmission.

For diagonal transmission additional investigations were carried out to assess the influence of the distance to the wall-floor-wall junction using five distances as shown in Figure 8.3b. Figure 8.10 shows average values of the transmission function for these five distances and positions above studs. Average values for positions in bays are shown in Figure 8.11.

For the stud and the bay excitation positions, the variation for the different distances is within ±4 dB below 500 Hz. For stud excitation the results are in a logical rank order above 500 Hz indicating higher values for positions closer to the junction. This can not be observed for bay excitation which could potentially be due to the empty cavities and for cavities filled with porous material it is likely to be different. Hence it can

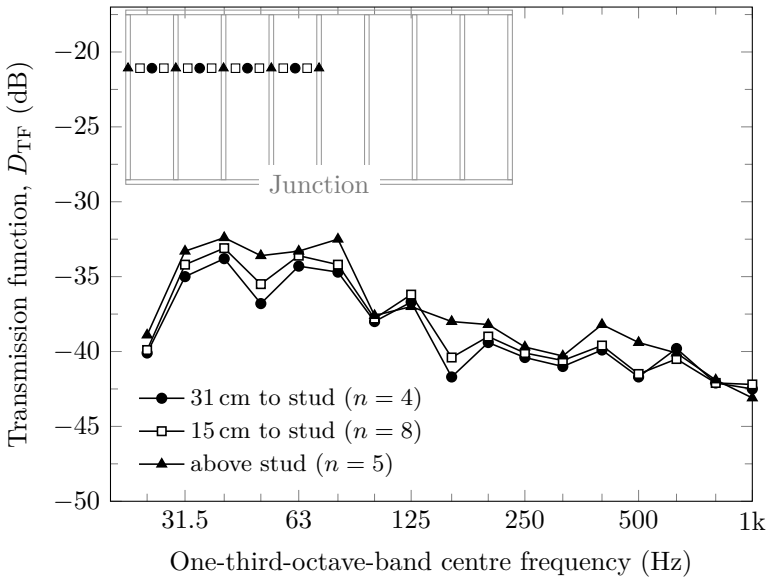

Figure 8.9: Laboratory measurements. Average transmission functions. Diagonal transmission measured above the stud and at different distances from the stud in the bay.

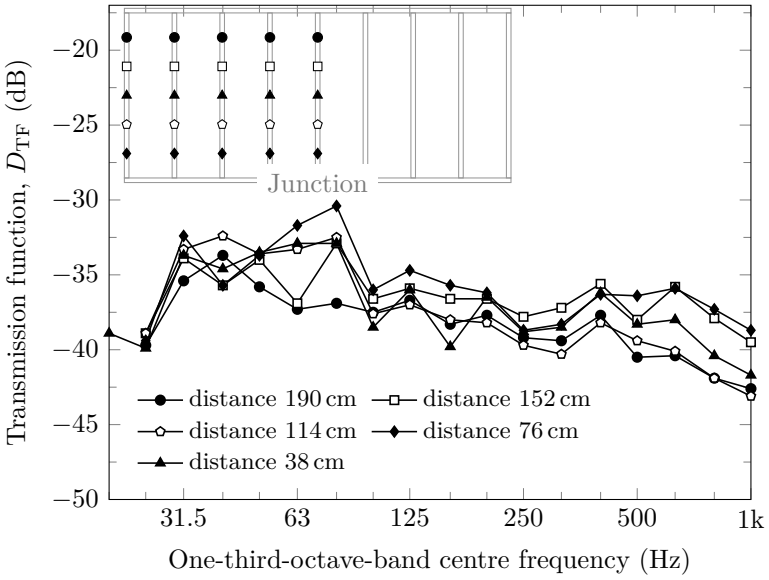

Figure 8.10: Laboratory measurements. Average transmission functions. Diagonal transmission measured above the stud ($n = 5$) at different distances from the junction.

be concluded that for frequencies below 500 Hz the transmission function is not significantly dependent on the choice of the excitation position.

Figure 8.12 shows the overall average of the chosen excitation position for horizontal and diagonal transmission including the 95 % confidence limits. The confidence limits are $\approx \pm 2$ dB for horizontal transmission and $\approx \pm 1$ dB for diagonal transmission. For diagonal transmission the S/N ratio was not sufficient in the 20 Hz band.

8.4.2 Field measurements

8.4.2.1 Case study: Transmission to adjacent and non-adjacent rooms

This case study is used to assess the limitations in using transient excitation to determine transmission functions. Therefore Figure 8.13 shows the average S/N ratio for the microphone positions in receiving rooms

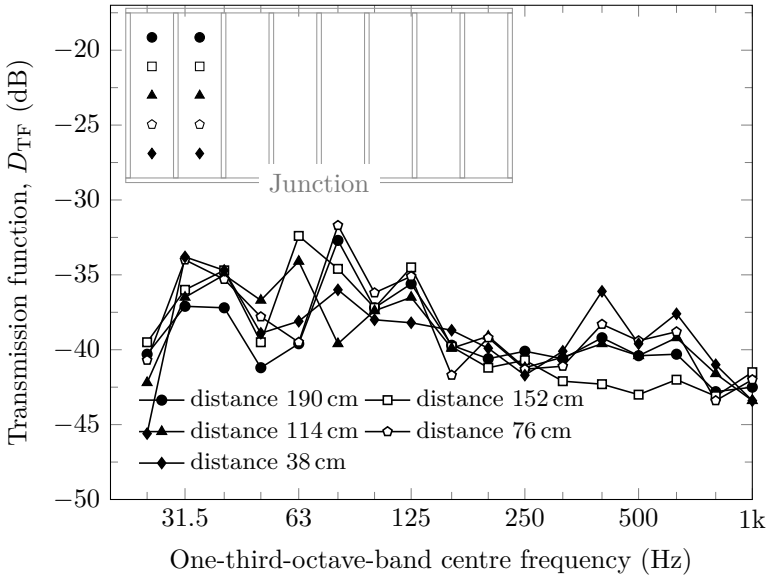

Figure 8.11: Laboratory measurements. Average transmission functions. Diagonal transmission measured in the bay ($n = 2$).

RR1 (adjacent), RR2 and RR3 for both metal and rubber tips on the force hammer. For ratios in the range between 6 dB and 10 dB the sound pressure levels were corrected by subtracting the background noise but for values below 6 dB the data was rejected.

For RR1 the S/N ratio is > 10 dB for the frequency range from 20 Hz to 1000 Hz for both hammer tips. Towards low frequencies (< 250 Hz) the rubber tip gives a higher S/N ratio than the metal tip. For the non-adjacent receiving rooms, RR2 and RR3, a S/N ratio >10 dB could not be achieved for all bands between 20 Hz and 1000 Hz in this field measurement. The background noise was particularly high in the 250 Hz band in this situation. Hence the values in this band had to be rejected as well as at low frequencies. The general trend shows that the rubber tip gives higher S/N ratios at low frequencies and the metal tip at high frequencies.

The results from these field measurements indicate that transient excitation can be used to determine the transmission function to adjacent

rooms in timber-frame buildings in the frequency range from 20 Hz to 1000 Hz. For non-adjacent rooms it is unlikely to be able to achieve sufficient S/N ratio for all bands in the range from 20 Hz to 1000 Hz. To increase the S/N ratio, measurements with a rubber and metal tip can be combined. However these findings are based on one particular building and background noise level. Other possibilities to increase the S/N ratio is the use different hammers (e. g. heavier) or low-noise microphones. Note that two of the three microphones in the receiving rooms in this case study were low-noise microphones.

To assess the range of transmission functions for rooms that are distant from the source room, MLS excitation was used to achieve a continuous transmission function in the frequency range from 20 Hz to 1000 Hz for the transmission from the source room SR to all receiving room RR1 to RR4. The results are shown in Figure 8.14. The transmission functions to RR1 is at least ≈ 10 dB higher than to RR2. The transmission function

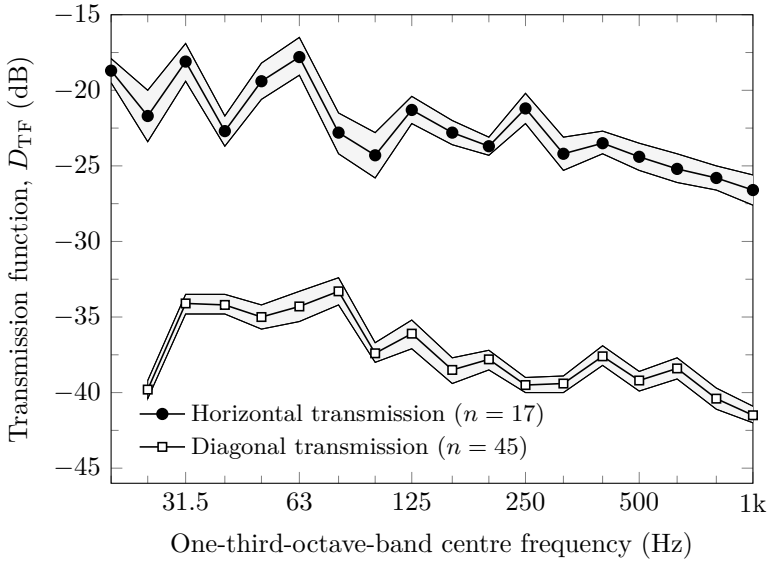

Figure 8.12: Laboratory measurements. Average transmission functions for horizontal and diagonal transmission from positions above studs and between studs with 95 % confidence limits.

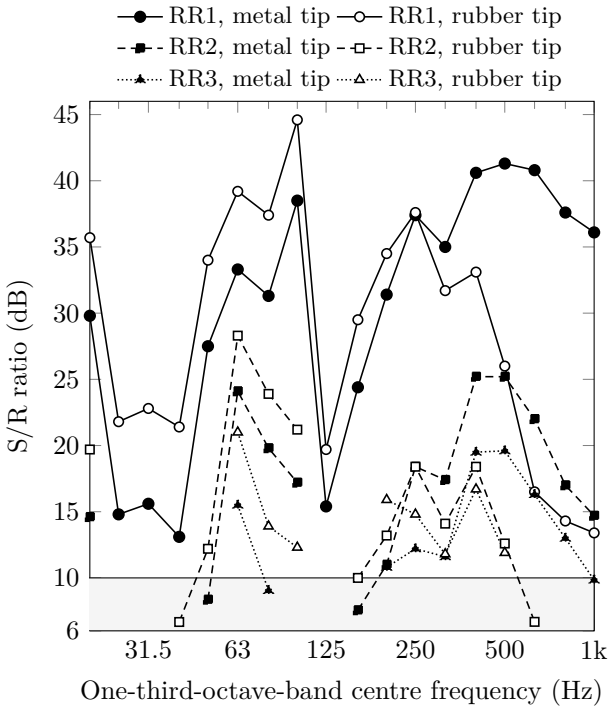

Figure 8.13: Field measurements: S/N ratio in receiving rooms RR1, RR2, and RR3 for transient excitation. Grey shading indicates S/N ratios between 6 and 10 dB.

to rooms RR3 and RR4 are similar indicating similar levels of flanking transmission.

8.4.2.2 Survey for different field constructions and transmission paths

The data measured in different buildings and constructions was grouped in terms of the direction of transmission and the type of construction. For the direction of transmission, horizontal, vertical or diagonal was concerned. Four construction types were available: (1) single framework walls which are commonly used as interior walls (an example is shown in Figure 4.5a), (2) single framework walls with additional lining that con-

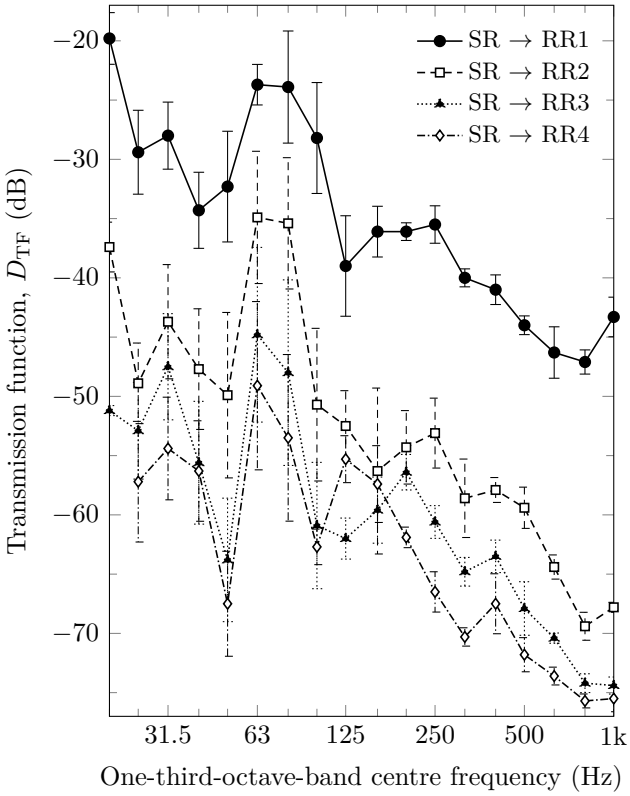

Figure 8.14: Field measurements. Transmission function to receiving rooms measured using an electrodynamic shaker and MLS at one excitation position. Results are shown as an average value with error bars indicating the 95% confidence limits (Student t distribution) where the variation is due to individual microphone positions.

tains pipework and is therefore typically used in bathrooms or kitchens (an example is shown in Figure 4.5b), (3) walls with separated framework which are commonly used as party walls (an example is shown in Figure 4.5c) and (4) exterior framed walls (an example is shown in Figure 4.5d).

With the available data from the field measurements in nine buildings, it was possible to form five groups of transmission functions in timber-frame constructions. A sixth group considers the transmission from the

basement to the ground floor. As household appliances are often positioned in the basement this is an important situation. However this involves both heavyweight and lightweight constructions as the basement exterior walls are made from concrete, the interior walls either masonry or concrete and the separating floor to the ground floor is made from concrete. The walls in the ground-floor are built using similar types of the timber-frame constructions shown in section 4.3. The range of transmission functions for these six groups are shown in the boxplots in Figure 8.15. Note that the data in this Figure uses $D_{\mathrm{TF,av}}$ according to equation (8.2) from 20 Hz to 40 Hz and $D_{\mathrm{TF,av,n}T}$ according to equation (8.3) from 50 Hz to 1000 Hz.

For horizontal transmission across single-framework walls (a), the interquartile range is between $\approx$ 10 dB to 15 dB from 20 Hz to 63 Hz and ranges between $\approx$ 5 dB to 10 dB from 80 Hz to 1000 Hz. This can be due to the use of $D_{\mathrm{TF,av}}$ below 50 Hz and $D_{\mathrm{TF,av,n}T}$ at and above 50 Hz. The spectral shape is relatively uniform and decreases slightly with increasing frequency, which is a similar trend to the laboratory results (see Figure 8.12). The spread of results is similar for horizontal transmission across a single-framework walls with additional lining (b). However the spectral shape differs slightly to single-framework walls without lining. There is stronger decrease with increasing frequency due to the additional layer. This however causes a potential deterioration at lower frequencies depending on the mass-spring-mass resonance frequency of the lining.

For horizontal transmission across party walls with a separated framework (c) two data-sets from two different buildings were measured. Both indicate a similar spectral shape with significant decrease towards high frequencies. However at frequencies below 50 Hz the values are in a similar range to single-framework walls.

For diagonal transmission with single-framework interior walls, the spread of results from six measurements is $\approx$ 10 dB to 15 dB on average between 20 Hz to 1000 Hz. In comparison to horizontal transmission (a), stronger decrease with increasing frequency can be observed. At low fre-

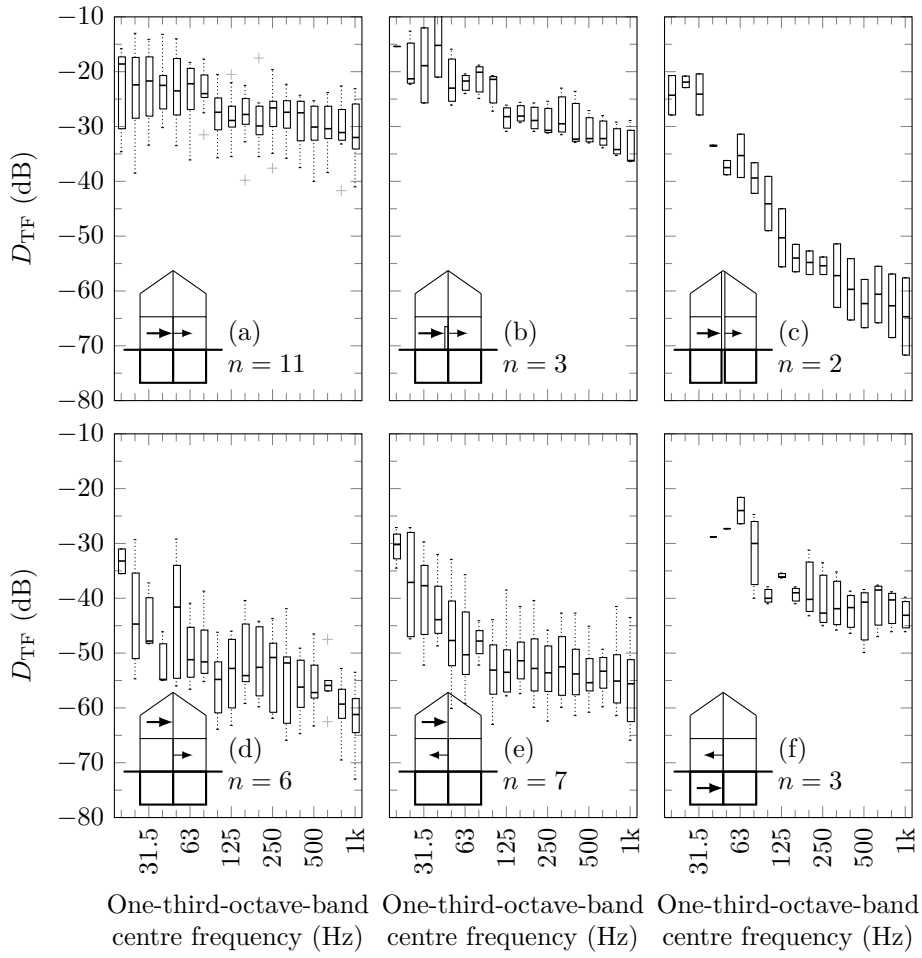

Figure 8.15: Field measurements. Survey of transmission functions measured with transient excitation in adjacent rooms.

quencies the values are about 10 dB below (a) and at high frequencies about 30 dB.

For vertical transmission (d) the behaviour is similar to diagonal transmission. However the trend indicates that the values are slightly higher than for diagonal transmission which can potentially be explained by the transmission path that does not cross the double wall.

The transmission from the basement to the ground floor was measured in three situations including diagonal and vertical paths. At low frequencies the S/N ratio was insufficient with transient excitation from a comparable light hammer (see Table 4.1) on a heavyweight concrete wall. The spectral shape is similar to vertical and diagonal transmission, however the values are higher, shifted by about 10 dB to 20 dB.

In general, the interquartile range for the chosen groups based on the available data is mainly up to 15 dB. However the spectral shape for all groups varies uniformly with frequency typically decreasing with frequency. The decrease is more pronounced for horizontal transmission across walls with additional constructive layers (linings or separated framework) or transmission across wall-floor-wall junctions. This survey gives an initial insight into the range of transmission functions that exist in timber-frame buildings. At present the data set is small and further measurements are necessary to develop robust groups. However the general trend shows that it is feasible to find groups to represent similar constructions and transmission directions. Average values from these groups can then be used in an empirical model to make a first estimate of the resulting sound pressure level in the receiving room.

8.4.3 Case studies: Application of transmission function for prediction of machinery noise

For two situations, the artificial source in the field and the ventilation system in the laboratory test structure, the sound pressure level was predicted by rearranging equation (8.1). The measured sound pressure level in the receiving room was corrected for background noise and airborne flanking using the same procedure applied for the determination of transmission function, where necessary.

8.4.3.1 Artificial source in the field

All four feet of the artificial source were attached to stud positions in the field transmission situation. The input power was calculated from

the source and receiver data using the two simplified approaches (a) and (e) described in section 6.4.2. Using the transmission function, this gives two predicted sound pressure levels, that only differ by the calculation method of the input power. The transmission function was measured with transient excitation at one of the four mounting positions of the source. The fixed microphone positions in the receiving room were not exactly the same for the measurement of the sound pressure level from the source and the sound pressure level to determine the transmission function. The predicted and measured spatial-average sound pressure levels in the receiving room are shown in Figure 8.16.

The difference between the measured and predicted sound pressure level for the artificial source in the timber-frame building are within ±10 dB and the 95 % confidence intervals mainly overlap. For frequencies at and above 400 Hz, the prediction tends to underestimate the sound pressure level by ≈6 dB (simplified approach (a)) and ≈4 dB (simplified approach (e)).

However on average there is close agreement (≈2 dB for simplified approach (a) and <1.0 dB for simplified approach (e)) between measurement and prediction. The summed and A-weighted SPL between 20 Hz and 1000 Hz is 55.3 dB for the measurement, 53.8 dB for prediction using simplified approach (a) and 55.9 dB for prediction using simplified approach (e).

8.4.3.2 Ventilation system in the laboratory

The ventilation system was attached to wall (a) (see Figure 4.1) of the laboratory test structure and the sound pressure level measured in the receiving room using the same microphone positions that were used for the determination of the transmission function. The input power was calculated from the source and receiver data using the full mobility matrices an simplified approach (e) described in section 6.4.2. For the transmission function, the spatial-average of 17 excitation positions (see Figure 8.12)

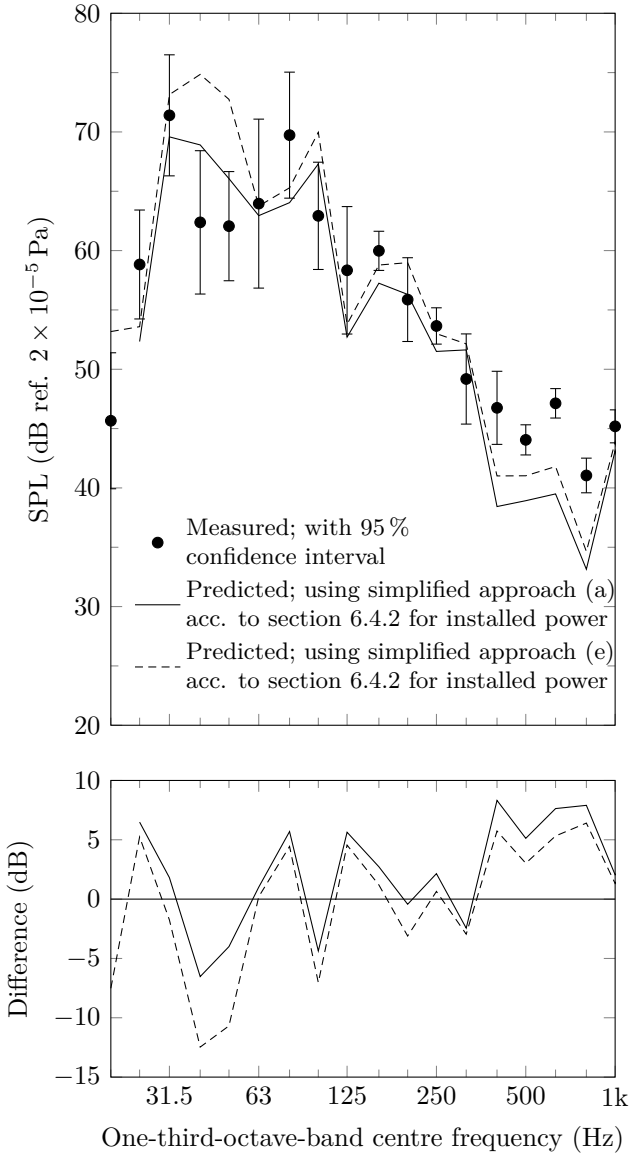

Figure 8.16: Artificial source in the field: Measured and predicted SPL.

was used. The predicted and measured spatial-average sound pressure levels in the receiving room are shown in Figure 8.17.

For the ventilation system in the laboratory test structure, the difference between the measured and predicted sound pressure levels is within ±10 dB and the 95 % confidence intervals mainly overlap. Similar to the artificial source in the field, the agreement is reasonable. However the predicted sound pressure level overestimates the maximum in the 50 Hz band. Note, that the first axial mode in the receiving room perpendicular to the wall is at 48 Hz. The peak of the installed power is in the 50 Hz band (see section 6.4.4) which can be a potential reason for the pronounced response in this band. Above 500 Hz the prediction tends to underestimate by ≈5 dB using full matrices and ≈3.5 dB using simplified approach (e), similar to the case study with the artificial source in the field. The summed and A-weighted SPL between 20 Hz and 1000 Hz is 30.7 dB for the measurement, 37.5 dB for prediction using full matrices and 38.0 dB for prediction using simplified approach (e).

8.4.3.3 Discussion

Both case studies show reasonable agreement on average. However for both situations the prediction tends to underestimate towards high frequencies. This could potentially be due to the fact that the transmission function only includes injected power from the force component perpendicular to the surface. In contrast, the measured sound pressure includes all excitation components and is therefore potentially higher if the force component is not dominant. In Figure 6.20 the relative importance of the out-of-plane force component in relation to the out-of-plane moment components is shown. As the data is very noisy it is not possible to identify clearly which components dominate. However in the mid-frequency range the trend shows that the force component dominates which is consistent with the close agreement of prediction and measurement between 63 Hz and 400 Hz in both case studies.

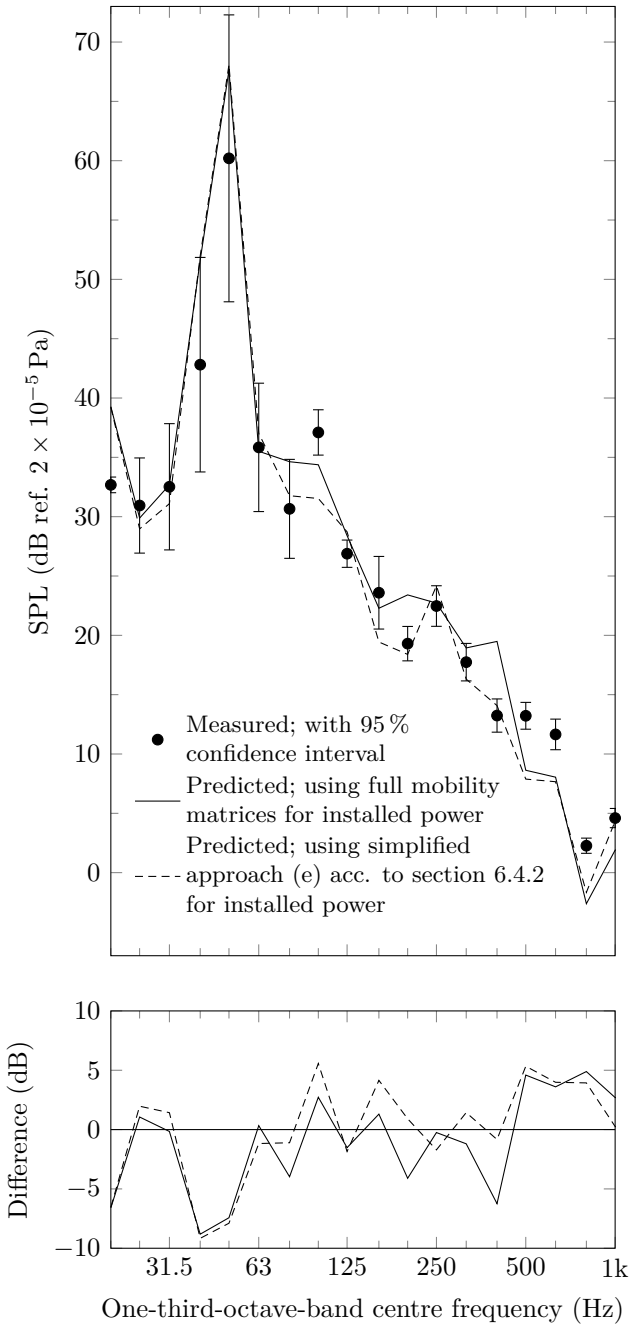

Figure 8.17: Ventilation system in the laboratory test-rig: Measured and predicted sound pressure level.

At low frequencies, the data from Figure 6.20 is too noisy to draw conclusions on a dominant component. However the differences between prediction and measurement are also due to uncertainties in the determination of the spatial-average sound pressure level at low frequencies. The prediction for the ventilation system overestimates the peak around 50 Hz and is therefore on the safe side. Towards high frequencies, Figure 6.20 indicates that moment components could potentially be significant. However, the spectrum of the ventilation system shows that only the low-frequency range is relevant as there is a significant decrease with increasing frequency. Even for the artificial source, that was driven with broadband noise the low-frequency range dominates. Hence the underestimation of the prediction at high frequencies is not problematic.

8.4.4 Using moment input power

Using the set-up shown in Figure 6.21 the timber-frame wall (a) of the laboratory test structure was excited with a moment. Both out-of-plane moments, M_x and M_y are considered. The active power in one-third octave bands was determined using the procedure to close gaps that occurred due to noisy results (see Figure 6.15 and section 6.3.2.2). Figure 8.18 shows the transmission function determined using the input power for moment excitation. For comparison, the average transmission function $D_{\mathrm{TF,av}}$ for 17 excitation position with force excitation is included.

Note that the transmission functions for moment excitation can only be regarded as indicating trends because there were a lot of gaps in the input data of the active power determined using the inverse procedure. However when these one-third octave bands with broad gaps were disregarded, the transmission functions for all three excitation components are very similar. Although the data does not allow strong conclusions, the results indicate, that if a machine is able to inject moment power, this will be transmitted with a similar effectiveness to the power injected by a pure force.

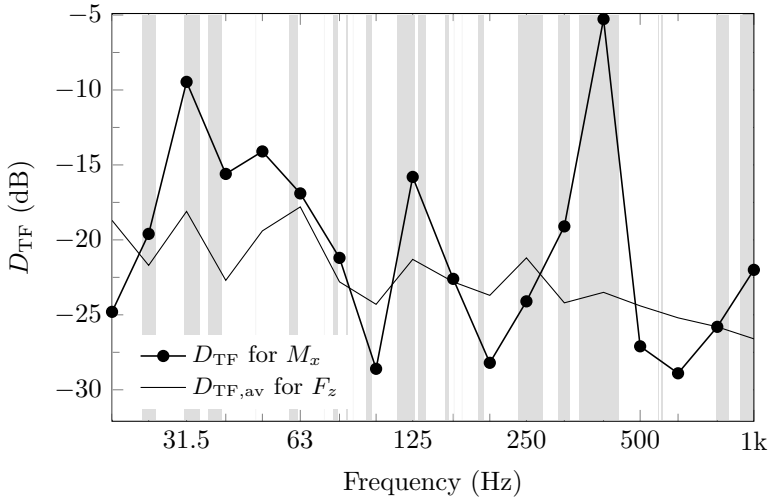

(a) Moment about x-axis, M_x.

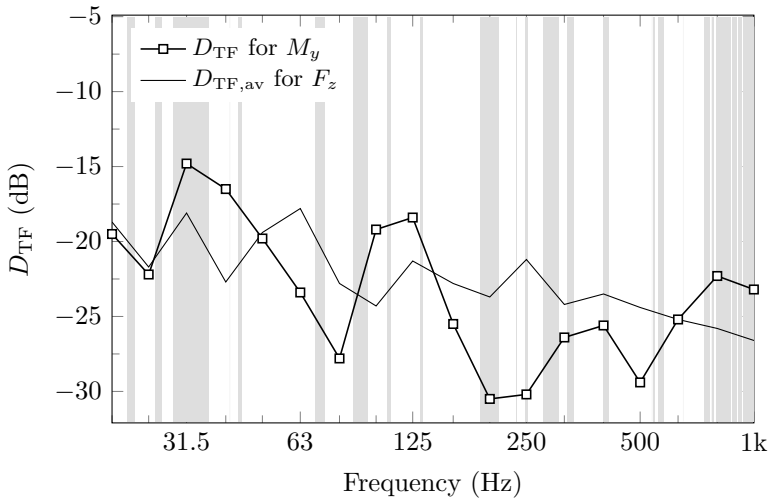

(b) Moment about y-axis, M_y.

Figure 8.18: Transmission function for moment excitation and horizontal transmission in laboratory test structure. The grey shaded areas indicated narrow band frequency ranges for which the active moment power determined with the inverse method was negative. For comparison the average transmission function for force excitation from Figure 8.12 is included.

8.5 Summary

In this chapter an approach was presented defining a measured transmission function for the transmission of structure-borne sound from machinery. This empirical approach is suited to estimation of machinery noise in building acoustic consultancy.

The quantity D_{TF} was introduced and the transmission function defined as the ratio between the spatial average sound pressure level and the structure-borne sound power input. Laboratory and field measurements were carried out to assess the procedure and to identify limitations in the experimental determination. To collect a data set as a basis for the empirical model, field measurements were carried out in nine timber-frame buildings. In case studies, transmission functions were applied for the prediction of machinery noise using measured sound pressure levels as reference. As machinery potentially also injects moment power, the transmission function was also determined for excitation with moment power.

Investigations to assess the procedure concerned the excitation type, issues with non-linearity and the dependence of the excitation position on the excited building element. Comparison of transient and steady-state excitation in the laboratory showed that in the relevant frequency range, the agreement between them is $<2\,\mathrm{dB}$. As transient excitation with a force hammer is more effective it is preferred especially for field measurements. This is a potentially quick and cost-effective method to obtain the data necessary for the empirical model. Investigations with different force levels for the excitation showed that there is no issue with non-linearity. Experiments that varied the excitation in the laboratory test structure showed that there is no dependence on the excitation position except at high frequencies for horizontal transmission. However as low frequencies are usually important for machinery noise this is not considered problematic, particularly as the deviations were only about $3\,\mathrm{dB}$ on average above $250\,\mathrm{Hz}$. For more complicated paths (i. e. diagonal paths which include flanking) the trend indicates that the dependence of

the excitation position becomes less important. In the laboratory investigation the overall confidence limits for all excitation positions was ±2 dB for horizontal/direct transmission and ±1 dB for diagonal transmission.

In a field case study the limitations of transient excitation were considered. It is concluded that transient excitation can be used to achieve transmission functions over the frequency range from 20 Hz to 1000 Hz for transmission to adjacent rooms. For distant rooms it is still applicable, however insufficient S/N ratios can occur in some one-third octave bands. The use of different hammer tips and/or hammers as well as low noise microphones can improve the signal-to-noise ratio and extend the application. Additionally low noise microphones can be used. This is beneficial because transient excitation offers advantages in field measurements where intermittent background noise can occur. In this situation a short measurement time is useful. If there is a constant high background noise level then excitation with MLS can be used as an alternative.

A survey of transmission functions measured in nine timber-frame buildings gives initial insights into the range of transmission functions. The available data was grouped into similar constructions and transmission directions which can be the basis for a catalogue that can be used for prediction. Based on the available data, the interquartile range within the groups was up to 15 dB. Further measurements could refine the groups and decrease the range within them. The promising feature about this survey is that the transmission functions vary uniformly with frequency and therefore seem to be suitable for an empirical model. Horizontal transmission across single-framework walls shows a flat spectrum that slightly decreases with frequency. For double-framework walls or longer paths, there is a more pronounced decrease in level in the spectrum with increasing frequency.

Using the artificial source and the ventilation system presented in chapter 6, the transmission function approach was applied by predicting and measuring the sound pressure level with these sources in operation. The differences were within ±10 dB. However on average in the frequency range from 20 Hz to 1000 Hz there is agreement. Towards high frequen-

cies the prediction tends to underestimate which could be due to additional excitation components that are not included in the transmission functions measured with a force hammer or shaker. In addition the rotational components are not included in the installed power of the sources that was determined for the force component only.

The moment power determined using inverse methods described in chapter 6 was used to obtain transmission functions for moment excitation. Although the data was affected by noise, the trend shows, that the transmission for all three out-of-plane excitation components are a similar order of magnitude. This indicates that if a machine is able to inject a moment power, this power is transmitted as effectively as power injected from a pure force.

9 Conclusions

The work reported in this thesis concerned the problem of machinery noise in timber-frame buildings. This required investigations into the vibro-acoustics of timber-frame structures excited by SBS sources which involves both the source emission and the transmission process. A general theme in the thesis was to take the complex aspects of SBS excitation and transmission in framed timber constructions and simplify them as engineering methods for the field of building acoustics.

The structure of the conclusions follows the stages involved in the emission (generation and coupling between source and receiver) and transmission (propagation and radiation) of SBS as shown in Figure 1.2. Finally recommendations for further work are given.

9.1 Structure-borne sound emission

To determine the SBS power for multi-point sources using the full mobility matrices requires extensive experimental work on the source and the receiving structure. For this reason, simplified approaches for the calculation of the transmitted power were investigated to try and reduce the required data. Only out-of-plane forces were regarded and the

simplified approaches were compared with full mobility matrices for all contact points. The simplified approaches considered omitting the transfer mobilities, using only one contact point of the source representative for all others, using averaged magnitudes of the mobilities and using a constant value for the mobility of the receiving structure (which tends to be relatively constant in lightweight buildings).

The results showed that the difference between the simplified approaches and the full mobility matrices was within ±5 dB for the majority of one-third octave bands between 20 Hz and 2000 Hz. Using a constant value for the receiver mobility the deviations were up to 10 dB in two one-third octave bands for the artificial source and in one one-third octave band for the ventilation system. For intermediate simplification steps (except using averaged magnitudes) the differences were within ±5 dB in the range from 20 Hz to 2000 Hz.

Further investigations into the source emission considered the importance of out-of-plane moment excitation. As moments can not be measured directly, this involved investigations into the applicability of inverse measurements to determine the moment power of unknown sources. Experiments were carried out with an idealized moment source that was a shaker attached parallel to the surface of the receiver with a lever. The results showed that inverse methods can be significantly affected by noise, but can be used to determine the moment power by closing gaps at troughs in the power data by setting negative real parts to zero. Using the reception plate power as reference, it was shown that the idealized source excited a moment.

To investigate the relative importance of moment excitation, one contact point of the artificial source was attached to a free chipboard plate. None of the three out-of-plane components clearly dominated because the results were noisy, but the trend indicated that the force dominated over the majority of the frequency range.

In terms of the transmission between the source and the timber-frame test structure, the spatial variation of the driving-point and moment mobilities was investigated experimentally. The results confirmed the use

of an equivalent orthotropic plate model at low frequencies and the consideration of only the sheeting plate at high frequencies. Considering moment mobilities, it was found that at excitation positions between beams, there is no difference between the two out-of-plane moment mobilities. However most machinery will be fixed above studs and above a beam there is a difference if the moment acts about the axis of the beam or perpendicular to the beam axis. It was shown that at low frequencies below 250 Hz infinite beam theory tends to give an upper limit for the moment mobility whereas infinite plate theory for an equivalent orthotropic plate tend to give a lower limit. The moment mobility that acts about the beam axis shows similar values to positions between beams. At high frequencies moment mobilities tend towards the behaviour of an infinite plate (with the properties of the sheeting material).

9.2 Building transmission

Considering the building transmission experimental work on a laboratory test structure was used to gain insight into the vibrational behaviour of timber-frame constructions excited by mechanical point excitation. The structure under test was a timber-frame wall with a single layer of tongue and grooved chipboard plates screwed to each side of the framework and empty cavities. The results confirmed three characteristics for different frequency regimes.

At low frequencies (below 50 Hz), where the spacing of the studs is smaller than half the bending wavelength of the sheeting material, the wall behaves as one single equivalent orthotropic plate. The stiffness parameters of this equivalent orthotropic plate can be estimated from the sheeting and stud parameters parallel and perpendicular to the stiffening ribs. At frequencies where half a bending wavelength of the sheeting material is smaller than the spacing of the studs but greater than the spacing of the point connections (screws or nails) along the beams, the structure indicates characteristics of ribbed-plates with line-connected behaviour. At frequencies above 140 Hz, where half a bending wavelength of the

sheeting material is smaller than the spacing of the point connections, the vibrational response can be described by the properties of the sheeting material only.

Although the behaviour indicates typical aspects of line-connected ribbed plate theory, these were not as pronounced as reported in previous work by Nightingale and Bosmans [1999] and Schoenwald [2008]. This indicates that the application of theory for periodic structures is not generally applicable to timber-frame building structures due to differences in the actual construction and variations in the material properties or craftsmanship.

The radiation efficiency was calculated using the model provided by Leppington et al. [1982] using either equivalent orthotropic plate properties or the properties of the sheeting plates. The results indicated a transition between these two approaches in the range from ≈80 Hz to ≈160 Hz. Additionally it was found that measured radiation efficiency follows the prediction when rectangular plates with the properties of the sheeting material and the size of the bays are considered above 160 Hz. At frequencies above 1250 Hz the radiation efficiency agrees with the prediction that uses the sheeting plate properties and the dimensions of the whole wall.

It is concluded that it is sufficient to consider an equivalent orthotropic plate at low frequencies and the sheeting plate properties at mid and high frequencies to describe the dynamic response of the wall. However to calculate the radiation efficiency it is necessary to consider rectangular plates with the size of the cavities in the mid frequency range.

Using structural intensity measurements it was observed that there is a significant decrease in the net-power flow in the direction perpendicular to beams with increasing frequency. The velocity level difference from the excited surface to the opposite surface of the wall showed high values close to the excitation point and ≈0 dB for the farthest sheets. Therefore a uniform distribution of energy can not be assumed for timber-frame walls or floors especially at mid and high frequencies. Using the measured phase relationship between positions on the source and receiving leaves it

was shown that both leaves are uncorrelated above the mass-spring-mass resonance frequency. For typical timber-frame constructions this occurs below 100 Hz. To model sound transmission with mechanical excitation from SBS sources, this means that SEA can potentially be used above ≈100 Hz.

Three SEA models were developed for direct transmission across the wall with mechanical point excitation. It was found that to predict the vibration levels on the source and receiving leaf, it is necessary to use a model that subdivides the structure into subsystems that represent the individual building elements, i. e. the beams and plates that form the wall. A typical six-subsystem model for cavity walls that uses the source and receiving room, the excited and opposite leaf, the cavity and the framework as subsystems was not suitable when point excitation is considered. However, comparison of SEA with the measured velocity levels showed that a 41-subsystem model that uses each timber stud and chipboard sheet as a subsystem can reproduce the vibration levels on both leafs with errors of up to ≈10 dB. As there is a significant decrease in vibration levels with distance, the region close to the excitation point is potentially the most important in terms of direct transmission, and the SEA model tends to have better accuracy in this region.

The SEA model can additionally be used to analyse sound transmission across different paths using SEA path analysis. This indicated the importance of including the room where point excitation is applied at frequencies above the critical frequency to model the decrease in vibration on the excited leaf. Below the critical frequency it was shown that the transmission is dominated by the structural transmission path across the framework which was modelled assuming rigid point connections between the plates and beams. For adjacent plates the dominant transmission path is across the beams to which both plates are coupled

An alternative approach to SEA describe the transmission from the injected power to the spatial average sound pressure level in a distant room was introduced based on measured transmission functions. The transmission function, D_{TF}, was defined as the ratio between the spatial-average

sound pressure level and the installed power and therefore describes the transmission including all flanking paths. However airborne flanking was excluded by applying a correction to the measured sound pressure level if SBS transmission was not dominant. The advantage of this approach is that the installed power, which is determined according to [EN 15657:2017] can directly be used as input data for prediction. In addition this transmission function can be written as a simple level difference which suits its application in building acoustic consultancy. The definition of D_{TF} and the associated measurement protocols in this thesis have been included in the latest revision of [ISO 10848-1:2017]. Villot [2017] has subsequently identified this approach as one of four possible methods for the prediction of sound levels generated by SBS source in lightweight buildings.

Laboratory investigations showed that the transmission function is not significantly dependent on the location of the excitation position on the timber-frame wall or floor. An average transmission function for a set of excitation positions can therefore be used to describe a transmission situation from a wall or floor to a distant room.

A field survey of D_{TF} was carried out in nine timber-frame buildings to identify the range of transmission functions that exist in timber-frame buildings. Within similar groups of constructions and transmission directions the interquartile range of the data is up to 15 dB. However the spectral shape for all identified groups varies uniformly with frequency. Hence there is the potential to refine the groups with more measurements to provide average transmission functions with low variation.

In two case studies, the data obtained from experimental source characterization was used to predict the sound pressure level by applying the transmission functions. The validation with measured sound pressure levels showed promising results with deviations of ± 10 dB in the range from 20 Hz to 1000 Hz with agreement on average in this frequency range.

Further laboratory investigations used the idealized moment source (shaker parallel to the surface) and inverse methods to determine the

transmission function for moment excitation. Although the inverse method was sensitive and delivered noisy results, the trend indicated that if a source is able to inject a moment power, this will be transmitted with similar efficiency as the same power input from out-of-plane force excitation.

9.3 Limitations of this work

The construction of the considered laboratory test-structure was chosen carefully to represent a typical timber-frame construction and the presented results are assumed to describe the typical vibrational behaviour of timber-frame structures undergoing mechanical point excitation. Nevertheless this is just one possible construction from a large variety of constructions that are described in the introduction.

Concerning the investigations on simplified approaches to predict the input power for multi-point sources, two case studies were considered. Although both were chosen carefully to represent typical building situations the specific results can not be applied to the full range of machinery that exists in practice. Although experimental investigations were carried out to assess the relative importance of moment excitation, noise in the measured data did not allow strong conclusions concerning this research question.

The application of an SEA model was presented for the frequency range from 100 Hz to 2000 Hz. Hence, concerning a detailed model no information could be given for frequencies below 100 Hz. There is potential to address the low-frequency range using a finite element model.

The suggested empirical approach to predict machinery noise gave promising results. However the measured set of data is currently too small to derive average transmission functions for prediction and to quantify the uncertainty.

9.4 Recommendations for further work

The application of inverse methods to determine moment excitation indicated that the procedure can be affected significantly by noise. Further research could focus on the effect of noise on inverse methods to improve the results in order to make clear statements about the relative importance of moment excitation in relation to out-of-plane force excitation.

Using infinite plate theory to predict moment mobilities gave reasonable agreement with measurements at mid and high frequencies except for moment mobilities above a stud perpendicular to the beam. Further work could concern the development of theory to predict moment mobilities for any position or direction on timber-frame structures.

Modelling the timber-frame wall undergoing mechanical point excitation using SEA required a 41-subsystem model. Results were presented in the range from 100 Hz to 2000 Hz. Further work could use FEM and measurements to assess whether the accuracy of the prediction can be improved. Modelling using FEM could provide the potential to expand the frequency range for prediction to lower frequencies.

The suggested approach of using measured transmission functions showed promising results. Further work is required to enlarge the existent database and characterize construction types for the development and establishment of a catalogue with average transmission functions in timber-frame buildings.

References

Allemang, R. J. (2003). "The Modal Assurance Criterion (MAC): twenty years of use and abuse". In: *Sound and Vibration Magazine* 37.8, pp. 14–23.

Arnold, J. and O. Kornadt (2014). "Beschreibung Körperschallinduzierter Schalldruckpegel mit Hilfe von Übertragungsfunktionen". In: *Bauphysik Kalender 2014*. Ed. by Fouad, N. A. D-69451 Weinheim, Germany: Wiley-VCH Verlag GmbH, pp. 641–663.

Bailhache, S. and M. Villot (2015). "Vibration response of lightweight building elements under structural excitation". In: *Proceedings of Inter-Noise 2015*. (Aug. 9–12, 2015). San Francisco, USA.

Bauman, P. D. (1994). "Measurement of structural intensity: analytical and experimental evaluytion of various techniques for the case of flexural waves in one-dimensional structures". In: *Journal of Sound and Vibration* 174.5, pp. 677–694.

Beranek, L. L. and G. A. Work (1949). "Sound transmission through multiple structures containing flexible blankets". In: *The Journal of the Acoustical Society of America* 21.4, pp. 419–428.

Betz, K. (2015). "Experimentelle Ermittlung der Körperschallleistung von haustechnischen Anlagen und der Körperschallübertragung in einem Holzbauprüfstand". Bachelorarbeit. Rosenheim: Hochschule Rosenheim.

Bietz, H. and V. Wittstock (2003). "Anmerkung zur Messung von Körperschall-Nachhallzeiten und Struktur Impedanzen in der Bauakustik". In: *CFA/DAGA*. Ed. by Deutsche Gesellschaft für Akustik e.V. Aachen.

Bosmans, I. and T. R. T. Nightingale (2001). "Modeling vibrational energy transmission at bolted junctions between a plate and a stiffe-

ning rib". In: *The Journal of the Acoustical Society of America* 109.3, pp. 999–1010.

Brunskog, J. and P. Hammer (2000). "Prediction models of impact sound insulation on timber floor structures; a literature survey". In: *Building Acoustics* 7.2, pp. 89–112.

Buhlert, K.-J. von and J. Feldmann (1979). "Ein Meßverfahren zur Bestimmung von Körperschallanregung und -übertragung". In: *Acustica* 42.3, pp. 108–113.

Champoux, Y., V. Cotoni, B. Paillard, and O. Beslin (2003). "Moment excitation of structures using two synchronized impact hammers". In: *Journal of Sound and Vibration* 263, pp. 515–533.

Churchill, C. and C. Hopkins (2016). "Prediction of airborne sound transmission across a timber–concrete composite floor using Statistical Energy Analysis". In: *Applied Acoustics* 110, pp. 145–159.

COST Action FP0702 (2012). *Net-acoustics for timber based lightweight buildings and elements: e-book*.

Craik, R. (1982). "The measurement of the material properties of building structures". In: *Applied Acoustics* 15.4, pp. 275–282.

Craik, R. J. M. (1996). *Sound transmission through buildings: Using Statistical Energy Analysis*. Aldershot, England and Brookfield, Vt., USA: Gower.

– (2003). "Non-resonant sound transmission through double walls using statistical energy analysis". In: *Applied Acoustics* 64.3, pp. 325–341.

Craik, R. J. M. and L. Galbrun (2005). "Vibration transmission through a frame typical of timber-framed buildings". In: *Journal of Sound and Vibration* 2005.281, pp. 763–782.

Craik, R. J. M., R. S. Ming, and R. Wilson (1995). "The measurement of structural intensity in buildings". In: *Applied Acoustics* 44, pp. 233–248.

Craik, R. J. M. and R. S. Smith (2000a). "Sound transmission through double leaf lightweight partitions: Part I: airborne sound". In: *Applied Acoustics* 61, pp. 223–245.

– (2000b). “Sound transmission through lightweight parallel plates: Part II: structure-borne sound”. In: *Applied Acoustics* 61, pp. 247–269.

Craik, R. J. (1981). “Damping of building structures”. In: *Applied Acoustics* 14.5, pp. 347–359.

Cremer, L. and M. A. Heckl (1967). *Körperschall: Physikalische Grundlagen und Anwendungen*. Berlin, Heidelberg, New York: Springer Verlag.

Crocker, M. J. and A. J. Price (1969). “Sound transmission using statistical energy analysis”. In: *Journal of Sound and Vibration* 9.3, pp. 469–486.

Davy, J. L. (2010). “The improvement of a simple theoretical model for the prediction of the sound insulation of double leaf walls”. In: *The Journal of the Acoustical Society of America* 127.2, pp. 841–849.

– (2012). “Sound transmission of cavity walls due to structure borne transmission via point and line connections”. In: *The Journal of the Acoustical Society of America* 132.2, pp. 814–821.

DIN 18041:2016-03. *Hörsamkeit in Räumen - Anforderungen, Empfehlungen und Hinweise für die Planung*. Ed. by Deutsches Institut für Normung e.V.

DIN 4109-1:2016-07. *Schallschutz im Hochbau - Teil 1: Mindestanforderung*.

DIN 4109-33:2016-07. *Schallschutz im Hochbau - Teil 33: Daten für die rechnerischen Nachweise des Schallschutzes (Bauteilkatalog) - Holz-, Leicht- und Trockenbau*.

Elliott, A. S. (2009). “Characterisation of stucture borne sound sources in-situ”. PhD thesis. Salford, UK: University of Salford.

Elliott, A. S., A. T. Moorhouse, and G. Pavic (2012). “Moment excitation and the measurement of moment mobilities”. In: *Journal of Sound and Vibration* 331, pp. 2499–2519.

EN 12354-1:2000. *Building acoustics – Estimation of acoustic performance of building from the performance of elements: Part 1: Airborne sound insulation between rooms*.

EN 12354-2:2000. *Building acoustics – Estimation of acoustic performance of building from the performance of elements: Part 2: Impact sound insulation between rooms.*

EN 12354-5:2009. *Building acoustics – Estimation of acoustic performance of building from the performance of elements: Part 5: Sound levels due to the service equipment.*

EN 13986:2004+A1:2015. *Wood-based panels for use in construction: Characteristics, evaluation of conformity and marking.*

EN 15657-1:2009. *Acoustic properties of building elements and of buildings – Laboratory measurement of airborne and structure-borne sound from building equipment: Part 1: Simplified cases where the equipment mobilities are much higher than the receiver mobilities, taking whirlpool baths as an example.*

EN 15657:2017. *Acoustic properties of building elements and of buildings - Laboratory measurement of structure-borne sound from building service equipment for all installation conditions.*

Fahy, F. J. (1995a). *Sound intensity.* 2nd ed. London: E & FN Spon.

– (1995b). "The vibro-acoustic reciprocity principle and applications to noise control". In: *Acustica* 81, pp. 544–558.

Flodén, O. (2014). "Vibrations in lightweight structures - Efficiency and reduction of numerical models". Dissertation. Lund, Sweden: Lund University, Sweden.

Galbrun, L. (2010). "Vibration transmission through plate/beam structures typical of lightweight buildings: Applicability and limitations of fundamental theories". In: *Applied Acoustics* 71.7, pp. 587–596.

Gardonio, P. and M. J. Brennan (2002). "On the origins and development of mobility and impedance methods in structural dynamics". In: *Journal of Sound and Vibration* 249.3, pp. 557–573.

– (2004). "Mobility and impedance methods in structural dynamics: Chapter 9". In: *Advanced Application in Acoustics, Noise and Vibration.* Ed. by Fahy, F. J. and Walker, J.

Gerretsen, E. (1979). "Calculation of the sound transmission between dwellings by partitions and flanking structures". In: *Applied Acoustics* 12.6, pp. 413–433.

Gerretsen, E. (1993). "Estimation of air-borne and structure-borne sound transmission from machinery in buildings". In: *Applied Acoustics* 40.3, pp. 255–265.

– (1994). "European developments in prediction models for building acoustics". In: *Acta Acustica* 2, pp. 205–214.

– (2000). "Prediction model for sound transmission from machinery in buildings: feasible approaches and problems to be solved". In: *Proceedings of Inter-Noise 2000*. (Aug. 27–30, 2000). Nice, France.

– (2015). "Extending EN 12354 sound insulation modelling to composed, light weight building systems". In: *Proceedings of Inter-Noise 2015*. (Aug. 9–12, 2015). San Francisco, USA.

Gibbs, B. M. (2003). "Towards a practical characterisation for sources of structure-borne sound". In: *Structural Dynamics - Recent Advances: Proceedings of the 8th International Conference*. (July 14, 2003–July 17, 2033). Southhampton, UK.

Gibbs, B. M. and A. R. Mayr (2012). "Estimates of mobility for prediction of structure-borne sound transmission in buildings". In: *Proceedings of ICSV19*. (July 8–12, 2012). Vilnius, Lithuania.

Gibbs, B. M. and B. A. T. Petersson (1996). "Measurement and characterisation of sources of structure-borne sound". In: *Proceedings of Inter-Noise 96*. (July 30–Aug. 2, 1996). Liverpool, UK, pp. 1307–1312.

Gibbs, B. M., N. Qi, and A. T. Moorhouse (2007). "A practical characterisation for vibro-acoustic sources in buildings". In: *Acta Acustica united with Acustica* 93.1, pp. 84–93.

Gross, D. et al. (2011). *Engineering Mechanics 2: Mechanics of Materials*. Berlin, Heidelberg: Springer-Verlag.

Grünewald, D. (2016). "Experimentelle Untersuchung der Schallabstrahlung einer Holzrahmenbauwand bei Punktanregung". Bachelorarbeit. Rosenheim: Hochschule Rosenheim.

Guigou-Carter, C. and M. Villot (2015). "Junction characteristics for predicting acoustic performance of lightweight wood-based buildings". In: *Proceedings of Inter-Noise 2015*. (Aug. 9–12, 2015). San Francisco, USA.

Guigou-Carter, C., M. Villot, and R. Wetta (2006). "Prediction method adapted to wood frame lightweight constructions". In: *Building Acoustics* 13.3, pp. 173–188.

Hammer, P. and J. Brunskog (2002). "Vibration isolation on lightweight floor structures". In: *Building Acoustics* 9.4, pp. 257–269.

Heckl, M. A. (1961). *Compendium of impedance formulas*. BBN Report No. 774. Bolt Beranek and Newman inc.

Höller, C. (2013). "Indirect methods of obtaining activity and mobility of structure-borne sound sources". PhD thesis. University of Liverpool.

Hongisto, V. (2006). "Sound insulation of double panels - Comparison of existing prediction models". In: *Acta Acustica united with Acustica* 92, pp. 61–78.

Hopkins, C. (2002). "Statistical energy analysis of coupled plate systems with low modal density and low modal overlap". In: *Journal of Sound and Vibration* 251.2, pp. 193–214.

– (2007). *Sound insulation*. Elsevier Butterworth-Heinemann.

Hopkins, C. and P. Turner (2005). "Field measurement of airborne sound insulation between rooms with non-diffuse sound fields at low frequencies". In: *Applied Acoustics* 66, pp. 1339–1382.

Huffington, N. J. (1967). "Bending athwart a parallel-stiffened plate". In: *Journal of Applied Mechanics* 34.2, pp. 278–282.

IEC 1043:1993. *Electroacoustics - Instruments for the measurement of sound intensity - Measurements with pairs of pressure sensing microphones*.

ISO 10848-1:2017. *Acoustics – Laboratory and field measurement of flanking transmission for airborne, impact and building service equipment sound between adjoining rooms: Part 1: Frame document*.

ISO 10848-2:2017. *Acoustics – Laboratory and field measurement of flanking transmission for airborne, impact and building service equipment*

sound between adjoining rooms: Part 2: Application to Type B elements when the junction has a small influence.

ISO 10848-3:2017. *Acoustics – Laboratory and field measurement of flanking transmission for airborne, impact and building service equipment sound between adjoining rooms: Part 3: Application to Type B elements when the junction has a substantial influence.*

ISO 10848-4:2017. *Acoustics – Laboratory and field measurement of flanking transmission for airborne, impact and building service equipment sound between adjoining rooms: Part 4: Application to junctions with at least one Type A element.*

ISO 12354-1:2017. *Building acoustics - Estimation of acoustic performance of buildings from the performance of elements: Part 1: Airborne sound insulation between rooms.*

ISO 12354-2:2017. *Building acoustics - Estimation of acoustic performance of buildings from the performance of elements: Part 2: Impact sound insulation between rooms.*

ISO 15712-1:2005. *Building acoustics - Estimation of acoustic performance of buildings from the performance of elements: Part 1: Airborne sound insulation between rooms.*

ISO 15712-2:2005. *Building acoustics - Estimation of acoustic performance of buildings from the performance of elements: Part 2: Impact sound insulation between rooms.*

ISO 16283-1:2014-06. *Acoustics – Field measurement of sound insulation in buildings and of building elements: Part 1: Airborne sound insulation.*

ISO 3382-2:2008. *Acoustics – Measurement of room acoustic parameters: Part 2: Reverberation time in ordinary rooms.*

ISO 3740:1980. *Acoustics; Determination of sound power levels of noise sources; Guidelines for the use of basic standards and for the preparation of noise test codes.*

ISO 3740:2000. *Acoustics - Determination of sound power levels of noise sources - Guidelines for the use basic standards.*

ISO 7626-2:1990-02. *Vibration and shock - Experimental determination of mechanical mobility: Part 2: Measurements using single-point translation excitation with an attached vibration exciter.*

ISO 7626-5:1994-07. *Vibration and shock - Experimental determination of mechanical mobility: Part 5: Measurements using impact excitation with an exciter which is not attached to the structure.*

ISO 9611:1996. *Acoustics - Characterisation of sources of structure-borne sound with respect to sound radiation from connected structures - Measurement of velocity at the contact points of machinery when resiliently mounted.*

ISO/DIS 10848-1:2016. *Acoustics – Laboratory and field measurement of the flanking transmission of airborne and impact sound between adjoining rooms: Part 1: Frame document.*

Jacobsen, F. and J. H. Rindel (1987). "Time reversed decay measurements". In: *Journal of Sound and Vibration* 117.1, pp. 187–190.

James, P. and F. J. Fahy (1994). *Weak coupling in statistical energy analysis.* ISVR Technical Report No. 228. Institute of Sound and Vibration Research.

Kihlman, T. (1978). "Urgent need for structure-borne sound source data". In: *Proceedings of Inter-Noise 78.* (May 8–10, 1978). San Francisco, USA.

Kimura, S. and K. Inoue (1989). "Practical calculation of floor impact sound by impedance method". In: *Applied Acoustics* 26, pp. 263–292.

Kohrmann, M. (2017). "Numerical methods for the vibro-acoustic assessment of timber floor constructions". PhD thesis. Munich: Technical University Munich.

Kouyoumji, J.-L. (2012). "Vibro-acoustic prediction of flanking transmission in lightweight timber framed constructions using SEA". In: *Proceedings of Inter-Noise 2012.* (Aug. 19, 2012–Aug. 22, 2013). New York City, USA.

Kruppa, P. (1986). "Measurement of structural intensity in building constructions". In: *Applied Acoustics* 19, pp. 61–74.

Kuttruff, H. (1979). *Room acoustics*. 2. ed. London: Applied Science Publ.

Leppington, F. G., E. G. Broadbent, and K. H. Heron (1982). "The acoustic radiation efficiency of rectangular panels". In: *Proceedings of the Royal Society A: Mathematical, Physical and Engineering Sciences* 382.1783, pp. 245–271.

Leppington, F. G., E. G. Broadbent, K. H. Heron, and S. M. Mead (1986). "Resonant and non-resonant acoustic properties of elastic panels. I. The radiation problem". In: *Proceedings of the Royal Society A: Mathematical, Physical and Engineering Sciences* 406.1831, pp. 139–171.

Leppington, F. G., K. H. Heron, E. G. Broadbent, and S. M. Mead (1987). "Resonant and non-resonant acoustic properties of elastic panels. II. The transmission problem". In: *Proceedings of the Royal Society A* 412.1843, pp. 309–337.

Lievens, M. (2008). "Characterising a washing machine as a structure borne sound source on a lightweight floor". In: *The Journal of the Acoustical Society of America* 123.5, p. 3502.

Lin, T. R. and J. Pan (2006). "A closed form solution for the dynamic response of finite ribbed plates". In: *The Journal of the Acoustical Society of America* 119.2, p. 917.

Ljunggren, F., C. Simmons, and K. G. Hagberg (2014). "Correlation between sound insulation and occupants' perception – Proposal of alternative single number rating of impact sound". In: *Applied Acoustics* 85, pp. 57–68.

London, A. (1950). "Transmission of reverberant sound through double walls". In: *The Journal of the Acoustical Society of America* 22.2, pp. 270–279.

Lu, J., B. Louvigne, J. C. Pascal, and J. Tourret (1990). "The perforated reception plate, a practical method for the characterization of structure-borne noise emitted by small equipments". In: *Proceedings of Inter-Noise 90*. (Aug. 13–15, 1990). Goteborg, Sweden, pp. 217–220.

Lyon, R. H. (1975). *Statistical energy analysis of dynamical systems - Theory and applications*. Cambridge, Mass.: MIT Press.

Lyon, R. H. and R. G. DeJong (1995). *Theory and application of statistical energy analysis*. 2nd ed. Newton, MA, USA: Butterworth-Heinemann.

Lyon, R. H. and G. Maidanik (1962). "Power flow between linearly coupled oscillators". In: *The Journal of the Acoustical Society of America* 34.5, p. 623.

Maidanik, G. (1962). "Response of ribbed panels to reverberant acoustic fields". In: *The Journal of the Acoustical Society of America* 34.6, pp. 809–826.

Mathiowetz, S. and H. A. Bonhoff (2013). "Multi-component power transmission from structure-borne sound sources into lightweight structures". In: *Proceedings of ICA 2013*. (June 2–7, 2013). Montreal, Canada.

Matsumoto, T., M. Uchida, H. Sugaya, and H. Tachibana (2006). "Development of multiple drywall with high sound insulation performance". In: *Applied Acoustics* 67.6, pp. 595–608.

Mayr, A. R. (2009). *Vibro-acoustic sources in lightweight buildings*. Berlin: Logos Verlag.

Mayr, A. R. and B. M. Gibbs (2011). "Point and transfer mobility of point-connected ribbed plates". In: *Journal of Sound and Vibration* 330, pp. 4798–4812.

– (2012). "Single equivalent approximation for multiple contact structure-borne sound sources in buildings". In: *Acta Acustica united with Acustica* 98, pp. 402–410.

– (2016). "Approximate method for obtaining source quantities for calculation of structure-borne sound transmission into lightweight buildings". In: *Applied Acoustics* 110, pp. 81–90.

Mead, D. J. (1996). "Wave propagation in continuous periodic structures: Research contributions from southampton, 1964–1995". In: *Journal of Sound and Vibration* 190.3, pp. 495–524.

Mead, D. J. and Š. Markuš (1983). "Coupled flexural-longitudinal wave motion in a periodic beam". In: *Journal of Sound and Vibration* 90.1, pp. 1–24.

Mecking, S. (2012). “Messung von Körperschall-Nachhallzeit an Holzbalkendecken”. Diplomarbeit. Rosenheim: Hochschule Rosenheim.

Mecking, S., A. R. Mayr, and U. Schanda (2012). “Messung von Körperschall-Nachhallzeiten inhomogener Strukturen am Beispiel einer Holzbalkendecke”. In: *Fortschritte der Akustik - DAGA*. Ed. by Deutsche Gesellschaft für Akustik e.V. Darmstadt.

Mitchell, L. D. and K. B. Elliott (1984). “How to design stingers for vibration testing of structures”. In: *Sound and Vibration* 18.4, pp. 14–18.

Mondot, J. M. and B. Petersson (1987). “Characterization of structure-borne sound sources: The source descriptor and the coupling function”. In: *Journal of Sound and Vibration* 114.3, pp. 507–518.

Moorhouse, A. T. (2001). “On the characteristic power of structure-borne sound sources”. In: *Journal of Sound and Vibration* 248.3, pp. 441–459.

Moorhouse, A. T., A. S. Elliott, and Evans. T. A. (2009). “In situ measurement of the blocked force of structure-borne sound sources.” In: *Journal of Sound and Vibration* 325.4, pp. 679–685.

Moorhouse, A. T. and B. M. Gibbs (1993). “Prediction of the stucture-borne noise emission of machines: Development of a methodology”. In: *Journal of Sound and Vibration* 1993.167 (2), pp. 223–237.

– (1995). “Measurement of structure-borne sound emission from resilently mounted machines in situ”. In: *Journal of Sound and Vibration* 1993.180 (1), pp. 143–161.

Moorhouse, A. T. et al. (2011). “Structure-borne sound and vibration from building-mounted wind turbines”. In: *Environmental research letters : ERL [Web site]* 6.3, p. 035102.

Nightingale, T. R. T. (1995). “Application of the CEN draft building acoustics prediction model to a lightweight double leaf construction”. In: *Applied Acoustics* 46.3, pp. 265–284.

Nightingale, T. R. T. and I. Bosmans (1999). “Vibration response of lightweight wood frame building elements”. In: *Building Acoustics* 6.3, pp. 269–288.

Nightingale, T. R. T. and I. Bosmans (2007). "Two modelling approaches for periodic rib-stiffend plates typical of floor assemblies". In: *Proceedings of ICSV14*. (July 9–12, 2007). Cairns, Australia.

Noiseux, D. U. (1970). "Measurement of power flow in uniform beams and plates". In: *The Journal of the Acoustical Society of America* 47.1B, pp. 238–247.

Ohlrich, M. (2011). "Predicting transmission of structure-borne sound power from machines by including terminal cross-coupling". In: *Journal of Sound and Vibration* 330.21, pp. 5058–5076.

Ohlrich, M. and C. Larsen (1994). "Surface and terminal source power for characterization of vibration sources at audible frequencies". In: *Proceedings of Inter-Noise 94*. (Aug. 29–31, 1994). Yokohama, Japan.

Pavic, G. (1976). "Measurement of structure borne wave intensity, Part I: formulation of the methods". In: *Journal of Sound and Vibration* 49.2, pp. 221–230.

Petersson, B. A. T. (1987). "On the use of giant magnetostrictive devices for moment excitation". In: *Journal of Sound and Vibration* 116.1, pp. 191–194.

– (1993a). "Structural acoustic power transmission by point moment and force excitation: Part I: Beam- and frame-like structures". In: *Journal of Sound and Vibration* 160.1, pp. 43–66.

– (1993b). "Structural acoustic power transmission by point moment and force excitation: Part II: Plate-like structures". In: *Journal of Sound and Vibration* 160.1, pp. 67–91.

Petersson, B. A. T. and B. M. Gibbs (2000). "Towards a structure-borne sound source characterization". In: *Applied Acoustics* 61, pp. 325–343.

Petersson, B. A. T. and J. Plunt (1980). *Structure-borne sound transmission from machinery to foundations*. Report 80-19. Chalmers University of Technology.

– (1982a). "On effective mobilities in the prediction of structure-borne sound transmission between a source structure and a receiving structure: Part I: Theoretical background and basic experimental studies". In: *Journal of Sound and Vibration* 82.4, pp. 517–529.

– (1982b). “On effective mobilities in the prediction of structure-borne sound transmission between a source structure and a receiving structure: Part II: Procedures for the estimation of mobilities”. In: *Journal of Sound and Vibration* 82.4, pp. 531–540.

Price, A. J. and M. J. Crocker (1970). “Sound transmission through double panels using statistical energy analysis”. In: *The Journal of the Acoustical Society of America* 47.3A, p. 683.

Rabold, A. (2010). “Anwendung der Finite Element Methode auf die Trittschallberechnung”. Dissertation. Technische Universität München.

Sanderson, M. A. (1995). “Direct measurement of moment mobility: Part II: An experimental study”. In: *Journal of Sound and Vibration* 179.4, pp. 685–696.

Scheck, J. (2011). “Characterisation of lightweight stairs as structure-borne sound sources”. Dissertation. University of Liverpool.

Scheck, J., S. Reinhold, P. Eschbach, and H.-M. Fischer (2016). “Messung und Prognose der Luft- und Körperschallübertragung von gebäudetechnischen Anlagen im Massivbau”. In: *Fortschritte der Akustik - DAGA*. (Mar. 14–17, 2016). Ed. by Deutsche Gesellschaft für Akustik e.V. Aachen.

Schoenwald, S. (2008). “Flanking sound transmission through lightweight framed double leaf walls: Prediction using statistical energy analysis”. PhD thesis. Technische Universität Eindhoven.

Scholl, W. (2005). “About a test facility for installation noise in wooden houses”. In: *Proceedings of Forum Acusticum 2005*. (Aug. 30–Sept. 2, 2005). Budapest, Hungary, pp. 1977–1981.

Schöpfer, F., C. Hopkins, A. R. Mayr, and U. Schanda (2017). “Measurement of transmission functions in lightweight buildings for the prediction of structure-borne sound transmission from machinery”. In: *Acta Acustica united with Acustica* 103, pp. 451–464.

Schroeder, M. R. (1965). “New method of measuring reverberation time”. In: *Journal of Sound and Vibration* 4972, pp. 409–412.

Sharp, B. H. (1978). "Prediction methods for the sound transmission of building elements". In: *Noise Control Engineering Journal* 11.2, pp. 53–63.

Sharp, B. H. and J. W. Beauchamp (1969). "The transmission loss of multilayer structures". In: *Journal of Sound and Vibration* 9.3, pp. 383–392.

Simmons, C. (1999). "Measurement of sound pressure levels at low frequencies in rooms. Comparison of available methods and standards with respect to microphone positions". In: *Acta Acustica united with Acustica* 85.1, pp. 88–100.

Soedel, W. (2004). *Vibrations of Shells and Plates*. 3rd ed. Mechanical Engineering Ser. Boca Raton: Chapman and Hall/CRC.

Späh, M. M. and B. M. Gibbs (2009). "Reception plate method for characterisation of structure-borne sources in buildings: Assumptions and application". In: *Applied Acoustics* 70, pp. 361–368.

Steel, J. A., R. J. M. Craik, and R. Wilson (1994). "A study of vibration transmission in a framed building". In: *Building Acoustics*, pp. 49–64.

Steenhoek, H. F. and T. Ten Wolde (1970). "The reciprocal mesurement of mechanical-acoustical transfer functions". In: *Acustica* 23, pp. 301–305.

Tanaka, N., S. D. Snyder, Y. Kikushima, and M. Kuroda (1994). "Vortex structural power flow in a thin plate and the influence on the acoustic field". In: *The Journal of the Acoustical Society of America* 96.3.

Ten Wolde, T. (1973). *Recipeocity experiments on the transmission of sound in ships: Proefschrift*. Delft: Drukkerij Hoogland en Waltman N.V.

Ten Wolde, T. and G. R. Gadefelt (1987). "Development of standard measurement methods for structureborne sound emission". In: *Noise Control Engineering Journal* 28.1, pp. 5–14.

Ten Wolde, T., J. W. Verheij, and H. F. Steenhoek (1975). "Reciprocity method for the measurement of mechano-acoustical transfer functions". In: *Journal of Sound and Vibration* 42, pp. 49–55.

Trochidis, A. (1982). "Körperschalldämpfung mittels Gas- oder Flüssigkeitsschichten". In: *Acta Acustica united with Acustica* 51.4, pp. 201–212.

Troitsky, M. S. (1976). *Stiffened plates: bending, stability and vibrations*. Amsterdam: Elsevier.

Vercammen, M. L. S. and P. H. Heringa (1989). "Characterising structure-borne sound from domestic appliances". In: *Applied Acoustics* 28, pp. 105–117.

Verheij, J. W., H. A. Janssens, and J. G. Charlier (1995). "Using pseudo-forces for characterization of structure-borne sound sources". In: *Proceedings of Inter-Noise 95*. Newport Beach,CA, USA.

Vigran, T. E. (2009). "Predicting the sound reduction index of finite size specimen by a simplified spatial windowing technique". In: *Journal of Sound and Vibration* 325.3, pp. 507–512.

– (2010). "Sound insulation of double-leaf walls – allowing for studs of finite stiffness in a transfer matrix scheme". In: *Applied Acoustics* 71.7, pp. 616–621.

Villot, M. (2017). "Predicting in situ sound levels generated by structure-borne sound sources in buildings". In: *Acta Acustica united with Acustica* 103.5, pp. 885–886.

Villot, M. and C. Guigou-Carter (2006). "Measurement methods adapted to wood frame lightweight constructions". In: *Building Acoustics* 13.3, pp. 189–198.

Villot, M. et al. (2016). "Predictions for lightweight constructions". In: *Inter-Noise 2016 - Satellite Syposium Building Acoustics*. (Aug. 25–16, 2016). Berlin, Germany.

Vogel, A. et al. (2016). "Prediction of sound pressure levels in rooms using EN 12354 and the characteristic structure-borne sound power of structure-borne sound sources". In: *Proceedings of Inter-Noise 2016*. (Aug. 21–24, 2016). Hamburg, Germany.

Warburton, G. B. (1954). "The Vibration of Rectangular Plates". In: *Proceedings of the Institution of Mechanical Engineers* 168.1, pp. 371–384.

White, M. F. and K. H. Liasjo (1982). "Measurement of mobility and damping of floors". In: *Journal of Sound and Vibration* 81.4, pp. 535–547.

Yap, S. H. and B. M. Gibbs (1998). "Structure-borne sound transmission from machines in buildings. Part 2: Indirect measurement of force and moment at the machine-receiver interface of a single point connected system by a reciprocal method". In: *Journal of Sound and Vibration* 1999.222 (1), pp. 99–113.